2024

Transitions To Two-Hadron States From Quantum Chromodynamics

Felipe Ortega Gama
College of William and Mary - Arts & Sciences, fgortegagama@wm.edu

Transitions to Two-Hadron States from Quantum Chromodynamics

Felipe Gilberto Ortega Gama

Toluca, Mexico, Mexico

Master of Science, The College of William and Mary, 2020
Master of Science, University of Waterloo, 2018
Bachelor of Science, Tecnológico de Monterrey, 2017

A Dissertation presented to the Graduate Faculty of
The College of William and Mary in Virginia in Candidacy for the Degree of
Doctor of Philosophy

Department of Physics

The College of William and Mary in Virginia
August, 2024

APPROVAL PAGE

This Dissertation is submitted in partial fulfillment of
the requirements for the degree of

Doctor of Philosophy

Felipe Gilberto Ortega Gama

Approved by the Committee, August 2024

Committee Chair
Jozef Dudek, Associate Professor, Physics
College of William & Mary

Eugeniy Mikhailov, Associate Professor, Physics
College of William & Mary

Justin Stevens, Associate Professor, Physics
College of William & Mary

Robert Edwards, Senior Staff Scientist, Theory Center
Thomas Jefferson National Accelerator Facility

Christian Weiss, Senior Staff Scientist, Theory Center
Thomas Jefferson National Accelerator Facility

ABSTRACT

The rich spectrum of hadrons reflects the complexity of interactions between the quarks and gluons confined within them. Most of these hadrons are extremely short-lived and are called resonances. Experimentally, they are observed indirectly through their effects on the energy distribution in scattering experiments. Additionally, the non-perturbative nature of Quantum Chromodynamics (QCD), which governs the dynamics of quarks and gluons, prevents the implementation of known analytical techniques for calculating transition and interaction rates between hadrons. Lattice QCD (LQCD), a numerical implementation of QCD, provides a non-perturbative approach to studying the spectrum, as long as we understand how to account for finite-volume and imaginary-time effects in our calculations. In this dissertation, we present two main results. First, the formalism for extracting the elastic form factors of resonances from LQCD, which is necessary to understand their internal structure. Second, we perform the first numerical calculation of a coupled-channel transition, the timelike form factor of the pion, extending into the inelastic region above the kaon-antikaon threshold, as well as its connection to the spacelike region. These developments open the door for future calculations that explore the non-trivial internal structure of QCD resonances.

TABLE OF CONTENTS

ACKNOWLEDGMENTS

I would like to thank the many members of the JLab theory group and the Hadspec collaboration for the guidance and discussions. A special thanks goes to my advisor Jozef Dudek, for his eagerness to teach and mentor me, as well as for his help whenever I needed him. Thanks to all my collaborators, Alessandro Baroni, Max Hansen, Keegan Sherman, Andrew Jackura, Robert Edwards and a big thanks to Raúl Briceño for introducing me to QCD and teaching me to ignore exponentially suppressed corrections. I thank the QCD graduate students that aided in one way or another along my PhD, the people in the lattice: Antoni, Archana, Chris C, Chris J, Chris K, Colin, Dan, Digonto, Marco, Tanjib; and my experimental colleagues: Amy, Edmundo, Rebecca, Sarah, Zach. Also I would like to mention that I really valued the discussions with the several postdocs, some now with permanent positions, with whom I have interacted throughout the years: Alessandro P, Arkaitz, Eloy, Emmanuel, Luka, Mischa, Sebastian. Feedback from different professors of the department proved invaluable, thank you Kostas, Chris M, Justin, and Eugeniy, and a very special thanks to the organizers of W&M Physicsfest: Patricia and Irina. I am very grateful for the wonderful staff members that I met at William & Mary: Paula, Ellie, Carol, Vicki and Blanca.

I thank all the friends I made along my six years in the Hampton Roads area, specially those who made COVID a little less isolating by letting me crash at the big physics house: Archana, Colin, Marco, Nik, Pat, Tanjib, and Yiqi. Thanks to the W&M Language Fellows and grad student friends for the many memories. Also thanks to my housemates Dan, Will, Richard and Nic for sharing a roof and a TV with me. A big thanks to the long distance friends for being always there: Pina, Ikki, Meme, Azul, Faviola, Nicho, Goyo, Mely, Maria, Annie, Jérémie, Niamh, Júlia and Kat.

Finally, thanks to my family, my dad, my mom and my brother Carlos, who have always supported me in every possible way.

In memory of my grandparents.

LIST OF TABLES

LIST OF FIGURES

Chapter 1

Introduction

1.1 Hadrons, amplitudes, and resonances

The strong nuclear interactions at low energies gives rise to a rich spectrum of particles called hadrons. The large amount of hadrons discovered in the past century quickly overwhelmed physicists, with one physics Nobel Laureate in the 1950's commenting that "...such a discovery now ought to be punished by a $10,000 fine." [1]. The recent access to colliders with higher luminosity, i.e. producing more events, for example at the Large Hadron Collider (LHC), has lead us to a similar experimental situation: in the past decade, 72 new hadrons have been discovered at the LHC [2], with more being added every year. An important difference from the time when fining experimentalists was suggested, is that now we possess a well-established theory that describes the underlying interactions responsible for the formation of hadrons: the theory of Quantum Chromodynamics (QCD).

QCD economically describes the strong nuclear interaction in terms of a few fundamental particles called quarks and gluons. One of the prominent characteristics of the theory is that while at high energies it is asymptotically free, at low energies it becomes non-perturbative, and quarks and gluons appear to be confined within hadrons. The residual interactions among the quarks and gluons confined in different hadrons is what gives rise to the nuclear force. It is generally agreed that the different possible arrangements of these

particles is what gives rise to the plethora of hadrons. However, the non-perturbative nature of QCD at hadronic scales renders most of the known analytic techniques of Quantum Field Theory (QFT) inapplicable, or to have uncontrolled systematic effects. This means that although we have good reasons to believe that QCD describes hadrons, there is not yet an analytic proof of how confinement arises in QCD, and how the hadron spectrum is dynamically related to its fundamental building blocks. Maybe now it would be reasonable to say that the theoretical physicists working on QCD are the ones that *ought* to be fined.

The phenomenological understanding of hadrons as bound states of quarks began with a classification based on their minimal quark content, calling mesons the boson states (with integer spin), while the fermionic states (with half-integer spin) are called baryons. Although this provides only a simplistic picture of the internal structure of a hadron, it has become a useful tool to categorize the spectrum. Hadrons that can be accommodated by this framework are called conventional states, while those defying it are known as exotics. Hadrons with certain combinations of quantum numbers, e.g. spin, intrinsic parity, charge parity, etc., are unequivocally exotic, and finding a hadron with those characteristics provides an instance of a system where either gluons, additional quark-anitquark pairs, or both, must contribute significantly to the structure of the hadron. For other combinations of quantum numbers both conventional and exotic states can exist, for instance the quantum numbers of the vacuum are consistent with a state composed only by gluons, called glueballs, but also with quark-antiquark states, and the states in the physical spectrum are expected to be mixtures of these constructions. Once we obtain precise quantitative descriptions of the internal properties of both conventional *and* exotic states, we could form a better picture of the dynamics happening inside of hadrons, and the mechanisms that lead to the spectrum of QCD. This research direction would also help to discriminate which hadrons are exotic whenever the quantum numbers alone cannot provide that information.

A helpful technique to probe into the internal degrees of freedom of hadrons is to study hadronic *transitions* mediated by external currents. For instance, the elastic scattering

of electrons off a proton at Stanford in the 1950's provided experimental evidence for the substructure of the hydrogen nucleus when deviations from the theoretical value for a point particle were observed [3]. This interpretation of the result is possible thanks to the perturbative nature of the electromagnetic interaction, where the first order contribution is proportional to the elastic transition of a proton mediated by an electromagnetic current. Research into the substructure of the proton has progressed significantly since then, leading to a greater understanding of the structure of the lightest baryon, e.g. with the recent apparent resolution of the proton radius puzzle [4], see also Ref. [5] for further discussion about the proton radius puzzle.

Other experimental setups have been devised to study the rest of the hadron spectrum, like electron-positron colliders that create hadrons from an intermediate electromagnetic current exciting the QCD vacuum. Similarly, elastic scattering of electrons off other hadrons has been performed to access their structure, for example of the pion, the lightest hadron in QCD.

However, the study of hadrons beyond the ground states of QCD is challenging because of the short-lived nature of hadronic excitations, which have lifetimes of the order of 10^{-22} s. Most hadrons are not observed directly experimentally since they decay before they can reach the detector, but instead they are observed as resonances in the energy distributions of the final states into which they decay. A prototypical example of a resonant state is the ρ-meson that decays most of the time into a pair of pions, meaning that the scattering cross-section of pions is enhanced for energies around the mass of the ρ. Other times their effect is obscured by interference with other resonances or with kinematic effects like the opening of thresholds. Therefore, for a rigorous study of resonances we need to disentangle dynamic and kinematic effects, and it is essential to have a quantitative description of cross-sections and transition rates that accommodates all of these effects.

As mentioned before, QCD at low energies is not amenable to analytic calculations where corrections are known to be suppressed by some perturbative hierarchy. Alternatively, Wilson proposed in the 1970's to numerically approximate the path integral of QCD

[6]. In this first-principles approach the degrees of freedom of the theory are placed in a four-dimensional mesh, which is why it is most commonly known as Lattice QCD (LQCD). The ultraviolet divergences typical of quantum field theories are tamed by the finite lattice spacing a, while a continuum limit can be recovered by extrapolating results in the limit $a \to 0$.

In this thesis we will describe techniques pertinent for the study of *transition amplitudes* within energy regimes where at most two stable hadrons can be produced. This includes transitions with two hadrons in the initial state, the final state, or both. We label these transitions $n \xrightarrow{\mathcal{J}} m$, with n/m the number of initial/final hadrons, and $\mathcal{J}$ the current mediating the transition. In particular, if a resonance decays into a two-hadron state within the studied energy region, we will show how its properties can be extracted from the mathematical description of the transition.

The rest of this chapter will describe the basic concepts associated with the dynamics of QCD and hadron spectroscopy. Chapter 2 will describe the state of the art utilized in numerical calculations of Lattice QCD related to the study of the hadron spectrum. In Chapter 3 we present a description of the analytic decomposition of $2 \xrightarrow{\mathcal{J}} 2$ transitions, needed to obtain a rigorous parameterization of the amplitude, and perform a well-defined extraction of hadron resonances properties. Then, in Chapter 4, we will describe the formulation of a prescription to extract $2 \xrightarrow{\mathcal{J}} 2$ transitions from LQCD, and a toy example demonstrating the importance of a new geometric function appearing in this formalism. Finally, in Chapters 5, 6, 7, and 8, we will describe a LQCD calculation of the production amplitude $0 \xrightarrow{\mathcal{J}} 2$ from an electromagnetic current. In particular we calculated the production of a pair of the lightest hadrons, the pions, as well as production in the energy region where not only pions can be produced, but also the lightest *strange* hadrons, the kaons. From this calculation the decay constant of the ρ-meson can be extracted, providing a proof of principle of the technique required to extract properties of other hadronic resonances which decay to multiple two-hadron channels. We present a summary of our results in Chapter 9, as well as an outlook for the future and the expected impact on the

field of the research efforts presented in this work.

1.2 The Standard Model and QCD

Currently, our best description of the fundamental building blocks of nature is given by the Standard Model (SM) of particle physics. This model relies on the theory of special relativity and the framework of quantum mechanics, which are combined together into QFT. In QFT all matter and interactions are embedded into particle fields, whose properties are restricted by the symmetries of a four-dimensional universe which is invariant under rotations, translations, and relativistic boosts. The matter in the standard model consists of spin-half fields with quanta known as fermions, and the interactions among them are dictated by force-carrying spin-one vector gauge bosons. Additionally, the Standard Model has a spin-zero scalar field, known as the Higgs, that gives mass to most of the SM particles. The SM describes three different interactions, i.e. three different types of spin-1 boson, each characterized by an internal symmetry group, also called the gauge group. One of them is the well-known quantum theory of light and matter interactions: quantum electrodynamics (QED). The second, known as the weak interaction, is responsible for radioactive beta decays among other phenomena. In this thesis we focus on the third of them: QCD, the so-called strong interactions, for which the symmetry group is $SU(3)$. The previously mentioned gluon corresponds to the QCD gauge-boson, while the quarks are the matter fields participating in QCD.

The connotation as the "strong" interaction is related to the fact that its coupling constant is significantly larger than that of the other forces in the SM, which in turn gives rise to its non-perturbative features. The $SU(3)$ symmetry is called color symmetry in analogy between its fundamental representation, which forms a 3 dimensional space, and the space of the basic colors $\{$*red*, *blue*, *green*$\}$. The Lagrangian of QCD can be stated in

the compact form

$$\mathcal{L}(x) = -\frac{1}{4} G^a_{\mu\nu}(x) G^{a\,\mu\nu}(x) + \sum_f \bar{\psi}^{(f)}(x)\big(i\not{D}(x) - m_f\big)\psi^{(f)}(x)\,, \tag{1.1}$$

where we will describe each of its terms next. The first term stands for the term describing the dynamics of the gluon gauge boson A^a_μ with,

$$G^a_{\mu\nu}(x) = \partial_\mu A^a_\nu(x) - \partial_\nu A^a_\mu(x) + g\, f^{abc} A^b_\mu(x) A^c_\nu(x)\,, \tag{1.2}$$

and the index a runs from 1 to 8, due to the fact that the gluons are embedded in the eight-dimensional *adjoint* representation of $SU(3)$. This part of the Lagrangian is also known as the Yang-Mills term, and as written, it is valid for an arbitrary $SU(N)$ gauge group. The coefficients f^{abc} are the structure constants of the Lie Algebra of the group, they ensure that the theory is renormalizable [7]. This ensures that any observable calculated from QCD only relies on fixing a finite number of inputs, the coupling g and the fermion masses $\{m_f\}$. Finally, different from QED where $f^{abc} = 0$, the coupling constant g shows up in here, allowing the gauge bosons to self-interact, making a pure Yang-Mills theory highly non-trivial.

The second term in the Lagrangian corresponds to the dynamics of the quarks, these are embedded in the fundamental representation of $SU(3)$. This term is a sum over the different "flavors" f of quarks. So far we have omitted both the Dirac and the color indices, these are of course summed over to have a scalar term in the Lagragian, which overall transforms trivially under the gauge group, but for clarity let us write them explicitly at least once for one of the flavors

$$\bar{\psi}^{(f)}\big(i\not{D} - m_f\big)\psi^{(f)} = \bar{\psi}^{(f)r}_\alpha \big(i\not{D} - m_f\big)^{rg}_{\alpha\beta} \psi^{(f)g}_\beta \tag{1.3}$$

where we have left implicit the spacetime dependence of the fields, D is a gauge covariant derivative and, as mentioned before, m_f stands for the bare mass of the quark field. The

latin indices run from 1 to 3, representing a component in color space, and the greek ones from 1 to 4, in Dirac space. In order to make this term a Lorentz scalar, gamma matrices γ^μ acting in the Dirac space are needed, these satisfy the Clifford algebra $\{\gamma^\mu, \gamma^\nu\} = 2\eta^{\mu\nu}$, where $\eta^{\mu\nu}$ is the metric of flat Minkowski space. The term contracting the barred and the unbarred fermion is known as the Dirac operator

$$\left(i\not{D} - m_f\right)^{rg}_{\alpha\beta} = i\gamma^\mu_{\alpha\beta}\left(\delta^{rg}\partial_\mu - igA^a_\mu[T^a]^{rg}\right) - m_f\,\delta^{rg}\delta_{\alpha\beta}\,, \tag{1.4}$$

where we again omit the spacetime dependence of this term, implicit in the case of the partial derivative. The quantities $[T^a]^{rg}$ are the matrix elements of the generators of the Lie Group in the fundamental representation, because this is the representation where the quarks are embedded, these are the Gell-Mann matrices.

All the particles of the SM that do not participate in QCD have been observed experimentally, i.e. the leptons, the electroweak bosons, and most recently the Higgs boson observed in the LHC in 2012 [8, 9]. However, no free quarks, gluons, or any composite particle with color charge, has ever been observed experimentally. Instead, only colorless hadrons have been observed, which are expected to be bound states of quarks and gluons belonging to color singlet combinations. One could ask how QCD, describing quarks and gluons carrying color, has become the accepted theory describing colorless hadrons. Part of the evidence supporting the existence of quarks came from the symmetries observed in the spectrum of hadrons, which could be understood precisely if they were bound states of quarks respecting these symmetries. As a bottom-up approach we will introduce first the relevant symmetries of the Lagrangian, and then elaborate on their consequences for the spectrum.

1.2.1 Symmetries of the QCD Lagrangian

The Lagrangian of QCD contains six different flavors of quarks. The mass difference between the two lightest, the *up* and *down* quarks, is small compared to hadronic scales,

which means that there is an approximate extra symmetry in the Lagrangian. To see this let us write the Dirac Lagrangian of these two quarks with the approximately equal light mass m_l

$$\mathcal{L}_D^{(l)} = \bar{u}(i\not{D} - m_l)u + \bar{d}(i\not{D} - m_l)d = \bar{q}(i\not{D} - m_l)q\,, \tag{1.5}$$

where q is a spinor in Dirac space, a vector in the fundamental color space and a two dimensional vector in *isospin* space, i.e. $q = (u, d)^T$. Now this term is not only a Lorentz scalar, and trivial under a color transformation, but it also admits an $SU(2)$ flavor transformation, which is called the isospin transformation, without changing the Lagrangian,

$$q \to Uq = q'\,, \quad U = e^{i\,\theta\,\hat{n}\cdot\vec{I}} \in SU(2)\,, \quad \mathcal{L}_D^{(l)} \to \mathcal{L}_D^{(l)\prime} = \mathcal{L}_D^{(l)}\,, \tag{1.6}$$

with $\vec{I}$ the generators of the isospin symmetry in the fundamental representation, i.e. proportional to the three Pauli matrices, θ an arbitrary real number modulo 2π, and $\hat{n}$ an arbitrary unit three-dimensional real vector.

An implication of this symmetry is that the hadron spectrum can be classified according to an isospin quantum number, I, into multiplets, with small mass differences among members of the same multiplet [1]. The pions for example belong to the $I = 1$ representation of isospin, where the charged pions $\pi^{\pm}$ have a mass $\approx$140 MeV, while the neutral component of the triplet, the π^0, has a mass $\approx$135 MeV, as reported by the PDG [10].

Another application of isospin is to decompose an operator, which could represent an external probe, into components in different representations of isospin, each of which will approximately act independently on hadrons. For example, the electromagnetic current constructed with quark fields, $\mathcal{J}^\mu = \sum_f Q_f \bar{\psi}^{(f)}\gamma^\mu\psi^{(f)}$, where Q_f corresponds to the

[1] On top of the corrections arising from the up and down mass difference, the electromagnetic interaction also breaks isospin symmetry, providing further splitting.

electromagnetic charge of the quarks, can be decomposed into its isospin components as

$$\mathcal{J}^\mu = \frac{2}{3}\bar{u}\gamma^\mu u - \frac{1}{3}\bar{d}\gamma^\mu d + \sum_h Q_h \bar{\psi}^{(h)}\gamma^\mu \psi^{(h)}\,, \tag{1.7}$$

$$= \frac{1}{2}(\bar{u}\gamma^\mu u - \bar{d}\gamma^\mu d) + \frac{1}{6}(\bar{u}\gamma^\mu u + \bar{d}\gamma^\mu d) + \sum_h Q_h \bar{\psi}^{(h)}\gamma^\mu \psi^{(h)}\,, \tag{1.8}$$

$$= \mathcal{J}^\mu_{I=1} + \frac{1}{3}\mathcal{J}^\mu_{I=0} + \mathcal{J}^\mu_h\,, \tag{1.9}$$

where the first term corresponds to an isovector current with $I_z = 0$, while the second term, and the contribution of the heavier $\{h\}$ quarks, belong to the isoscalar current, i.e. the singlet representation of isospin.

Lorentz invariance of the Lagrangian also implies a discrete symmetry of the action, i.e. the simultaneous action of time inversion, spatial parity, and charge conjugation, i.e. CPT-symmetry. In general, a Lorentz-invariant theory is not necessarily symmetric under the individual action of each of the CPT discrete transformations. However, current experimental evidence points to QCD being invariant under these individual transformations, which is reflected in the formulation of the Lagrangian of Eq. (1.1).

In the light sector of QCD we can combine C and a fixed isospin rotation to define a transformation which leaves the theory invariant. Charge conjugation exchanges the charged pions $\pi^\pm$, but leaves the neutral pion π^0 unchanged, with eigenvalue $+1$ of the charge conjugation operator. In order to make the whole isotriplet an eigenstate of a transformation we combine C with an isospin rotation of 180° around the I_2 axis. Let us call this combination G-parity, mathematically defined as

$$G \equiv C e^{i\pi I_2}\,, \tag{1.10}$$

for which the isovector of pions will be an eigenstate with eigenvalue equal to -1. Indeed, it is observed experimentally, that states of even and odd number of pions have small mixing. Multi-hadron states formed only by light quarks l, or with net zero heavy flavor

h, i.e. with $\bar{h}h$ flavor components, can be decomposed into states of definite G.

A further extension of the isospin symmetry is to assume that the *three* lightest quarks are degenerate, the up, down, and *strange* quarks. This is called $SU(3)_f$ flavor symmetry. Because the mass difference between the strange and the light quarks is greater than the mass difference between the two light quarks, $SU(3)_f$ has larger corrections than the isospin symmetry. For example, the pions, the charged and neutral kaons ($K^{\pm}$, K^0, $\overline{K}^0$), and the η-meson, belong to an octet representation, with masses approximately equal to 140 MeV, 495 MeV, and 550 MeV. Nonetheless, it still proves useful to classify the hadron spectrum, although the mass difference within different members of the same multiplet can be significant.

Additionally to the mass difference, the absolute value of the masses of these three quarks is small when compared with the typical scales of QCD: we might expect hadron dynamics to be described by a Lagrangian with these three quark masses set to zero with small corrections from the non-zero masses. This zero mass approximation is called the chiral limit. In the chiral limit, *axial* symmetries are introduced to the Lagrangian, with associated axial transformations, and the corresponding conserved currents transform under Lorentz symmetry as axial vectors. The isospin symmetry, or $SU(3)_f$, have conserved currents transforming as Lorentz vectors. This means that the two linear combinations of axial and vector symmetries involve only the right-hand or the left-hand components of the quark fermions, from which the chiral denomination arises. Naively this implies a near degeneracy between partners of opposite parity in the hadron spectrum, but this is not supported by the observed spectrum.

An explanation for this mismatch is that the QCD vacuum experiences a spontaneous chiral symmetry breaking, such that the vector transformations remain a symmetry of the QCD vacuum, but not the axial ones. This mechanism implies, by Goldstone's theorem, the existence of a multiplet of massless bosons in the spectrum. Experimentally, the lightest pseudoscalar multiplet, that of the pion, the kaon and the η, although it is massive, is identified as the pseudo-Goldstone bosons of the axial symmetry of QCD, with a mass

arising from the explicit symmetry breaking due to the non-zero quark masses. This explains why this multiplet is significantly lighter than the rest of the hadron spectrum, since in the chiral limit it becomes massless, while the rest of hadrons would still have masses on the order of the hadronic scale.

Unlike the spontaneous symmetry breaking of the electroweak sector of the SM, explained by the Higgs potential, the dynamical origin of the spontaneous chiral symmetry breaking of the QCD vacuum is not completely understood. In addition to this, the non-zero quark masses represent a small contribution to the total mass of hadrons, indicating a dynamical mass generation of QCD. Furthermore, it is expected that the Yang-Mills Lagrangian has a mass gap even though all states are composed of massless gluons [11]. Chiral symmetry breaking, dynamical mass generation, and confinement remain elusive dynamical aspects of QCD. From the study of the hadronic spectrum, e.g. confirming or explaining the experimental evidence for the plethora of hadronic state candidates, we expect to gain further understanding of the dynamics of QCD. In particular, first-principles descriptions of the composition of each of the states, e.g. the structure of each hadron in terms of quarks and gluons, can guide the development of better descriptions of QCD dynamics.

1.3 The low-lying hadron spectrum

As described in the previous section, the symmetries of the QCD Lagrangian provide some expectations about the allowed hadronic states of the theory. First, we will describe some basic nomenclature, some of which we have already been using in the previous section. The hadrons with integer spin are known as mesons, while those with half-integer spin are baryons. The phenomenological restriction of confinement means that the simplest bound states are those comprising a quark-antiquark pair forming a meson, or three quarks forming a baryon. The work presented in this thesis is focused on meson systems with light and strange quarks, and as such here we only describe the phenomenology of light

and strange mesons.

As mentioned before, isospin and $SU(3)_f$, being approximate symmetries of the QCD Lagrangian, can be used to organize the spectrum. In particular, because the isospin breaking corrections are small, the Particle Data Group (PDG) has opted to adopt a naming convention in part based on isospin symmetry, and hence G-parity [10]. This naming convention is listed in Table 1.1, from which we can observe, for instance, that by isospin symmetry a ρ-meson can only decay into an even number of pions (π), but cannot decay into any number of η mesons.

A quark-antiquark system can be described by its total quark-antiquark spin $S \in \{0, 1\}$, and orbital angular momentum L, with overall angular momentum of J. This system is a spatial parity eigenstate, with parity quantum number P equal to $(-1)^{L+1}$. If the quark and antiquark are the same flavor, the charge conjugation of this system yields a factor C equal to $(-1)^{L+S}$. There are certain J^{PC} combinations that are not allowed by this simplistic quark model. For those cases, gluons and extra quark-antiquark pairs would have to manifest non-trivial configurations inside the meson to reach the desired quantum numbers. We list these cases in the last column of Table 1.1.

Table 1.1: Naming scheme introduced by the PDG for light mesons, and exotic combinations of quantum numbers. The G parity is constrained to $G = C(-1)^I$, so that the empty cells are inconsistent combinations of quantum numbers. Note that only the neutral member of the isotriplets are eigenstates of C. Two names are available for isoscalars because they can be formed as combinations of two linearly independent states of $SU(3)_f$, one from the octet and one from the singlet.

J^{PC}	$I^G = 0^+$	$I^G = 0^-$	$I^G = 1^+$	$I^G = 1^-$	exotic
J^{--}		ω_J/ϕ_J	ρ_J		$J = 0$
J^{-+}	η_J/η'_J			π_J	odd J
J^{+-}		h_J/h'_J	b_J		even J
J^{++}	f_J/f'_J			a_J	

The states with zero orbital angular momentum have J^{PC} quantum numbers equal to $0^{-(+)}$ and $1^{-(-)}$, for $S = 0$ and $S = 1$ respectively. From $SU(3)_f$ symmetry we expect an octet and a singlet appearing in the spectrum of quark-antiquark mesons. We list the properties of the lightest particles with these quantum numbers grouped by isospin

multiplets in Table 1.2. As mentioned before, for the pseudoscalars ($0^{-(+)}$), the octet consists of the isotriplet pions, two isodoublets of kaons (K), and an isoscalar η meson, while there is an η' singlet. We illustrate the flavor content of each of these mesons in Fig. 1.1. The vectors ($1^{-(-)}$) consist of the ρ taking the role of the pion, the $K^\star$ instead of K, and the ω/ϕ instead of the η/η'. However, we can notice that the mass pattern in the pseudoscalars differs significantly from that of the vectors. This is explained qualitatively by the chiral symmetry breaking of the QCD Lagrangian.

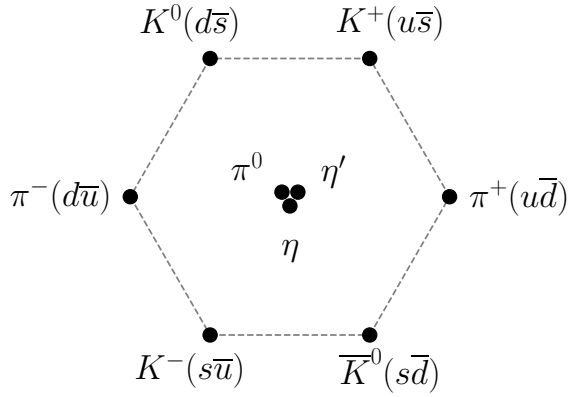

Figure 1.1: Pseudoscalar nonet, octet plus singlet, with the valence quark content of each meson. The mesons in the center have a zero third component of isospin. The corresponding quark content are $\pi^0 = u\overline{u} - d\overline{d}$, $\eta = u\overline{u} + d\overline{d} - 2s\overline{s}$, and $\eta' = u\overline{u} + d\overline{d} + s\overline{s}$, where the last two being isoscalars can in principle mix for a broken $SU(3)_f$.

As already mentioned, chiral symmetry breaking in the chiral limit requires the presence of a multiplet of massless states. This is realized experimentally in a set of massive pseudo-Goldstone bosons, pseudo because of the explicit symmetry breaking arising from the quark masses. In the case of the chiral limit of the light quarks, this multiplet consists of isovector states, identified with the pions, explaining their low mass. The K-mesons and the η-meson are also interpreted as pseudo-Goldstone because the strange quark is also close to the chiral limit relative to the scale of QCD. The $SU(3)_f$ singlet state η' is much more massive than its octet partners. This is explained by the singlet axial symmetry being anomalous in QFT, and no spontaneous symmetry breaking mechanism with an associated Goldstone boson can be used to describe this state.

The nature of the vector mesons is not associated with the chiral symmetry breaking mechanism, and instead the dynamical mass generation mechanism is responsible for their mass. This also implies that the isoscalar member of the octet, and the $SU(3)_f$ singlet, can mix following the dynamics of the broken $SU(3)_f$, with no axial anomaly preventing it. From their preferred decay channel, $\omega \to \pi\pi\pi$ and $\phi \to K\overline{K}$, it is inferred that their flavor wavefunction is an ideal mixing, with ϕ being mostly an $\bar{s}s$ state, while ω has mostly a light composition. This has been translated to the phenomenological OZI rule, indicating that decays mediated through only gluons are heavily suppressed, like that of a pure $s\bar{s}$ meson to $\pi\pi\pi$, even if the phase space to that decay channel is larger than the one of $\overline{K}K$. This flavor content is further supported by the near degeneracy of the ρ and ω mesons.

Table 1.2: Particle properties of the lowest lying pseudoscalar and vector mesons, masses correspond to the approximate value of the corresponding isomultiplet.

	π	η/η'[b]	K	ρ	ω/ϕ[b]	$K^\star$
J^{PC}	$0^{-(+)}$	0^{-+}	0^-[a]	$1^{-(-)}$	1^{--}	1^-
I^G	1^-	0^+	$\frac{1}{2}$[a]	1^+	0^-	$\frac{1}{2}$[a]
M[MeV]	140	550/958	495	770	782/1020	892

[a] The kaons, because of their strange flavor content, are not eigenstates of charge conjugation or G-parity. Kaon-antikaon systems, $K\overline{K}$, can be constructed to have definite isospin, and positive or negative G-parity.

[b] The η/η' and ω/ϕ mesons differ by their strange flavor content. While η' resembles the singlet of $SU(3)_f$, ω and ϕ are found to be an ideal mixing of the $SU(3)_f$ singlet and octet, where ϕ is mostly $s\bar{s}$.

We could try to keep applying this classification to radial or orbital excitations, and although it works well in several cases, in others it fails to give an adequate qualitative picture of the spectrum. A prominent example of this is in the scalar $0^{+(+)}$ sector, which can mix with "glueballs", bound states of gluons, and where states have also been proposed to contain tetraquark components, or two-meson molecules [12]. A rigorous understanding of these states, especially states with suspected exotic components, can be extracted from first-principle calculations. We will expand more on this idea in Chapters 3 and 4, and show the result of a LQCD calculation rigorously determining the decay constant of the

ρ-vector meson, to be described in Chapter 8. Future calculation of other structural properties of resonances, like the Q^2 dependence of their elastic form factors, can help us pinpoint their nature. For instance, comparison with more familiar mesons, like the π and K pseudoscalars, can serve as a model-independent description of their internal properties.

Before we describe Lattice QCD, and how we can extract hadronic information from numerical calculations, we will first review the experimental status of the observables for which we present numerical results. Similarly a brief review of S-matrix theory is given to describe how resonant states are described mathematically in QFT.

1.4 The pseudoscalar form factor

1.4.1 Pair-production of hadrons

Electron-positron colliders provide a powerful laboratory for the study of hadrons, free from hadronic effects in the initial state. For a recent review of the current experimental efforts and their impact on hadron spectroscopy see Ref. [13]. In the study of multi-hadron interactions, these experiments have the advantage of little model dependence in describing the production of hadrons, as opposed to experiments that employ hadronic production processes.

There are two main experimental techniques that electron-positron colliders utilize to explore the hadron spectrum. The first one consists of varying the beam energy of the leptons so that detectors can directly perform an energy sweep to study the energy dependence of multi-hadron production cross-sections. The CMD and SND detectors have used this experimental approach to measure the $e^+e^- \to \pi^+\pi^-$ cross-section [14, 15, 16, 17, 18, 19].

The second option is employed in colliders that mostly operate at a fixed beam energy. In that case the process of initial state radiation (ISR) $e^+e^- \to e^+e^-\gamma \to \text{hadrons} + \gamma$,

also called radiative return to low energies, is exploited to study the energy dependence of e^+e^- to hadrons production. The ISR photon, γ, takes away some of the beam energy, allowing a measurement of hadronic production at energies all the way down to the $\pi\pi$ threshold. The interference from final state radiation, in this case considered a background, can be controlled by applying appropriate cuts to the data, e.g. angular separation between the tagged photon and the hadrons. A description of this procedure and an estimation of the systematic effect in the case of the DAΦNE collider appears in Ref. [20]. The detectors KLOE-2, BaBar and BESIII have used this experimental approach to measure $e^+e^- \to \pi^+\pi^-(\gamma)$ [21, 22, 23, 24, 25, 26, 27].

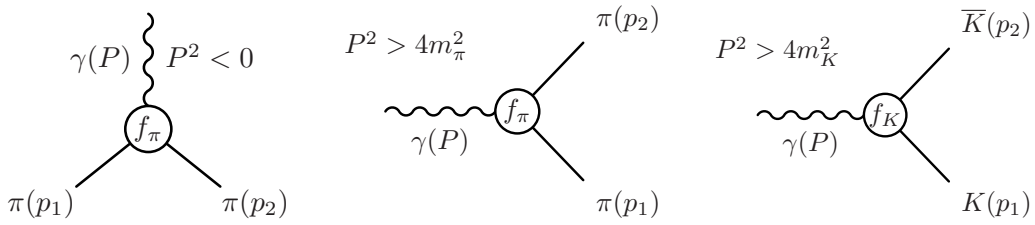

(a) Spacelike π form factor.

(b) Timelike π form factor.

(c) Timelike K form factor.

Figure 1.2: Diagrams representing of the (a) spacelike and (b) timelike pion form factor, as well as the (c) timelike kaon form factor. The spacelike and timelike form factors of the pion are aspects of a single function of the photon virtuality, P^2.

In an electron-positron annihilation, to leading order in the electromagnetic interaction, the mechanism to produce hadrons is through a single intermediate virtual photon, like in the Figs. 1.2b and 1.2c. This process combines the perturbative properties of QED, that allows us to approximate it by a single photon intermediate state, with the final state interactions of the hadrons, which are governed by non-perturbative QCD dynamics. The allowed hadronic states produced in this manner have the quantum numbers of the photon, $J^{PC} = 1^{--}$, with contributions of both $I = 0$ and $I = 1(I_z = 0)$, making these experiments specially suitable for the study of neutral vector states.

From higher order electromagnetic processes, suppressed by further factors of $\alpha_{\rm EM} \approx 1/137$, other values of J^{PC} are accessible. For example, from the two-photon process of

the form $e^+e^- \to e^+e^- + 2\gamma \to e^+e^- + X$, hadronic final states with quantum numbers $0^{\pm+}$ and $2^{\pm+}$ can be also accessed. Furthermore, studies from weak or radiative decays of heavy vector mesons, also provide access to multihadron amplitudes. Finally, the decay of τ leptons, which can be produced via $e^+e^- \to \tau^+\tau^-$, gives experimental access to the isovector $I_z = \pm 1$ components of multi-hadron production amplitudes, e.g. the process $\tau^- \to \pi^-\pi^0\nu_\tau$ [28].

The production of pairs of pseudoscalars $\pi\pi$ and $K\overline{K}$ is governed by the electromagnetic form factors $f_\pi(P^2)$ and $f_K(P^2)$, respectively, where $P^2 = s$, indicates the center-of-momentum energy squared of the system. We will use the symbols P^2 and s interchangeably. The form factor describes the non-perturbative rescattering that the pair of pseudoscalars undergoes once it is produced. These form factors are related to the crossed version of the amplitude, see Fig. 1.2a, which will be discussed in a subsequent section. The main idea here is that a single function describes the form factor for a photon with timelike virtuality $s > (2m_\pi)^2$ which is able to produce a pair of pions, as well as the photon with spacelike virtuality $s < 0$, mediating the elastic interaction of a single pion with a virtual photon. That this is the case is illustrated by the fit retrieved from Ref. [29] and shown in Fig. 1.3, together with a compilation of experimental data.

In Figure 1.3 the effect of the ρ-meson is evidenced by the enhancement of the data near the virtuality of 0.6 GeV^2. This bump also presents a shoulder on the right hand side, which can be explained from an isospin violating contribution from the decay of an ω-meson to two pions. This feature disappears in the case of the form factor being measured from the τ decay, as no $I_z = 0$ states can contribute, with no ω interference, this is can be observed in the experimental data of Fig. 1.4. In order to perform a rigorous description of the properties of the ρ that can be extracted from the form factors we will briefly describe how these resonant states are described mathematically in QFT in the next section. We will finalize this section by commenting on previous LQCD calculations of the pion form factor $f_\pi(P^2)$ in the timelike region.

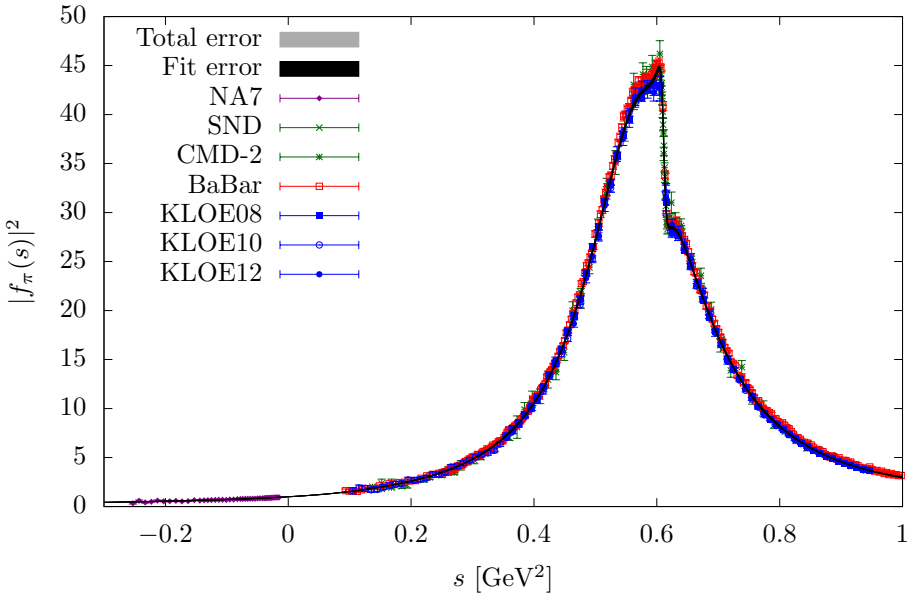

Figure 1.3: Experimental data for the form factor of the pion across the timelike and spacelike region compiled by Ref. [29]. In that reference the form factor dependence on the photon virtuality is fitted with a parameterization describing a ρ-meson resonance, as well as interference from the isospin violating contributions of the ω-meson as observed by the shoulder of the peak near $s = 0.6$ GeV^2.

1.4.1.1 Previous lattice calculations of the timelike form factor

There has been general interest in studying the ρ vector-isovector resonance on the lattice for several reasons. The first being that experimentally it appears to decay strongly almost exclusively into two pions, and that the two-pion system scatters elastically to a good approximation up to ∼1 GeV. Measurement of the production cross-section of the four pion system in e^+e^- colliders shows no significant interactions for energies below ∼ 1 GeV [30], and similarly for the $\pi\pi\eta$ channel [31].

The second reason is that the energy dependence of $\pi\pi$ scattering has the simplest behavior expected from a nearby resonance, it manifests with a characteristic 'bump' peaking around the resonance mass. This can be contrasted with the behavior of the lightest resonance, the scalar $f_0(500)$ also known as the σ, which has a large width impacting a broad energy region of isoscalar $\pi\pi$ scattering. This requires the implementation of dispersive methods to describe the energy dependence and extraction of the resonance parameters

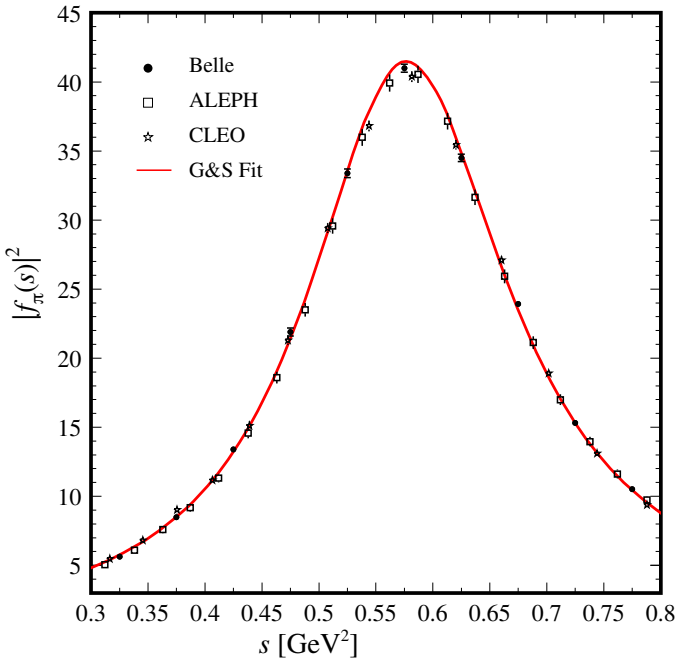

Figure 1.4: Experimental data of the form factor of the pion extracted from τ decays from Ref. [28]. In this case the final two-pion state is charged, preventing the interference with isospin breaking terms such that no ω shoulder is observed.

[32], otherwise large systematic errors can be introduced. The case of the ρ is quite different, with little systematic introduced by less sophisticated methods to describe the energy dependence produced by the resonance, e.g. using a Breit-Wigner parameterization [33].

A review describing the progress in the extraction of ρ-meson properties can be found in Ref. [34]. There are previous calculations of the decay constant of the ρ in Refs. [35, 36], which neglect the finite volume corrections described in Chapter 2. Three previous works have employed LQCD to calculate the timelike form factor of the pion restricted to the elastic scattering region [37, 38, 39]. In the lattice calculation of this work we aim to extend this calculation beyond the elastic timelike region, into the coupled channel region, as well as to describe jointly both the timelike and the spacelike region.

1.4.2 Elastic lepton-meson scattering

The elastic scattering of electrons and pions, $e\pi \to e\pi$, can be measured experimentally with a pion beam incident on a hydrogen target. As before we can describe this process at leading order in the electromagnetic interaction as the exchange of a virtual photon, with the photon-pion vertex shown in Fig. 1.2a. That this vertex is described by the same form factor $f_\pi(s)$ introduced earlier, albeit in a different kinematic region, is expected from general properties of QFT, which we will describe in the next section.

This process gives access to $f_\pi(s)$ in the spacelike region of photon virtuality, i.e. $s < 0$. For spacelike virtualities it is also common to utilize the variable $Q^2 = -s$. The most precise data was measured with a π^- beam with a momentum of 300 GeV [40], and is shown in the negative region of s in Fig. 1.3.

A second experimental setup is through pion electroproduction from a hydrogen target. The extraction of the pion form factor is model dependent in this case, as the data needs to be extrapolated to an unphysical kinematic region. This approach has been used by the F_π collaboration at JLab to explore the high Q^2 behavior of the form factor [41, 42, 43, 44].

In the forward limit, $Q^2 = 0$, the form factor is constrained to be equal to the hadron charge, and deviation from unity for $Q^2 > 0$ indicates the existence of a non-trivial internal structure of the pion, different from the point-like behavior of the SM leptons. In particular, the non-zero slope at $s = 0$ is used to define the 'charge radius' $\langle r_\pi^2 \rangle^{1/2}$, where[2]

$$\langle r_\pi^2 \rangle \equiv 6 \, \frac{d}{ds} f_\pi(s) \bigg|_{s=0} , \tag{1.11}$$

with the current experimental value of $\langle r_\pi^2 \rangle^{1/2} = 0.659(4)$ fm as reported by the Particle Data Group (PDG) [10]. For comparison, the experimental value of the charge radius of the kaon reported by the PDG is $\langle r_K^2 \rangle^{1/2} = 0.560(31)$ fm, while for the proton is $\langle r_p^2 \rangle^{1/2} = 0.8409(4)$ fm [10].

[2]See Ref. [45], and references therein, for a discussion about the proper interpretation of this quantity when it is comparable to the Compton wavelength of the system.

1.4.3 The Kaon timelike form factor

The isovector component of the electromagnetic kaon timelike form factor can also be measured from τ decays [46]. This measurement has been described by a data driven prediction, using as input the experimental pion form factor and the $\pi\pi \to K\overline{K}$ cross-section, see Ref. [47]. Finally, continuum methods employing the Schwinger-Dyson equations have also been used to calculate the kaon form factor [48]. The Schwinger-Dyson equations results could in principle be compared to the lattice calculation presented in Chapter 8 of this work by tuning the input parameters to reproduce the masses of the pseudoscalars on this lattice.

1.5 Amplitudes and resonances

Particle states in a QFT manifest mathematically as poles of momentum-space correlation functions of the theory. The pole of a given particle is located at its physical mass, and pole residues can be related to matrix elements involving the state. For example, in the Lehmann-Symanzik-Zimmermann (LSZ) reduction formula, the S-matrix describing particle scattering is extracted from the residue of appropriately chosen correlation functions. For stable hadrons these poles are located along the real energy axis, but resonant states have their poles moved into the complex energy plane. We will be after the location of these poles, and their residues, in order to extract properties of the resonant members of the hadron spectrum.

1.5.1 The S-matrix and the scattering amplitude

Similar to how stable particles appear as poles in correlation functions, resonant states are also associated with poles appearing, for example, in the S-matrix. Before defining this matrix let us introduce a few kinematic variables related to the scattering of a two-meson system without spin, shown in the diagram of Fig. 1.5. We use $P^\mu \equiv (E, \mathbf{P})$ to represent the initial and final state 4-momenta, while the individual momenta of each of

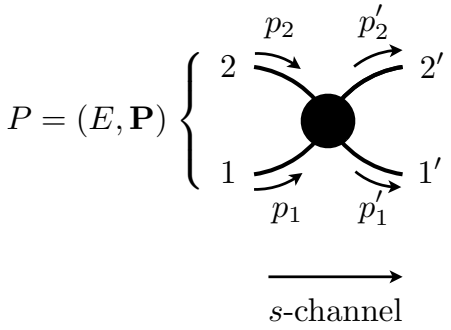

Figure 1.5: Diagram depicting the scattering of two hadrons labeling the four-momentum flow of each particle, and the total four-momentum of the system.

the incoming(outgoing) particles is equal to $p_1^{(\prime)}$ and $p_2^{(\prime)}$. We will describe a system with several channels, where the two mesons in each channel are degenerate with mass m_a, we label each channel with latin index $a, b, \ldots$. For channel a the magnitude of relative momentum between mesons in the center-of-momentum (CM) frame is equal to

$$k_a^\star(s) = \sqrt{\frac{s}{4} - m_a^2}\,, \tag{1.12}$$

where $s = P^2 = (p_1 + p_2)^2 = (p_1' + p_2')^2$, we will use the $\star$ symbol throughout this work to indicate the value of quantities in the CM frame. The relative momentum enters the definition of the phase space factor ρ_a

$$\rho_a(s) = \frac{1}{16\pi}\left(\frac{2k_a^\star(s)}{\sqrt{s}}\right). \tag{1.13}$$

It is convenient to also define the following Lorentz invariants, which together with variable s are known as the Mandelstam variables,

$$t = (p_1 - p_1')^2\,, \tag{1.14}$$

$$u = (p_1 - p_2')^2\,, \tag{1.15}$$

and satisfy the relation $s + t + u = 4m_a^2$ in the case of elastic scattering of channel a. Scattering of two-meson systems can be described as a function of s and t, where t can be related to the angle $\theta^\star$ between incoming and outgoing states in the CM frame. Angular momentum conservation allows us to decompose any function of t into its different partial-wave ℓ components,

$$f(t) = \sum_{\ell=0}^{\infty} (2\ell + 1)\, f_\ell\, P_\ell(\cos\theta^\star)\,, \tag{1.16}$$

where $P_\ell(z)$ is the ℓ-th Legendre polynomial. For the following discussion we will treat the S-matrix, and the rest of the amplitudes defining scattering, as being partial-wave projected, but we will not explicitly show the ℓ index to avoid clutter, unless it is needed to avoid confusion.

The S-matrix is defined to be the overlap between *asymptotic* states in the infinite past and the infinite future, more commonly labeled *in* and *out* states, $S_{ab} = \langle a, \text{out}|b, \text{in}\rangle$. In order to describe scattering we are interested only in the component where particles interact, and not only fly past each other, for that we introduce the *scattering amplitude* $\mathcal{M}$,

$$S = \mathbb{I} + i\sqrt{2\rho}\,\mathcal{M}\,\sqrt{2\rho}\,, \tag{1.17}$$

where the identity takes into account the non-interacting piece, and here ρ represents a diagonal matrix with components equal to $\rho_a(s)$ and zero below threshold, acting as a conventional normalization. In this case the scattering amplitude will be a function of s.

That the resonance poles are in the complex energy plane is a consequence of a few general properties that we expect this matrix to satisfy based on physical arguments. We will focus on the three properties of unitarity, analyticity, and crossing symmetry. These three mathematical properties are consequences of demanding the S-matrix to conserve probabilities, respect causality, and be able to describe the reaction $A + B \to X + Y$, as well as $A + \overline{Y} \to X + \overline{B}$, where $\overline{Z}$ corresponds to the anti-particle of particle Z.

The unitarity requirement simply imposes $SS^\dagger = 1$. This equation together with Eq. (1.17), relates the imaginary part of the inverse of $\mathcal{M}$ to the negative of the phase

space,

$$\mathrm{Im}(\mathcal{M}^{-1}) = -\rho\,, \tag{1.18}$$

we will use this property to formulate parameterizations of the scattering amplitude extracted from LQCD. The phase space matrix features branch points in the complex s plane at the threshold $s_{a,\mathrm{thr}} = (2m_a)^2$, and a Riemann sheet structure of 2^{N_a} sheets, where N_a is the number of two-meson channels. This analytic structure in s is inherited by the $\mathcal{M}$ amplitude. The branch cut associated with each branch point is, by convention, directed towards positive s, which defines a physical sheet where $\mathrm{Im}(k_a^\star(s)) \geq 0$, with physical scattering occurring just above the cut at $s + i\epsilon$. These analytic properties of the amplitude are named right-hand cuts.

The analyticity requirement states that no pole singularities can be present above the lowest threshold on the real s axis, or anywhere in the upper half-plane of the physical Riemann sheet. It does not prevent poles appearing below threshold on the real s axis, which would be associated with a bound state of the system. However, any pole from a resonance coupling to a two-particle system is moved away from the physical Riemann sheet. We illustrate this behavior with Fig. 1.6 in the case of a single channel, with a nearby resonance pole in the unphysical sheet (II). The shoulder of the pole in the real s axis, where physical scattering takes place, is observed as an enhancement of $\mathcal{M}$ close to the mass of the resonance.

The scattering amplitude must be a real function over the real s axis below threshold according to Eq. (1.18). According to the Schwarz reflection principle, the value of the scattering above the real s axis is related to its complex conjugate below the real s axis,

$$\mathcal{M}(s)^* = \mathcal{M}(s^*)\,. \tag{1.19}$$

We can analytically continue this property to apply all over the physical Riemann sheet,

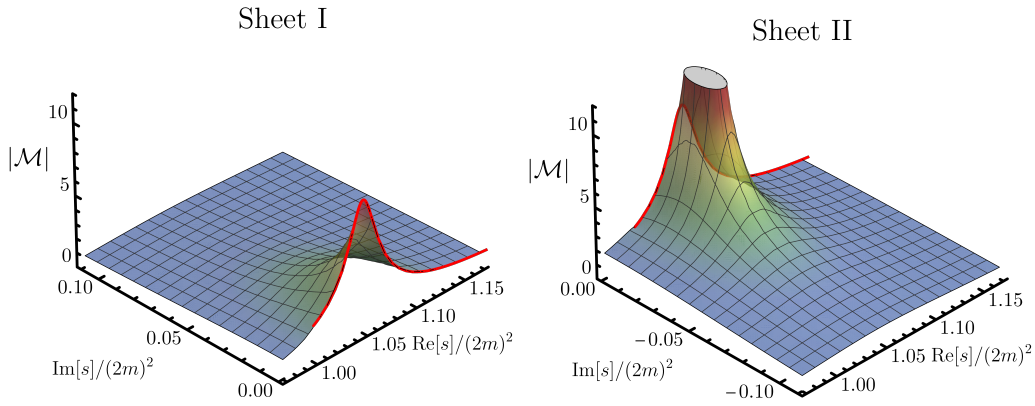

Figure 1.6: Upper and lower half complex s plane for the physical (I) and unphysical (II) sheets of an scattering amplitude featuring a nearby resonance. The red line follows the value of $|\mathcal{M}|$ on the real s axis where physical scattering occurs.

and recast the unitarity requirement in the form

$$\mathcal{M}(s+i\epsilon) - \mathcal{M}(s-i\epsilon) = 2i\mathcal{M}(s+i\epsilon)\,\rho(s+i\epsilon)\,\mathcal{M}(s+i\epsilon)^\dagger\,, \tag{1.20}$$

with physical scattering happening for the limit of $\epsilon \to 0$ from above. The left hand side of this equation represents a discontinuity of the scattering amplitude above threshold, along the real s axis

$$\mathrm{Disc}\,\mathcal{M} = 2i\mathcal{M}(s)\,\rho\,\mathcal{M}(s)^\dagger\,. \tag{1.21}$$

which is realized in the presence of the branch cut that opens at threshold.

Analyticity of the scattering $\mathcal{M}(s,t)$ is also expected in the t complex plane close to each threshold $s_{a,\mathrm{thr}}$ [3]. In particular, the partial-wave expansion of Eq. (1.16) introduces a spurious singularity from the Legendre polynomials, which behave like

$$P_\ell(\cos\theta^\star(s \sim s_{a,\mathrm{thr}}, t)) \sim \left(\frac{t}{2k_a^{\star 2}(s)}\right)^\ell. \tag{1.22}$$

In order for $\mathcal{M}(s,t)$ to remain analytic in t close to threshold, each of the partial waves

[3] Singularities in t manifest as left-hand cuts in the partial-wave amplitudes, and although interesting on their own right, we will not be discussing them here.

must behave like

$$\mathcal{M}_{\ell,ab}(s) \sim \left(k_a^\star(s) k_b^\star(s)\right)^\ell , \tag{1.23}$$

this property has an intuitive explanation acting as a centrifugal barrier, i.e. partial-waves with large values of angular momentum will be suppressed close to threshold. For the production amplitudes $0 \xrightarrow{\mathcal{J}} 2$, which we label $\mathcal{H}$, the partial-wave projection is only applied to the final state, leading to the condition

$$\mathcal{H}_{\ell,a}(s) \sim \left(k_a^\star(s)\right)^\ell . \tag{1.24}$$

Finally, crossing symmetry states that a single amplitude describes processes where particles are exchanged from the initial and final states, and vice-versa. Of particular interest for us is the pair production amplitude of Fig. 1.2b, which by crossing symmetry is related to the spacelike form factor of Fig.1.2a. Crossing symmetry states that both processes are described by a single amplitude. Also by imposing analyticity and crossing symmetry, we can conclude that $\mathcal{M}$ cannot feature pole singularities in the first Riemann sheet except on the real s axis between the right hand and the left hand cuts.

The poles in an unphysical sheet and near the physical scattering region of the partial-wave projected $\mathcal{M}(s)$ are associated with the resonances of the theory. Each resonance will couple to all channels with the same quantum numbers, and the strength of this coupling can be quantitatively described by the residues c_a at the pole,

$$\mathcal{M}_{ab}^{\text{II}}(s \sim s_R) \sim -16\pi \frac{c_a\, c_b}{s - s_R} , \tag{1.25}$$

where the index II indicates that it is evaluated on Sheet II. In general, resonances can appear in any of the 2_a^N sheets, except sheet I. The location of the pole itself, s_R, is associated with the mass m_R and width Γ_R of the resonance,

$$\sqrt{s_R} = m_R - i\frac{\Gamma_R}{2} . \tag{1.26}$$

This pole will appear in every channel at this location in the complex energy plane, unless $c_a = 0$, reflecting that the resonance parameters are not channel dependent, and describe the properties of a state of the theory.

1.5.1.1 Scattering amplitude in the elastic region

In the case of elastic scattering in a single channel, where the squared CM energy s satisfies $s_{a,\text{thr}} < s < s_{b,\text{thr}} < s_{c,\text{thr}} \ldots$, Eq. (1.18) provides a constraint for the complex quantity $\mathcal{M}_{aa}$. We can apply this constraint to describe the energy dependence of scattering in terms of a real function $\delta(s)$, known as the phase-shift,

$$\mathcal{M}_{aa}(s) = \frac{1}{\rho_a(s)} \sin\delta(s)\, e^{i\delta(s)}\,. \tag{1.27}$$

From Eq. (1.23), we can derive the behavior of the phase-shift close to threshold to be equal to

$$\delta(s) \sim \left(k_a^\star(s)\right)^{2\ell+1}. \tag{1.28}$$

1.5.1.2 Scattering amplitude for multiple two-meson channels

For values of energy above the first inelastic threshold, the scattering amplitude of channel a can no longer be described in terms of a single real function. Instead it is conventional to use two real functions,

$$\mathcal{M}_{aa}(s) = \frac{\eta_a(s)e^{i2\delta_a(s)} - 1}{2i\rho_a(s)}\,, \tag{1.29}$$

where $\eta(s)$ is known as the inelasticity. In the case where $\eta(s) = 1$ we recover Eq. (1.27) describing elastic scattering. This same description can be used for every diagonal element of the two-meson scattering amplitude $\mathcal{M}_{ab}$.

In the case of a two-channel system, based on the restriction of Eqs. (1.18), the inelasticities of both channels are equal, $\eta = \eta_a = \eta_b$, and the off-diagonal element of the

scattering amplitude is

$$\mathcal{M}_{a\neq b}(s) = \frac{\sqrt{1-\eta(s)^2}\, e^{i(\delta_a(s)+\delta_b(s))}}{2\sqrt{\rho_a(s)\rho_b(s)}}\,. \tag{1.30}$$

Alternatively, we can employ the restrictions of Eqs. (1.18) and (1.23) to parameterize the scattering amplitude in terms of a real-valued $\mathcal{K}$ matrix,

$$\mathcal{M}^{-1}_{\ell,ab} = \frac{1}{(2k_a^\star)^\ell}\frac{\mathcal{K}^{-1}_{\ell,ab}}{16\pi}\frac{1}{(2k_b^\star)^\ell} - i\delta_{ab}\,\rho_a\,. \tag{1.31}$$

For energies in the physical region, over the real s axis above threshold, this parameterization can be described in terms of Eqs.(1.29) and (1.30). The advantage of describing the scattering in this form is that we can analytically continue it into the complex s plane to search for nearby resonances. The parameterization of Eq. (1.31) is also valid for the elastic case.

An undesired property of Eq. (1.31), is that the phase space ρ has unphysical singularities in the first Riemann sheet appearing below threshold. This singularity spoils the analyticity properties of $\mathcal{M}$—for degenerate masses there is a branch point singularity at $s = 0$. To fix this, we can exchange the phase space ρ with a dispersive integral, known as the Chew-Mandelstam factor,

$$I_{a,\mathrm{CM}}(s) = \frac{s}{\pi}\int_{s_{a,\mathrm{thr}}}^{\infty} ds'\,\frac{\sqrt{1-s_{a,\mathrm{thr}}/s'}}{s'(s'-s+i\epsilon)}\,, \tag{1.32}$$

which by construction satisfies $\mathrm{Im}(I_{a,\mathrm{CM}}) = 16\pi\rho_a$, and it only contains a square root singularity at threshold in the first Riemann sheet. The integral $I_{a,\mathrm{CM}}(s)$ has a subtraction at $s = 0$, which imposes $\mathrm{Re}\, I_{a,\mathrm{CM}}(0) = 0$, but different subtraction points can be employed, e.g. at the pole mass of the associated K-matrix. This dispersive integral can be calculated analytically, and in the case of degenerate masses it is equal to

$$I_{a,\mathrm{CM}}(s) = i\sqrt{1-\frac{s_{a,\mathrm{thr}}}{s}} + \frac{2}{\pi}\left(1+\sqrt{1-\frac{s_{a,\mathrm{thr}}}{s}}\log\left(\frac{\sqrt{s}-\sqrt{s-s_{a,\mathrm{thr}}}}{\sqrt{s_{a,\mathrm{thr}}}}\right)\right)\,. \tag{1.33}$$

The scattering amplitude in terms of the Chew-Mandelstam phase space is equal to

$$\mathcal{M}^{-1}_{\ell,ab} = \frac{1}{16\pi}\left[\frac{1}{(2k^\star_a)^\ell}\mathcal{K}^{-1}_{\ell,ab}\frac{1}{(2k^\star_b)^\ell} - \delta_{ab}\, I_{a,\mathrm{CM}}\right]. \tag{1.34}$$

1.5.2 Pair production amplitude

We have already introduced the amplitude describing the pair production of pseudoscalars from an electromagnetic current. This amplitude is given by the overlap of the electromagnetic current $\mathcal{J}^\mu$ and a two-meson state

$$\mathcal{H}^\mu_a(p_1,p_2) \equiv \langle p_1 p_2, a|\mathcal{J}^\mu(x=0)|0\rangle\ . \tag{1.35}$$

The electromagnetic current is conserved, and the production amplitude must reflect this by satisfying the equation $P_\mu\mathcal{H}^\mu = 0$. This also implies that $\mathcal{H}^\mu$ behaves as a vector under Lorentz transformations. This allows us to perform a Lorentz decomposition of the amplitude,

$$\mathcal{H}^\mu_a = (p_1 - p_2)^\mu f_a(P^2)\,, \tag{1.36}$$

where the orthogonal combination p_1+p_2 is forbidden by current conservation. The Lorentz scalar $f_a(s)$ corresponds to the electromagnetic form factor of the meson in channel a, which in the case of $\pi\pi$ production we identify with the form factor f_π described in Sec. 1.4.

We need to partial-wave project the production amplitude into the P-wave to match the quantum numbers $J^{PC} = 1^{--}$ associated with the current,

$$\mathcal{H}^\mu_{a,m_\ell}(P) = \int \frac{\mathrm{d}\Omega^\star_k}{\sqrt{4\pi}} Y^*_{1m_\ell}(\Omega^\star_k)\mathcal{H}^\mu_a(p_1,p_2)\,, \tag{1.37}$$

$$= \frac{2\,k^\star_a(s)}{\sqrt{3}}\epsilon^{\mu *}(P,m_\ell) f_a(P^2)\,. \tag{1.38}$$

where $\epsilon^\mu(P,m_\ell)$ is the polarization vector of a state with momentum P and spin-projection into the z-axis equal to m_ℓ. From this projection we learn that the requirement of $\mathcal{H}_\ell \sim (k^\star)^\ell$ is explicitly satisfied by the Lorentz decomposition, and that f_a does not need to

vanish as some power of $k^\star$ at threshold, although it will still feature a branch point singularity at threshold.

We can impose unitarity on f_a by calculating its discontinuity, and by extension its imaginary part. In the case of production amplitudes this is associated with final state rescattering, rather than conservation of probability, although these two concepts are equivalent,

$$k_a^\star(s)\,\mathrm{Im} f_a(s) = \sum\nolimits_b k_b^\star(s)\, f_b(s) \rho_b(s)\, \mathcal{M}_{ba}^*(s)\,, \tag{1.39}$$

where we explicitly show the channel indices, and the relative momentum factors are the result of the centrifugal barrier behavior. It is not difficult to find a solution of Eq. (1.39), for example

$$f_a = \sum\nolimits_b \frac{1}{k_a^\star}\, \mathcal{M}_{ab} \frac{1}{k_b^\star}\, \mathcal{F}_b\,, \tag{1.40}$$

where $\mathcal{F}_b$ is the component of a vector in channel space of *real* functions with no right-hand discontinuities. In the case of elastic scattering, the solution simplifies to

$$f_\pi = \frac{\mathcal{M}_{\pi\pi,\pi\pi}}{k_{\pi\pi}^{\star 2}} \mathcal{F}\,, \tag{1.41}$$

where we drop the channel index in $\mathcal{F}$ only when describing exclusively $\pi\pi$ elastic scattering. Equation (1.41) enforces, at least in the elastic region, that the form factor has the same phase as that of the scattering amplitude. This matching of phases is known as Watson's theorem [49]. Other solutions exists, for example constructed from the Omnès function [50], which we will describe in the next section.

Finally, if a resonance appears near the physical region, a coupling between the resonance and the photon, f_R, can be extracted from the relation

$$f_a^{\mathrm{II}}(s \sim s_R) \sim -\frac{c_a\, f_R}{s - s_R}\,. \tag{1.42}$$

Again the location of the pole in the production amplitude is expected to coincide with the pole in the scattering amplitude. Resonances should appear not only in scattering, but

in transitions involving the final state into which they can decay.

1.5.2.1 Omnès function

In addition to Eq. (1.40), we can find another parameterization of the form factor by employing a dispersion relation to solve Eq. (1.39). In the case of the elastic scattering the solution is known as the Omnès function [50]. In this energy region, where only the two-pion channel is above threshold, Eq. (1.39) simplifies to

$$\mathrm{Im} f_\pi(s) = f_\pi(s) \sin\delta_1^{\pi\pi} e^{-i\delta_1^{\pi\pi}}\,, \tag{1.43}$$

where we used Eq. (1.27) to express the scattering amplitude in terms of the pion P-wave phase-shift, $\delta_1^{\pi\pi}$. We can then use the Schwarz reflection principle to identify $f_\pi^*(s+i\epsilon) = f_\pi(s-i\epsilon)$ and find that the form factor differs across the right hand cut by a phase,

$$f_\pi(s+i\epsilon) = e^{2i\delta_1^{\pi\pi}} f_\pi(s-i\epsilon)\,. \tag{1.44}$$

To solve this equation we use the ansatz

$$f_\pi(s) = \Omega(s)\,\mathcal{F}_\Omega(s)\,, \tag{1.45}$$

where the function $\mathcal{F}_\Omega$ is real and free of singularities, i.e. it satisfies $\mathrm{Im}\mathcal{F}_\Omega = 0$ over the energy region of interest. The function $\Omega(s)$, known as the Omnès function, has a discontinuity of the form

$$\mathrm{Disc}\log\left(\Omega(s)\right) = 2i\,\delta_1^{\pi\pi}(s)\,. \tag{1.46}$$

We can express the value of $\Omega(s)$ at any complex value of s with Cauchy's integral formula, and we can push the integration contour to lie around the discontinuity,

$$\log\Omega(s) = \frac{s}{\pi}\int_{s_{\mathrm{thr}}}^{\infty} \mathrm{d}s' \frac{\delta_1^{\pi\pi}(s')}{s'(s'-(s+i\epsilon))}\,. \tag{1.47}$$

where we also imposed $\Omega(0) = 1$ by applying a subtraction to this dispersive integral. The integral can be split into its real and imaginary parts, where the imaginary part can be easily calculated, while the real part corresponds to the principal value prescription (P.V.)

$$\Omega(s) = e^{i\delta_1^{\pi\pi}(s)} \times \exp\left(\frac{s}{\pi}\,\text{P.V.}\int_{s_{\text{thr}}}^{\infty} \mathrm{d}s' \frac{\delta_1^{\pi\pi}(s')}{s'(s'-s)}\right), \tag{1.48}$$

and we observe that the phase of $f_\pi = \Omega\,\mathcal{F}_\Omega$ is equal to the scattering phase-shift, satisfying Watson's theorem.

Equation (1.45), with $\Omega(s)$ given by Eq. (1.47), is a dispersive representation of the form factor, which satisfies more general analytic properties than the representation of Eq. (1.40). For instance, it does not have any singularity over the complex s plane other than the right-hand cut associated with Eq. (1.43). However, this Omnès function does not take into account the contribution of inelastic channels, which could be parameterized by the function $\mathcal{F}_\Omega$ by implementing non-analytic behavior at the inelastic threshold.

In principle, to compute the function Eq. (1.47) we need a description of the phase-shift for *all* values of energy above threshold, although, in practice, we only have knowledge of its behavior over a limited energy range. For that we can either compute the integral with a cut-off, or propose a functional form for the high energy behavior. Either option only introduces variations on the smooth part of Ω over the elastic region, which can be compensated by the function $\mathcal{F}_\Omega$, so that both options reproduce the same physical values for f_π over the elastic energy region.

Finally, because of its improved analytic properties, the Omnès parameterization of Eq. (1.45) can satisfy crossing symmetry, meaning that it can be used to rigorously describe timelike *and* spacelike data simultaneously. We turn now to the description of the spacelike form factor of the pion.

1.5.3 Spacelike form factor

For completeness we also provide the Lorentz decomposition of the process shown in Fig. 1.2a, where the photon virtuality is spacelike,

$$\left\langle \pi^+(p_1)\middle|\mathcal{J}^\mu(\vec{q})\middle|\pi^+(p_2)\right\rangle = (p_1+p_2)^\mu f_\pi(-Q^2)\,, \tag{1.49}$$

where $Q^2 = -(p_1-p_2)^2$, and where we have imposed current conservation by dropping the contribution of a term proportional to $(p_1-p_2)^\mu$. In the spacelike region, the argument of $f_\pi(s=-Q^2)$ is restricted to negative values. A consequence of current conservation is that the spacelike form factor at zero virtuality is equal to the charge of the particle in elementary charge units, i.e. $f_\pi(0)=1$. This property will be exploited to renormalize the current operator in the lattice.

In this chapter we have commented on some of the goals and challenges of hadron spectroscopy, and described the general mathematical principles describing the scattering amplitude $\mathcal{M}$, the form factors $f_a(s)$, and resonant states. In Chapter 3 we will continue to study analytic properties of amplitudes, in the case of the two-to-two transition. Before that, in the next chapter we will describe how $\mathcal{M}$ and $f_a(s)$ can be extracted from a LQCD calculation.

Chapter 2

Two-hadron amplitudes in a finite volume

In this chapter we review the state-of-the-art technology used to extract two-meson amplitudes from Lattice QCD. We begin by introducing the formulation of QCD on the lattice, and reviewing the key concepts going into a LQCD calculation. Access to the amplitudes of interest relies upon extraction of finite-volume spectra and matrix elements. We describe the connection between finite and infinite volume quantities, as well as the technology required to get the finite volume quantities. We close this chapter by describing the parameters of the lattice used for the calculation presented later in this work.

2.1 Non-perturbative finite-volume QCD

Lattice QCD is based on the Euclidean path integral formulation of QCD. The QCD path integral involves an infinite amount of integration variables, which distinguishes it from quantum mechanics. To obtain physical results from QFT it is necessary to tame the infinities, such as through the perturbative renormalization procedure in QED. Wilson proposed regularizing the path integral by placing the theory in a 4-dimensional Euclidean lattice, with inter-site spacing a, and a finite 4-dimensional volume [6]. Typically, to study

zero-temperature QCD, the lattice is defined with a larger Euclidean time size T than spatial size L, resulting in a total size of $L^3 \times T$.[1]

A discretization of the Lagrangian of QCD must be formulated such that, in the limit as $a \to 0$, the continuum Lagrangian of Eq. (1.1) is recovered. Numerous discretization options have been studied in the literature, each with different discretization errors. However, they all share the common feature that quark fields are placed at the lattice sites, while gluon fields are represented by "gauge links", denoted as U. These gauge links correspond to group elements of $SU(3)$ color associated with each link of the lattice. Their purpose is to parallel transport quarks between sites, allowing for the formation of gauge-invariant terms involving quarks at different sites. This is essential, for instance, when writing a discretized derivative that under gauge transformations transforms covariantly.

Discretization errors can be mitigated by adding irrelevant operators to the Lagrangian that effectively cancel out the leading effects due to the lattice spacing a, and vanish in the continuum limit. This procedure is known as the Symanzik improvement program [51]. Another technique that reduces discretization effects is the smearing of the fields. The idea is that more smooth, or smeared, fields will depend less on ultraviolet modes, which are the most sensitive to the discretization. Of course smearing procedures cannot be too aggressive, otherwise they could significantly modify the long-distance properties of the theory.

The lattice formulation replaces the calculation of Feynman diagrams of perturbative QFT, for the calculation of Euclidean n-point correlation functions from the QCD path integral,

$$\langle O_1(x_1) \dots O_n(x_n) \rangle = \frac{1}{\mathcal{Z}} \int \mathcal{D}\psi \, \mathcal{D}\bar{\psi} \, \mathcal{D}U \, O_1(x_1) \dots O_n(x_n) \, e^{-S_E[\psi, \bar{\psi}, U]} \,, \tag{2.1}$$

where the operators $O_i(x_i)$ are defined in terms of quark and gluon fields, while S_E is a dis-

[1] The Euclidean time direction T can be associated with the inverse temperature at which the correlation functions of the theory are extracted. To obtain vacuum expectation values we need correlation functions at zero-temperature.

cretized version of the Euclidean QCD action, and the normalization $\mathcal{Z} = \int \mathcal{D}\psi\, \mathcal{D}\bar{\psi}\, \mathcal{D}U\, e^{-S_E}$. The Euclidean action S_E is related to the action associated with the Lagrangian (1.1) through a Wick rotation.

Somewhat surprisingly, the fermionic part of the path integral can be carried out analytically, thanks to the properties of the Grassman numbers used to represent fermions. Under this operation the Dirac Lagrangian in the Euclidean action becomes the determinant of the Dirac operator. If any of the operators O_i in Eq. (2.1) involves fermion fields, they are replaced by the fermion propagator according to the appropriate Wick contractions. The propagator is equal to the inverse of the Dirac operator, which is a matrix in color, Dirac, and coordinate space that only depends on the gluon fields.

The gluonic path integral is estimated with Monte Carlo *importance sampling*. The Boltzmann factor, $e^{-S_E}/\mathcal{Z}$, assigns weights to field configurations based on the significance of their contribution to the path integral. In the context where the fermion variables have already been integrated, e^{-S_E} should be interpreted as also including the appropriate factors of the Dirac operator determinant. To estimate the path integral, an ensemble of N configurations is generated according to the probability distribution $e^{-S_E}/\mathcal{Z}$, and the integral's value is obtained from the average value of the operators $O_1(x_1) \dots O_n(x_n)$ across the ensemble. The error associated with this stochastic process, i.e. the statistical error, decreases as the number of configurations increases at a $1/\sqrt{N}$ rate. For a more extensive description of the lattice formulation of QCD, alternative discretizations of the action, and more details about the implementation of LQCD, the reader is referred to Ref. [52].

The advantage of this formulation of QCD lies in its independence from a perturbative expansion in powers of the coupling g, i.e., correlation functions incorporate the *non-perturbative* dynamics of the theory. For instance, the spectrum of the LQCD Hamiltonian consists of bound color singlet states, as expected from the phenomenological observation of confinement. The energy of these states and their matrix elements with the operators O_i, determine the value of the correlation function of Eq. (2.1). We will write this relation explicitly in Sec. 2.2.2. In practice, the spectrum and finite-volume matrix elements are

extracted by modeling the time dependence of the correlation functions estimated from a configuration ensemble.

The results obtained from LQCD are systematically improvable because the errors associated with each of the approximations can be made arbitrarily small, albeit at the cost of increased computational resources. Calculations can be performed at decreasingly small values of a and increasingly large values of L, allowing for extrapolation to the infinite volume continuum. For example, in the single particle sector of the theory, increasing the spatial size L helps remove finite-volume effects on energies and matrix elements. These effects are expected to behave like $e^{-m_\pi L}$, where m_π is the mass of the lightest hadron in the spectrum, i.e. the pion. As we will describe below, the finite-volume effects in the multi-particle sector have a more intricate behavior.

The mass of the quarks in the theory serves as an input, allowing us to study the quark mass dependence of observables. These parameters can also be tuned to reduce the amount of open channels into which a resonance can decay, simplifying the extraction of poles. Calculations are labeled by the number of flavors, N_f, of dynamic quarks used, and are typically performed in the isospin limit where the up and down quarks are degenerate.

On the topic of masses, let us comment on the scale setting procedure of LQCD. After the lattice has been used to regularize the theory, we need to renormalize the theory by imposing renormalization conditions. This allows us to determine the physical value of the lattice spacing a. In the case of pure Yang-Mills theory, the value of a will depend on the only free parameter in the Lagrangian: the coupling g. A common procedure to determine a is to calculate the static color potential between color sources, and demand that the force between between them takes its phenomenological value when the distance is equal to the Sommer scale $r_0 \approx 0.5$ fm [53]. By finding what the Sommer scale is in lattice units, we can reverse this relation to find the value of a in physical units. The process of determining the potential involves the calculation of Wilson loops, a gauge invariant product of gauge links along a loop in the lattice. The static potential between quarks is extracted from the temporal size dependence of the loop, following the procedure that we will describe in

Sec. 2.2.2. Naturally, the spatial dependence of the potential is extracted from the spatial size of the loop.

In the case of full QCD, the quark mass parameters also affect the scale setting according to the renormalization group equations. The scale is no longer a function of only g but also of the quark masses, nonetheless the scale setting can still be performed by finding the Sommer scale. In the case of two different quark masses, like in a $N_f = 2 + 1$ calculation, two more conditions are needed to tune the bare parameters of the Lagrangian. For example, we could tune the quark masses so that the mass of the nucleon, composed of mostly light quarks, and the mass of the Ω baryon, composed mostly by strange quarks, reproduce their physical values, while the Sommer scale is used to determine a. Alternatively, the scale can be set using only hadron masses and their ratios by identifying them to their physical value.

As mentioned before, calculations can be performed away from the physical value of the quark masses. This provides a computational laboratory to study, for example, the chiral evolution of observables. The triumph of QCD, and the rest of the SM, stems from the fact that once we have chosen a handful of observables to tune the bare parameters such that the theory is set at the "physical point", all the other observables can be predicted with no further experimental input. The particular importance of LQCD is that it allows us to make predictions in the non-perturbative regime of QCD.

2.1.1 Scattering in a box

Despite the ability of the lattice to handle non-perturbative dynamics, it has some limitations. In particular, if we are interested in scattering processes that involve real-time evolution, the Euclidean time of the lattice prevents us from performing a direct calculation. Direct calculations are mostly restricted to the spectrum of the theory in a finite volume, and local matrix elements, e.g. the spacelike form factor of hadrons.

According to the Maiani-Testa no-go theorem [54], the lack of real-time evolution prevents the direct extraction of amplitudes involving two or more hadrons, except at the en-

ergy of the lowest multi-particle threshold. However, the seminal work by Lüscher [55, 56] provided the basis for a framework to indirectly extract multi-hadron amplitudes from the finite-volume spectrum and matrix elements.[2] The key insight of this idea is that for a multi-hadron system trapped within a box, there is a deviation of its energy away from its non-interacting value due the infinite-volume inter-hadron interactions. This extraction is only possible as long as their interaction does not extend infinitely, a condition ensured by the fact that all experimentally observed hadrons are massive.[3]

This Lüscher quantization condition, in the energy region where only channels of two stable hadrons can go on shell, is given by

$$\det\left[\mathcal{M}(s) + F^{-1}(E, \mathbf{P}, L)\right] = 0\,. \tag{2.2}$$

where the determinant is taken over partial-wave and channel space, $\mathcal{M}$ is the scattering amplitude matrix, diagonal in partial-wave space but in general dense in channel space, and F is a known geometric function with finite-volume L dependence, in general dense in partial-wave space, but diagonal in channel space. The arguments of these two functions are related via $s = E^2 - |\mathbf{P}|^2$. See Refs. [58, 59] for explicit expressions of F and numerical techniques for its calculation. In a finite volume, the spatial momentum of the system, $\mathbf{P}$, is quantized. In the case of spatial periodic boundary conditions, the momentum of a state can take values equal to $\frac{2\pi}{L}\mathbf{d}$, where $\mathbf{d}$ is a vector of integers. The solutions to Eq. (2.2), up to $e^{-m_\pi L}$ corrections and restricted to the energy region where only two hadrons can go on shell, correspond to the finite volume spectrum.

The reason for F being dense in the partial-wave space is that the boundary conditions in a box break rotational symmetry, leading to the mixing of partial-waves. For example, in a lattice with a cubic spatial volume, the rotational symmetry group gets broken from

[2] It has been proposed that a Quantum Computer could calculate real time evolution, with research directed to formulations of scattering extractions from real-time finite volume correlation functions, for example in Ref. [57].

[3] In the chiral limit, with vanishing quark masses, the pseudoscalar mesons become massless, and hadronic interactions would be of infinite range. In that scenario the Lüscher quantization condition is not reliable.

$O(3)$ to the full octahedral O_{h} group. In a cube, the total spin J is no longer a good quantum number, but the leftover symmetries of $O(3)$ in the O_{h} group replace the infinite number of irreducible representations J with the ten irreducible representations of O_{h}, dubbed *irreps*, which we label with the symbol Λ. We call rows the different components of a state in a lattice irrep.

The matrices in Eq. (2.2) can be block-diagonalized and an independent quantization condition appears for each of the lattice irreps. In this process, partial-waves are matched with one or multiple irreps of the lattice, these patterns are known as the subductions of the corresponding partial-wave. For a system in flight, with $\mathbf{P} \neq 0$, the symmetry is further reduced to the little group of $\mathbf{P}$ inside a box, we list these little groups in Table 2.1 for different values of $\mathbf{P}$ in Schönflies notation. For reference, we list the subduction pattern for integer J's up to 4 for a system at rest, and up to 3 for an in-flight system in Table 2.1. The elements of the projector matrices that implement this subduction are called the subduction coefficients, these can be found in Refs. [60, 61].

The subduction patterns that apply for partial-waves of definite spin-parity also apply to stable particles of spin J inside a box. This means that the different spin projections of a hadron that form part of the representation J in the continuum, will get distributed across states in different irreps of the lattice. For example, if the ρ-meson was stable and at rest, its three spin-projections would behave as the three components of a state in the T_1^- irrep. If it had momentum of the form $\frac{2\pi}{L}[00n]$, its zero helicity component would be a state in the A_1 irrep, and a mix of the non-zero helicity components would be the two components of a state in the E_2 irrep.

The relationship between the continuum components and the lattice irrep components are given by the same subduction coefficients introduced above. This means that the previous example also describes the subduction pattern of the scattering channel with same J^P as a ρ-meson. The determinant of Eq. (2.2), when the system has momentum $\frac{2\pi}{L}[00n]$, splits into independent determinants, i.e. one for A_1 and two identical copies for E_2.

In general, we denote the solutions of Eq. (2.2) as $\{E_\mathfrak{n}\}$, where the index $\mathfrak{n}$ encodes all the quantum numbers of the state, e.g. its momentum, irrep, row, and energy level.

Table 2.1: Integer spin-parity (J^P) subduced to each of the lattice irreps, in flight irreps subduce helicities, but we list the corresponding J^P that would contribute to that helicity. For each irrep we list its dimension in parenthesis. For the case of zero momentum, there is one irrep per parity. Adapted from Ref. [62].

O_h	$\mathbf{P} = \frac{2\pi}{L}[000]$	C_{4v}	$\mathbf{P} = \frac{2\pi}{L}[00n]$	C_{2v}	$\mathbf{P} = \frac{2\pi}{L}[0nn]$
$A_1(1)$	0, 4 ...	$A_1(1)$	0^+, 1^-, 2^+, 3^- ...	$A_1(1)$	0^+, 1^-, $2^\pm$, $3^\pm$ ...
$A_2(1)$	3 ...	$A_2(1)$	0^-, 1^+, 2^-, 3^+ ...	$A_2(1)$	0^-, 1^+, $2^\pm$, $3^\pm$ ...
$E(2)$	2, 4 ...	$E_2(2)$	$1^\pm$, $2^\pm$, $3^\pm$ ...	$B_1(1)$	$1^\pm$, $2^\pm$, $3^\pm$ ...
$T_1(3)$	1, 3, 4 ...	$B_1(1)$	$2^\pm$, $3^\pm$ ...	$B_2(1)$	$1^\pm$, $2^\pm$, $3^\pm$ ...
$T_2(3)$	2, 3, 4 ...	$B_2(1)$	$2^\pm$, $3^\pm$ ...		

C_{3v}	$\mathbf{P} = \frac{2\pi}{L}[nnn]$	C_2	$\mathbf{P} = \frac{2\pi}{L}[nm0]$ or $= [nnm]$
$A_1(1)$	0^+, 1^-, 2^+, $3^\pm$ ...	$A_1(1)$	0^+, $1^\pm$, $2^\pm$, $3^\pm$ ...
$A_2(1)$	0^-, 1^+, 2^-, $3^\pm$ ...	$A_2(1)$	0^-, $1^\pm$, $2^\pm$, $3^\pm$ ...
$E_2(2)$	$1^\pm$, $2^\pm$, $3^\pm$ ...		

The Lüscher quantization has been successfully applied to several systems of coupled-channel scattering, see Refs. [63, 64, 65, 66, 67, 68, 69, 70, 71, 72], with an efficient strategy to solving Eq. (2.2) in the coupled-channel case presented in Ref. [73]. This technique is reviewed in Ref. [74].

The concept of the finite-volume extraction of the scattering amplitude was extended by Lellouch and Lüscher to transition amplitudes by deriving the finite-volume correction of the weak decay amplitude $K \to \pi\pi$ [75]. Extensions to arbitrary transitions involving two-hadrons in the initial or final state were later developed [76, 77, 78]. In the case of a production amplitude $\mathcal{H}$ from a local current $\mathcal{J}$, the finite-volume matrix elements of the states within the two-hadron energy region can be "finite-volume corrected" by the following prescription

$$|\,{}_L\langle 0|\mathcal{J}(x=0)|\mathfrak{n}\rangle_L|^2 = \frac{1}{2E_\mathfrak{n}L^3}\mathcal{H}(E_\mathfrak{n})\cdot\widetilde{\mathcal{R}}(E_\mathfrak{n},L)\cdot\mathcal{H}(E_\mathfrak{n})^\intercal\,, \tag{2.3}$$

$$\widetilde{\mathcal{R}}(E_\mathfrak{n},L) = 2E_\mathfrak{n}\lim_{E\to E_\mathfrak{n}}\frac{E-E_\mathfrak{n}}{\mathcal{M}(s)+F^{-1}(E,L)}\,, \tag{2.4}$$

where $|\mathfrak{n}\rangle_L$ is a unit-normalized finite-volume state of energy $E_\mathfrak{n}$, and we have left implicit the $\mathbf{P}$ dependence of F. In this case $\mathcal{H}$ represents a vector with partial-wave and channel space components corresponding to each of the production channels. The matrix $\widetilde{\mathcal{R}}$, and variations of it, are referred to as the Lellouch-Lüscher (LL) factor. The LL factor is a matrix in partial-wave and channel space, but needs to be of rank one to be consistent with causality [77]. In other words, only one of the eigenvalues of the matrix $\mathcal{M}+F^{-1}$ can vanish at the quantization condition energy. This allows to decompose $\widetilde{\mathcal{R}}$ into an outer product, featuring the eigenvector $\mathbf{v}_0$ of the vanishing eigenvalue of $\mathcal{M}+F^{-1}$,

$$\widetilde{\mathcal{R}} = \frac{2E_\mathfrak{n}}{\lambda_0'}\,\mathbf{v}_0\,\mathbf{v}_0^\intercal\,, \tag{2.5}$$

where λ_0' is the slope in energy of the vanishing eigenvalue at $E_\mathfrak{n}$. Although in practice it is more convenient [79] to use the matrix $\mathcal{M}\widetilde{\mathcal{R}}\mathcal{M}$,

$$\begin{aligned}\mathcal{M}\,\widetilde{\mathcal{R}}\,\mathcal{M} &= -2E_\mathfrak{n}\cdot\lim_{E\to E_\mathfrak{n}}\frac{E-E_\mathfrak{n}}{\mathcal{M}^{-1}(s)+F(E,L)}\,,\\ &= -\frac{2E_\mathfrak{n}^\star}{\mu_0'^\star}\,\mathbf{w}_0\,\mathbf{w}_0^\intercal\,,\end{aligned} \tag{2.6}$$

where $\mu_0'^\star$ is the slope in $E^\star$ of the vanishing eigenvalue of $\mathcal{M}^{-1}+F$, which is seen to control the normalization, while the eigenvector, $\mathbf{w}_0$, distributes strength across the channel and partial-wave space. This formalism has been used to calculate the timelike form factor of the pion in the elastic region, as mentioned in Sec. 1.4.1.1.

In the next section we describe how the energy levels going into the quantization condition of Eq. (2.2), and the finite volume matrix elements needed in the LL formalism of Eq. (2.3) are obtained from lattice correlation functions.

2.2 Lattice technology

There are a several developments that have allowed the field of LQCD to reach sufficient maturity to perform calculations of amplitudes involving several particles, we present an overview of the main technological developments in the following subsections. We begin by summarizing the parameters of the lattice employed in the calculation of Chapters 5, 6, 7, and 8.

2.2.1 Lattice parameters

The lattice calculation presented in this work was performed on a $N_f = 2 + 1$ lattice obtained by the HadSpec collaboration [80]. The gauge field is realized from an $O(a^2)$-improved Symanzik action, while the quark contribution uses the Clover action, a type of Symanzik improvement, with "stout-link" smearing of the spatial gauge links; more details of the implementation are given in [81]. The HadSpec collaboration uses an anisotropic formulation, with finer temporal than spatial spacing, $a_t < a_s$, to increase the energy cut-off without significant increase to the computational cost. Because of the anisotropy $\xi = a_s/a_t$, on top of choosing the bare coupling and the bare masses, the action has anisotropy parameters that need to be tuned to reproduce space-time symmetry. The tuning of the anisotropic gauge action is performed with Wilson loops, by demanding that their spatial dependence relates to their temporal dependence according to the target anisotropy [81]. The tuning of the anisotropic fermion action is performed with the dispersion relation of the energy $E_{\mathbf{P}}$ of a stable hadron with momentum $\mathbf{P}$ and mass m, which should satisfy

$$(a_t E_{\mathbf{P}})^2 = (a_t m)^2 + |a_s \mathbf{P}|^2/\xi^2 \,. \tag{2.7}$$

This $N_f = 2+1$ lattice has two degenerate light quarks with larger than physical mass, and a strange quark with approximately physical mass, such that the pion has a mass of approximate twice its physical value, 284 MeV, while the kaon has a mass close to its

physical value, 520 MeV. The volume of the lattice is equal to $L^3 \times T = (24a_s)^3 \times 256a_t$, where $a_t^{-1} = 5.988(17)$ GeV and the anisotropy is equal to $\xi = 3.455(6)$, as reported in Ref [82]. The scale is set by identifying the mass of the Ω baryon in the lattice to be equal to its physical value. This is possible thanks to the tuning of the bare strange quark mass to a value close to its physical value. This tuning was performed by identifying combinations of pseudoscalar masses with a leading chiral behavior dependent on individual quark masses. In this work we employ the Lüscher quantization condition, the LL formalism, and identify stable hadrons in the lattice with their continuum counterparts. Residual finite-volume effects not taken into account scale as $e^{-m_\pi L}$, but given that $m_\pi L \approx 4$ we expect them to have a negligible impact compared to other sources of error, e.g. statistical fluctuations.

This lattice has been used in previous computations of $\pi\pi$ scattering [83, 84], πK scattering [82] and the electromagnetic transition $\gamma K \to K\pi$ [85].

2.2.2 Energy levels and the variational method

A short outline of the variational method is given at the beginning of Sec. III of Ref. [80]. More details of the practicalities of the implementation can be found in [86]. Here I summarize the main conceptual points.

The finite-volume spectrum of QCD can be obtained from the time dependence of correlation functions. We can perform a spectral decomposition of correlation functions to obtain the Euclidean time dependence given by a sum of decaying exponentials. In the case of two-point functions, neglecting finite-T effects, the time dependence is of the form

$$C_{ij}(t) \equiv \left\langle O_i(t) O_j^\dagger(0) \right\rangle = \sum_{\mathfrak{n}=0} Z_i^{\mathfrak{n}} Z_j^{\mathfrak{n}*} e^{-E_{\mathfrak{n}} t} \,, \tag{2.8}$$

where $E_{\mathfrak{n}}$ corresponds to the energy of state $|\mathfrak{n}\rangle$, and $Z_i^{\mathfrak{n}}$ is equal to the overlap of the operator O_i with that state, i.e. $Z_i^{\mathfrak{n}} = \langle 0|O_i(0)|\mathfrak{n}\rangle$. From Eq. (2.8) we observe that the ground state will dominate the sum of contributions at large time, and in order to obtain the energy of several states we need to disentangle the different exponential terms. Obtaining

the energy of excited states is desirable if we want to extract $\mathcal{M}$ from Eq. (2.2) over a wide kinematic region.

If we form a matrix of correlation functions with elements of the form of Eq. (2.8), $Z^{\mathfrak{n}}$ can be thought of as a vector in the space of the operator basis that we are using. The spectrum for each momentum, irrep, and internal quantum numbers is independent, and we can form a matrix for each of the available combinations of quantum numbers consistent with the channel of interest. If we want to extract the A lowest energy levels, we need at least A operators to form a linearly independent basis with the $Z^{\mathfrak{n}}$ vectors to disentangle the time dependence associated with each level. For that we introduce the generalized eigenvalue problem (GEVP)

$$C(t)v^{\mathfrak{n}} = C(t_0)v^{\mathfrak{n}}\lambda^{\mathfrak{n}}(t,t_0)\,, \tag{2.9}$$

where $v^{\mathfrak{n}}$ is a vector in the operator space, and $\lambda^{\mathfrak{n}}$ is the generalized eigenvalue, also known as principal correlator. If we split the correlation matrix into two terms

$$C_{ij}(t) = C^0_{ij}(t) + C^1_{ij}(t) = \sum_{\mathfrak{n}=0}^{A-1} Z_i^{\mathfrak{n}} Z_j^{\mathfrak{n}*} e^{-E_{\mathfrak{n}}t} + \sum_{\mathfrak{n}=A} Z_i^{\mathfrak{n}} Z_j^{\mathfrak{n}*} e^{-E_{\mathfrak{n}}t}\,, \tag{2.10}$$

we can solve exactly for $\lambda^{\mathfrak{n}}_{(0)}(t,t_0)$, the generalized eigenvalue of the truncated matrix $C^0(t)$. We begin the derivation by first writing $C^0(t)$ in the matrix notation

$$C^0(t) = ZE(t)Z^\dagger\,, \quad [Z]_{\mathfrak{n}i} = Z_i^{\mathfrak{n}}\,, \quad [E(t)]_{\mathfrak{n}\mathfrak{m}} = \delta_{\mathfrak{n}\mathfrak{m}}e^{-E_{\mathfrak{n}}t}\,. \tag{2.11}$$

If the $Z^{\mathfrak{n}}$ vectors are linearly independent, then the matrix Z has an inverse, and we can convert the generalized eigenvalue problem in a conventional eigenvalue problem

$$E(t-t_0)Zv^{\mathfrak{n}} = Zv^{\mathfrak{n}}\lambda^{\mathfrak{n}}_{(0)}(t,t_0)\,, \tag{2.12}$$

where we have used that the inverse of $E(t)$ is $E(-t)$ and that $E(t_1)E(t_2) = E(t_1+t_2)$. For

the sake of readability we are denoting this zero-th order approximation of the generalized eigenvectors as $\{v\}$. Relation (2.12) is an eigenvalue equation with eigenvectors $Zv^{\mathfrak{n}}$. The matrix $E(t-t_0)$ is diagonal, and we can directly read that

$$\lambda^{\mathfrak{n}}_{(0)}(t,t_0) = e^{-E_{\mathfrak{n}}(t-t_0)}\,, \tag{2.13}$$

and the $\mathfrak{n}$-th eigenvector is $\sum_j Z^{\mathfrak{m}}_j v^{\mathfrak{n}}_j \propto \delta^{\mathfrak{n}\mathfrak{m}}$, where the index $\mathfrak{m}$ corresponds to the components of the eigenvector in this space. For convenience we choose the normalization

$$\sum_j Z^{\mathfrak{m}}_j v^{\mathfrak{n}}_j = \delta^{\mathfrak{n}\mathfrak{m}} e^{E_{\mathfrak{n}} t_0/2}\,, \tag{2.14}$$

which makes the generalized eigenvectors orthonormal over the metric $C^0(t_0)$,

$$v^{\mathfrak{m}\dagger} C^0(t_0) v^{\mathfrak{n}} = \delta_{\mathfrak{n}\mathfrak{m}}\,. \tag{2.15}$$

We can also treat $C^1_{ij}(t)$ as a perturbation, and calculate the first-order correction to add to $\lambda^{\mathfrak{n}}$, which is of the form [87],

$$\lambda^{\mathfrak{n}}_{(0)}(t,t_0) + \lambda^{\mathfrak{n}}_{(1)}(t,t_0) = (1-b_{\mathfrak{n}})e^{-E_{\mathfrak{n}}(t-t_0)} + b_{\mathfrak{n}} e^{-E_{A+1}(t-t_0)}\,, \tag{2.16}$$

where the exponential term of the correction is driven by the energy of the $(A+1)$-th level in the spectrum, and the coefficient $b_{\mathfrak{n}}$ decreases exponentially with increasing t_0. It is known that this remains the leading correction to all orders as long as $2t_0 \geq t$ [87]. The regular eigenvalues of $C_{ij}(t)$ have a similar dependence on time than $\lambda^{\mathfrak{n}}_{(0)}(t,t_0)$, but the leading correction for the $\mathfrak{n}$-th eigenvalue is driven by the energy of the $(\mathfrak{n}+1)$-th state [88]. For this reason, solving the GEVP has a considerable advantage over the regular eigenvalues of the correlation matrix.

It is more stable to perform independent fits of the time dependence of multiple principal correlators, where each fit function has one or two exponential contributions, than

attempting to extract multiple energies from a single correlation function of the form of Eq. (2.8). Additionally, this technique allows to disentangle contributions of degenerate states, or degenerate up to statistical precision, whereas a multi-exponential fit would not.

It might appear advantageous to use large values of t_0 for a couple of reasons. At a larger t_0, the energy levels above the A-th state will have decayed and can be treated as a perturbation, where the principal correlators can be properly modeled with Eq. (2.16). Otherwise, the imposition of the orthonormality condition of Eq. (2.15) might force the operators into a metric that does not correspond to that of the lowest A states, and the time dependence of $\lambda^{\mathfrak{n}}(t, t_0)$ would not necessarily be that of Eq. (2.16). This behavior was explored with a toy model in App. C of Ref. [86]. Even in the best scenario, where Eq. (2.16) is a valid model, increasing t_0 reduces the magnitude of the $b_{\mathfrak{n}}$ coefficient, minimizing the pollution from higher energy states to the principal correlator.

However, the correlation functions have an associated uncertainty due to the Monte Carlo estimation of LQCD. This noise is expected to increase exponentially with the time separation for all correlation functions except the one of the lightest meson of the theory, for which the noise to signal ratio is expected to stay constant, this is known as the Parisi-Lepage scaling [89, 90]. In that sense a compromise has to be reached when choosing t_0, where the correlation function has not been swamped by noise yet, but the contributions from energy states above the A-th state have had enough time that $C^0(t_0)$ becomes a good approximation of $C(t_0)$.

As mentioned before, having a large basis is a requirement to obtain a large set of energies. Furthermore, the larger the basis, the higher the energy of the $(A+1)$-th state, and the more quickly that contribution decays away. This will be true as long as the basis is diverse enough to describe the different types of states in the low lying spectrum. In the multi-hadron energy region it has been observed that this diversity is necessary to obtain an accurate spectrum. For instance in Ref. [91], it was observed that removing specific types of operators from the basis can lead to a qualitatively different spectrum. In there, it is explained that if the operator set is not diverse enough to be able to span the space of

the lowest energy states, even if the operators on a reduced basis have a sizeable overlap to all states, the principal correlators will take a significant amount of time to relax to the correct value of each energy state.

Once the spectrum has been obtained from the principal correlators, taking into account the caveats described above, we can use the eigenvectors to construct *optimized operators*. We choose to construct these operators with the following normalization

$$\Omega^\dagger_{\mathfrak{n}} \equiv \sqrt{2E_{\mathfrak{n}}} e^{-E_{\mathfrak{n}} t_0/2} \sum_{j=1}^{A} v_j^{\mathfrak{n}} \, O_j^\dagger \, . \tag{2.17}$$

The overlap of these operators with the low-lying states in the spectrum is equal to

$$\langle \mathfrak{n} | \Omega^\dagger_{\mathfrak{m}}(0) | 0 \rangle = \sqrt{2E_{\mathfrak{n}}} \, \delta_{\mathfrak{n},\mathfrak{m}} \, , \tag{2.18}$$

so that correlation functions with these operators at the source $t = 0$, and sink t, is equal to

$$\Big\langle \Omega_{\mathfrak{m}}(t) \, \Omega^\dagger_{\mathfrak{n}}(0) \Big\rangle = \delta_{\mathfrak{m},\mathfrak{n}} 2E_{\mathfrak{n}} e^{-E_{\mathfrak{n}} t} + \mathcal{O}\big(e^{-E_{A+1} t}\big) \, , \tag{2.19}$$

where we observe that each linear combination of operators will optimally overlap to only one of the low-lying states, with corrections typically arising from the $(A+1)$-th energy level.

When solving the GEVP, we can obtain a set of eigenvectors $v^{\mathfrak{n}}$ for every timeslice available. If the operator basis and the value of t_0 is selected properly the eigenvectors will only have a weak dependence on t. In practice, we observe that selecting a timeslice $t_Z > t_0$ for the eigenvector set, the condition of Eq. (2.19) is best satisfied.

In summary, we have found that the energies $\{E_{\mathfrak{n}}\}$ and optimized operators $\Omega^\dagger_{\mathfrak{n}}$ can be extracted from the eigenvalues and eigenvectors of the generalized eigenvalue problem of $C_{ij}(t)$. In the following subsections we will describe the type of operators used in scattering extraction calculations.

2.2.3 Operators

In this section we will describe the two type of operators relevant for the extraction of states in the two-meson sector. We will utilize operators projected to definite momentum, $O_{\mathbf{P},i}(t) = \sum_{\mathbf{x}} e^{-i\mathbf{P}\cdot\mathbf{x}} O_i(t,\mathbf{x})$, which sample all spatial sites on a timeslice.

2.2.3.1 Fermion bilinears

An operator type that we expect to have a strong overlap with the low-lying meson spectrum is a local fermion bilinear sandwiching the gamma matrix structure, $\mathbf{\Gamma}$, necessary to match the meson spin and parity, i.e. $O(x) = \bar{\psi}(x)\,\mathbf{\Gamma}\,\psi(x)$. We list in Tab. 2.2 the particles, and their quantum numbers, that can be interpolated by all the possible gamma structures. The flavor of the interpolator is determined by the flavor of the quark fields. For example, in isoscalar channels, the mixture of bilinears of the form $\mathcal{O}^{\ell} = \bar{u}\mathbf{\Gamma}u + \bar{d}\mathbf{\Gamma}d$ with those like $\mathcal{O}^{s} = \bar{s}\mathbf{\Gamma}s$ can be studied. This was employed in Ref. [92], where the light-strange mixing of isoscalars was estimated from the overlaps of the finite volume levels to these operators.

To study mesons of higher spin than those shown in Tab. 2.2, and to produce multiple operators with the same quantum numbers and enlarge our variational basis, we can use non-local fermion bilinears. These can be produced from combining, with the appropriate Clebsch-Gordan coefficients, gamma matrices and gauge-covariant derivatives in a circular basis, then sandwiching the result between quark-antiquark fields, such that these operators have definite $J^{P(C)}$ quantum numbers. The local fermion bilinears only feature quark-antiquark in a color-singlet, while non-local bilinears featuring one or more covariant derivatives will also contain the quark-antiquark in the octet combination, some of them even featuring *only* color-octet quark-antiquark contributions. More details about the conventions taken in this construction are given in Ref. [60]. In that reference, it is also mentioned how these continuum-spin operators are subduced into the irreps of the cubic group. The pattern of overlaps of an operator subduced to different irreps can be useful to identify (stable) states with their continuum counterpart, as long as the lattice spacing

is small enough to restore rotational symmetry at small distances.

For mesons in-flight, the helicity, instead of spin z-component, is the continuum conserved quantum number. Operators of definite helicity can be constructed via a Wigner-D matrix acting on an operator of definite spin z-component with non-zero momentum. Then these operators are subduced into the corresponding *little group* irrep of the lattice. The details of this construction are presented in Ref. [61].

Table 2.2: Fermion bilinears quantum numbers, and the corresponding particle state they overlap into when they are projected to zero momentum, following the PDG naming scheme shown in Tab. 1.1, where the isovector combination of quark flavors has been chosen. In the case of the Wick rotated Euclidean fermion action, the gamma matrices change as they have to satisfy the algebra $\{\gamma^\mu, \gamma^\nu\} = \delta^{\mu\nu}$, and the labeling convention of the greek indices goes from 1 to 4, instead of from 0 to 3. If we make the substitution $\gamma^0 \to \gamma^4$, the overlap pattern presented here remains equal for the Euclidean theory.[a]

	$\bar{\psi}\psi$	$\bar{\psi}\gamma^5\psi$, $\bar{\psi}\gamma^0\gamma^5\psi$	$\bar{\psi}\gamma^i\psi$, $\bar{\psi}\gamma^0\gamma^i\psi$	$\bar{\psi}\gamma^i\gamma^5\psi$	$\bar{\psi}[\gamma^i, \gamma^j]\psi$
P	$+1$	-1	-1	$+1$	$+1$
C	$+1$	$+1$	-1	$+1$	-1
Overlap	a_0	π	ρ	a_1	b_1

[a] The $\bar{\psi}\gamma^0\psi$ operator does not overlap to a $\bar{q}q$ state because it has the exotic quantum numbers $J^{PC} = 0^{+-}$.

2.2.3.2 Two-meson operators

When thinking about studying scattering, the most natural choice of interpolators are those resembling multiple mesons. In Ref. [93] the construction of these type of operators is described. In that reference it is advocated to construct multi-meson operators by combining single meson operators that are already subduced to an irrep of the lattice. It is also convenient to use single-meson-like operators that have been optimized to overlap to the ground state mesons. The coefficients of this linear combination will be given by the Clebsch-Gordan coefficients coupling the irreps of the single mesons to the irrep of the total momentum. This is preferred over the subduction of a multi-meson operator which has been partial-wave projected, i.e. which was constructed from meson operators of definite helicity. In the latter case the subduced multi-meson operator will, in general,

be formed by single hadrons in multiple irreps.

Following this prescription, the construction of a two-meson-like operator, in the case of two pions, is given by

$$[\pi\pi]^{\Lambda\mu}_{\mathbf{P}}(t) = \sum_{R} C^{\Lambda\mu,\mathbf{P}}_{\Lambda_1,R\,\mathbf{p}_1;\Lambda_2,R\,\mathbf{p}_2}\, \pi^{\Lambda_1}_{R\,\mathbf{p}_1}(t)\, \pi^{\Lambda_2}_{R\,\mathbf{p}_2}(t)\,, \tag{2.20}$$

where $C^{\Lambda\mu,\mathbf{P}}_{\Lambda_1,R\,\mathbf{p}_1;\Lambda_2,R\,\mathbf{p}_2}$ are the Clebsch-Gordan coefficients of the induced representations of the little groups of each momenta in the O_h group. In this equation the sum runs over the allowed lattice rotations R that leave the momentum $\mathbf{P}$ invariant, i.e. the little group of $\mathbf{P}$, such that for all rotations $R\,\mathbf{p}_1 + R\,\mathbf{p}_2 = \mathbf{P}$. For the target state, we indicated a row μ within the irrep Λ, necessary for a multidimensional irrep Λ, see Tab. 2.1; the pions, being spinless, always appear in unidimensonal irreps. When constructing two-meson operators involving single vector-mesons the summation in Eq. (2.20) is also required over the rows of the vector-meson irrep. Explicit examples of these Clebsch-Gordan coefficients are given in Ref. [93]. This same procedure can be iterated to formulate operators with more than two mesons, as described in Ref. [69].

An important advantage of the two-meson-like operators, over the single-meson-like operators is that they sample the lattice volume differently. While the fermion bilinears projected to a given momentum are the linear combination of operators localized around a lattice site, the two-meson operators are linear combinations of operators separated by all the allowed distances in the box. This makes them more efficient at interpolating states that do not behave like single hadrons.

2.2.4 Matrix elements from correlation functions

To obtain *production* amplitudes, the required finite-volume matrix elements are extracted from two-point correlation functions, $\left\langle \mathcal{J}(t)\, \Omega^\dagger_{\mathfrak{n}}(0) \right\rangle$, which feature the electromagnetic current $\mathcal{J}$. To constrain the amplitude over a wide range of kinematics we employ optimized operators, $\Omega_{\mathfrak{n}}$, for the ground state and multiple excited states of each irrep. In Eq. (1.9)

we showed how this current can be decomposed into components of definite isospin. The current operator needs to be renormalized, with a renormalization constant for each quark of different mass. The electromagnetic current, including light and strange quarks, in terms of lattice currents is equal to

$$\mathcal{J} = Z_V^l \tfrac{1}{\sqrt{2}} \left(\mathcal{J}_{\rho,\mathrm{lat}} + \tfrac{1}{3} \mathcal{J}_{\omega_l,\mathrm{lat}} \right) + Z_V^s \left(-\tfrac{1}{3} \mathcal{J}_{\omega_s,\mathrm{lat}} \right) , \tag{2.21}$$

where we define the isospin-basis currents with the following normalizations,

$$\mathcal{J}_\rho \equiv \tfrac{1}{\sqrt{2}} \big(\bar{u} \Gamma u - \bar{d} \Gamma d \big), \mathcal{J}_{\omega_l} \equiv \tfrac{1}{\sqrt{2}} \big(\bar{u} \Gamma u + \bar{d} \Gamma d \big), \mathcal{J}_{\omega_s} \equiv \bar{s} \Gamma s \,, \tag{2.22}$$

and the spatially directed vector current whose improvement at $\mathcal{O}(a)$ is consistent with the anisotropic Clover quark action is [94],

$$\bar{q} \Gamma q = \bar{q} \gamma^k q + \tfrac{1}{4} (1 - \xi)\, a_t \partial_4 \big(\bar{q} \sigma^{4k} q \big) \,, \tag{2.23}$$

where $\sigma^{4k} = \frac{1}{2}[\gamma^4, \gamma^k]$.

In the case where production of $\pi\pi$ is considered, only the isovector component, $\mathcal{J}_\rho$, appears, and the multiplicative renormalization factor, Z_V^l, is determined non-perturbatively using the pion form factor at zero virtuality extracted from three-point correlation functions, $\Big\langle \Omega_\pi(\Delta t)\, \mathcal{J}(t)\, \Omega_\pi^\dagger(0) \Big\rangle$, as described in Ref. [85], and Sec. 6.3.

Following the spectral decomposition of correlation functions given in Eq. (2.8), the two-point function featuring the electromagnetic current will be of the form

$$\Big\langle \mathcal{J}(t)\, \Omega_{\mathfrak{n}}^\dagger(0) \Big\rangle = e^{-E_{\mathfrak{n}} t} \sqrt{2E_{\mathfrak{n}}}\, L^3 \, \langle 0 | \mathcal{J}(x=0) | \mathfrak{n} \rangle_L + \mathcal{O}\big(e^{-E_{A+1} t} \big) \,, \tag{2.24}$$

where the volume factor L^3 arises if the current operator has been projected to definite momentum, i.e. if $\mathcal{J}(t) = \sum_{\mathbf{x}} e^{-i\mathbf{P}\cdot\mathbf{x}} \mathcal{J}(t, \mathbf{x})$. The matrix element can then be extracted from the time dependence of this two-point function. Alternatively, we can form the ratio

of correlation functions

$$\frac{\left\langle \mathcal{J}(t)\Omega^{\dagger}_{\mathfrak{n}}(0)\right\rangle}{\left\langle \Omega_{\mathfrak{n}}(t)\Omega^{\dagger}_{\mathfrak{n}}(0)\right\rangle} = \frac{L^3}{\sqrt{2E_{\mathfrak{n}}}}\left\langle 0|\mathcal{J}(0)|\mathfrak{n}\right\rangle_L + \mathcal{O}\Big(e^{-(E_{A+1}-E_{\mathfrak{n}})t}\Big)\,, \tag{2.25}$$

and extract the matrix element from the time dependence of the ratio. The ratio typically features reduced timeslice-to-timeslice data correlation, which helps avoid the D'Agostini bias [95].

To extract spacelike matrix elements for a stable hadron we require the use of three-point functions. In the case of the pion spacelike form factor, we employ optimized pion operators, Ω_π, at the source and sink, and insert a current operator in between. This three-point function has the spectral decomposition

$$\left\langle \Omega_{\pi,\mathbf{p}_f}(\Delta t)\,\mathcal{J}(t)\,\Omega^{\dagger}_{\pi,\mathbf{p}_i}(0)\right\rangle = \left\langle \pi(\mathbf{p}_f)|\mathcal{J}(0)|\pi(\mathbf{p}_i)\right\rangle e^{-E_{\pi,\mathbf{p}_f}(\Delta t-t)}e^{-E_{\pi,\mathbf{p}_i}t} + \dots\,, \tag{2.26}$$

where the subleading time dependence will arise from matrix elements associated with higher energy states with the quantum number of a pion. Note that we explicitly label the momentum projection of each of the optimized operators, and employ a relativistic finite-volume normalization for the pion states

$$\left\langle \pi(\mathbf{p}_f)|\pi(\mathbf{p}_i)\right\rangle = 2E_{\pi,\mathbf{p}_f}L^3\delta_{\mathbf{p}_f,\mathbf{p}_i}\,, \tag{2.27}$$

where $E_{\pi,\mathbf{p}}$ is the energy of the pion following the dispersion relation of Eq. (2.7). This normalization choice is motivated by the fact that single-meson states receive only exponentially suppressed volume corrections. Similar to the case of production matrix elements, we can also form ratios to reduce timeslice-to-timeslice data correlation,

$$\frac{\left\langle \Omega_{\pi,\mathbf{p}_f}(\Delta t)\,\mathcal{J}(t)\,\Omega^{\dagger}_{\pi,\mathbf{p}_i}(0)\right\rangle}{\left\langle \Omega_{\pi,\mathbf{p}_f}(\Delta t-t)\Omega^{\dagger}_{\pi,\mathbf{p}_f}(0)\right\rangle\left\langle \Omega_{\pi,\mathbf{p}_i}(t)\Omega^{\dagger}_{\pi,\mathbf{p}_i}(0)\right\rangle} = \frac{1}{2E_{\pi,\mathbf{p}_f}2E_{\pi,\mathbf{p}_i}}\left\langle \pi(\mathbf{p}_f)|\mathcal{J}(0)|\pi(\mathbf{p}_i)\right\rangle + \dots\,, \tag{2.28}$$

the matrix element on the right hand side of the equation can be related to the pion form factor $f_\pi(s)$ with Eq. (1.49).

2.2.5 Distillation

To compute correlation matrices with multi-meson operators, i.e. having multiple fermion bilinear operators at the source and at the sink, we need to perform matrix inversions of the Dirac operator to obtain the propagator. Even though the Dirac operator might be sparse, the propagator is not. For example, for a lattice with 20^4 sites, the propagator has $\mathcal{O}(10^{12})$ entries, making a direct calculation prohibitively expensive.

Instead, we can compute the inversions over a subspace that more efficiently samples the low-lying spectrum in which we are interested. For that we employ a quark-field smearing method known as *distillation* [96]. This method consists of using a projector operator on each quark field to filter out ultraviolet modes. This projector is invariant under rotations and is covariant under gauge transformations, such that the rotation properties and quantum numbers of the operators previously described are left unchanged by the smearing procedure.

The smearing process for the operator $\bar{\psi}\,\mathbf{\Gamma}^{\mathbf{P}}\,\psi = \sum_{\mathbf{x}} \bar{\psi}(t,\mathbf{x})\, e^{-i\mathbf{P}\cdot\mathbf{x}}\, \mathbf{\Gamma}(t,\mathbf{x})\, \psi(t,\mathbf{x})$, where $\mathbf{\Gamma}(t,\mathbf{x})$ represents a combination of gamma matrices and covariant derivatives, goes as follows. First, from the spatial Laplacian at timeslice t, which is a matrix in coordinate and color space, $\{\mathbf{x}, a\}$, we compute the N_{vecs} eigenvectors, $\xi_n(\mathbf{x}, a; t)$, with the smallest eigenvalues. Then, we form the smearing operator

$$\square(\{\mathbf{x}, a\}, \{\mathbf{y}, b\}; t) = \sum_{n=1}^{N_{\text{vecs}}} \xi_n(\mathbf{x}, a; t)\, \xi_n^\dagger(\mathbf{y}, b; t)\,, \tag{2.29}$$

which behaves as a projector, i.e. $\square^2 = \square$. This operator is applied to each quark field, and because it consists of a sum over external products of eigenvectors, we can factorize

the meson operator into

$$\bar{\psi}\,\Box\,\mathbf{\Gamma}^{\mathbf{P}}\,\Box\,\psi = \sum_{n,m=1}^{N_{\text{vecs}}} \bar{\tilde{\psi}}(t,n)\,\Phi_{nm}(t)\,\tilde{\psi}(t,m)\,, \tag{2.30}$$

where we defined the "elemental" matrix Φ_{nm}, the smeared quark field $\tilde{\psi} = \xi^{\dagger}\psi$, and we suppressed the sum over spin indices.

When the fermionic path integral is performed, the quark fields are replaced by their Wick contractions, e.g. $\bar{\psi}\overbrace{\psi} = (i\not{D} - m)^{-1} = M^{-1}$. In this case the smearing procedure will be applied to the quark propagators to form "perambulators", $\tau_{nm}(t',t) \equiv \xi_n^{\dagger}(t')M^{-1}(t',t)\xi_m(t)$. Once this smearing has been performed, correlation functions become products of matrices over distillation space. Furthermore, since the perambulators are independent of the operators of the meson elemental, the inversions required to calculate them can be done once and then they can be stored and reused in multiple calculations.

Finally, local current insertions, like the electromagnetic current, should not be smeared, and in those cases we use a "generalized perambulator",

$$J_{nm}(\Delta t, t, t_s) = \xi_n^{\dagger}(\Delta t)\big[M^{-1}(\Delta t, t)\,\mathbf{\Gamma}\,M^{-1}(t, t_s)\big]\xi_m(t_s)\,. \tag{2.31}$$

The generalized perambulator is constructed by first calculating the inversions of the Dirac operator from the distillation vectors at t_s and Δt acting as sources, these two inversions can then be contracted at t to form J_{nm}. Notice that we cannot employ this technique for a *disconnected* current insertion, because in that case the Wick contraction only involves unsmeared fields. The calculations presented in this work only feature connected current contributions.

2.2.6 Statistical methods

In addition to smearing, another technique employed to reduce fluctuations is to average over multiple time sources, i.e.

$$C_{ij}(t) = \frac{1}{N_{\text{src}}} \sum_{t_{\text{src}}} \left\langle O_i(t + t_{\text{src}}) O_j^\dagger(t_{\text{src}}) \right\rangle . \tag{2.32}$$

In our case with a lattice of temporal length of $256a_t$, we employ four equally separated values of t_{src} along the temporal direction for the calculation of the correlation matrix going into the GEVP of Chapter 5.

2.2.6.1 Error propagation

Resampling methods are commonly used in LQCD calculations to propagate the Monte Carlo statistical error from the correlation functions to the final results. The most popular methods are bootstrap and jackknife [97]. In this work we employed single elimination jackknife for error propagation. This method proceeds as follows: from an ensemble of N samples $\mathcal{O}_i$ of a random variable $\mathcal{O}$, e.g. an n-point function ensemble from LQCD, where the index i enumerates the elements in the ensemble, we form a *downscaled* ensemble

$$\mathcal{O}_i^{\text{JK}} \equiv \frac{1}{N-1} \sum_{j \neq i}^{N} \mathcal{O}_j \, . \tag{2.33}$$

Each element of the downscaled ensemble is basically the mean of the ensemble after eliminating one of its elements. After that, we apply any number of operations, $y = g(\mathcal{O})$, to the downscaled ensemble, e.g. fitting the timeslice dependence to obtain the energy, or the matrix element. Finally we *upscale* the ensemble of results $y_i^{\text{JK}} = g(\mathcal{O}_i^{\text{JK}})$,

$$y_i = y_i^{\text{JK}} - N \left(y_i^{\text{JK}} - \frac{1}{N} \sum_j y_j^{\text{JK}} \right) . \tag{2.34}$$

The value and statistical error of the quantity $\hat{y} = \langle g(\mathcal{O}) \rangle$ can be calculated with standard statistical techniques applied to the ensemble y_i. Furthermore, if another operation needs to be applied to the quantity y, e.g. obtaining the scattering amplitude from the spectrum, we can downscale the y ensemble and repeat these steps.

This concludes our description of the state-of-the-art calculation techniques for lattice QCD. The next chapter returns to the ideas of scattering in the infinite volume, but after that, we will return to the finite volume.

Chapter 3

On-shell decomposition of the infinite-volume $2 \xrightarrow{\mathcal{J}} 2$ transition

As mentioned in Chapter 1, most of our current understanding of strong resonant states is based on their mass, width, and coupling to asymptotic states. However, more information is needed to form a complete picture of their nature and structure. Building on the study of the internal structure of *stable* hadrons by probing them with external currents, we envision the possibility of studying *resonances* in a similar fashion. This Chapter presents the first novel results of this work, which were first presented in Ref. [98]. The figures presented in this Chapter were similarly taken from Ref. [98].

In this chapter we study amplitudes of the form $2 \xrightarrow{\mathcal{J}} 2$, which we label $\mathcal{W}$, and formulate a decomposition of these amplitudes that respects analyticity and unitarity. We call this result the *on-shell* decomposition because it is built in terms of the amplitudes describing possible subprocesses, with each of these evaluated as if its external particles were on their mass shell. This on-shell projection will always apply to Lorentz scalar form factors, but not to the kinematic Lorentz tensors associated with the current insertion. If the meson-meson asymptotic states couple to a resonance or a bound state, we will show how to extract the elastic form factor of that state from the on-shell decomposition.

As reviewed in Chapter 1, unitarity and causality impose analytical constraints on the

functional form of scattering amplitudes. Once these conditions have been satisfied, we can confidently move away from the real energy axis in the search of the complex pole of a resonance. In a similar way, the analytical properties of multi-body amplitudes can be studied, to then find further properties of resonances.

This formalism describes $\mathcal{W}$ in terms of amplitudes of subprocesses, known kinematic functions, and dynamical functions describing the short range interactions associated with the meson-meson states and the current. The energy dependence of amplitudes associated with each subprocess, as well as that of the amplitude $\mathcal{W}$ itself, could be obtained from a LQCD calculation of the necessary spectra and finite-volume matrix elements. These quantities would need to be mapped to infinite volume amplitudes, as described in Chapters 2 and 4.

The decomposition of the amplitude $\mathcal{W}$ is model-independent and encodes the contributions from all orders of the strong coupling. However, the result is only valid over the energy region where at most two mesons can go on shell. This limits the current momentum to be below any production threshold if it is timelike, but can have an arbitrary spacelike value. In other words, the results can only be used for an elastic two-meson system, or a system of multiple coupled two-meson channels.

To derive the results of this chapter we will describe amplitudes in terms of a skeleton expansion of all the diagrams in a generic effective field theory (EFT). We will not need to make any explicit reference to the parameters of the EFT, we only need to assume that the theory contains stable mesons that will feature in the propagators and kernels of the diagram expansion of $\mathcal{W}$. An additional ingredient not present in the on-shell decomposition of $\mathcal{M}$, which is given by the K-matrix representation, is the presence of the so-called *triangle diagram*, which contributes logarithmic singularities to $\mathcal{W}$.

In Section 3.1 we introduce the subprocesses appearing in $\mathcal{W}$, then in Sec. 3.2 we show the resulting on-shell decomposition. In Sec. 3.3 we illustrate the analytic continuation and extraction of the resonance elastic form factor. In Sec. 3.4 we sketch the derivation of the decomposition, and in Sec. 3.5 we present the derivation of a function reproducing the

singularities of the kinematic triangle contribution.

The decomposition presented in Ref. [98] applies to multiple two-meson channels with arbitrary masses, where each of the external mesons does not possess spin degrees of freedom, but the two-meson systems can be described by an arbitrary number of partial-waves, allowing to extract form factors of arbitrary integer spin resonances. For simplicity we will show the derivation of the amplitude associated with an elastic channel of two degenerate mesons of mass m where only the lowest partial-wave is relevant, and afterwards briefly discuss the generalization to multiple channels, and partial-waves. Furthermore we will assume that the two particles are not identical, and only one of them couples to the external current, such that no symmetry factors are required for diagrams with bubble loops.

3.1 Amplitudes of subprocesses

Let us first introduce the two amplitudes associated with subprocesses of the amplitude $\mathcal{W}$. The first of them is the $2 \to 2$ scattering amplitude, $\mathcal{M}$, which we already introduced in Sec. 1.5. The second is the one-meson transition $1 \xrightarrow{\mathcal{J}} 1$, which we label w. Both the transitions $\mathcal{W}$ and w are mediated by a local current $\mathcal{J}^A(x=0)$, where A represents all the quantum numbers associated with the current, e.g. the Lorentz indices for a tensor current, the flavor, parity, etc.

The current insertion is defined in terms of a matrix element of the current sandwiched by one-meson states

$$\langle k_f|\mathcal{J}^A(0)|k_i\rangle = \sum_j K_j^A(k_f,k_i)\, f_j(Q^2)\,, \tag{3.1}$$

where we label the momentum of the final/initial meson $k_{f/i}$, and where we perform a Lorentz decomposition of the matrix element in terms of scalar form factors, f_j, and Lorentz tensors K_j, where we define $Q^2 = -(k_f - k_i)^2$. By definition, the external momenta here are on the mass shell, i.e. $k_{f/i}^2 = m^2$. We illustrated this decomposition in the case of a

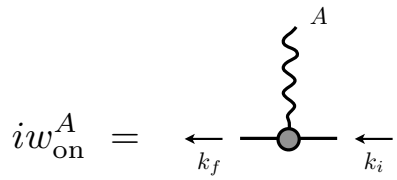

Figure 3.1: Diagrammatic representation of $w_{\rm on}$, the one-meson transition partially projected on shell. The grey kernel symbolizes that while the form factors are projected on shell, the kinematic factors can be evaluated for off shell values of the momenta k_f and k_i.

conserved vector current in Eq. (1.49).[1]

In general, when one-meson current insertions appear as a subprocess of $\mathcal{W}$, the value of momenta k_f or k_i will not necessarily be on the mass shell. To extend the definition of w to arbitrary values of momenta we simply evaluate the tensors K_j in terms of k_f and k_i, but we keep the form factors projected on shell as a function of only Q^2. We label this extension with the symbol $w_{\rm on}$, where the subscript "on" reminds us that the form factor take their on shell value. The definition of $w_{\rm on}$ is still given by Eq. (3.1), but valid for arbitrary value of momenta. We illustrate this partially on-shell projected amplitude in Fig. 3.1. This defines a prescription for the individual terms in our decomposition, but the combination of all terms should be prescription independent.

3.2 On shell decomposition

We define the $2+\mathcal{J}\to 2$ amplitude, which we label as $\mathcal{W}$, via the matrix element,

$$\mathcal{W}^A(P_f,\hat{\mathbf{p}}'^\star_f;P_i,\hat{\mathbf{p}}^\star_i)\equiv\left\langle P_f,\hat{\mathbf{p}}'^\star_f;\text{out}\right|\mathcal{J}^A(0)\left|P_i,\hat{\mathbf{p}}^\star_i;\text{in}\right\rangle_{\rm conn}\,. \tag{3.2}$$

Here the two-meson asymptotic initial(final) states are defined in terms of a total momentum $P_{i(f)}$, and the relative momentum direction $\hat{\mathbf{p}}^{(\prime)\star}_{i(f)}$ in the initial(final) CM frame. The subscript "conn" emphasizes that this matrix element only takes into account connected

[1] In this chapter and the next one the single particle form factors are not considered in the timelike region, and we employ the notation $f(Q^2)$ for the spacelike form factors, whereas in the rest of this work, where we are primarily interested in the timelike form factors, we use $f(-Q^2)$ or $f(s<0)$ for the spacelike form factors.

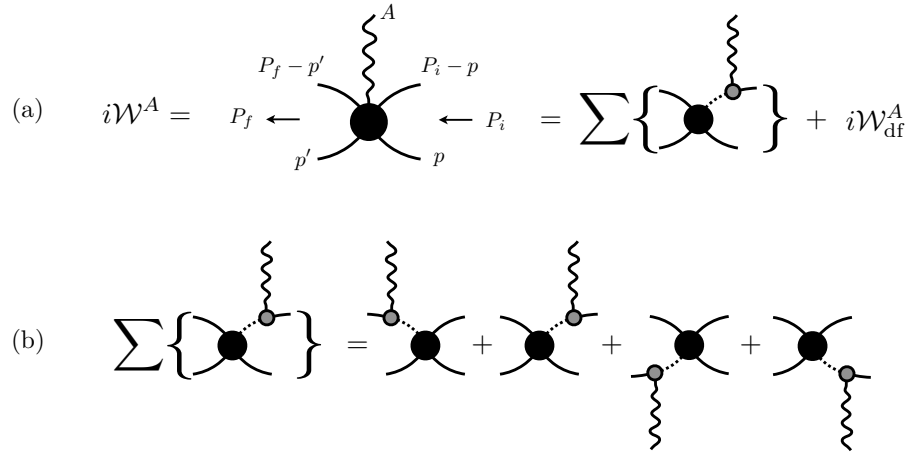

Figure 3.2: (a) Diagrammatic representation of the amplitude $\mathcal{W}$ describing the $2 \xrightarrow{\mathcal{J}} 2$ process. The initial/final state momentum is given by $P_{i/f}$, and the current quantum numbers are labeled with index A. The dashed line represents the pole piece D of the fully dressed propagator. The solid kernels represent all diagrams contributing to a given amplitude. (b) Long range contributions associated with current insertions to the external legs of the amplitude.

contributions, we do not consider diagram topologies in the skeleton expansion where the hadrons do not interact with each other or with the current.

In Sec. 3.4 we derive the on-shell decomposition to be equal to

$$i\mathcal{W}^A(P_f, \hat{\mathbf{p}}'^{\star}_f; P_i, \hat{\mathbf{p}}^{\star}_i) = \sum \left\{ i w^A_{\rm on} \, iD \, i\mathcal{M} \right\} + i\mathcal{W}^A_{\rm df}(P_f, \hat{\mathbf{p}}'^{\star}_f; P_i, \hat{\mathbf{p}}^{\star}_i) \, . \tag{3.3}$$

We illustrate the decomposition diagrammatically in Fig. 3.2, where we also label the momentum of each of the external hadrons. The first term represents the long range process whenever the current insertion probes one of the external legs of the amplitude. Here we introduce the pole piece of the fully dressed propagator,

$$iD(k) = \frac{i}{k^2 - m^2 + i\epsilon} \, . \tag{3.4}$$

If the current only couples to one of the particle species, the individual contributions of

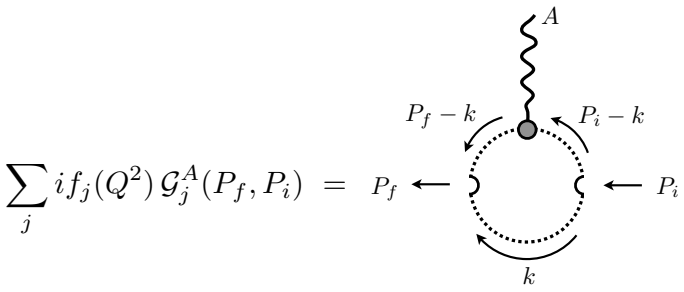

Figure 3.3: Triangle-function contribution to $\mathcal{W}_{\rm df}$, Eq. (3.6), written in terms of the single-hadron form factors (f_j) and the triangle loops ($\mathcal{G}_j$) defined in Eq. (3.7). The gray circle and dashed lines were defined in Figs. 3.1 and 3.2, respectively.

the first term are equal to

$$\sum \left\{ i w^A_{\rm on}\, iD\, i\mathcal{M} \right\} = i w^A_{\rm on}(p'_f, p'_i)\, iD(p'_i)\, i\mathcal{M}(s_i) + i\mathcal{M}(s_f)\, iD(p_f)\, i w^A_{\rm on}(p_f, p_i)\,, \qquad (3.5)$$

where $p^{(\prime)}_{i/f}$ is a shorthand for $P_{i/f} - p^{(\prime)}$, and $s_{i(f)} = P^2_{i(f)}$. Here we assumed that the scattering amplitude $\mathcal{M}$ only has contributions from the S-wave, meaning that it is independent of the relative momenta direction in the respective CM frames. Note that there are physical values of the external momenta for which the pole pieces can diverge.

The second term in Eq. (3.3) will be the center of attention in Sec. 3.3, which we label with a subscript "df", which stands for *divergence free*, referring to the lack of long distance poles given by Eq. (3.5). In Sec. 3.4 we prove that it can be written in an on-shell projected form as,

$$i\mathcal{W}^A_{\rm df}(P_f, P_i) = \mathcal{M}(s_f) \left[i\mathcal{A}^A_{22}(P_f, P_i) + \sum_j i f_j(Q^2) \mathcal{G}^A_j(P_f, P_i) \right] \mathcal{M}(s_i)\,, \qquad (3.6)$$

where again, because only the S-wave is allowed to contribute, we dropped the dependence on the relative momenta direction in the respective CM frames. The kernel $\mathcal{A}^A_{22}$, in general, can be expressed in a Lorentz decomposition, similar to Eq. (3.1), with each Lorentz scalar being a *real and regular function* in s_i, s_f, and Q^2 over the kinematic region of interest.

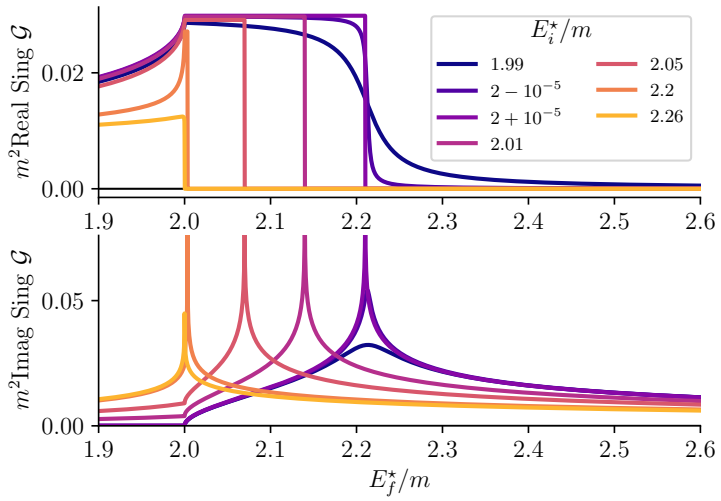

Figure 3.4: Singularities of the $\mathcal{G}$ function as reproduced by the contributions of $\mathcal{G}$ given explicitly in Eq. (3.8). We choose values below and above threshold of the initial and final state energies $E_i^\star = \sqrt{s_i}$, $E_f^\star = \sqrt{s_f}$. We fix the value of the spatial momentum of the initial state in the CM frame of the final state to $|\mathbf{P}_i^\star| = 1.05m$.

The remaining quantity to define is the triangle function $\mathcal{G}_j$, diagrammatically shown in Fig. 3.3, which occurs when the current probes a single meson in the intermediate state. In Eq. (3.3) we again assume that the current only couples to one of the mesons,

$$\mathcal{G}_j^A(P_f, P_i) \equiv \int \frac{d^4k}{(2\pi)^4} \frac{iK_j^A(k_f, k_i)}{(k^2 - m^2 + i\epsilon)(k_f^2 - m^2 + i\epsilon)(k_i^2 - m^2 + i\epsilon)}\,, \tag{3.7}$$

where $k_{i/f} \equiv P_{i/f} - k$ and K_j are the kinematic functions defined in Eq. (3.1).

In addition to having threshold singularities, this kinematic function also has a new class of singularities, known as the *triangle singularities*, or *anomalous threshold singularities* [99]. For example, in the case where both the initial and final states are in a S-wave, for $K_j = 1$, the triangle function is given by,

$$\mathcal{G}(P_f, P_i) = \frac{i}{32\pi\sqrt{(P_f \cdot P_i)^2 - P_i^2 P_f^2}} \left[\log\left(\frac{1 + z_f^\star + i\epsilon}{1 - (z_f^\star + i\epsilon)}\right) + \log\left(\frac{1 + z_i^\star + i\epsilon}{1 - (z_i^\star + i\epsilon)}\right)\right] + \dots\,, \tag{3.8}$$

where the ellipsis represent regular terms, $z_f^\star$ is a function of P_i, P_f, and the masses of the

external particles,

$$z_f^\star = \frac{P_i \cdot P_f - s_i}{2k^\star(s_f)\sqrt{(P_f \cdot P_i)^2/s_f - s_i}}\,, \tag{3.9}$$

while $z_i^\star$ is the same function but with the labels f and i switched. We label $\mathrm{Sing}\,\mathcal{G}$ the contribution to $\mathcal{G}$ given explicitly in Eq. (3.8) that contains all its singularities and discontinuities of $\mathcal{G}$.

We plot $\mathrm{Sing}\,\mathcal{G}$ given in Eq. (3.8) in Fig. 3.4 for various values of the initial and final state energies, while fixing the spatial momentum of the initial state relative to the final state. In addition to the threshold singularities at $\sqrt{s} = 2m$, we observe singularities that appear above threshold and have a logarithmic behavior, diverging in the imaginary part, while the real part exhibits a discontinuity at the same energy. This energy is the threshold at which all three particles in the triangle are able to be on their mass shell simultaneously, also known as the anomalous threshold [2].

3.3 Resonance form factors

If there is a resonance present in $\mathcal{M}$, then $\mathcal{W}$ will inherit the singular behavior, as is evident from Eq. (3.6). The relationship between the residues of the poles in $\mathcal{W}$ and the desired elastic form factors can be obtained using the LSZ reduction procedure. This is illustrated diagrammatically in Fig. 3.5. The following describes the extraction corresponding to a scalar resonance and a scalar current. In this case, quantities with superscript A defined above behave like Lorentz scalars, meaning that we can exchange their dependence from the four-momenta (P_f, P_i) to the Lorentz scalars (s_f, Q^2, s_i).

In Eq. (1.25) we illustrated that resonances appear as complex-valued poles (s_R) in the analytic continuation of the scattering amplitude onto the unphysical Riemann sheet. To determine the elastic form factor of the resonance, $f_{R\to R}(Q^2)$, we can extract the

[2] In the case of loosely bound states, like the deuteron with mass $M = 2m - \epsilon$ and binding energy $\epsilon \ll m$, m being the nucleon mass, the anomalous threshold lies near the physical region of the deuteron form factor. The contribution of the anomalous threshold is associated in non-relativistic quantum mechanics to the spatial extent of the bound state's wavefunction [100].

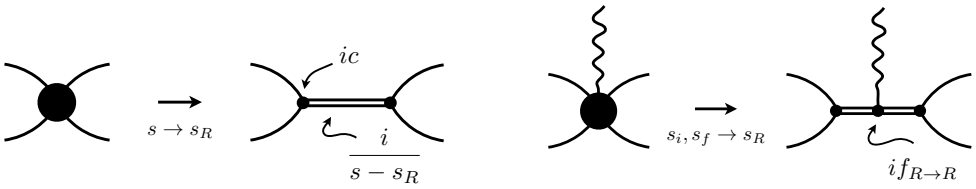

Figure 3.5: Amplitudes (a) $\mathcal{M}$ and (b) $\mathcal{W}$, near the resonance pole s_R. The resiudes at the pole define the coupling c, and the elastic-resonance form factor, $f_{R\to R}$.

corresponding residue of $\mathcal{W}$ via the LSZ reduction as

$$\lim_{s_i,s_f\to s_R} \mathcal{W}^{\text{II,II}}(s_f,Q^2,s_i) = \lim_{s_i,s_f\to s_R} \mathcal{W}^{\text{II,II}}_{\text{df}}(s_f,Q^2,s_i)\,, \tag{3.10}$$

$$= 16\pi \frac{-c}{s_f - s_R}\, f_{R\to R}(Q^2)\, \frac{-c}{s_i - s_R}\,, \tag{3.11}$$

where $f_{R\to R}(Q^2)$ is defined for initial and final energy $s_i = s_f = s_R$. We write two II superscripts to emphasize that one must continue the amplitude in both s_i and s_f planes in order to evaluate at the resonance pole. In the first equality, we have used the fact that the difference between $\mathcal{W}$ and $\mathcal{W}_{\text{df}}$, given in Eq. (3.3), only features either the initial or final resonance pole but not both. [3]

The $\mathcal{W}_{\text{df}}$ amplitude on the second Riemann sheet in both variables can be derived from the on shell representation Eq. (3.6),

$$\mathcal{W}^{\text{II,II}}_{\text{df}}(s_f,Q^2,s_i) = \mathcal{M}^{\text{II}}(s_f)\left[\,\mathcal{A}_{22}(s_f,Q^2,s_i) + f(Q^2)\mathcal{G}^{\text{II,II}}(s_f,Q^2,s_i)\,\right]\mathcal{M}^{\text{II}}(s_i)\,, \tag{3.12}$$

where the function $\mathcal{G}^{\text{II,II}}$ is given by the analytic continuation of the triangle function in both s_i and s_f into the Riemann sheet II,

$$\mathcal{G}^{\text{II,II}}(s_f,Q^2,s_i) = \mathcal{G}(s_f,Q^2,s_i) - 2i\,\text{Im}\,\mathcal{G}(s_f,Q^2,s_i)\,. \tag{3.13}$$

[3] This procedure is followed in Ref. [12] for studying the σ as well as in Refs. [101, 102, 103] for theories with bound states.

Note that in Eq. (3.12), we exploited the fact that $\mathcal{A}_{22}$ is regular in the kinematic region considered. A proof of Eq. (3.12) is provided in Appendix B.

To determine the form factor we can invert Eq. (3.10) and combine it with Eq. (3.12) to obtain

$$f_{R\to R}(Q^2) \equiv \frac{1}{16\pi} \lim_{s_i, s_f \to s_R} \frac{s_i - s_R}{-c} \frac{s_f - s_R}{-c} \mathcal{W}_{\text{df}}^{\text{II,II}}(s_f, Q^2, s_i) \tag{3.14}$$

$$= 16\pi c^2 \left[\mathcal{A}_{22}(s_R, Q^2, s_R) + f(Q^2)\, \mathcal{G}^{\text{II,II}}(s_R, Q^2, s_R)\right] . \tag{3.15}$$

Although this discussion applies for scalar currents and S-wave scattering systems, the relations can be generalized to arbitrary currents, partial waves, and channels. The kinematic Lorentz tensors for a current with non-trivial Lorentz structure do not alter the analytic structure of $\mathcal{W}$. For multiple scattering channels, one must take care on which sheet the amplitude is continued to, following the same methodology as presented in, for example, Ref. [104].

Conserved vector currents are of special interest, as they can represent the physical electromagnetic interaction. It was shown in Ref. [101] that current conservation constrains the forward direction of the $\mathcal{W}$ amplitude. For example, assuming only S-wave scattering is non-negligible, the amplitude for a system consisting of one neutral and one charged particle must follow the relation,

$$\lim_{P_i \to P_f} \mathcal{W}_{\text{df}}^{\mu}(P_f, P_i) = 2P^{\mu} \mathrm{Q}_0 \frac{\partial}{\partial s} \mathcal{M}(s) , \tag{3.16}$$

where Q_0 is the charge of the particle. This identity imposes further constraints on $\mathcal{A}_{22}$, namely that in the forward limit

$$\mathcal{A}_{22}^{\mu}(P, P) = -2\mathrm{Q}_0 P^{\mu} \frac{\partial}{\partial s} \mathcal{K}^{-1}(s) - \mathrm{Q}_0 \mathrm{Re}\, \mathcal{G}^{\mu}(P, P) , \tag{3.17}$$

which follows directly from Eq. (3.6) and noting that the imaginary part of $\mathcal{G}^{\mu}$ in the

forward limit is proportional to $\partial\rho/\partial s$, ensuring that $\mathcal{A}_{22}$ is a real function.

If there is a resonance in this system, then at the resonance pole Eq. (3.16) imposes that the form factor of the resonance at $Q^2 = 0$ is the charge of the resonant state. We define the form factor for a scalar resonance with a vector current in an analogous way to Eq. (3.10) as

$$(P_f + P_i)_\mu f_{R\to R}(Q^2) \equiv \lim_{s_i, s_f \to s_R} \frac{s_f - s_R}{c} \mathcal{W}^{\mathrm{II,II}}_{\mathrm{df},\mu}(P_f, P_i) \frac{s_i - s_R}{c}\,. \tag{3.18}$$

Taking the $P_i \to P_f$ limit of Eq. (3.18), we then use Eq. (3.16) to find

$$2P^\mu f_{R\to R}(0) = 2P^\mu \mathrm{Q}_0 \lim_{s\to s_R} \frac{(s - s_R)^2}{c^2} \frac{\partial}{\partial s} \mathcal{M}^{\mathrm{II}}(s), \tag{3.19}$$

$$= 2P^\mu \mathrm{Q}_0\,. \tag{3.20}$$

Therefore, we conclude that the resonance form factor for a conserved vector current yields its charge at $Q^2 = 0$ as one may expect. The use of the Ward-Takahashi identity to impose additional constraints on two-hadron resonances has been explored, e.g. in Ref. [105] for the Roper and in Ref. [106] for the Δ.

3.4 Derivation of the decomposition

To derive the on shell decomposition of an amplitude, we will express it in terms of Feynman diagrams of a generic EFT to all orders in the interaction coupling. In the case of the two-meson amplitudes of interest, we can reorganize this expansion in terms of a skeleton expansion of two-particle irreducible (2PI) kernels. Then, we can reformulate the all-orders diagram expansion in terms of integral equations. Non-trivial analytical constraints can be derived from these equations by exploiting the properties of two-particle irreducible (2PI) kernels on the kinematic region below the three-particle threshold.

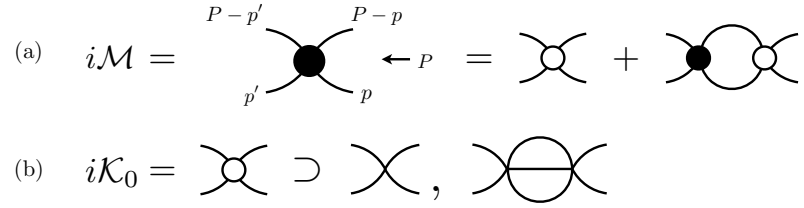

Figure 3.6: Diagrammatic representation of (a) $\mathcal{M}$ and its integral equation, and (b) $\mathcal{K}_0$ and examples of 2PI diagrams.

3.4.1 Scattering amplitude warm up

Before deriving the on-shell representation of $\mathcal{W}$, we will first illustrate our method in the case of $\mathcal{M}$ and reproduce the well-known result of the K-matrix representation. In the case of the $2 \to 2$ process we can reorganize all diagrams in skeletons with increasing number of 2PI kernels, connected with one another with s-channel bubble loops. The integral equation describing this skeleton expansion of $\mathcal{M}$ is illustrated in Fig. 3.6a. If we recursively substitute the scattering amplitude given by the right hand side of the equation into the scattering amplitude appearing in the second term of the right hand side of the equation we will recover the infinite series of diagrams contributing to $\mathcal{M}$.

The 2PI kernels include all diagrams where the initial and final legs cannot be separated by cutting two internal propagators of the diagram. In Fig. 3.6b we show two examples of 2PI diagrams in the case without a current insertion. We label $\mathcal{K}_0$ the 2PI kernel containing all such diagrams, this kernel is closely related to the K-matrix of Eq. (1.31) as we will show later. The diagrams in Fig. 3.6b are 2PI because the first has no internal lines to cut, while the second stays connected after cutting two of its internal propagators. The last diagram in Fig. 3.6a is not 2PI because it can be separated by cutting the two propagators in the middle.

Let us write the integral equation of the all-orders expansion of the $\mathcal{M}$ amplitude

$$i\mathcal{M}(p',p) = i\mathcal{K}_0(p',p) + \int \frac{d^4k}{(2\pi)^4} i\mathcal{M}(p',k) i\Delta(k) i\Delta(P-k) i\mathcal{K}_0(k,p)\,, \tag{3.21}$$

where the value of the external momenta for each leg is illustrated in Fig. 3.6a, and does

not need to be on its mass shell. We choose the propagators to have unit residue at the pole mass,

$$i\Delta(k) = \frac{i}{k^2 - m^2 + i\epsilon} + iS(k)\,, \tag{3.22}$$

$$\equiv iD(k) + iS(k)\,, \tag{3.23}$$

where the function S is regular at the pole. For the kinematic region of interest, $i\mathcal{K}_0$ behaves as a regular function of s because none of the diagrams it represents contain an intermediate state that can go on shell. We can recover the on-shell amplitude for each of the kernels by placing the external legs on shell

$$\mathcal{M}(s) = \mathcal{M}(p', p)\Big|_{p^2=p'^2=(P-p)^2=(P-p')^2=m^2}\,, \tag{3.24}$$

where again we are assuming that only the S-wave is relevant so that the scattering amplitude has no angular dependence.

3.4.1.1 The bubble loop integral

The goal of the on shell decomposition is to group contributions to an amplitude according to their analytic behavior. The bubble loop has two types of contributions, a part that remains real in the kinematic region of interest, and a piece proportional to the phase space with a square root singularity at threshold. To show this let us demonstrate it with a generic bubble loop, written here in full notation,

$$\mathcal{I}_0(P) = \int \frac{d^4k}{(2\pi)^4} i\mathcal{L}(p', k) i\Delta(k) i\Delta(P-k) i\mathcal{R}(k, p)\,, \tag{3.25}$$

where the $\mathcal{L}$ and the $\mathcal{R}$ are generic kernel functions that appear as endcaps of the loop, these will have the same analytic properties as the kernel $\mathcal{K}_0$ described before.

We expand the endcaps around their on shell value, as defined in Eq. (3.24). Because

we will be neglecting all but one partial-wave, the on shell value will be independent of the loop momentum,

$$i\mathcal{L}(p',k) = i\mathcal{L}(s) + [i\mathcal{L}(p',k)]\delta\,, \tag{3.26}$$

$$i\mathcal{R}(k,p) = i\mathcal{R}(s) + \delta[i\mathcal{R}(k,p)]\,, \tag{3.27}$$

when we generalize to arbitrary partial-waves, the dependence of the loop momentum in the on-shell piece will be encoded in solid spherical harmonics given in Eq. (3.73), so that the following derivations still hold. The terms with a δ operator next to them are inspired by the notation introduced in Ref. [107], in this case they will vanish when both internal legs of the loop are on-shell and therefore will be proportional to at least one factor of $(k^2-m^2)((P-k)^2-m^2)$. This means that a term with a δ operator times the propagators will be regular. Furthermore, in order to obtain the singular contribution of the integral, we just need to consider the term with the propagators replaced by their singular pieces,

$$\mathcal{I}_0(P) = i\mathcal{L}(s)\left[\int \frac{d^4k}{(2\pi)^4} iD(k)iD(P-k)\right] i\mathcal{R}(s) + \delta\mathcal{I}_0(P)\,, \tag{3.28}$$

where $\delta\mathcal{I}_0$ is purely regular in the kinematic region of interest.

To obtain the singularity of the integral shown in Eq. (3.28), we calculate its discontinuity across the real s axis in the complex s plane using Cutkosky rules [108], which amounts to replacing the propagators with Dirac delta functions,

$$iD(k) \to 2\pi\delta(k^2-m^2)\theta(k^0)\,, \tag{3.29}$$

After doing the substitution, carrying out two integrals with the help of the Dirac deltas, and performing the remaining angular integration we obtain the well-known discontinuity of the bubble loop

$$\frac{1}{2}\mathrm{Disc}\,\mathcal{I}_0(P) = i\mathcal{L}(s)\left[\frac{k^\star(s)}{8\pi\sqrt{s}}\theta\left(s-s_{\mathrm{thr}}\right)\right] i\mathcal{R}(s)\,. \tag{3.30}$$

where the relative momentum $k^\star(s)$, given in Eq. (1.12), has a branch point at threshold and generates the right hand cut in the amplitude. This term is proportional to the phase space $\rho(s)$ defined in Eq. (1.13).

Putting all the terms together we find that

$$\mathcal{I}_0(P) = i\mathcal{L}(s)\,\rho(s)\,i\mathcal{R}(s) + \delta\mathcal{I}_0'(P)\,, \tag{3.31}$$

where the kernel $\delta\mathcal{I}_0'$ includes $\delta\mathcal{I}_0$, as well as the regular contributions that do not contribute to the discontinuity of the integral in Eq. (3.28). We rewrite this result with the following shorthand notation,

$$\mathcal{I}_0 = i\mathcal{L}\,\rho\,i\mathcal{R} + i\mathcal{L}\cdot i\mathcal{S}\cdot i\mathcal{R}\,, \tag{3.32}$$

where the first term indicates a product of kernels, whereas the '$\cdot$' operator indicates that there is a remaining loop integral to be evaluated, but the $\mathcal{S}$ kernel reminds us that the resulting value of this integral remains regular in s in the kinematic region of interest. Here we have demonstrated that we can split the loop diagrams into a term with singular behavior, i.e. a branch point, and a term with regular behavior: real and without discontinuities over the kinematic region of interest.

3.4.1.2 The infinite series

To calculate the on shell decomposition of $\mathcal{M}$ we will rewrite Eq. (3.21) as a geometric series. Then we can use the result of Eq. (3.31), together with some identities given in App. A, to simplify the result. The goal of this exercise is to separate all contributions proportional to the phase space, with a square root singularity, from those which remain real.

First, let us introduce a shorthand representation of Eq. (3.21),

$$i\mathcal{M} = i\mathcal{K}_0 + i\mathcal{M}\cdot\mathcal{D}\cdot i\mathcal{K}_0\,, \tag{3.33}$$

where we use $\mathcal{D}$ to represent the bubble loop integral and the two propagators in it.

As we mentioned before, we can recursively use the definition of $\mathcal{M}$ to express it in a form reminiscent of a geometric series

$$i\mathcal{M} = i\mathcal{K}_0 + i\mathcal{K}_0 \cdot \mathcal{D} \cdot i\mathcal{K}_0 + i\mathcal{K}_0 \cdot \mathcal{D} \cdot i\mathcal{K}_0 \cdot \mathcal{D} \cdot i\mathcal{K}_0 + \dots \,, \tag{3.34}$$

$$= i\mathcal{K}_0 \cdot [\mathcal{D} \cdot i\mathcal{K}_0]^g \tag{3.35}$$

where we define the shorthand notation for a geometric series $[A]^g = 1 + A + A \cdot A + \dots$. We then use the result of Eq. (3.32) to rewrite this equation

$$i\mathcal{M} = i\mathcal{K}_0 \cdot [(\rho + i\mathcal{S}) \cdot i\mathcal{K}_0]^g \,, \tag{3.36}$$

$$= i\mathcal{K}_0 \cdot [i\mathcal{S} \cdot i\mathcal{K}_0]^g [\rho \, i\mathcal{K}_0 \cdot [i\mathcal{S} \cdot i\mathcal{K}_0]^g]^g \,, \tag{3.37}$$

where in the second line we use the identity of Eq. (A.6). Note that for kernels hitting a phase space factor, ρ, we can drop the '$\cdot$', representing integration, between them, as they will be projected on shell, and there is only a multiplication between them.

Finally, we can regroup all the contributions without a discontinuity in what is commonly known as the K-matrix,

$$i\mathcal{K} = i\mathcal{K}_0 \cdot [i\mathcal{S} \cdot i\mathcal{K}_0]^g \,, \tag{3.38}$$

to arrive to the well known result,

$$i\mathcal{M} = i\mathcal{K}[\rho \, i\mathcal{K}]^g = \frac{i}{\mathcal{K}^{-1} - i\rho} \,. \tag{3.39}$$

where in the last equality we used the identity of Eq. (A.3). The K-matrix parameterization provides a parameterization of the two-meson scattering amplitude, where we only need to provide a real function, with the appropriate threshold behavior, and the complex phases required by unitarity are automatically implemented into $\mathcal{M}$. We have packed into the

K-matrix all the short-range dynamical contributions arising from, among other diagrams, off shell intermediate states with three or more hadrons.

3.4.2 The two-meson transition decomposition

We will follow a similar procedure to derive the on shell decomposition of the two-meson transition amplitude. First, as before, we define the on shell limit,

$$\mathcal{W}^A(P_f, \hat{\mathbf{p}}_f'^\star; P_i, \hat{\mathbf{p}}_i^\star) = \mathcal{W}^A(P_f, p'; P_i, p)\Big|_{p^2=p'^2=(P_i-p)^2=(P_f-p')^2=m^2}, \tag{3.40}$$

so that first we will work with amplitudes and kernels with external legs off shell, and project them on shell while separating pieces with different analytic properties.

For convenience we split the derivation into two parts. We first consider topologies where the current cannot couple directly to one of the mesons in an s-channel bubble, but only within 2PI diagrams – we label these diagrams $\mathcal{W}_{\not{1B}}$. In this category we also include five-point vertices representing short-range interactions between the current and the incoming and outgoing mesons. The second type will be those with single-meson current insertions in s-channel bubble loops, forming triangle loops, see Fig. 3.3, as well as insertions on to one of the external legs, contributing to the terms in Eq. (3.5). We label this second category of diagrams $\mathcal{W}_{1B}$, so that the amplitude is given by the sum

$$i\mathcal{W}^A = i\mathcal{W}^A_{\not{1B}} + i\mathcal{W}^A_{1B}\,. \tag{3.41}$$

We show in Fig. 3.7 the diagrammatic representation of the skeleton expansion of $\mathcal{W}_{\not{1B}}$ and $\mathcal{W}_{1B}$. In the following two subsections we derive the decomposition of each of these two terms.

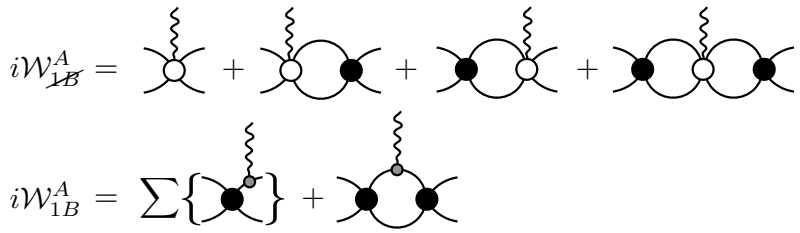

Figure 3.7: Diagrammatic representation of the two types of contributions to the $\mathcal{W}$ amplitude, the contributions where the current attaches to 2PI kernels, and when it attaches to single-meson states.

3.4.2.1 Without coupling to single mesons in the skeleton expansion

We begin by first identifying the 2PI kernel with two mesons in the initial and final state, plus a current insertion, with the variable $\mathbf{W}_{0|0}$. This kernel is illustrated by the first term to the right hand side of the equation on the first line of Fig. 3.7, Dressing this kernel with all two-particle scattering to all orders in the strong interactions, one can show that $\mathcal{W}_{\not{1}\not{B}}$ obeys the following equation,

$$\begin{aligned} i\mathcal{W}^A_{\not{1}\not{B}}(P_f,p';P_i,p) &= i\mathbf{W}^A_{0|0}(P_f,p';P_i,p) \\ &\quad + \int\frac{d^4k}{(2\pi)^4} i\mathcal{M}(p',k)i\Delta(k)i\Delta(k_f)i\mathbf{W}^A_{0|0}(P_f,k;P_i,p) \\ &\quad + \int\frac{d^4k}{(2\pi)^4} i\mathbf{W}^A_{0|0}(P_f,p';P_i,k)i\Delta(k)i\Delta(k_i)i\mathcal{M}(k,p) \\ &\quad + \int\frac{d^4k'}{(2\pi)^4}\int\frac{d^4k}{(2\pi)^4} i\mathcal{M}(p',k')i\Delta(k')i\Delta(k'_f) \\ &\qquad \times i\mathbf{W}^A_{0|0}(P_f,k';P_i,k)i\Delta(k)i\Delta(k_i)i\mathcal{M}(k,p)\,, \end{aligned} \tag{3.42}$$

where we remind the reader of the shorthand notation $k_i \equiv P_i - k$, and similarly for the final state and k' momenta. Equation (3.42) is represented diagrammatically in Fig. 3.7.

We can reuse the shorthand notation introduced in Sec. 3.4.1 to rewrite Eq. (3.42),

$$i\mathcal{W}^A_{\not{1}\not{B}} = i\mathbf{W}^A_{0|0} + i\mathbf{W}^A_{0|0}\cdot\mathcal{D}\cdot i\mathcal{M} + i\mathcal{M}\cdot\mathcal{D}\cdot i\mathbf{W}^A_{0|0} + i\mathcal{M}\cdot\mathcal{D}\cdot i\mathbf{W}^A_{0|0}\cdot\mathcal{D}\cdot i\mathcal{M}\,, \tag{3.43}$$

$$= [i\mathcal{K}_0\cdot\mathcal{D}]^g\cdot i\mathbf{W}^A_{0|0}\cdot[\mathcal{D}\cdot i\mathcal{K}_0]^g\,. \tag{3.44}$$

Like we did before we will split the s-channel bubble loops into two contributions with different analytic behavior, i.e. $\mathcal{D} = \rho + i\mathcal{S}$. In this case, the bubble loops can appear before or after the current insertion, and carry the momentum P_i and P_f, respectively. To distinguish these two cases we will use the notation $\rho_{i/f}$ for the contribution of the phase space.

Following a similar procedure to that shown in Eq. (3.37), we can simplify Eq. (3.44),

$$i\mathcal{W}^A_{\not{1}\not{B}} = [i\mathcal{K}\,\rho_f]^g i\mathbf{W}^A_{\not{1}\not{B}}[\rho_i\, i\mathcal{K}]^g\,, \tag{3.45}$$

where $\mathcal{K}$ was defined in Eq. (3.38), and where we also introduced the dressed regular kernel

$$i\mathbf{W}^A_{\not{1}\not{B}} = [i\mathcal{K}_0 \cdot i\mathcal{S}]^g \cdot i\mathbf{W}^A_{0|0} \cdot [i\mathcal{S} \cdot i\mathcal{K}_0]^g\,. \tag{3.46}$$

In the case where the external current does not couple to individual hadrons, this would complete our derivation. We find most convenient to exchange the function $\mathbf{W}_{\not{1}\not{B}}$ parameterizing the short-distance dynamics with

$$i\mathbf{W}^A_{\not{1}\not{B}} = \mathcal{K}\, i\mathcal{A}^A_{\not{1}\not{B},22}\,\mathcal{K}\,, \tag{3.47}$$

and the 'df' on-shell decomposition is given by

$$i\mathcal{W}^A_{\not{1}\not{B},\mathrm{df}} = \mathcal{M}\,[i\mathcal{A}^A_{\not{1}\not{B},22}]\,\mathcal{M}\,, \tag{3.48}$$

where this result only holds in the absence of one-body current insertions.

3.4.2.2 Contributions with coupling to single mesons

The second line of Fig. 3.7 illustrates the diagrams contributing to $\mathcal{W}_{1B}$. These contributions are given in full notation by the following integral equation

$$i\mathcal{W}^A_{1B}(P_f,p';P_i,p) = iw^A(p'_f,p'_i)\,i\Delta(p'_i)\,i\mathcal{M}(p',p) + i\mathcal{M}(p',p)\,i\Delta(p_i)\,iw^A(p_f,p_i) + \int\frac{d^4k}{(2\pi)^4} i\mathcal{M}(p',k)\,i\Delta(k)\,i\Delta(k_f)\,iw^A(k_f,k_i)\,i\Delta(k_i)\,i\mathcal{M}(k,p)\,. \quad (3.49)$$

where the single-meson insertion, w^A contains all the one-particle irreducible diagrams with a current insertion. It can be decomposed, according to the Lorentz strucutre of the current, into a summation of Lorentz tensors multiplied by scalar form factors,

$$w^A(k_f,k_i) = \sum_j K^A_j(k_f,k_i)\,f_j(Q^2,k_f^2,k_i^2)\,, \quad (3.50)$$

note that when the meson momenta are on their mass shell, $k_f^2 = k_i^2 = m^2$, $f_j(Q^2,k_f^2,k_i^2)$ corresponds to the form factors f_j introduced in Eq. (3.1).

We rewrite Eq. (3.49) into short hand notation,

$$i\mathcal{W}_{1B} = iw^A\,i\Delta\,i\mathcal{M} + i\mathcal{M}\,i\Delta\,iw^A + i\mathcal{M}\cdot\triangle\cdot i\mathcal{M}\,, \quad (3.51)$$

$$= iw^A\,i\Delta\,i\mathcal{K}_0\cdot[\mathcal{D}\cdot i\mathcal{K}_0]^g + [i\mathcal{K}_0\cdot\mathcal{D}]^g\cdot i\mathcal{K}_0\,i\Delta\,iw^A + [i\mathcal{K}_0\cdot\mathcal{D}]^g\cdot i\mathcal{K}_0\cdot\triangle\cdot i\mathcal{K}_0\cdot[\mathcal{D}\cdot i\mathcal{K}_0]^g\,, \quad (3.52)$$

where we introduce the symbol $\triangle$ to describe the triangle loop integral, with the three propagators and the single-meson current insertion.

When a current is inserted on a leg connected to a kernel, we will split the propagator in between the kernel and the current insertion according to Eq. (3.23). This yields a contribution with a pole singularity, which allows us to place that leg on shell, and a regular term. If we expand the skeleton expansion shown in the second line of Fig. 3.7 into 2PI kernels, we will find kernels with current insertions on their external legs, like the one

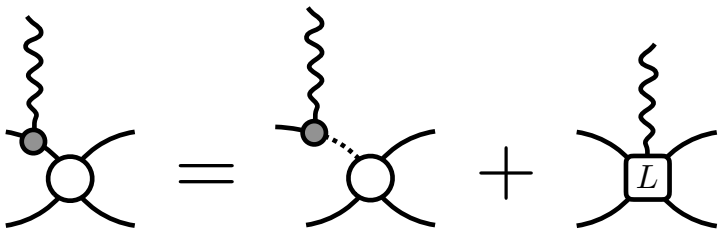

Figure 3.8: Diagrammatic representation of Eq. (3.53), where the 2PI kernel with a current insertion in one of its external legs is split into the term with the pole singularity of the propagator (dashed line), and a real kernel $\mathbf{W}_{L|0}$.

shown in Fig. 3.8. In Fig. 3.8 we illustrate the removal of the singularity associated with the propagator, from which we obtain a regular kernel

$$i\mathbf{W}^A_{L|0} \equiv i\mathcal{K}_0\, i\Delta\, iw^A - i\mathcal{K}_0\, iD\, iw^A_{\rm on}\,. \tag{3.53}$$

In our prescription the kernels in the last term can be placed on shell, because any off shell behavior will cancel the propagator pole and contribute to the regular kernel. We also introduce the regular kernel $\mathbf{W}_{0|R}$ for the case when the external leg with a current insertion is one of the mesons in the initial state,

$$i\mathbf{W}^A_{0|R} \equiv iw^A\, i\Delta\, i\mathcal{K}_0 - iw^A_{\rm on}\, iD\, i\mathcal{K}_0\,. \tag{3.54}$$

The triangle loop diagram, see Fig. 3.9, is the first term in this decomposition that features an analytic structure not present in the decomposition of the scattering amplitude. We split it into three different terms according to the analytic behavior of each of them, this is derived in Sec. 3.5, and illustrated in Fig. 3.9. In shorthand notation the different analytic contributions to the triangle diagram are given by

$$i\mathcal{K}_0 \cdot \triangle^A \cdot i\mathcal{K}_0 = i\mathbf{W}^A_{0|C|0} + i\mathbf{W}^A_{0|R}\,\rho_i\, i\mathcal{K}_0 + i\mathcal{K}_0\,\rho_f\, i\mathbf{W}^A_{L|0} + \mathcal{K}_0\Big[\sum\nolimits_j if_j\,\mathcal{G}^A_j\Big]\mathcal{K}_0\,. \tag{3.55}$$

The first term is associated with the real part of the loop, which we call $\mathbf{W}_{0|C|0}$, which

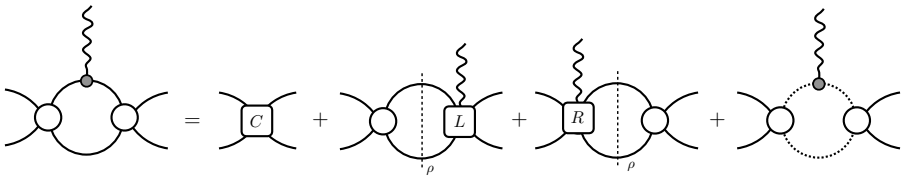

Figure 3.9: Diagrammatic representation of the triangle loop expansion into terms with different analytic properties. The cuts over the diagrams represent contributions proportional to the phase space, the kernel $\mathbf{W}_{0|R}$ is defined analogous to $\mathbf{W}_{L|0}$, but with the current insertion in one of the initial state legs. We introduce the real kernel $\mathbf{W}_{0|C|0}$.

does not have discontinuities or singularities in the elastic scattering region. The second and third terms contain a factor of ρ_i and ρ_f for the final and initial state respectively. These terms arise from removing the pole singularity of one of the propagators next to the current insertion, so it effectively becomes a bubble loop, and they also feature regular kernels of the form of $\mathbf{W}_{L|0}$ and $\mathbf{W}_{0|R}$.

Finally, the last term, in addition to the branch cuts associated with the phase space, also contains singularities that do not arise in bubble loops, the so-called triangle singularities, which we discuss further in Sec. 3.5. For now it suffices to indicate that these singularities will be described by the kinematic function $\mathcal{G}$ introduced in Eq. (3.7), while the form factors f_j can be placed on shell and taken out of the triangle integral.

We can now substitute Eqs. (3.53), (3.54), and (3.55) into Eq. (3.52) to obtain

$$\begin{aligned} i\mathcal{W}^A_{1B} = {} & iw^A_{\rm on}\, iD\, i\mathcal{M} + i\mathcal{M}\, iD\, iw^A_{\rm on} + \mathcal{M}\Big[\sum\nolimits_j f_j \mathcal{G}^A_j\Big]\mathcal{M} \\ & + [i\mathcal{K}_0\cdot\mathcal{D}]^g\cdot i\mathcal{K}_0\cdot i\mathbf{W}^A_{0|C|0}\cdot i\mathcal{K}_0\cdot[\mathcal{D}\cdot i\mathcal{K}_0]^g \\ & + [i\mathcal{K}_0\cdot\mathcal{D}]^g\cdot i\mathbf{W}^A_{0|R}(1+\rho_i\, i\mathcal{M}) + (1+i\mathcal{M}\,\rho_f) i\mathbf{W}^A_{L|0}\cdot[\mathcal{D}\cdot i\mathcal{K}_0]^g\,, \end{aligned} \tag{3.56}$$

where we observe algebraic structures similar to those appearing in Eq. (3.44).

We simplify Eq. (3.56) employing a similar procedure to that of previous sections. For that we define another dressed regular kernel,

$$i\mathbf{W}^A_{1B} = [i\mathcal{K}_0\cdot i\mathcal{S}]^g\cdot i\mathcal{K}_0\cdot i\mathbf{W}^A_{0|C|0}\cdot i\mathcal{K}_0\cdot[i\mathcal{S}\cdot i\mathcal{K}_0]^g + [i\mathcal{K}_0\cdot i\mathcal{S}]^g\cdot i\mathbf{W}^A_{0|R} + i\mathbf{W}^A_{L|0}\cdot[i\mathcal{S}\cdot i\mathcal{K}_0]^g\,, \tag{3.57}$$

and use it to write the one body contribution to the $2 + \mathcal{J} \to 2$ transition

$$i\mathcal{W}^A_{1B} = iw^A_{\rm on}\, iD\, i\mathcal{M} + i\mathcal{M}\, iD\, iw^A_{\rm on} + \mathcal{M}\Big[\sum\nolimits_j if_j\mathcal{G}^A_j\Big]\mathcal{M} + [i\mathcal{K}\,\rho_f]^g i\mathbf{W}_{1B}[\rho_i\, i\mathcal{K}]^g\,. \quad (3.58)$$

3.4.2.3 On-shell result for $\mathcal{W}$

We put together the results of Eqs. (3.45) and (3.58) to find the on shell decomposition including all diagrams,

$$i\mathcal{W}^A = iw^A_{\rm on}\, iD\, i\mathcal{M} + i\mathcal{M}\, iD\, iw^A_{\rm on} + \mathcal{M}\Big[\sum\nolimits_j if_j\mathcal{G}^A_j\Big]\mathcal{M} + [i\mathcal{K}\rho]^g i\mathbf{W}^A[\rho i\mathcal{K}]^g\,, \quad (3.59)$$

where we have defined $\mathbf{W} = \mathbf{W}_{1B} + \mathbf{W}_{\cancel{1B}}$. We end this section with the divergence free amplitude

$$i\mathcal{W}^A_{\rm df} = i\mathcal{W}^A - iw^A_{\rm on}\, iD\, i\mathcal{M} - i\mathcal{M}\, iD\, iw^A_{\rm on}\,, \quad (3.60)$$

$$= \mathcal{M}\Big[i\mathcal{A}^A_{22} + \sum\nolimits_j if_j\mathcal{G}^A_j\Big]\mathcal{M}\,, \quad (3.61)$$

which agrees with Eq. (3.6) when rewritten in full notation, and where we implicitly defined the regular function $\mathcal{A}_{22}$ through

$$i\mathbf{W}^A = \mathcal{K}\, i\mathcal{A}^A_{22}\, \mathcal{K}\,. \quad (3.62)$$

This finishes the derivation of the on shell decomposition of the amplitude. In the next section we will give a more thorough description of the triangle singularities appearing in $\mathcal{W}$.

3.5 Triangle function

Let us begin by introducing the triangle diagram loop function in full notation with the kernels $\mathcal{K}_0$ as endcaps,

$$\mathcal{I}_1(P_f, P_i, Q^2) = \int \frac{d^4k}{(2\pi)^4} i\mathcal{K}_0(p', k) i\Delta(k) i\Delta(k_f) i w^A(k_f, k_i) i\Delta(k_i) i\mathcal{K}_0(k, p) \tag{3.63}$$

where w was introduced in Eq. (3.50) in terms of known kinematic tensors K_j and the off shell form factors. The expansion around the on shell value of these form factors is

$$if_j(Q^2, k_f^2, k_i^2) = if_j(Q^2) + \delta[if_j(k_f^2, Q^2)] + [if_j(Q^2, k_i^2)]\delta + \delta[if_j(Q^2, k_f^2, k_i^2)]\delta\,, \tag{3.64}$$

where the δ operator acts as in Eq. (3.27), making terms proportional to $(k_f^2 - m^2)$ or $(k_i^2 - m^2)$ when it appears to the left or right of the form factor. For each of these terms, the lack of explicit dependence on one of the external momenta signifies that it has been placed on shell.

We expand Eq. (3.63) and use the definitions of the kernels given in Eqs. (3.53) and (3.54) to find a decomposition into pieces with different analytic behavior,

$$\begin{aligned}\mathcal{I}_1(P_f, P_i, Q^2) = i\mathcal{K}_0(s_f) \left[\sum_j if_j(Q^2) \int \frac{d^4k}{(2\pi)^4} iD(k) iD(k_f) K_j^A(k_f, k_i) iD(k_i)\right] i\mathcal{K}_0(s_i) \\ + i\mathbf{W}^A_{0|R}(P_f, P_i)\,\rho_i\, i\mathcal{K}_0(s_i) + i\mathcal{K}_0(s_f)\,\rho_f\, i\mathbf{W}^A_{L|0}(P_f, P_i) + \delta\mathcal{I}_1(P_f, P_i, Q^2)\end{aligned} \tag{3.65}$$

where we can see that the first term is proportional to the triangle loop integral $\mathcal{G}_j$ of Eq. (3.7), and the last term, $\delta\mathcal{I}_1$, is a regular function for the kinematics of interest.

To obtain the singularities of $\mathcal{G}_j$ we can use the Cutkosky rules to extract discontinuities of the loops, and verify with the Landau conditions [99] that all the singularities associated with the diagram are being described. In the case of the triangle loop, the Cutkosky rules require at least three cuts, one for each of the vertices. Since we are interested in the

kinematic region where the current insertion energy is below the particle creation threshold, only two cuts contribute to the discontinuities associated with the triangle loop. These contain the branch-cuts associated with the initial/final two-particle states.

After we perform the cuts, following the prescription given in Eq. (3.29), we can perform two of the integrals, with the remaining angular integral given by

$$\mathrm{Disc}\,\mathcal{G}_j(P_f,P_i) = -2i\,\rho_f\,\theta\,(s_f - s_{\rm thr})\,\mathrm{P.V.}\!\int \frac{d\Omega_f^\star}{4\pi} K_j(k_f,k_i)\,D(k_i)\Big|_{k^0=\omega_k^\star,\left|\mathbf{k}_f^\star\right|=k^\star(s_f)} + \dots\,, \tag{3.66}$$

where we only write the contribution of one of the cuts, the other contribution is identical but with labels f and i exchanged. Here we introduced the energy of a meson on shell $\omega_k^\star = \sqrt{k^{\star 2}+m^2}$. In this term, the angular integration is to be taken in the CM frame of the final state. Here we use the principal value prescription to integrate over the propagator pole, defined by

$$\int dx \frac{f(x)}{x-x'-i\epsilon} = \mathrm{P.V.}\int dx \frac{f(x)}{x-x'} + i\pi\int dx\,\delta(x-x')f(x)\,, \tag{3.67}$$

and the terms proportional to the Dirac delta from the cuts around the final and initial vertex cancelling each other.

We need to make explicit the angular dependence of the remaining propagator in the respective CM frame. We have the freedom to define the final CM frame such that $P_i^{\mu\star} = (\sqrt{s_i+|\mathbf{P}_i^\star|^2}, |\mathbf{P}_i^\star|\hat{\mathbf{z}})$, and the propagator in this frame is equal to

$$D(k_i) = \frac{1}{(\sqrt{s_i+|\mathbf{P}_i^\star|^2}-\omega_k^\star)^2 - \mathbf{P}_i^{\star 2} - k^{\star 2}(s_f) + 2|\mathbf{P}_i^\star|\,|k^\star(s_f)\cos\theta_f^\star - m^2 + i\epsilon}\,, \tag{3.68}$$

$$= \frac{1}{2|\mathbf{P}_i^\star|\,k^\star(s_f)\,(\cos\theta_f^\star - z_f^\star + i\epsilon)}\,, \tag{3.69}$$

where $z_f^\star$, in terms of Lorentz scalars, is given by

$$z_f^\star = \frac{P_i\cdot P_f - s_i}{16\pi\rho_f\sqrt{(P_f\cdot P_i)^2 - s_f\,s_i}}\,. \tag{3.70}$$

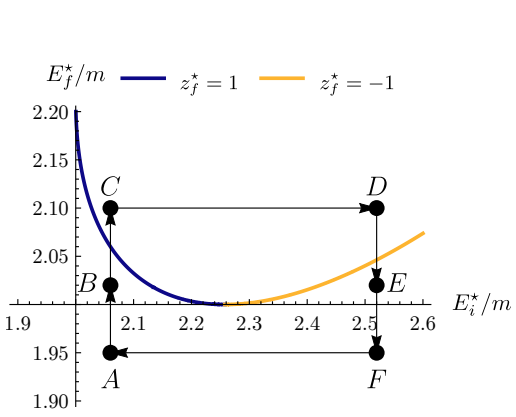

(a) A trajectory over the $E_i^\star = \sqrt{s_i}$, $E_f^\star = \sqrt{s_f}$ plane.

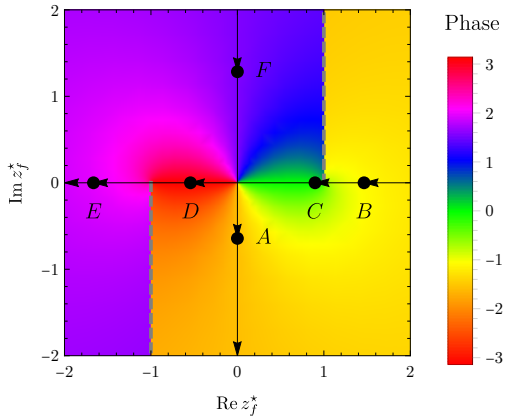

(b) Phase of $\log\big((1+z_f^\star)/(1-z_f^\star)\big)$ over the complex $z_f^\star$ plane.

Figure 3.10: Behavior of the $z_f^\star$ variable in a closed trajectory over the $E_i^\star = \sqrt{s_i}$, $E_f^\star = \sqrt{s_f}$ plane for particles of equal mass m, and $|\mathbf{P}_i^\star| = 1.05m$.

After carrying out the trivial azimuthal integral, and using the principal value prescription for the polar integral, we obtain

$$\mathrm{Disc}\,\mathcal{G}(P_f, P_i) = \frac{i}{16\pi\sqrt{(P_f\cdot P_i)^2 - s_f\, s_i}}\left[\theta\left(s_f - s_{\mathrm{thr}}\right)\log\left|\frac{1+z_f^\star}{1-z_f^\star}\right| + \theta\left(s_i - s_{\mathrm{thr}}\right)\log\left|\frac{1+z_i^\star}{1-z_i^\star}\right|\right]. \quad (3.71)$$

Careful inspection of the behavior of the $z^\star$ variables as a function of the external kinematics, yields that only when $z_f^\star = z_i^\star = 1$ there is a logarithmic singularity in $\mathrm{Disc}\,\mathcal{G}$. Also we find that $\mathrm{Disc}\,\mathcal{G}$ generically features square-root-type singularities at threshold. This is in agreement with the analysis of the Landau conditions of this diagram, see Ref. [109] for a detailed review of this procedure. What is more, the imaginary part of the loop yields all the information about its singularities, i.e. its nature and their coefficients. Once we know the coefficient of each singularity, we can make a continuation of the $\mathrm{Disc}\,\mathcal{G}$ function to also reproduce its real part.

However, given the behavior of the $z^\star$ variables as a function of the external kinematics, only a specific continuation around the branch points of the log function is consistent. To

illustrate this, we will describe the behavior of the $z_f^\star$ variable while moving in the trajectory shown in Fig. 3.10a in the $\sqrt{s_i}$, $\sqrt{s_f}$ plane with fixed $|\mathbf{P}_i^\star| = 1.05m$.

Six points labeled A through F have been chosen on this plane. Correspondingly, the value of $z_f^\star$ at each of these points has been placed on the complex $z_f^\star$ plane in Fig. 3.10b. The color background on the latter figure represents the phase of the function $\log\Big((1+z_f^\star)/(1-z_f^\star)\Big)$, which generates the Riemann sheet structure of the $\log(1+x) - \log(1-x)$ function. In this figure we have chosen to push the branch cut of the logs, which would conventionally run from -1 to 1, to run from -1 to infinity in the negative imaginary semiplane and then come back to 1 through the positive imaginary semiplane. The branch cut is indicated by a gray dashed line. [4] This choice, as shown shortly, will allow the variable $z_f^\star$ to remain on the same sheet for the values of $\sqrt{s_i}$ and $\sqrt{s_f}$ within our kinematic region of interest.

To describe the behavior of $z_f^\star$ let us begin in the kinematic region when $\sqrt{s_f}$ is below threshold. By extending the domain of ρ_f below threshold within the physical Riemann sheet in the s_f complex plane, one sees from Eq. (3.70) that $z_f^\star$ becomes purely imaginary, and takes positive or negative imaginary values depending on the value of s_i. As a result, when moving from point F to point A, $z_f^\star$ will pass through zero, motivating the choice to not have a branch cut there. When moving from point A to point B, one must cross the threshold of the final two-particle states, where $z_f^\star$ diverges, see Eq. (3.70). Given that there is no branch point at infinity in the $z_f^\star$ plane, one should remain in the same sheet when making this move from A to B. This motivates having the negative imaginary infinity and the positive real infinity on the same side of the cut. In the trajectory $BCDE$ there are *a priori* four options to go around the branch points, but only by going below the branch point at 1 and above the branch point at -1, as shown in Fig. 3.10b, the points E and F will be connected to form a closed trajectory. This choice around the branch points

[4] Since most software places the branch cut of the logarithms on the negative real axis, our choice of branch cut is implemented numerically with the function $\log\big(-i(z_f^\star+1)\big) - \log\big(i(z_f^\star-1)\big)$.

can be encoded as an addition of $i\epsilon$ to the argument of the logs,

$$\log\left(\frac{1+z_f^\star+i\epsilon}{1-(z_f^\star+i\epsilon)}\right), \tag{3.72}$$

where no absolute value of the argument of the logarithm is taken, and its range is extended into the complex plane. This reproduces the expression presented Eq. (3.8) that describes all the singularities of $\mathcal{G}$ in our kinematic region of interest.

This concludes the description of the on shell decomposition of $\mathcal{W}$ in the case of elastic S-wave scattering. The present arguments have been generalized to describe any number of partial-waves and two-meson channels in Ref. [98]. One of the main differences when including partial waves with angular momentum $\ell > 0$, is that the projection on shell is performed through a partial-wave expansion, so that the loop integrals need to include factors of spherical harmonics

$$\mathcal{Y}_{\ell m_\ell}(\mathbf{k}^\star) = \sqrt{4\pi}\, Y_{\ell m_\ell}(\hat{\mathbf{k}}^\star)\left(\frac{|\mathbf{k}^\star|}{k^\star(s)}\right)^\ell . \tag{3.73}$$

where the variable $\mathbf{k}^\star$ is the spatial part of the loop momentum in the CM frame associated with the total momentum of the partial-wave expanded kernel, while $k^\star(s)$ is the on-shell relative momentum of the mesons in the CM frame. The last factor is known as the barrier factor, which is needed to cancel the unphysical singularities that will appear from the mismatch between $k^\star(s_i)$ and $k^\star(s_f)$, more details are given in Refs. [107, 98].

However, the result in the more general case for $\mathcal{W}_{\text{df}}$ remains structurally the same as Eq. (3.6), with the change of promoting every factor into a matrix in channel and partial-wave space, which we repeat here for convenience

$$i\mathcal{W}^A_{\text{df}}(P_f,P_i) = \mathcal{M}(s_f)\left[i\mathcal{A}^A_{22}(P_f,P_i) + \sum_j i f_j(Q^2)\mathcal{G}^A_j(P_f,P_i)\right]\mathcal{M}(s_i)\,, \tag{3.74}$$

This equation keeps the same singularity structure as described here, and allows the discussion given in Sec. 3.3 about the extraction of resonance form factors to remain valid for that more general case, as long as all terms are promoted to matrices in the more general space. In a practical implementation, given that the scattering amplitude $\mathcal{M}$ of the two-to-two process, and the single particle form factors $f_j(Q^2)$ were known, only the regular kernel $\mathcal{A}_{22}$ needs to be constrained by either experimental data, or a lattice QCD calculation. The $\mathcal{A}_{22}$ appears to be unique to the $\mathcal{W}$ process, and can only be constrained by an amplitude of the form $2 \xrightarrow{\mathcal{J}} 2$, or an amplitude where $\mathcal{W}$ appears as a subprocess, similar to the appearance of $\mathcal{M}$ within $\mathcal{W}$. An example of the latter is the transition $1 \xrightarrow{\mathcal{J}^A,\mathcal{J}^B} 2$, where this notation symbolizes the insertion of two local external currents mediating the hadronic transition. The on shell decomposition of $1 \xrightarrow{\mathcal{J}^A,\mathcal{J}^B} 2$ is presented in Ref. [110].

Chapter 4

Finite-volume formalism for the $2 \xrightarrow{\mathcal{J}} 2$ transition

The pioneering ideas of Lüscher, as described in Sec. 2.1.1, have allowed to connect finite-volume energies obtained via LQCD to two-body scattering. Furthermore, connections have been established between matrix elements and production amplitudes. In this Chapter we report on the current progress of the formalism, that up to corrections that are suppressed exponentially in the volume, connects matrix elements calculated in LQCD to two-to-two $\mathcal{W}$ transitions, and presents the novel improvements that were first introduced in Ref. [111]. We finish this chapter with a test of the significance of the finite-volume effects formulated in Ref. [111] with an illustration of the LQCD extraction of the electromagnetic charge of a shallow resonance coupling to a two-hadron state within a toy model.

Initial attempts to derive this formalism relied in some approximation, e.g. that one-body currents do not contribute [112], using an effective field theory (EFT) of the hadronic system and expanding into the leading order coefficients of the EFT [113], or by performing an expansion in inverse powers of L [114]. A more general result was first described in Ref. [107], where one-body currents are taken into account, the result is model-independent, to all orders in a generic effective field theory, and with no power-law volume corrections,

but only exponential volume corrections of the form $e^{-m_\pi L}$.

A second version of this finite volume formalism was derived in Ref. [111]. This second formulation differed from the previous one in that all infinite-volume quantities are Lorentz covariant and the $1 \xrightarrow{\mathcal{J}} 1$ matrix elements have been reformulated in terms of standard form factors. This new result was reached by making minor adjustments to the derivation presented in Ref. [107]. For example, in that work finite-volume effects are expressed as sums over poles of the form $1/[2\omega_k(k^0 - \omega_k)]$, whereas in Ref. [111] the same effects are expressed via Lorentz invariant poles, $1/(k^2 - m^2)$.

In this chapter, which draws from Ref. [111], we describe a mapping between finite-volume matrix elements of two-particle states and the infinite-volume $2 \xrightarrow{\mathcal{J}} 2$ amplitude. The result is summarized by the flow-chart shown in Fig. 4.1. This formalism requires knowledge of the following quantities:

- the two-particle finite-volume spectrum,
- the $1 \xrightarrow{\mathcal{J}} 1$ form factors,
- the finite-volume two-particle matrix elements of $\mathcal{J}$,

which can be used to then systematically constrain the $2 \xrightarrow{\mathcal{J}} 2$ amplitude in the kinematic window in which only two-meson channels can go on shell. The finite-volume relation requires the generalized Lellouch-Lüscher factors [75, 77, 107], that enter multiplicatively in the conversion, as well as a new finite-volume function, denoted G, that appears in an *additive* correction, together with the single-particle form factor as well as the two-to-two scattering amplitude.

4.1 Finite volume correction of two-to-two matrix elements

In this set-up, we consider a matrix element in which the local current $\mathcal{J}$ is sandwiched between two finite-volume states, each of which has the quantum numbers of the two-particle system. This LQCD observable is related to the infinite-volume $2 \xrightarrow{\mathcal{J}} 2$ transition

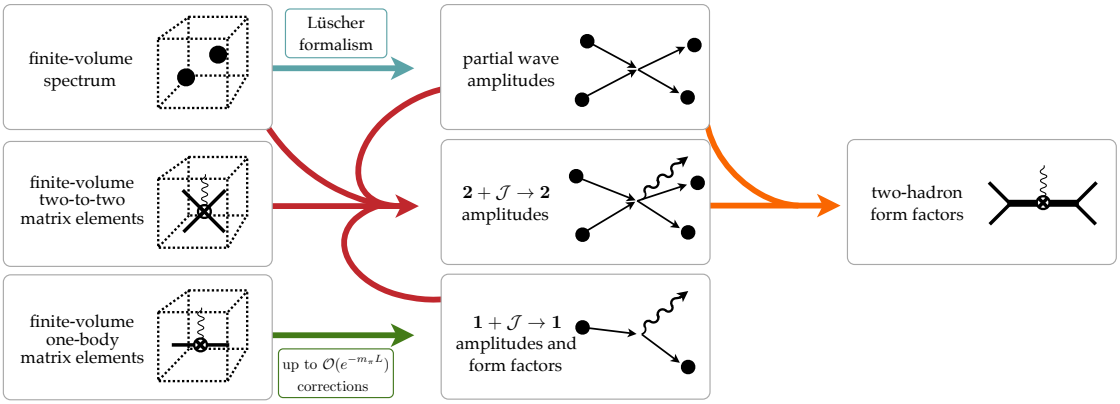

Figure 4.1: Road map of the formal approach outlined in this Chapter. The four red arrows merging together represent how the present approach combines various finite- and infinite-volume information to extract the $2 \xrightarrow{\mathcal{J}} 2$ amplitudes. Analytically continuing these to the resonance-pole location gives a rigorous, model-independent definition of the resonance form factor. Figure from Ref. [111].

amplitude via

$$\left|{}_L\langle \mathfrak{n}|\mathcal{J}^A(0)|\mathfrak{m}\rangle_L\right|^2 = \frac{1}{4E_\mathfrak{n}E_\mathfrak{m}L^6}\,\mathrm{tr}\Big(\widetilde{\mathcal{R}}_\mathfrak{n}\mathcal{W}^A_{L,\mathrm{df}}\widetilde{\mathcal{R}}_\mathfrak{m}\mathcal{W}^A_{L,\mathrm{df}}\Big)\,, \tag{4.1}$$

where $\widetilde{\mathcal{R}}_\mathfrak{n}$ is the LL factor of Eq. (2.5). The trace is over partial-waves and channel space. The second step entails to reassemble the long-distance contributions that cannot appear in a finite-volume amplitude

$$\mathcal{W}^A_{\mathrm{df}}(P_f,P_i) = \mathcal{W}^A_{L,\mathrm{df}}(P_f,P_i) - \mathcal{M}(s_f)\left[\sum_j f_j\, G^A_j(P_f,P_i,L)\right]\mathcal{M}(s_i)\,, \tag{4.2}$$

where f_j is the one-body matrix element. The term on the left hand side of the equation is the amplitude of Eq. (3.6). If there is a resonance appearing in the two-hadron channel, we can extract its elastic form factors by applying the results of Chapter 3.

The formalism connecting finite volume matrix elements and the amplitude $\mathcal{W}$ is similar to the formalism of the production amplitude $0 \xrightarrow{\mathcal{J}} 2$ in that there is a multiplicative correction from the LL factors. Additionally, there is an *additive* finite volume correction, G, that represents the difference between the infinite volume and the finite volume contribu-

tion of an intermediate state where the current $\mathcal{J}$ couples to only one of the hadrons in the system. This additive correction subtracts contributions from finite volume singularities and adds the singularity structure of the infinite volume amplitude.

The function G, derived in Ref. [111], in the case of a vector current, and a two-meson system in an S-wave, is given by

$$G_j^\mu(P_f, P_i, L) = \left[\frac{1}{L^3}\sum_{\mathbf{k}} - \int \frac{d^3\mathbf{k}}{(2\pi)^3}\right] \frac{K_j^\mu}{2\omega_k}\, D(P_f - k)\, D(P_i - k)\,, \tag{4.3}$$

where $\omega_k = \sqrt{|\mathbf{k}|^2 + m^2}$, K_j^μ was defined in Eq. (3.1), and $D(k)$ was defined in Eq. (3.4). The summation goes over all allowed lattice momenta $\mathbf{k} = \frac{2\pi}{L}\mathbf{d}$, with $\mathbf{d}$ a triplet of integers.

The function G, similar to the function F appearing in the Lüscher quantization condition, represents the difference between a loop diagram in finite and infinite volume, F and G corresponding to the bubble and triangle loop, respectively. The finite volume contribution of G consists of a sum of poles at the non-interacting energies of the two-hadron system. This sum can be numerically saturated using an appropriate high-energy cutoff prescription. The infinite volume contribution involves an integral over the loop momentum, which must also adhere to the same high-energy cutoff prescription for consistency. This second contribution can be split into two terms. The first term is an integral where the pole singularities of the propagators in the loop are removed, allowing for direct numerical integration. The second term corresponds to integrals appearing in perturbation theory of a generic QFT, enabling the use of well-known techniques such as Feynman parameter integration.

4.2 Toy example: Finite volume effects for shallow bound states

We employ the formulation described in Sec. 4.1 to evaluate the impact of the finite volume function G on the determination of the matrix elements of a shallow bound state in the

forward limit, i.e. $P_f = P_i$, which yields $Q^2 = 0$. It is expected that bound states, being stable, receive only exponentially suppressed volume corrections for their energy and matrix elements. In the case of shallow bound states, the leading finite-volume correction is of the form $e^{-\kappa L}$, where $\kappa \equiv -ik^\star(s) > 0$ is the binding momentum of the bound state, instead of $e^{-m_\pi L}$, which applies to deeply bound states with $\kappa \gg m_\pi$ [115]. We expect a similar finite-volume behavior for matrix elements of shallow bound states.

In this case, we find that ignoring the finite-volume function G when predicting matrix elements of finite-volume states introduces a sizeable fractional error. We compare this to the fractional error of the prediction of the finite-volume energy when ignoring the finite-volume function F. In both cases we can observe that the error vanishes as $e^{-\kappa L}$ when modifying the scattering parameters such that the binding energy increases. However, in the case of ignoring G the numerical coefficient of the exponential is observed to be significantly larger.

Let us consider a conserved electromagnetic current, so that only one form factor appears in the decomposition of Eq. (3.1), and in the forward limit the single particle form factor $f_1(0) = \mathrm{Q}_0$. Furthermore, we again consider distinct particles, with one of them neutral, and the other having charge Q_0.

We want to estimate the matrix element of a shallow bound state, with the formulation of Sec. 4.1,

$$\langle E_{0,L}|\mathcal{J}^0|E_{0,L}\rangle = \mathcal{W}^0_{L,\mathrm{df}}\widetilde{\mathcal{R}}(E_{0,L},L) = (\mathcal{W}^0_{\mathrm{df}} + \mathrm{Q}_0\mathcal{M}G^0_1(E_{0,L},L)\mathcal{M})\widetilde{\mathcal{R}}(E_{0,L},L) \qquad (4.4)$$

where the finite volume state $|E_{0,L}\rangle$, has energy $E_{0,L}$ and relativistic normalization, i.e. $\langle E_{0,L}|E_{0,L}\rangle = 2E_{0,L}L^3$. This matrix element is simply the application of the charge density operator and so we expect it to be equal to $2E_{0,L}\mathrm{Q}_0$.

We know that the infinite volume transition amplitude in the forward direction is fixed

by an application of the Ward identity [101]

$$\mathcal{W}_{\rm df}^0(E,E) = \mathrm{Q}_0 \frac{\partial}{\partial P^0}\mathcal{M}(E) = -\mathrm{Q}_0 \mathcal{M}\frac{\partial}{\partial P^0}\big(\mathcal{M}^{-1}\big)\mathcal{M}\,. \tag{4.5}$$

This makes the matrix element be equal to

$$\langle E_{0,L}|\mathcal{J}^0|E_{0,L}\rangle = \mathrm{Q}_0\bigg(\frac{\partial}{\partial P^0}\big(\mathcal{M}^{-1}\big) - G_1^0\bigg)\mathcal{M}\widetilde{\mathcal{R}}(E_{0,L},L)\mathcal{M}\,. \tag{4.6}$$

If we neglect the finite volume functions F and G, we will find the expected matrix element for a deeply bound state

$$\langle E_{0,L}|\mathcal{J}^0|E_{0,L}\rangle = \mathrm{Q}_0\bigg(\frac{\partial}{\partial P^0}\mathcal{M}^{-1}(E)\bigg)\frac{1}{\frac{\partial}{\partial P^0}\mathcal{M}^{-1}(E)} = \mathrm{Q}_0 \tag{4.7}$$

where we employed Eq. (2.6), but neglecting the finite volume function F. The functions F and G are exponentially suppressed when $\kappa L \gg 1$.

We now calculate the finite volume correction from the G function. Following [111], for $P_i = P_f = P$,

$$G_1^0(E) = 2P^0 G(E,L) - 2G^\mu(E,L)\,, \tag{4.8}$$

where the finite volume $G(E,L)$ and $G^\mu(E,L)$ are given by Eq. (4.3) with $K = 1$ and $K = k^\mu$, respectively. Reference [111] describes an efficient method to calculate this quantity, which we employed here.

In this toy example, each of the constituent particles will have a mass of $m = 1155$ MeV, and we fix the coupling to the bound state to be $g/\sqrt{16\pi} = 4.3$ fm^{-1}, i.e. the square root of the residue at the pole of the scattering amplitude. We fix the volume of the lattice to $mL \approx 16$. We describe the scattering amplitude phase-shift δ_0 with an effective range expansion

$$k^\star \cot\delta_0 = \frac{1}{a} + \frac{1}{2}rk^{\star 2}\,, \tag{4.9}$$

and vary the parameters a and r in such a way to modify the location of the bound state

pole, $m_b \equiv 2\sqrt{m^2 - \kappa^2}$, and the binding energy $B \equiv 2m - m_b$, but keep fixed the coupling to the scattering channel, g, to the constant shown before. The amplitude $\mathcal{W}_{\rm df}$ is, in the forward limit, directly related to the scattering amplitude, with the relationship of Eq. (4.5).

To observe the impact of the G-function in the calculation of matrix elements of bound states we plot the prediction of the lattice matrix element in two cases. In the first case we make use of the complete finite volume correction, including the G function contribution, whereas for the second one, we only correct for the normalization of the finite volume state, ignoring the G function. As a benchmark we can also compare the value of the prediction of the finite-volume ground state energy $E_{0,L}$, and a prediction ignoring the finite volume function F, which corresponds to the infinite-volume bound state mass m_b.

In Fig. 4.2 we observe that the finite-volume effect in the energy $E_{0,L}$ is exponentially decaying as we increase the value of B. As we increase the binding energy, B, the finite volume energy $E_{0,L}$ asymptotes the infinite volume mass m_b. For example, with a binding energy of 10 MeV, which is minuscule when compared to the total energy of the system of ~ 2 GeV, the fractional error between the predicted finite-volume energy from Lüscher and the energy when ignoring F, is on the order of 1%.

On the other hand, neglecting the contribution from the G function for the finite-volume matrix element prediction, as shown by the red band of Fig. 4.3, has a much more sizeable effect. For $B = 10$ MeV the fractional error between the proper finite volume prediction and one that neglects G, is of the order of 50%, and although the finite-volume error appears to decay exponentially as the binding energy increases, we observe that the effect is more sizeable than for the energy.

The reason for such a large effect is likely related to the nearby infinite-volume singularity in the triangle diagram, the so-called anomalous threshold. In the forward limit, the G function generically features a $1/k^\star$ singularity, which can have large finite-volume effects impacting the matrix element of a shallow bound state determined with lattice QCD.

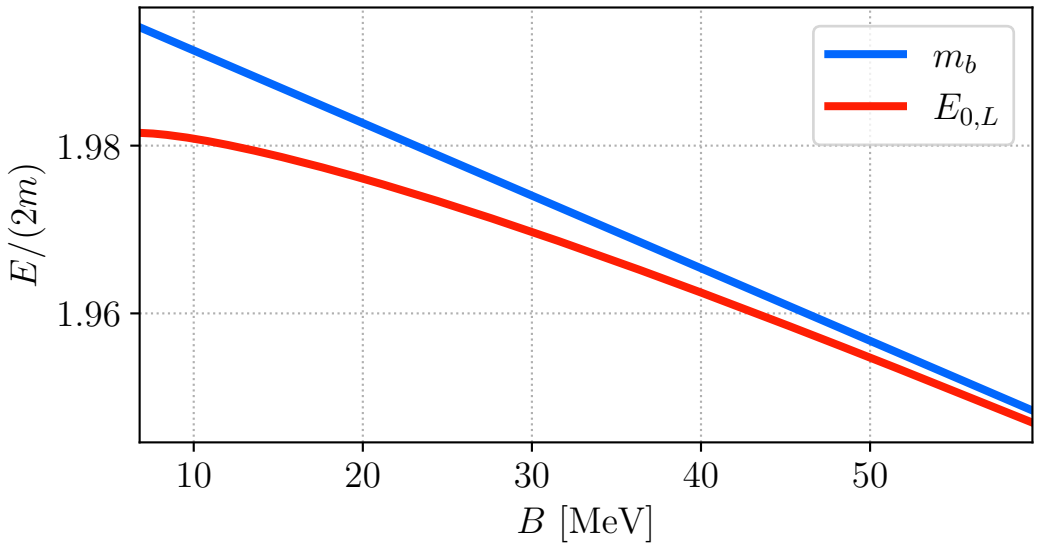

Figure 4.2: Finite volume effect on the mass of a shallow bound state. In red is the value of the finite-volume energy predicted with the Lüscher quantization condition, and in blue the location of the pole in $\mathcal{M}$, which would correspond to a prediction of the finite-volume energy which completely neglects the geometric function F.

This concludes our analysis of the $2 \xrightarrow{\mathcal{J}} 2$ amplitudes in this work. In the subsequent Chapters we will describe a practical implementation of the $0 \xrightarrow{\mathcal{J}} 2$ finite volume formalism in a LQCD calculation.

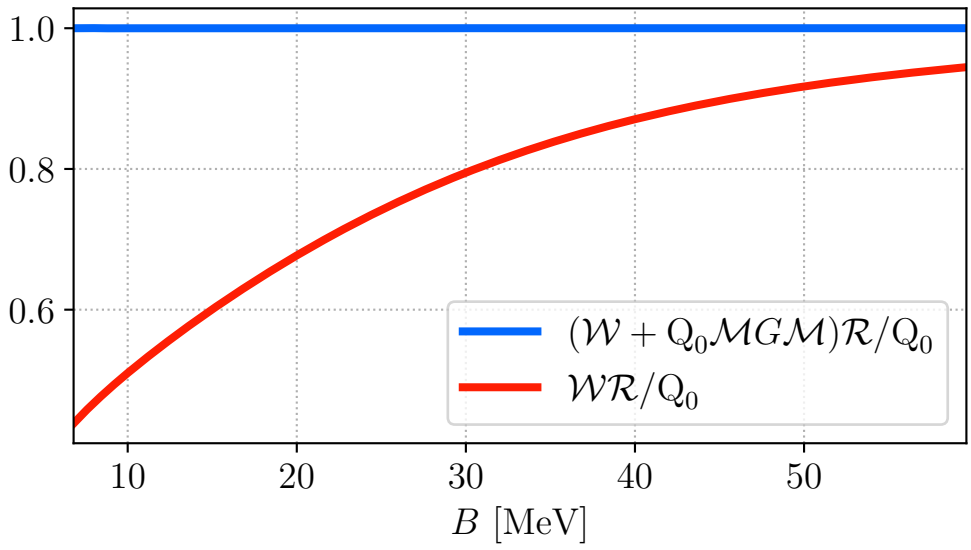

Figure 4.3: Prediction of the finite volume matrix element of a shallow bound state, from the full finite-volume two-to-two formalism in blue, and the prediction ignoring the $G(E, L)$ function in red.

Chapter 5

Scattering of $\pi\pi/K\overline{K}$ from LQCD

This and the following chapters describe a Lattice QCD calculation with the goal of extracting the pseudoscalar form factors shown in Fig. 1.2. As mentioned in Sec. 2.1.1, we can use the lattice spectrum and matrix elements to extract the pseudoscalar timelike form factors. To achieve that, we need to perform a non-trivial finite-volume correction to the matrix elements. These corrections require knowledge of the scattering amplitude, which can be determined using the lattice spectra.

This chapter will focus on the calculation of the lattice spectra and the extraction of the coupled channel $\pi\pi/K\overline{K}$ scattering amplitude. We find that the amplitude contains a ρ-meson resonance, and we determine the pole location in the complex energy plane as well as its coupling to each of the channels. From the calculation of the spectra we also obtain optimized operators that allow us to compute production matrix elements of the lattice ground state and multiple excited levels.

5.1 Spectrum calculation

In this case we are interested in knowledge of the scattering of the $\pi\pi$ and $K\overline{K}$ channels in the isovector sector ($I^G = 1^+$), and with spin-parity $J^P = 1^-$. These are the quantum numbers of the component of the electromagnetic current that couples to the $\pi\pi$ final state shown in Fig. 1.2b. The timelike form factor of the kaon has contributions from

both isovector and isoscalar components of the electromagnetic current, but we restrict our analysis to the isovector component. Experimentally it is observed that dynamics of the isoscalar component, in the energy region that we are interested in, can be captured by the production of the narrow ϕ-meson resonance [47]. An extraction of the isoscalar component from the lattice will also require the description of the finite-volume effects of the three-pion channel, which even in this work using heavier than physical pions has a lower threshold than $K\overline{K}$. A formalism is in place and future work will likely address the calculation of this component [116].

To calculate the lattice spectrum we employ the techniques described in Sec. 2.2. We calculate a matrix of two-point correlations and compute the eigenvalues and eigenvectors of the GEVP associated with this matrix. The energy levels are extracted from fits to the Euclidean time dependence of the eigenvalues, or principal correlators.

In Sec. 2.2.1 we described the general characteristics of the lattice used for this study. The two-point correlation functions were calculated using an ensemble of 400 gauge configurations, the fermion fields were smeared using distillation with $N_{\text{vecs}} = 162$ vectors, and four different time sources were used and averaged over. Correlation functions were calculated with sink-source separation of $0 \leq t/a_t < 40$. In Table 5.1 we list the masses of relevant stable mesons on this lattice, as well as thresholds of multi-meson states with quantum numbers $I^G = 1^+$ up to $a_t E^\star \sim 0.22$.

We calculate the spectra of the system with zero momentum, with respect to the lattice frame, and with momenta up to $(L|\mathbf{P}|/(2\pi))^2 \leq 4$. The relevant irreps into which the $J^P = 1^-$ partial-wave is subduced can be read off Tab. 2.1, and we list them in Tab. 5.2. We will discuss the possible contribution of unwanted partial-waves in our spectra once we describe the set of operators selected for the basis.

We use single-meson-like and two-meson-like operators to form the basis for our correlation matrix. For single-meson-like operators we employed fermion bilinears with all relevant gamma matrix and covariant derivative combinations, with up to three derivatives for operators at rest, and up to two derivatives for operators with non-zero momentum.

This includes operators with continuum spin up to $J = 4$ for the system at rest, and $J = 3$ for the systems in-flight. The number of single-meson operators, $\bar{\psi}\mathbf{\Gamma}\psi$, included in the basis of each irrep is listed in Tab. 5.2.

Table 5.1: Lattice meson masses in temporal lattice units and relevant multi-meson thresholds. Some of these values were first reported in Ref. [82].

meson	$a_t m$	threshold	$a_t E_{\text{thr}}$
π	0.0474	$\pi\pi$	0.0947
K	0.0866	$K\overline{K}$	0.1732
η	0.0960	$\pi\pi\pi\pi$	0.1894
ω	0.1422	$\pi\omega$	0.1896
ϕ	0.1709	$\pi\pi\eta$	0.1908
		$\pi\phi$	0.2183
		$\pi K\overline{K}$	0.2206

In this work we include $\pi\pi$ and $K\overline{K}$ two-meson-like operators such that their non-interacting CM energies satisfy $a_t E^{\star}_{\text{n.i.}} \lesssim 0.22$. The non-interacting energies in the CM frame are given by

$$E^{\star 2}_{\text{n.i.}} = \left(\sqrt{m_1^2 + |\mathbf{p}_1|^2} + \sqrt{m_2^2 + |\mathbf{p}_2|^2}\right)^2 - |\mathbf{P}|^2 \,, \tag{5.1}$$

where m_1 and m_2 are the masses of the single mesons used to construct the two-meson operator, and the momenta correspond to those introduced in Eq. (2.20). For some irreps we also included $\pi\omega$ and $\pi\phi$ two-meson-like operators with non-interacting energies up to $a_t E^{\star}_{\text{n.i.}} \lesssim 0.24$. These extra operators were included to test their impact on the spectrum, and evaluate if the $\pi\pi/K\overline{K}$ channels decouple from the pseudoscalar-vector channels in the energy region of interest.

All the two-meson-like operators considered in this work are listed in Tab. 5.2 in the form $\mathbb{M}^{(1)}_{\mathbf{d}_1}\mathbb{M}^{(2)}_{\mathbf{d}_2}$, where $\mathbb{M}^{(i)}$ describes the flavor of the i-th single-meson-like operator used in the construction, and $\mathbf{d}_i$ is its momentum type in units of $2\pi/L$. Note that $\mathbf{d}_i$ are listed in some conventional direction, but that in practice they are rotated such that $\mathbf{d}_1 + \mathbf{d}_2 = \mathbf{d}$, where $\mathbf{d}$ is the total momentum of the system in units of $2\pi/L$, and all allowed rotations are included as described by Eq. (2.20).

Table 5.2: Operator basis in each of the irreps used to form the matrix $C_{ij}(t)$. We indicate with $\{N\}$ when a two-meson subduction into that irrep has a multiplicity $N > 1$. The vector-pseudoscalar operators were used to test the dynamical mixing of the $\omega\pi/\phi\pi$ and $\pi\pi/K\overline{K}$ channels, but were dropped from the basis to calculate the spectrum used to extract the scattering amplitudes.

$[000]\ T_1^-$	$[100]\ A_1$	$[110]\ A_1$	$[111]\ A_1$	$[200]\ A_1$
$11 \times \bar{\psi}\mathbf{\Gamma}\psi$	$8 \times \bar{\psi}\mathbf{\Gamma}\psi$	$9 \times \bar{\psi}\mathbf{\Gamma}\psi$	$10 \times \bar{\psi}\mathbf{\Gamma}\psi$	$11 \times \bar{\psi}\mathbf{\Gamma}\psi$
$\pi_{[100]}\pi_{[100]}$	$\pi_{[100]}\pi_{[000]}$	$\pi_{[110]}\pi_{[000]}$	$\pi_{[111]}\pi_{[000]}$	$\pi_{[200]}\pi_{[000]}$
	$K_{[100]}\overline{K}_{[000]}$	$K_{[110]}\overline{K}_{[000]}$	$\pi_{[110]}\pi_{[100]}$	$K_{[200]}\overline{K}_{[000]}$
	$\pi_{[110]}\pi_{[100]}$	$\pi_{[111]}\pi_{[100]}$	$K_{[111]}\overline{K}_{[000]}$	
			$K_{[110]}\overline{K}_{[100]}$	

$[100]\ E_2$	$[110]\ B_1$	$[110]\ B_2$	$[111]\ E_2$	$[200]\ E_2$
$17 \times \bar{\psi}\mathbf{\Gamma}\psi$	$12 \times \bar{\psi}\mathbf{\Gamma}\psi$	$15 \times \bar{\psi}\mathbf{\Gamma}\psi$	$12 \times \bar{\psi}\mathbf{\Gamma}\psi$	$15 \times \bar{\psi}\mathbf{\Gamma}\psi$
$\pi_{[110]}\pi_{[100]}$	$\pi_{[100]}\pi_{[100]}$	$\omega_{[110]}\pi_{[000]}$	$\pi_{[110]}\pi_{[100]}$	$\pi_{[110]}\pi_{[110]}$
	$\omega_{[110]}\pi_{[000]}$	$\pi_{[111]}\pi_{[100]}$	$\omega_{[111]}\pi_{[000]}$	
	$K_{[100]}\overline{K}_{[100]}$	$\pi_{[110]}\pi_{[110]}$	$K_{[110]}\overline{K}_{[100]}$	
	$\pi_{[110]}\pi_{[110]}$	$\phi_{[110]}\pi_{[000]}$	$\phi_{[111]}\pi_{[000]}$	
	$\phi_{[110]}\pi_{[000]}$	$\{2\}\omega_{[100]}\pi_{[100]}$	$\{3\}\omega_{[110]}\pi_{[100]}$	
	$\omega_{[100]}\pi_{[100]}$	$\omega_{[000]}\pi_{[110]}$		

From Table 5.1 we note that multiple channel thresholds open at energies close to the $K\overline{K}$ threshold, leaving a narrow energy window where only the $\pi\pi$ and $K\overline{K}$ channels are above threshold. This is relevant because if we want to apply the Lüscher quantization condition of Eq. (2.2) up to a given energy, we need to consider all channels whose energy thresholds lie below that energy. Furthermore, Eq. (2.2) is restricted to two-meson channels, and although the extension to three-meson channels is known, see for example the calculation of Ref. [117], there is still no formalism that can handle the four-pion channel.

We justify neglecting some of these channels based on the following experimental observations. Experimentally the $\pi\pi\pi\pi$ channel is found to be weakly interacting up to 300 MeV above its threshold [118], and we expect the lack of $\pi\pi\pi\pi$-like operators to have a minimal impact in our analysis. A similar situation occurs for the $\pi\pi\eta$ channel with a small cross-section at energies below the effective threshold for $\rho\eta$, so that the amplitude can be described by an isobar model [119]. The (negligible) impact of this channel in finite-volume was explored in a study similar to the present one in Ref. [69]. Furthermore,

the lattice $\pi\pi\eta$-like operator with lowest non-interacting energy in this volume has an CM energy $a_t E^{\star}_{\text{n.i.}} > 0.23$ when coupling the $\pi\pi$ in a ρ-isobar, which lies above the energy cut-off we selected for our $\pi\pi/K\overline{K}$-like operator basis.

The $\omega\pi$ channel appears in the irreps listed in Tab. 5.2 in a P-wave with spin-parity $J^P = 1^-$. For the irreps in flight that are not A_1 the $\omega\pi$ system also appears in a mixture of S- and D-wave with spin-parity $J^P = 1^+$. The positive parity partial-waves are expected to be dominated by the b_1 resonance, which based on the results of Ref. [69] should affect the energy levels around $a_t E^{\star} \sim 0.21$. The $J^P = 1^-$ $\omega\pi$ partial-wave, is not expected to resonate in this energy region according experimental observations [120], and its mixing to the $\pi\pi/K\overline{K}$ channels, is expected to be suppressed by a centrifugal barrier factor. If the off-diagonal elements of the $J^P = 1^-$ scattering amplitude $\mathcal{M}(\omega\pi|\pi\pi)$ and $\mathcal{M}(\omega\pi|K\overline{K})$ are negligible in the energy region of interest, the quantization condition of the $J^P = 1^+$ $\omega\pi$ and $J^P = 1^-$ $\pi\pi/K\overline{K}$ channels will decouple.

The $\pi\pi$ and $K\overline{K}$ channels with quantum numbers $I^G = 1^+$ must have an antisymmetric spatial wave function, i.e. we only need to consider odd partial-waves. The relevant rest frame irrep, T_1^-, mixes $J^P = 1^-, 3^-, \ldots$. For non-zero momentum, the symmetry of the system is further reduced, and in the irreps considered we expect contributions of $J^P = 1^-, 3^-, \ldots$. However, the centrifugal barrier factor will suppress the F-wave with respect to the P-wave amplitude, and no resonant behavior in the F-wave is expected until much higher energies, see for instance the spectrum extracted with single meson operators in Fig. 11 of Ref. [121]. To further support this approximation, we note that in Ref. [65], at a lighter pion mass of $\sim$ 239 MeV, the F-wave contribution to the $\pi\pi$ channel was found to be consistent with zero. Based on these arguments we neglect the pseudoscalar partial-waves with $J \geq 3$.

Once we have selected an operator basis for each irrep, the two-point correlation matrix is calculated, and the GEVP is solved for each available timeslice. We select a value of t_0

based on the heuristics described in Sec. 2.2.2. We perform a correlated fit to the timeslice dependence of each principal correlator with a one or two exponential functional form, given by Eqs. (2.13) and (2.16), from which we extract the energy levels of the irrep. We verify that the spectrum is robust under reasonable variations of the following choices: the fit timeslice window, variations of the number of fermion bilinears included in the basis, and variations of t_0.

As an example, we show in Fig. 5.1 the principal correlators extracted from the correlation matrix of the $[111]\,A_1$ irrep. We plot the principal correlators in the form $e^{E_{\mathfrak{n}}(t-t_0)}\lambda^{\mathfrak{n}}(t,t_0)$ to remove the contribution of the leading exponential, and more easily evaluate the relaxation to a single exponential behavior. In this case we found that all principal correlators are best described by a two-exponential fit. Only for the first five states do we find that the noise allows fits up to timeslices close to $t/a_t = 39$. For higher states, the signal to noise ratio deteriorates more quickly.

In the case of the first five principal correlators, the contribution from excited energy levels is small. The coefficient of the second exponential $b_{\mathfrak{n}} \lesssim 0.01$ for these states, and stays below 0.1 for the rest of the states, except for state 9 in which case it is equal to 0.19. The energy of the second exponential of all fits satisfies $a_t E_{A+1} > 0.5$, greater than the energies of the highest states.

However, as discussed before, since we only include two-meson operators with non-interacting energies up to $a_t E^{\star}_{\text{n.i.}} \sim 0.22$, and do not include further multi-meson operators, we do not expect the energy levels extracted above that energy to faithfully represent the spectrum of the lattice. In this case we will only keep the first five levels for the scattering analysis. A similar analysis was carried out for the rest of the irreps considered in this work. Across all irreps, including timeslice fits to extract the overlap factors $Z^i_{\mathfrak{n}}$, we performed on the order of ~ 1000 fits. However, as we describe below, only the results of the fits to the timeslice dependence of the principal correlator for the 32 lowest lying levels will be used for the rest of our analysis.

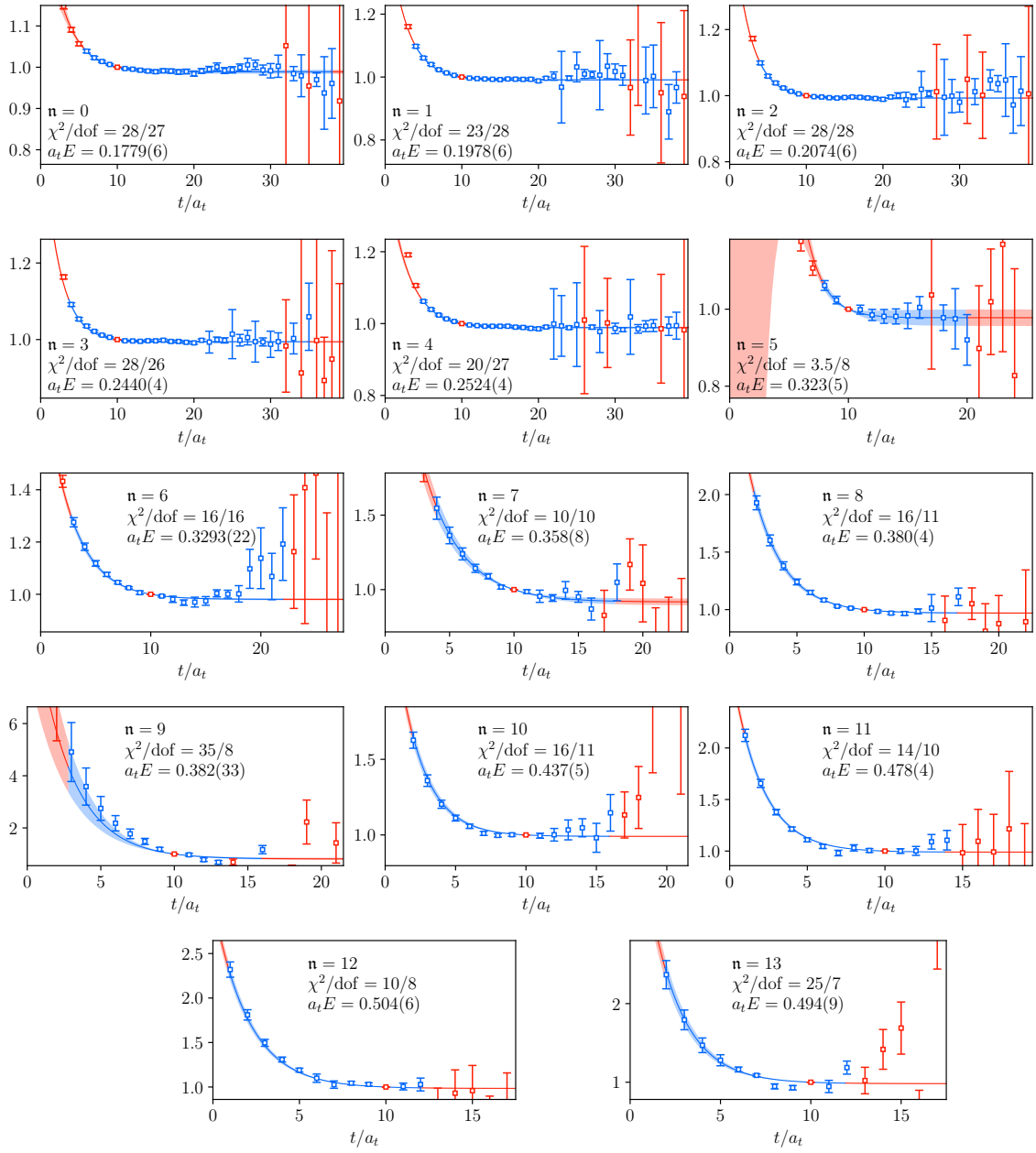

Figure 5.1: Principal correlators of irrep [111] A_1 with $t_0 = 10a_t$. We plot $e^{E_{\mathfrak{n}}(t-t_0)}\lambda^{\mathfrak{n}}(t,t_0)$ to better observe the relaxation to a single exponential for large timeslices. The basis of operators of the matrix of two-point correlation functions is listed in Tab. 5.2. Points in blue are included in the fit, while points in red, e.g. $t = t_0$, are not used.

To evaluate the impact of the vector-pseudoscalar channels on the spectrum we carried out the energy-level extraction through the solution of the GEVP with correlation matrices

with and without $\omega\pi$-like and $\phi\pi$-like two-meson operators in the basis for some of the irreps that mix $J^P = 1^\pm$. An example of this is shown in Fig. 5.2, showing the extracted discrete spectrum in the $[111]\,E_2$ irrep including such operators (left), and excluding them (right).

As expected, the low-lying spectrum, well below the $\pi\omega$ threshold, is unaffected by the inclusion of the extra operators whose non-interacting energies lie much higher, and the overlaps, $Z^i_{\mathfrak{n}} = \langle \mathfrak{n}|\mathcal{O}^\dagger_i|0\rangle$, for these states with those operators are observed to be negligible.

Above the $\pi\omega$ threshold we can identify by the operator-state overlaps that some states are generated predominantly by the $\pi\omega$-like or $\pi\phi$-like operators.

Because the variational analysis approach is able to separate contributions to the matrix of correlation functions from multiple levels, even if they are almost degenerate, we can observe that the spectrum on the left contains a very precise energy level right on top of the $K_{110}\overline{K}_{100}$ non-interacting energy with dominant overlap onto a $K\overline{K}$-like operator The energy of this state is statistically consistent with another three levels overlapping dominantly with $\pi\omega$-like and $\pi\phi$-like operators. This $K\overline{K}$-like level remains essentially unchanged in an analysis that does not include the $\pi\omega$-like and $\pi\phi$-like operators, justifying their removal for the spectrum determination, and their further exclusion from the timelike form factor calculation. Comparable observations can be made in the other irreps considered here.

Once the energy levels from each irrep have been extracted from the principal correlators, we calculate the CM energies,

$$(a_t E^\star)^2 = (a_t E_{\mathbf{P}})^2 - |a_s \mathbf{P}|^2/\xi^2\,, \tag{5.2}$$

where we add in quadrature the statistical error associated with the energies to the uncertainty associated with the anisotropy. This completes the calculation of the lattice spectra, which is shown in Fig. 5.3.

Let us now comment on the spectra obtained across the 10 irreps considered. We find

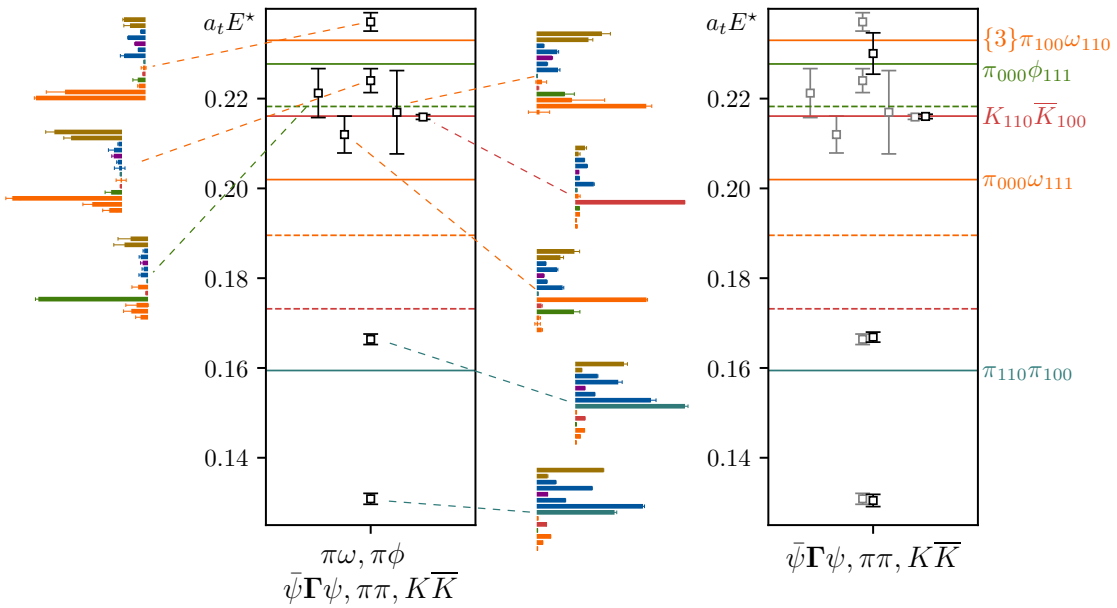

Figure 5.2: Extracted finite-volume spectrum in the [111] E_2 irrep from variational analysis of (left) correlation matrix including $\pi\omega$-like and $\pi\phi$-like operators, and (right) excluding such operators. Dashed lines indicate meson-meson thresholds, and solid lines the non-interacting energy levels in this volume, with color coding as indicated below. The histograms show the relative sizes of overlap factors for each state for each operator in the basis, color coded as: subduced single-meson with $J^P = 1^-$ (dark blue), $J^P = 1^+$ (brown), and $J^P = 2^-$ (purple), $\pi\pi$ (teal), $K\overline{K}$ (red), $\pi\omega$ (orange) and $\pi\phi$ (green). The spectrum from the left panel is reproduced on the right panel as the grey points to aid comparison.

32 energy levels below our energy cut-off at $a_t E^\star \sim 0.22$ (with the vector-pseudoscalar operators removed from the operator basis). Of these, 17 are located within the elastic $\pi\pi$ energy region. We observe that the spectra feature an extra energy level with respect to the expectation from counting the possible non-interacting energies on this volume. This extra level is manifested as an isolated level around $a_t E^\star \sim 0.135$, or as an avoided level crossing if a non-interacting $\pi\pi$ energy is located around $a_t E^\star \sim 0.135$ for this volume.

This behavior indicates the presence of a narrow-width resonance with mass close to $a_t E^\star \sim 0.135$. To determine the precise characteristics of this resonance we need to analyze the energy levels with the Lüscher quantization condition, and extract the pole parameters from a parameterization of the amplitude that describes well the lattice spectra.

In the case of the 15 energy levels above the $K\overline{K}$ threshold, we observe that each of

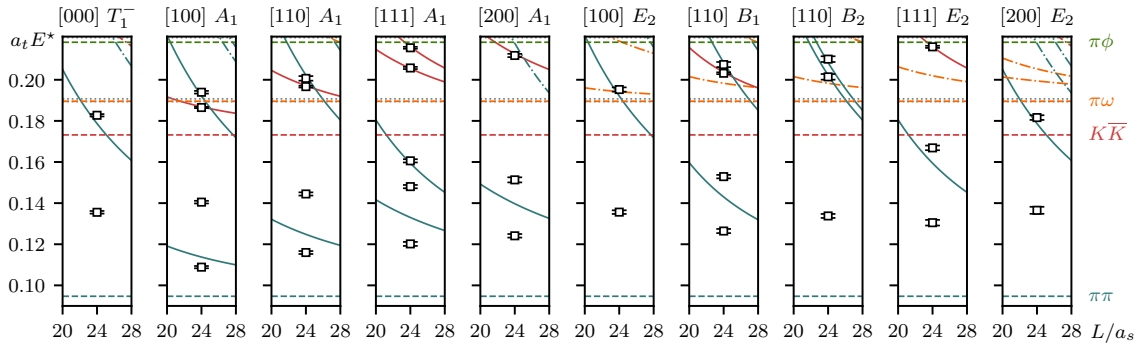

Figure 5.3: Finite-volume spectra obtained for all irreps considered in this analysis. Dashed lines show meson-meson thresholds, while solid lines show non-interacting meson-meson energies as a function of L, color-coded according to the meson pair (dot-dashed indicating non-interacting energies where the associated operator was not included in the variational basis). Grey dotted lines indicate thresholds for higher-multiplicity scattering ($\pi\pi\pi\pi$, $\pi\pi\eta$, $K\overline{K}\pi$).

them lies within a few standard deviations of a non-interacting energy. In particular, we find that the energy levels close to $K\overline{K}$ non-interacting energies have the least amount of statistical error. This is an indication that the $\pi\pi/K\overline{K}$ system is weakly coupled, and that each individual channel has a small interaction strength over this energy region. Furthermore, the levels in the $\pi\pi$ elastic region have similar overlaps to single-meson-like operators and to two-meson-like operators, whenever there are non-interacting energies nearby. In the case of levels above the $K\overline{K}$ threshold, most states only have strong overlap with the two-meson-like operator associated with the nearby non-interacting energy.

This pattern of state overlaps can be observed in Fig. 5.2, for the levels below $K\overline{K}$ threshold and the level with small error close to the $K\overline{K}$ non-interacting energy. In that same figure, the $\omega\pi$ operators can be seen overlapping to levels that also have a sizeable overlap to $J^P = 1^+$ single-meson-like operators, likely due to the nearby b_1 resonance discussed earlier. Further evidence associating these levels to the $J^P = 1^+$ partial-wave is that they have negligible overlap with operators having negative parity.

We close this section by commenting on the optimized operators defined by the eigenvector of the GEVP. The values of t_0 and t_Z, defined in Sec. 2.2.2, used in each irrep to obtain the optimized operators that will be used for the calculation of production am-

plitudes are given in Tab. 5.3,. Because of the small contamination from excited energy levels, optimized operators formed with Eq. (2.17), will not quite have the normalization of Eq. (2.18), but instead

$$\langle \mathfrak{n}|\Omega^{\dagger}_{\mathfrak{m}}(0)|0\rangle = \sqrt{1-b_{\mathfrak{n}}}\sqrt{2E_{\mathfrak{n}}}\,\delta_{\mathfrak{n},\mathfrak{m}}\,. \tag{5.3}$$

To compensate we simply redefine the optimized operators to be equal to

$$\bar{\Omega}^{\dagger}_{\mathfrak{n}} \equiv \sqrt{\frac{2E_{\mathfrak{n}}}{1-b_{\mathfrak{n}}}}e^{-E_{\mathfrak{n}}t_0/2}\sum_{j=1}^{A} v_j^{\mathfrak{n}}\,O_j^{\dagger}\,, \tag{5.4}$$

and for convenience we will drop the bar, but advise the reader that in the rest of this work the optimized operators refer to Eq. (5.4).

Table 5.3: Values of t_0 and t_Z used to determine the optimized operators in each lattice irrep associated with the continuum quantum numbers $I^G = 1^+$, $J^P = 1^-$.

Irrep	t_0	t_Z
$[000]\,T_1^-$	10	15
$[100]\,A_1$	10	15
$[110]\,A_1$	11	15
$[111]\,A_1$	10	17
$[200]\,A_1$	10	13
$[100]\,E_2$	10	13
$[110]\,B_1$	10	13
$[110]\,B_2$	9	13
$[111]\,E_2$	10	13
$[200]\,E_2$	10	17

5.2 Amplitude extraction

5.2.1 Elastic $\pi\pi$ scattering

In the case of a single channel and a single partial wave, the determinant of Eq. (2.2) has a single entry, and becomes an algebraic equation relating each energy level with a value of the elastic phase-shift. We can calculate the P-wave $\pi\pi$ phase-shift, $\delta_1^{\pi\pi}$, associated with

the spectra within the elastic energy region shown in Fig. 5.3. We show the phase-shift data in Fig. 5.4 as grey points, with the propagated error from the CM energy.

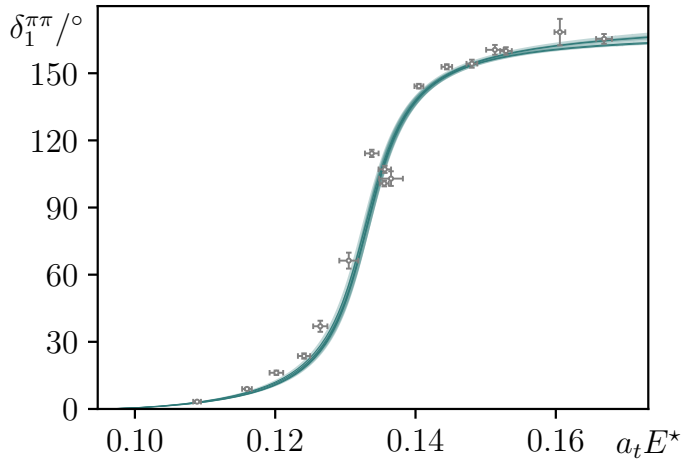

Figure 5.4: Elastic $\pi\pi$ P-wave phase-shift constrained by energy levels below $K\overline{K}$ threshold in Fig. 5.3. Bands shows parameterizations including the *reference elastic* parameterization of Eq.(5.6).

The behavior of the data strongly suggests a rapid phase-shift increase, crossing 90° at an energy around $a_t E^\star = 0.135$, which can be efficiently parameterized by including a pole term in the K-matrix. To describe the spectrum, we consider a *reference elastic* scattering amplitude of the form

$$\begin{aligned} \mathcal{M}(s) &= \frac{16\pi}{\frac{1}{(2k^\star)^2}\mathcal{K}^{-1}(s) - I_{\mathrm{CM}}(s)}\,, \\ \mathcal{K}(s) &= \frac{g^2}{m^2 - s} + \gamma\,, \end{aligned} \tag{5.5}$$

where I_{CM} was given in Eq. (1.33). From this parameterization of $\mathcal{M}$ we can generate the finite-volume spectra in the elastic energy region for a given set of parameters using Eq. (2.2). These spectra are compared to the lattice CM energies with a correlated χ^2 function. We minimize the χ^2 by varying the parameters and we find that the best fit to the lattice energy levels is with parameter values,

$$\begin{aligned} m &= 0.1335\,(5)\cdot a_t^{-1} \\ g &= 0.445\,(10) \\ \gamma &= (3.4\pm 2.2)\cdot a_t^2 \end{aligned} \qquad \begin{bmatrix} 1 & -0.3 & -0.3 \\ & 1 & 0.7 \\ & & 1 \end{bmatrix}$$

$$\chi^2/N_{\rm dof} = \tfrac{17.0}{17-3} = 1.21 \ . \tag{5.6}$$

The elements in the matrix correspond to the correlation between model parameters for the best fit, $\mathrm{cov}(a,b)/(\sigma_a\sigma_b)$, these are calculated via jackknife.

In order to determine the sensitivity of the extracted scattering to the specific form of the parameterization, we used various parameterizations to describe the finite-volume spectra. A general feature of all amplitudes that are able to successfully describe the energy levels is a rapid increase of the phase-shift around $a_t E^\star = 0.135$.

Our variations concern what degree of polynomial is added to the pole, and whether a simple, or dispersively improved phase-space is used. Table 5.4 summarizes four variations used for the elastic amplitude. The explicit form of the relativistic Breit-Wigner parameterization can be found in Ref. [91]. The other parameterizations are of the form of Eq. (5.5), and the one satisfying $\gamma = 0$ corresponds to the Gounaris-Sakurai form [122].

We found little variation in the energy dependence from different functional forms, as illustrated by the bands in Fig. 5.4. Similarly the various parameterizations have commesurate values of $\chi^2/N_{\rm dof}$.

Parameterization	$N_{\rm pars}$	$\chi^2/N_{\rm dof}$
Relativistic Breit-Wigner	2	1.23
$\mathcal{K} = \frac{g^2}{m^2-s}$ (Gounaris-Sakurai)	2	1.29
$\mathcal{K} = \frac{g^2}{m^2-s} + \gamma$ (With $-i\rho$ phase space)	3	1.23
$\mathcal{K} = \frac{g^2}{m^2-s} + \gamma$	3	1.21

Table 5.4: P-wave elastic amplitude parameterization variations.

The behavior observed in Fig. 5.4 is clearly that of a narrow resonance, and indeed the *reference elastic* amplitude is found to feature a pole on the unphysical Riemann sheet at

$$a_t\sqrt{s_R} = 0.1328(5) - \tfrac{i}{2}0.0096(5)\,, \tag{5.7}$$

with a coupling to $\pi\pi$ defined at the pole, $\mathcal{M}(s \sim s_R) \sim 16\pi \frac{c^2}{s_R - s}$, of value,

$$a_t \, c_{\pi\pi} = 0.0426(11) \, e^{-i\pi \cdot 0.047(3)} \, . \tag{5.8}$$

The other parameterizations also feature a pole with parameters statistically consistent to the ones shown above.

5.2.2 Coupled-channel $\pi\pi/K\overline{K}$ scattering

For a coupled-channel system, we no longer have a one-to-one mapping of individual energies to the value of individual elements of the scattering amplitude matrix, in channel space, at that energy. Instead we can only fit parameterizations of the amplitude to the spectra. Based on the results in the elastic region we propose a *reference coupled-channel* amplitude with a similar structure to the reference elastic amplitude,

$$\begin{aligned} \left[\mathcal{M}^{-1}\right]_{ab}(s) &= \tfrac{1}{16\pi} \left(\tfrac{1}{2k_a^\star} \left[\mathcal{K}^{-1}(s)\right]_{ab} \tfrac{1}{2k_b^\star} - \delta_{ab} \, I_{\mathrm{CM},a}(s) \right) , \\ \mathcal{K}_{ab}(s) &= \frac{g_a \, g_b}{m^2 - s} + \gamma_{ab} \, , \end{aligned} \tag{5.9}$$

and we find the best fit to all of our energy levels with the parameter values,

$$\begin{aligned} m &= \; 0.1338\,(5) \cdot a_t^{-1} \\ g_{\pi\pi} &= \; 0.441\,(9) \\ g_{K\overline{K}} &= \; 0.17\,(30) \\ \gamma_{\pi\pi,\pi\pi} &= \; (2.9 \pm 0.9) \cdot a_t^2 \\ \gamma_{\pi\pi,K\overline{K}} &= \; -(2.4 \pm 5.0) \cdot a_t^2 \\ \gamma_{K\overline{K},K\overline{K}} &= \; -(2.2 \pm 4.0) \cdot a_t^2 \end{aligned} \qquad \begin{bmatrix} 1 & -0.2 & 0.0 & -0.2 & 0.2 & -0.1 \\ & 1 & -0.4 & 0.6 & -0.4 & -0.4 \\ & & 1 & -0.2 & 0.8 & 0.9 \\ & & & 1 & -0.2 & -0.1 \\ & & & & 1 & 0.8 \\ & & & & & 1 \end{bmatrix}$$

$$\chi^2/N_{\mathrm{dof}} = \tfrac{28.7}{32-6} = 1.10 \, . \tag{5.10}$$

We show the phase-shifts $\delta_1^{\pi\pi}$, $\delta_1^{K\overline{K}}$, and the inelasticity η of this parameterization in Fig. 5.5.

Similar to the elastic amplitude, we observe a rapid increase of the $\pi\pi$ phase-shift, which crosses 90° at an energy $a_t E^\star \sim 0.135$. Above the $K\overline{K}$ threshold the $\pi\pi$ phase-shift

increases slowly towards 180°, indicating weak interactions for those energies. The $K\overline{K}$ phase-shift turns on slowly, as dictated by the centrifugal barrier of the P-wave, and takes a small negative value, indicating that the $K\overline{K}$ system is weakly repulsive over this energy region.

Finally, we observe that the inelasticity η, stays consistent with one in this energy region. As explained in Sec. 1.5.1.2, this indicates that the two channels remain decoupled to a good approximation, or with a very weak coupling between them.

As in the case of the elastic amplitude we can look for poles and residues in the scattering, which for a coupled-channel system have the following behavior

$$\mathcal{M}_{ab}(s \sim s_R) \sim 16\pi \, \frac{c_a \, c_b}{s_R - s} \,, \tag{5.11}$$

where the amplitude factorizes at the pole, indicating that the coupling of the resonance to each of the channels is independent to each other.

The amplitude of Eq. (5.10) presents a pole consistent with the pole found for the reference elastic amplitude, as expected for a resonance lying below the inelastic threshold,

$$a_t \sqrt{s_R} = 0.1331(4) - \tfrac{i}{2} 0.0095(4) \,, \tag{5.12}$$

on the sheet closest to the physical scattering below the $K\overline{K}$ threshold, where the imaginary parts of $\pi\pi$ and $K\overline{K}$ momenta are negative and positive, respectively. The residues at the pole are equal to

$$\begin{aligned} a_t \, c_{\pi\pi} &= 0.0424(8) \, e^{-i\pi \cdot 0.047(2)} \,, \\ a_t \, c_{K\overline{K}} &= 0.019(33) \, e^{i\pi \cdot 0.47(5)} \,, \end{aligned} \tag{5.13}$$

which are observed to be close to real for the kinematically open $\pi\pi$ channel, and close to imaginary for the kinematically closed $K\overline{K}$ channel. The coupling to the $\pi\pi$ channel is also consistent with the elastic result. The value of the coupling to the $K\overline{K}$ channel is

poorly constrained from this analysis, as expected for a resonance lying below threshold, as the effects of this channel on the finite-volume spectrum get exponentially suppressed below its threshold.

Finally, owing to the P-wave nature of the resonance, it is relevant to quote the value of the couplings with the barrier factor associated with each channel divided out,

$$\begin{aligned}\sqrt{16\pi}\,|\hat{c}_{\pi\pi}| &\equiv \sqrt{16\pi}\left|\frac{c_{\pi\pi}}{k^{\star}_{\pi\pi}(s_R)}\right| = 6.41 \pm 0.13\,,\\ \sqrt{16\pi}\,|\hat{c}_{K\overline{K}}| &\equiv \sqrt{16\pi}\left|\frac{c_{K\overline{K}}}{k^{\star}_{K\overline{K}}(s_R)}\right| = 2.4 \pm 4.0\,.\end{aligned} \tag{5.14}$$

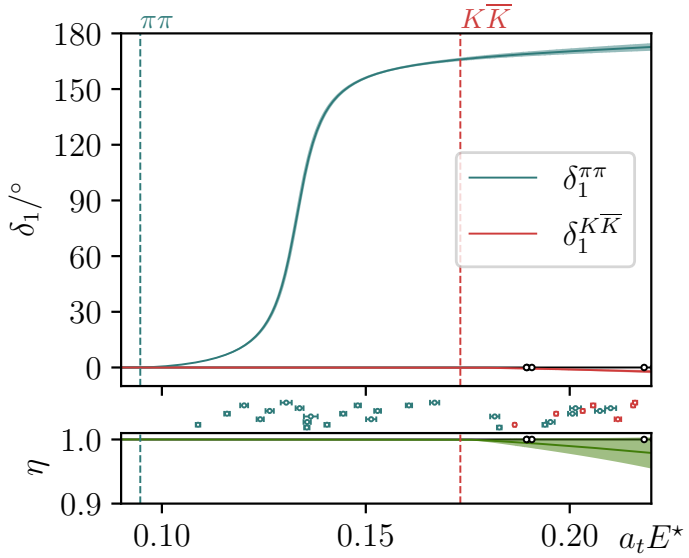

Figure 5.5: Phase-shifts and inelasticity for coupled-channel $\pi\pi, K\overline{K}$ scattering corresponding to the amplitude given in Eq. (5.10). The constraining energy level locations are shown between the panels, with levels lying close to $K\overline{K}$ non-interacting energies colored in red. White circles show the thresholds for $\pi\pi\pi\pi$, $\omega\pi$ and $\phi\pi$ production, in that order.

To evaluate the sensitivity of this result to the parameterization choice, we also consider further variations of the scattering amplitude. Table 5.5 summarizes 23 of such variations for the coupled-channel case. We find these parameterizations in overall agreement with the reference coupled-channel amplitude, with slight variations seen on the energy dependence of the inelasticity, but statistically consistent values of the phase-shifts $\delta_1^{\pi\pi}$ and $\delta_1^{K\overline{K}}$. The

variations for the resonance pole position s_R and coupling to the $\pi\pi$ channel, $c_{\pi\pi}$, fall within the statistical uncertainty of the previously quoted results. However, the coupling to the $K\overline{K}$ channel is poorly determined in each parameterization, with some models differing from each other at the level of up to two standard deviations. We expect that the uncertainty on $c_{K\overline{K}}$ will dominate the uncertainty and parameterization variation of our determination of the timelike form factor of the kaon because of the experimental observation that this amplitude is dominated by the tail of the ρ-meson resonance peak [47].

To illustrate the results with the largest variation associated with the parameterization, we select two of these coupled-channel amplitudes for propagation into the production amplitude analysis. The first is the coupled-channel reference amplitude of Eq. (5.9), the first entry of Tab. 5.5, while the second, which we label "$\gamma^{(1)}$", has functional form,

$$\mathcal{K}_{ab}(s) = \frac{g_a\, g_b}{m^2 - s} + \gamma_{ab}^{(0)} + \gamma_{ab}^{(1)} s\,, \tag{5.15}$$

corresponding to the tenth entry of Table 5.5. The resonance pole of the "$\gamma^{(1)}$" parameterization is located at

$$a_t\sqrt{s_R} = 0.1327(5) - \tfrac{i}{2}0.0096(4)\,, \tag{5.16}$$

consistent with Eq. (5.12), while the channel couplings are,

$$\begin{aligned} a_t\, c_{\pi\pi} &= 0.0424(9)\, e^{-i\pi\cdot 0.055(4)}\,, \\ a_t\, c_{K\overline{K}} &= 0.097(24)\, e^{i\pi\cdot 0.484(10)}\,, \end{aligned} \tag{5.17}$$

where we observe a noticeable variation on $c_{K\overline{K}}$ as compared to the reference amplitude case in Eq. (5.13).

Parameterization	Restrictions	N_{pars}	χ^2/N_{dof}
$\mathcal{K}_{ab} = \frac{g_a g_b}{m^2 - s} + \gamma_{ab}$	–	6	1.10
	$g_{K\overline{K}} = 0$	5	1.07
	$\gamma_{K\overline{K},K\overline{K}} = 0$	5	1.07
	$\gamma_{\pi\pi,K\overline{K}} = 0$	5	1.08
	$\gamma_{\pi\pi,\pi\pi} = 0$	5	1.47
$\mathcal{K}_{ab} = \frac{g_a g_b}{m^2 - s} + \gamma^{(1)}_{ab} s$	–	6	1.05
	$g_{K\overline{K}} = 0$	5	1.03
	$\gamma^{(1)}_{K\overline{K},K\overline{K}} = 0$	5	1.02
	$\gamma^{(1)}_{\pi\pi,K\overline{K}} = 0$	5	1.02
$\mathcal{K}_{ab} = \frac{g_a g_b}{m^2 - s} + \gamma_{ab}(s)$ $\gamma_{ab}(s) = \gamma^{(0)}_{ab} + \gamma^{(1)}_{ab} s$	–	9	1.05
	$g_{K\overline{K}} = 0$	8	1.11
	$\gamma^{(1)}_{K\overline{K},K\overline{K}} = 0$	8	1.07
	$\gamma^{(1)}_{\pi\pi,K\overline{K}} = 0$	8	1.06
	$\gamma^{(1)}_{\pi\pi,\pi\pi} = 0$	8	1.08
$\mathcal{K}_{ab} = \frac{g_a(s) g_b(s)}{m^2 - s} + \gamma_{ab}$ $g_a(s) = g^{(0)}_a + g^{(1)}_a s$	–	8	1.15
	$g^{(1)}_{\pi\pi} = 0$	7	1.11
	$\gamma_{\pi\pi,\pi\pi} = 0$, $\gamma_{\pi\pi,K\overline{K}} = 0$	6	1.10
	$\gamma_{\pi\pi,\pi\pi} = 0$, $\gamma_{K\overline{K},K\overline{K}} = 0$	6	1.11
	$\gamma_{\pi\pi,K\overline{K}} = 0$, $\gamma_{K\overline{K},K\overline{K}} = 0$	6	1.10
$\mathcal{K}_{ab} = \frac{g_a g_b}{m^2 - s} + \gamma_{ab}$ $I_{ab} = -i\,\delta_{ab}\,\rho_a$	–	6	1.12
	$g_{K\overline{K}} = 0$	5	1.11
	$\gamma_{K\overline{K},K\overline{K}} = 0$	5	1.12
	$\gamma_{\pi\pi,K\overline{K}} = 0$	5	1.11

Table 5.5: P-wave coupled-channel amplitude parameterization variations.

Chapter 6

Finite-volume matrix elements of the $1 \xrightarrow{\mathcal{J}} 1$ and $0 \xrightarrow{\mathcal{J}} 2$ transitions

Matrix elements in a lattice calculation can be extracted following the techniques described in Sec. 2.2.4. In this Chapter we will describe the extraction of matrix elements associated with the pion spacelike form factor, and the pion and kaon timelike form factors. We will describe the kinematic factors associated with the subduction to the irreps of the lattice, and the tensors from the Lorentz decomposition of the matrix elements in the form of Eq. (3.1). We will then be able to extract finite-volume form factors, which for the spacelike pion form factor we can immediately identify with the infinite volume form factor. The spacelike form factor at zero photon virtuality will be used to determine the current renormalization. Finally, we will describe the fit strategies employed to model the correlation functions with current insertions, from which the matrix elements are extracted.

6.1 Kinematic factors

We begin by considering the spacelike matrix elements. In this case the subduction of the hadron states is trivial: single-pion states being spinless only subduce to one-dimensional irreps, with subduction coefficient equal to 1. We will drop the irrep coefficient for the

single-meson states for convenience, so we can focus on the subduction of the vector current

$$\langle \pi(\mathbf{p}_f)|\mathcal{J}^{\Lambda\mu}(0)|\pi(\mathbf{p}_i)\rangle = \sum_{\lambda,j} \mathcal{S}_\lambda^{\Lambda\mu} \boldsymbol{\epsilon}^j(\mathbf{q},\lambda)\, \langle \pi(\mathbf{p}_f)|\mathcal{J}^j(0)|\pi(\mathbf{p}_i)\rangle \ , \tag{6.1}$$

where $\boldsymbol{\epsilon}(\mathbf{q},\lambda)$ is the three dimensional polarization vector for a state of momentum $\mathbf{q}$ and helicity λ, and $\mathcal{S}_\lambda^{\Lambda\mu}$ are the subduction coefficients for spin-one states, introduced in Sec. 2.1.1, projecting the current with $J^P = 1^-$ into the lattice irrep and row $\Lambda\mu$. In this work we will only consider the spatial part of the vector current, $\mathcal{J}^i$.

We can employ the Lorentz decomposition of the current sandwiched by pion states, given in Eq. (1.49), and the expression of the subduction coefficients from [60, 61], to obtain an expression of the form

$$\langle \pi(\mathbf{p}_f)|\mathcal{J}^{\Lambda\mu}(0)|\pi(\mathbf{p}_i)\rangle = K_{\rm sl}(\Lambda,\mu,\mathbf{p}_f,\mathbf{p}_i)\, f_\pi(-Q^2)\,, \tag{6.2}$$

where we remind the reader that $Q^2 = -(p_f - p_i)^2$, with $p_{i(f)}$ the four momentum of the initial(final) pion. The kinematic factor for spacelike current momentum, $K_{\rm sl}$, is equal to

$$K_{\rm sl}(\Lambda,\mu,\mathbf{p}_f,\mathbf{p}_i) = \sum_{\lambda,j} \mathcal{S}_\lambda^{\Lambda\mu} \boldsymbol{\epsilon}^j(\mathbf{q},\lambda)(\mathbf{p}_f + \mathbf{p}_i)^j\,. \tag{6.3}$$

To decrease statistical fluctuations we can average matrix elements having the same value of Q^2, $\left|\mathbf{p}_{i/f}\right|$, and current irrep, but different momenta orientations, $\hat{\mathbf{p}}_f$ and $\hat{\mathbf{p}}_i$, and rows μ.

In this work, for every value value of Q^2, we employed a fixed direction of momentum for the current insertion, $\mathbf{q} = \mathbf{p}_f - \mathbf{p}_i$, and calculated the current projected to all pertinent irreps and rows. We calculate various rotations of the initial and final momenta, $R\mathbf{p}_f$ and $R\mathbf{p}_i$, where the rotation R belongs to the little group of $\mathbf{q}$.

The form factor can be extracted from the following weighted average,

$$f_\pi(-Q^2) = \frac{1}{|K_{\rm sl}(\Lambda, \mathbf{p}_f, \mathbf{p}_i)|^2} \sum_{R,\mu} K^*_{\rm sl}(\Lambda, \mu, R\mathbf{p}_f, R\mathbf{p}_i) \, \langle \pi(R\mathbf{p}_f)|\mathcal{J}^{\Lambda\mu}(0)|\pi(R\mathbf{p}_i)\rangle \ , \quad (6.4)$$

where $|K_{\rm sl}|^2 = \sum_{R,\mu} K_{\rm sl} K^*_{\rm sl}$. This prescription is equivalent to the SVD inversion used to extract multiple form factors from rotational equivalent matrix elements described in Ref. [94].

For example, in the case of $\mathbf{q} = 0$, $\mathbf{p} = \mathbf{p}_f = \mathbf{p}_i$, the current subduces into the irrep T_1^-, and the three polarization vectors are projected to the different rows of T_1^-. In this case we can calculate $|K_{\rm sl}|^2$ easily by exploiting the completeness relation of the polarization vectors, and that the subduction coefficients have been normalized to form unitary matrices, to find

$$\left|K_{\rm sl}(T_1^-, \mathbf{p}, \mathbf{p})\right|^2 = 4N_R|\mathbf{p}|^2 \, , \quad (6.5)$$

where N_R are the number of different rotations, R, over which we average.

To extract the form factors from correlation functions, we define the rotational average of the ratio of three- to two-point correlation functions

$$R_{\rm 3pt}(\Delta t, t) = \frac{4E_{\pi,|\mathbf{p}_f|}E_{\pi,|\mathbf{p}_i|}}{\sqrt{2}|K_{\rm sl}(\Lambda, \mathbf{p}_f, \mathbf{p}_i)|^2} \sum_{R,\mu} K^*_{\rm sl}(\Lambda, \mu, R\mathbf{p}_f, R\mathbf{p}_i) \times \frac{\left\langle \Omega_{\pi,R\mathbf{p}_f}(\Delta t)\, \mathcal{J}^{\Lambda\mu}_{\rho,\rm lat}(t)\, \Omega^\dagger_{R\pi,\mathbf{p}_i}(0)\right\rangle}{\left\langle \Omega_{\pi,\mathbf{p}_f}(\Delta t - t)\Omega^\dagger_{\pi,\mathbf{p}_f}(0)\right\rangle \left\langle \Omega_{\pi,\mathbf{p}_i}(t)\Omega^\dagger_{\pi,\mathbf{p}_i}(0)\right\rangle} \, . \quad (6.6)$$

For large time separations, this ratio plateaus to

$$R_{\rm 3pt}(\Delta t, t) = \frac{1}{Z_V^l} f_\pi(-Q^2) + \dots \, , \quad (6.7)$$

where Z_V^l is the renormalization constant of the isovector local vector current introduced in Eq. (2.21). In practice, even when using optimized operators, we will observe pollution from higher energy states close to $t = 0$ and $t = \Delta t$. To disentangle the leading contribution

we perform a correlated timeslice fit of the quantity $R_{3\mathrm{pt}}(\Delta t, t)$ to the following functional forms: a constant, a constant plus a decaying exponential at the source, a constant plus a decaying exponential at the sink, or a constant plus a decaying exponential both at the source and the sink. All these functional forms can be described by the function

$$R_{3\mathrm{pt}}(\Delta t, t) = \frac{f_\pi(-Q^2)}{Z_V^l} + f_f\, e^{-\delta E_f(\Delta t - t)} + f_i\, e^{-\delta E_i\, t}\,. \tag{6.8}$$

Although matrix elements corresponding to the same value of Q^2, but with the current projected to a different irrep, or having different values of $\left|\mathbf{p}_{i/f}\right|$, are proportional to the same form factor $f_\pi(-Q^2)$, we only form rotational and row averages of correlation functions as described above. Even if these correlation functions should plateau to statistically consistent values, they typically present quite different excited state pollution, and can have different signal to noise ratios. In those cases we will first fit the time dependence of the ratios of Eq. (6.6), and after that, combine the fit results by a correlated fit to a constant.

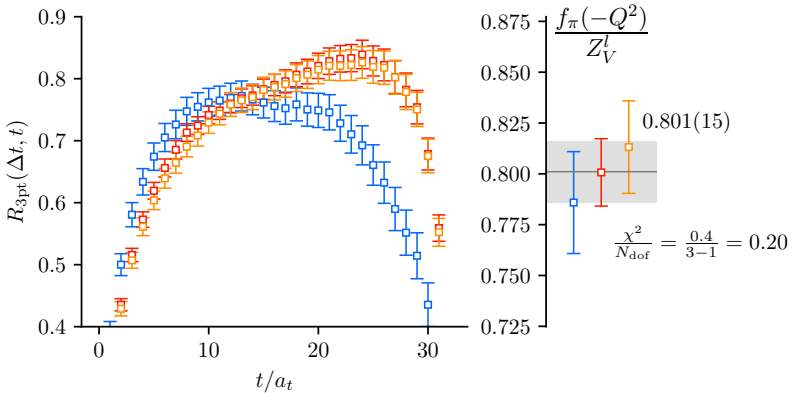

Figure 6.1: Example of three $R_{3\mathrm{pt}}(\Delta t, t)$ ($\Delta t = 32a_t$) with the same value for Q^2, but with the current projected to different irreps. On the left we show a correlated fit to a constant with the result of the three different fits.

We show an example of this in Fig. 6.1 for three different $R_{3\mathrm{pt}}(\Delta t, t)$ with $\Delta t = 32a_t$ and kinematic variables $\left(\frac{L}{2\pi}|\mathbf{p}_i|\right)^2 = 3$, $\left(\frac{L}{2\pi}|\mathbf{p}_f|\right)^2 = 5$ and $\left(\frac{L}{2\pi}|\mathbf{q}|\right)^2 = 2$. The blue data points correspond to the A_1 current irrep, subduced from the zero helicity component,

while the red and orange correspond to subduction of the ± 1 helicity components to the B_1 and B_2 irreps, respectively. A common plateau cannot be easily identified for the three datasets, but once the excited state pollution is taken into account with the fit procedure, we find a consistent value for $f_\pi(-Q^2)/Z_V^l$. We will give more details about the timelsice fitting procedure in Sec. 6.3.

In the case of the timelike production matrix element, we have to consider the subduction of the hadronic state in addition to the subduction of the current. Let us begin by presenting the Lorentz decomposition of a production matrix element in the infinite-volume continuum,

$$\langle \rho(P,\lambda)|\mathcal{J}^i(0)|0\rangle = (\epsilon^i(P,\lambda))^*\, f_V P^2\,, \tag{6.9}$$

where $|\rho(P,\lambda)\rangle$ represents a stable meson state, which we use only to illustrate the Lorentz decomposition of the current overlap with a state with quantum numbers $J^{PC} = 1^{--}$, four-momentum P and helicity λ. The four-dimensional polarization vector of state $|\rho(P,\lambda)\rangle$ is $\epsilon^\nu(P,\lambda)$ and f_V is commonly called the vector-meson decay constant.[1] Note that the vectors $\boldsymbol{\epsilon}^i$, introduced in Eq. (6.1), and ϵ^i are equal for non-zero helicities, but different for $\lambda = 0$, in that case each of them is equal to

$$\boldsymbol{\epsilon}^i(\mathbf{P},0) = \hat{\mathbf{P}}^i\,, \quad \epsilon^i(P,0) = \gamma\,\hat{\mathbf{P}}^i\,, \tag{6.10}$$

where we used the relativistic factor $\gamma = P^0/\sqrt{P^2}$.

The finite-volume subduction follows a similar procedure than the one used for the

[1] With this normalization, the decay constant, f_V, is unitless. Other normalizations have been used in the literature, see for example Ref. [123] that uses $f_\rho = \sqrt{2}\sqrt{P^2}\, f_V$.

$\Lambda(\mathcal{J}^\mu)$	$T_1^-(\mathcal{J}^i)$	$A_1(\mathcal{J}^0)$	$A_1(\mathcal{J}^i)$	$E_2, B_1, B_2(\mathcal{J}^i)$
$K_{\text{tl}}(\Lambda, P)$	$\sqrt{\frac{4}{3}}$	$\sqrt{\frac{4}{3}}\gamma\beta$	$\sqrt{\frac{4}{3}}\gamma$	$\sqrt{\frac{4}{3}}$

Table 6.1: Kinematic factor of the subduced finite volume matrix elements into irrep Λ from the temporal, $\mathcal{J}^0$, or spatial, $\mathcal{J}^i$, components of a vector current.

spacelike matrix elements

$$\left\langle \rho(P,\Lambda'\mu')\middle|\mathcal{J}^{\Lambda\mu}(0)\middle|0\right\rangle = \sum_{\lambda,\lambda',i} \mathcal{S}_\lambda^{\Lambda\mu}\boldsymbol{\epsilon}^i(\mathbf{P},\lambda)\left\langle \rho(P,\lambda')\middle|\mathcal{J}^i(0)\middle|0\right\rangle \mathcal{S}_{\lambda'}^{\Lambda'\mu'}\,, \tag{6.11}$$

$$= \left[\sum_{\lambda,\lambda',i} \mathcal{S}_\lambda^{\Lambda\mu}\boldsymbol{\epsilon}^i(\mathbf{P},\lambda)\big(\epsilon^i(P,\lambda')\big)^*\mathcal{S}_{\lambda'}^{\Lambda'\mu'}\right] f_V P^2\,, \tag{6.12}$$

where the term in square brackets will be the kinematic factor.

Even though in our calculation the states in the production matrix element cannot be identified with a stable single-particle state, they have the same quantum numbers as the example of before, meaning that the subduction procedure remains the same. For the states with energy within the two-meson sector, $|\mathfrak{n}\rangle_L$, found in Chapter 5, we choose a decomposition with the following normalization

$${}_L\langle\mathfrak{n}|\mathcal{J}^{\Lambda\mu}(0)|0\rangle = \tfrac{1}{\sqrt{2E_\mathfrak{n}L^3}}\,K_{\text{tl}}(\Lambda,P)\,\mathcal{F}_\mathfrak{n}^{(L)}\,, \tag{6.13}$$

where $\mathcal{F}_\mathfrak{n}^{(L)}$ is the "finite-volume form factor" and the kinematic factor is given by

$$\delta_{\Lambda\Lambda'}\delta_{\mu\mu'}K_{\text{tl}}(\Lambda,P) = \sqrt{\frac{4}{3}}\sum_{\lambda,\lambda',i}\mathcal{S}_\lambda^{\Lambda\mu}\boldsymbol{\epsilon}^i(\mathbf{P},\lambda)\big(\epsilon^i(P,\lambda')\big)^*\mathcal{S}_{\lambda'}^{\Lambda'\mu'} \tag{6.14}$$

and the numerical coefficient was chosen for convenience, as it will later cancel against a factor given in Eq.(1.38). We list the value of these kinematic factors in Tab. 6.1.

As before, we define a ratio of correlation functions from which we will be able to

extract the finite-volume production matrix elements,

$$R_{\mathfrak{n}}(t) \equiv \frac{\sqrt{2E_{\mathfrak{n}}}}{K_{\mathrm{tl}}(\Lambda, P)} \frac{\langle 0|\mathcal{J}(t)\,\Omega_{\mathfrak{n}}^{\dagger}(0)|0\rangle}{\langle 0|\Omega_{\mathfrak{n}}(t)\,\Omega_{\mathfrak{n}}^{\dagger}(0)|0\rangle} = \sqrt{\tfrac{L^3}{2E_{\mathfrak{n}}}}\mathcal{F}_{\mathfrak{n}}^{(L)} + \dots\,, \tag{6.15}$$

where in the last equality we are neglecting pollution terms with exponentially decaying time dependence coming from higher energy states. We emphasize again that by using the optimized operators we will be able to access the production matrix element of the finite-volume ground state and of multiple excitations, allowing access to $\mathcal{F}_{\mathfrak{n}}^{(L)}$ over a wide range of kinematics.

In this case we will extract the leading constant contribution by performing a correlated fit of the time dependence of $R_{\mathfrak{n}}(t)$ to functions of the form

$$R_{\mathfrak{n}}(t) = \sqrt{\tfrac{L^3}{2E_{\mathfrak{n}}}}\mathcal{F}_{\mathfrak{n}}^{(L)} + \mathcal{F}_s\, e^{-\delta E_s\, t}\,. \tag{6.16}$$

We found that $\left\langle \mathcal{J}(t)\Omega_{\mathfrak{n}}^{\dagger}(0)\right\rangle$ two-point correlation functions were statistically precise, and an average over momentum rotations or irrep rows was not carried out.

6.2 Correlation functions and fitting strategy

To calculate correlation functions with insertions of a local current we employ the distillation framework, which requires the inclusion of generalized perambulators, Eq. (2.31). We computed two- and three-point correlation functions with current insertions over a subset of 348 configurations out of the 400 configurations used to extract the spectra. The correlation functions were constructed with quark fields smeared using distillation with $N_{\mathrm{vecs}} = 162$. In the case of three-point functions we fixed the source-sink separation to $\Delta t = 32a_t$, and inserted the current at the timeslices $0 \leq t/a_t \leq 32$. For two-point functions the current was inserted at the sink, and we calculated sink-source separations of $0 \leq t/a_t < 32$.

To extract the spacelike form factor covering a wide kinematic region, correlators were

computed with optimized pion operators of momenta up to $|\mathbf{p}|^2 \leq 6\,\left(\frac{2\pi}{L}\right)^2$, and a current momentum insertion with momenta up to $|\mathbf{q}|^2 \leq 4\,\left(\frac{2\pi}{L}\right)^2$. A total of 532 three-point functions were employed in this calculation, which were reduced by rotational and row averages to 51 ratios of the form of Eq. (6.6), and a correlated timeslice fit was performed to each of them to extract the form factor. After averaging the fit results of the form factors with equivalent Q^2, we were left with 20 different kinematic values spanning $0 \leq Q^2 \lesssim 1.6$ GeV^2.

To extract the finite-volume timelike production matrix elements we computed correlation functions with the current at the sink and at the source we employed the 32 optimized operators associated with the 32 levels extracted in Chapter 5 presented in Fig. 5.3. This spans the energy region from the two-pion threshold at ~ 570 MeV, passing the kaon-antikaon threshold at ~ 1 GeV, and up to ~ 1.3 GeV, or in energy squared the timelike matrix elements span the kinematic region $0.3\ \text{GeV}^2 < s < 1.7\ \text{GeV}^2$.

To fit the data we need to select among several choices of timeslice ranges $[t_{\text{min}}, t_{\text{max}}]$, and functional forms. To decrease the possible bias in this selection we follow the prescription suggested by Jay and Neil [124]. For both $R_{\mathfrak{n}}$ and $R_{3\text{pt}}$, we begin by picking a minimum number of timeslices N_t, and performing fits to a constant.

In the case of $R_{3\text{pt}}$, we perform constant fits to all time windows larger or equal to N_t. For each of the fits we form a version of the Akaike Information Criterion (AIC) weight, by combining the correlated χ^2 and the number of degrees of freedom, N_{dof}, according to $w = \exp\left[-(\chi^2/2 - N_{\text{dof}})\right]$. Fits with functional forms describing contributions from pollution terms, e.g. Eq. (6.8), are performed only to time windows containing the subset of data associated with the maximum value of w for a constant fit.

After that, we fit using the functional form of Eq. (6.8) with $f_f(f_i)$ fixed to zero, with time ranges such that $t_{\text{min}}(t_{\text{max}})$ is less(greater) than the corresponding $t_{\text{min}}(t_{\text{max}})$ of the best constant fit, according to the value of w, while leaving $t_{\text{max}}(t_{\text{min}})$ equal to that of the

best constant fit. We also perform fits to the functional form of Eq. (6.8) by using values of $t_{\rm min}$ and $t_{\rm max}$ less than and greater those of the best constant fit, respectively. We then calculate the AIC weight, w, for all successful fits.

In the case of $R_{\mathfrak{n}}$, we perform fits to a constant with varying values of $t_{\rm min}$ but a fixed value of $t_{\rm max}$. We label t^* the value of $t_{\rm min}$ for the time window for a given $t_{\rm max}$ with the maximum value of w. Then, a constant plus an exponential, i.e. Eq. (6.16), is used to perform fits with $t_{\rm min} < t^*$. We repeat this procedure for all values of $t_{\rm max}$ allowed by N_t, and calculate the AIC weight for each successful fit.

Each fit, α, provides a value and a statistical error for the constant contribution, which we generically label $C_\alpha \pm \sigma_{C,\alpha}$ for $R_{\rm 3pt}$ and $R_{\mathfrak{n}}$, which can be ranked according to their respective value of AIC weight w_α. Finally, a *model average* of C is calculated from a weighted average of the set $\{C_\alpha\}$ associated with the fits with largest weights,

$$C^{\rm mod.avg.} = \frac{\sum_\alpha w_\alpha C_\alpha}{\sum_\alpha w_\alpha}\,, \tag{6.17}$$

$$\sigma_C^2 = \frac{\sum_\alpha w_\alpha \sigma_{C,\alpha}^2}{\sum_\alpha w_\alpha} + \frac{\sum_{\alpha\beta} w_\alpha w_\beta (C_\alpha - C_\beta)^2}{2(\sum_\alpha w_\alpha)^2}\,. \tag{6.18}$$

To make this process compatible with the jackknife resampling technique, described in Sec. 2.2.6.1, we employ the following prescription, based on the method presented in Ref. [125]. For each fit we can obtain an ensemble $\{C_{\alpha,i}\}$, where the index i indicates an element of the upscaled jackknife ensemble. Then we can define the model averaged ensemble

$$C_i^{\rm (avg)} = \frac{\sum_\alpha w_\alpha\, C_{\alpha,i}}{\sum_\alpha w_\alpha}\,. \tag{6.19}$$

As we show in App. C, the average of this ensemble is equal to the value given in Eq. (6.17), but the variance is less than or equal to Eq. (6.18). In the case of our data set, we find the fractional difference between these two variances to be $\lesssim 10\%$. We can fix this mismatch by adding Gaussian noise, η_i, to $C_i^{\rm (avg)}$, as long as the variable η_i has zero mean and a

variance such that the variance of

$$\overline{C}_i^{(\mathrm{avg})} = C_i^{(\mathrm{avg})} + \eta_i \,, \tag{6.20}$$

matches the value required by Eq. (6.18). The Gaussian noise variables are drawn from a multidimensional uncorrelated Gaussian distribution, so that this prescription does not impact the covariance among different matrix elements. Reference [124] does not address the model average of the covariance among different variables, but we assume that it is best to not modify it. These ensembles are used for all subsequent analysis in this work.

6.3 Vector current renormalization

We non-perturbatively determine the renormalization of the isovector local vector current as described in Sec. 2.2.4. This boils down to demanding that the charge of the positive pion is equal to one elementary charge unit, i.e., requiring that $f_\pi(0) = 1$.

In a previous analysis of some of these correlation functions presented in Ref. [85], the leading time dependence was removed by forming the combination,

$$\widetilde{C}_{3\mathrm{pt}}(\Delta t, t) = \sum_{R,\mu} \frac{K^*_{\mathrm{sl}}(\Lambda, \mu, R\mathbf{p}_f, R\mathbf{p}_i)}{\sqrt{2}|K_{\mathrm{sl}}(\Lambda, \mathbf{p}_f, \mathbf{p}_i)|^2} \frac{\langle 0|\Omega_{\pi,\mathbf{R}\,p_f}(\Delta t)\,\mathcal{J}(t)\,\Omega^\dagger_{\pi,\mathbf{R}\,p_i}(0)|0\rangle}{e^{-E_{\mathbf{p}_f}(\Delta t - t)} e^{-E_{\mathbf{p}_i} t}} \,. \tag{6.21}$$

It can be the case that the timeslice-to-timeslice data correlation for this quantity is considerable, resulting in fits with reasonable values of χ^2 which undershoot the data. One such case is presented in panel (a) of Fig. 6.2.

Here we follow an alternative approach with the ratio of correlation functions, $R_{3\mathrm{pt}}$, containing two-point correlation functions with optimized operators, which will have the same constant contribution as $\widetilde{C}_{3\mathrm{pt}}$, but differing excited-state contributions. This combination proves to have much smaller timeslice-to-timeslice data correlation, and fits follow more closely the data points. This is illustrated in panel (b) of Fig. 6.2.

In these plots the lines correspond to the fit with the largest AIC weight, and we show

the results of the set of fits with the largest AIC weights on the right panel of each graph. The columns on the right of each of the plots of Fig. 6.2 show the results with the largest AIC weights, with the orange graph illustrating the value of w_i. Each fit is described by the time window $[t_{\text{min}}, t_{\text{max}}]$, and the number of exponentials at the source, n_{src}, or sink, n_{snk}. In practice we observe that the "model average" is dominated by only four or five fits which have large weight and the averaged error is dominated by the statistical error on these.

The difference with respect to the previous method using $\widetilde{C}_{3\text{pt}}(\Delta t, t)$ is modest, but is the origin of any differences in the current analysis with that in Ref. [85], such as for the light-quark vector current renormalization as shown in Fig. 6.3. The rest of this work considers only renormalized currents, such that all matrix elements have been renormalized according to Eq. (2.21), i.e. we have multiplied them by Z_V^l.

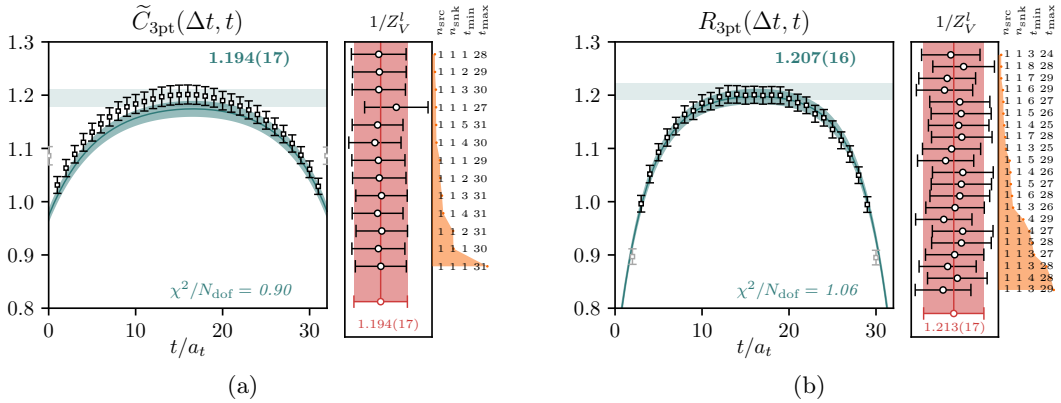

Figure 6.2: Fits to three-point correlation functions with $\mathbf{p}_1 = \mathbf{p}_2 = \frac{2\pi}{L}[110]$ (averaged over rotations and directions of current insertion) and fixed $\Delta t = 32\, a_t$ using either (a) Eq. (6.21) or (b) Eq. (6.6). Fitted constant value in this case corresponds to $1/Z_V^\ell$, the vector current renormalization constant. Variation of fit window is shown in the right columns, along with the model-averaged result.

6.4 Finite-volume timelike production matrix elements

We obtain finite-volume matrix elements following the procedure described in the previous sections. To illustrate the results, the timeslice behavior of $R_{\mathfrak{n}}(t)$ corresponding to the two

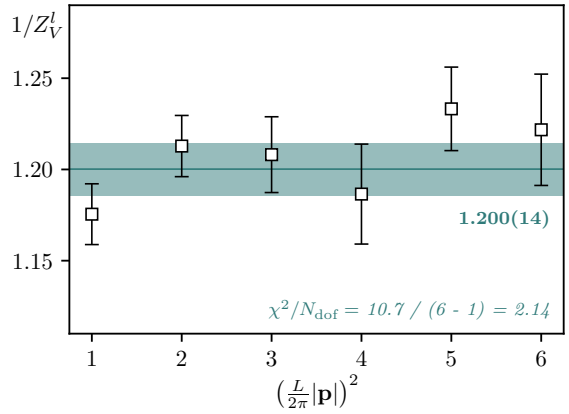

Figure 6.3: Determination of light-quark vector current renormalization Z_V^l by correlated fitting of extractions from six values of pion momentum.

lowest lying states of the [111] A_1 irrep are shown in Fig. 6.4. The observed relaxation to a constant value for $t \gtrsim t_0 = 10\, a_t$, even for the excited state, is a result of making use of optimized operators. We show separately the contributions of the two terms in Eq. (2.23), where the $\mathcal{O}(a)$ improvement term is observed to impact at the level of $5 - 10\%$ of the leading term. For the anisotropic lattice considered in this work, the improvement enters proportional to the energy difference between the initial and final states of the matrix element, which is larger in magnitude in the current case of production than in the case of three-point functions used to extract the spacelike pion form factor. Again, we observe that the "model average" is dominated by only four or five fits.

The use of optimized operators is a powerful technique owing to their overlap with other states in the spectrum being highly suppressed, $\langle \mathfrak{m}|\Omega_{\mathfrak{n}}^\dagger(0)|0\rangle \ll 1$, for $\mathfrak{m} \neq \mathfrak{n}$. However, we do encounter cases where a hierarchy of matrix elements for different states can compensate for this suppression, i.e. where $\mathcal{F}_{\mathfrak{m}}^{(L)} \cdot \langle \mathfrak{m}|\Omega_{\mathfrak{n}}^\dagger(0)|0\rangle \sim \mathcal{F}_{\mathfrak{n}}^{(L)}$.

For those cases, the ratio of correlation functions of Eq. (6.15) has non-negligible additive contributions from states other than $\mathfrak{n}$ of the form,

$$\varepsilon_{\mathfrak{m},\mathfrak{n}}(t) = \varepsilon_{\mathfrak{m},\mathfrak{n}}\, e^{(E_{\mathfrak{n}} - E_{\mathfrak{m}})t}\,, \tag{6.22}$$

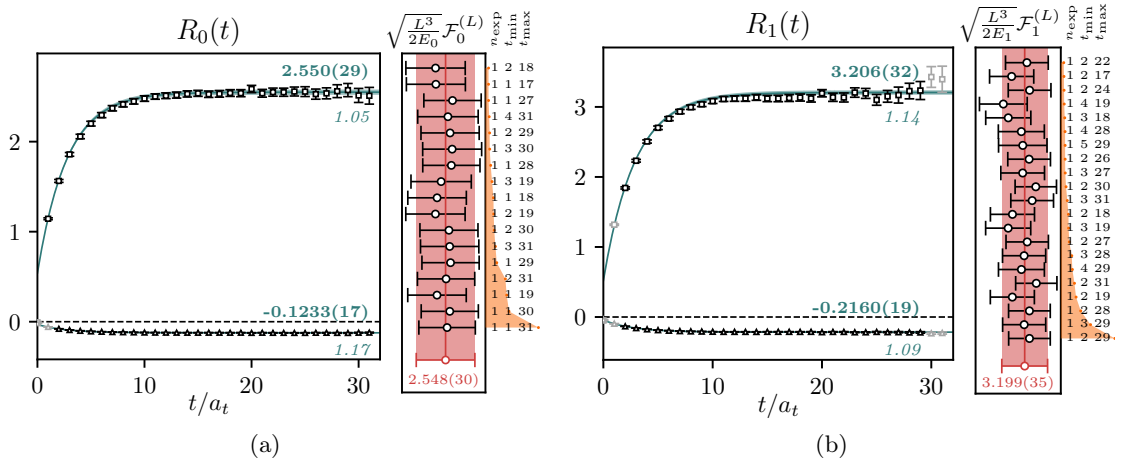

Figure 6.4: Time dependence of $R_{\mathfrak{n}}(t)$ defined in Eq. (6.6) for the two lowest discrete energy levels in the [111] A_1 irrep. Squares/triangles show data for the unimproved/improvement term currents (first and second terms in Eq. (2.23)). Curves show the timeslice description having largest AIC weight, with the constant fit value and the χ^2/N_{dof} of the fit also shown. Variations in the constant fit value over different timeslice fit windows are shown in the right column, together with the AIC weight (in orange), and the "model average" (in red).

where $\varepsilon_{\mathfrak{m},\mathfrak{n}} \propto \mathcal{F}_{\mathfrak{m}}^{(L)} \cdot \langle \mathfrak{m}|\Omega_{\mathfrak{n}}^{\dagger}(0)|0\rangle$, such that states lighter than $\mathfrak{n}$ will cause a *rising* time-dependence, visible at late times, that is not accounted for in our default timeslice fitting form.

Use of a GEVP solution at an appropriately large value of t_0 to form the optimized operators places some constraints on the scale of these late-time pollutions. The optimized correlation function matrix, $\langle 0|\Omega_{\mathfrak{m}}(t)\Omega_{\mathfrak{n}}^{\dagger}(0)|0\rangle$, is diagonal at $t = t_0$, and close to diagonal for timeslices close to t_0.[2] The two-point current correlation functions, $\langle 0|\mathcal{J}(t)\Omega_{\mathfrak{n}}^{\dagger}(0)|0\rangle$, are calculated on the same ensemble, and with the same time sources as the matrix of correlators used in the GEVP, leading to a significant correlation between the contributions $\varepsilon_{\mathfrak{m},\mathfrak{n}}(t)$ and the off-diagonal elements of the matrix of optimized correlators, suggesting that $\varepsilon_{\mathfrak{m},\mathfrak{n}}(t)$ will be also suppressed for timeslices around t_0 [3].

In this work, only the energy levels lying close to non-interacting $K\overline{K}$ energies and

[2] In practice this matrix is not *exactly* diagonal because the optimized operators are constructed with the ensemble averaged vectors $v_{\mathfrak{n}}$.

[3] Contributions from terms like Eq. (6.22) to $R_{\mathfrak{n}}(t)$ are not relevant for $t < t_0$, where pollution from states *higher* in energy come to dominate correlation functions.

having dominant overlap onto $K\overline{K}$-like operators, are found to have a production matrix element that is significantly smaller in magnitude than the matrix element for a lighter state, and hence where this 'late-time' pollution needs to be considered. For these levels, based upon the logic above, we restrict the time-windows for constant and constant-plus-exponential fit forms to more modest values of $t_{\rm max} \sim 1.5\, t_0$, thus excluding late-times where the pollution from lighter states begins to become significant. In practice, we only need to impose this fitting-window restriction explicitly for three states, the second excited energy level of each of the irreps $[100]\, A_1$, $[110]\, A_1$, and $[111]\, E_2$. Four other states lying close to non-interacting $K\overline{K}$ energies in other irreps show a modest late-time enhancement of the form suggested by Eq. (6.22), but the AIC weight favored fits with lower values of $t_{\rm max}$ anyway.

We present below an example case supporting the arguments presented above, in which we will reconstruct the time-dependence of correlation functions in terms of contributions of the form of Eq. (6.22). For convenience of presentation we will suppress kinematic factors not relevant to the illustration, by introducing unit-normalized optimized operators $\langle \mathfrak{n}|\Omega'^{\dagger}_{\mathfrak{m}}(0)|0\rangle = \delta_{\mathfrak{n},\mathfrak{m}}$, and the ratio

$$R'_{\mathfrak{n}}(t) \equiv \frac{\langle 0|\mathcal{J}(t)\, \Omega'^{\dagger}_{\mathfrak{n}}(0)|0\rangle}{\langle 0|\Omega'_{\mathfrak{n}}(t)\, \Omega'^{\dagger}_{\mathfrak{n}}(0)|0\rangle}\,, \tag{6.23}$$

with the constants $\mathfrak{f}^{(L)}_{\mathfrak{n}}$ describing the leading constant time-dependence of $R'_{\mathfrak{n}}(t)$.

Objects,

$$\widehat{\varepsilon}'_{\mathfrak{m},\mathfrak{n}}(t) \equiv \mathfrak{f}^{(L)}_{\mathfrak{m}} \frac{\langle 0|\Omega'_{\mathfrak{m}}(t)\Omega'^{\dagger}_{\mathfrak{n}}(0)|0\rangle}{\langle 0|\Omega'_{\mathfrak{n}}(t)\Omega'^{\dagger}_{\mathfrak{n}}(0)|0\rangle}\,, \tag{6.24}$$

are analogous to Eq. (6.22) for the ratio $R'_{\mathfrak{n}}(t)$, whenever $E_{\mathfrak{n}} > E_{\mathfrak{m}}$. It follows that we should be able to reconstruct the ratio $R'_{\mathfrak{n}}$ with the terms

$$\widehat{R}'_{\mathfrak{n}}(t) = \mathfrak{f}^{(L)}_{\mathfrak{n}} + \sum_{\mathfrak{m}<\mathfrak{n}} \widehat{\varepsilon}'_{\mathfrak{m},\mathfrak{n}}(t)\,, \tag{6.25}$$

and this will have the same time-dependence as $R'_{\mathfrak{n}}(t)$ for times after the small-time de-

caying excited state contributions have died out.

Comparisons between $R'_{\mathfrak{n}}(t)$ and $\widehat{R}'_{\mathfrak{n}}(t)$ for levels in the $[100]\,A_1$ irrep are shown in Fig. 6.5. The values of $\mathfrak{f}^{(L)}_{\mathfrak{m}}$ for $\mathfrak{m} < \mathfrak{n}$ needed in Eq. (6.24) are obtained serially from timeslice fits to the lower-lying energy level correlation functions. Level 2 meets our criteria for having non-negligible late-time pollution since its $\mathfrak{f}^{(L)}$ value is significantly smaller than the corresponding values for levels 0 and 1, with the value for level 1 being over ten times larger in absolute value. We see that while the contribution of lower-lying states to levels 1 and 3 is negligible, for level 2, the contribution of the nominally suppressed level 1 is observably large. We also see that restricting timeslice fits to values of $t_{\max} \lesssim 1.5t_0$ will reduce the impact of this pollution considerably.

The resulting values of $\mathcal{F}^{(L)}_{\mathfrak{n}}$ from timeslice fits for energy levels across all irreps considered are summarized in Fig. 6.6. The data is visibly enhanced near the resonance energy $a_t E^\star \sim 0.135$, while for higher energies it does not appear to have any simple energy dependence, with a strong dependence on the irrep of state $\mathfrak{n}$ being observed even for very similar values of $a_t E^\star_{\mathfrak{n}}$. This is as expected given the need for finite-volume corrections, which will be addressed in the next Chapter.

This Chapter described the extraction of finite-volume matrix elements. To extract the timelike form factors we need to perform the finite volume correction described in Sec. 2.1.1, which will be done in the next Chapter.

The rest of the kinematic points $Q^2 \neq 0$ for the spacelike form factor are calculated following the methods described in Secs. 6.1 and 6.3. We will show the resulting values of the spacelike form factor in Chapter 8, once we have performed the finite volume correction to the production matrix elements.

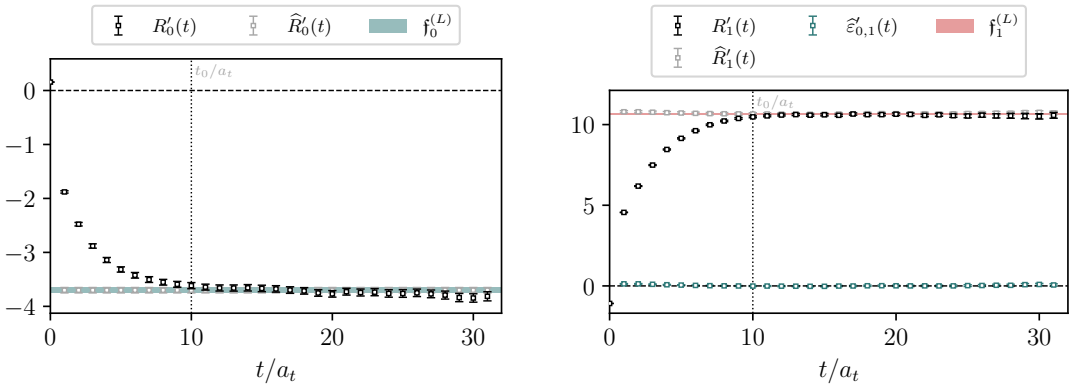

(a) Level 0.

(b) Level 1.

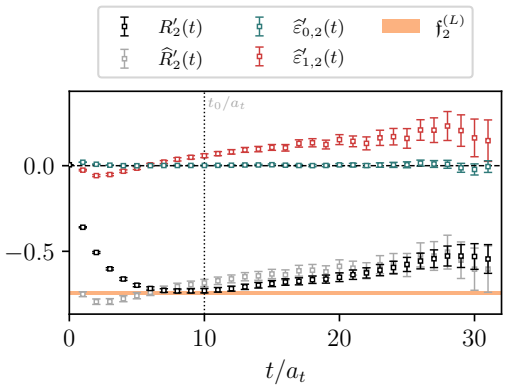

(c) Level 2.

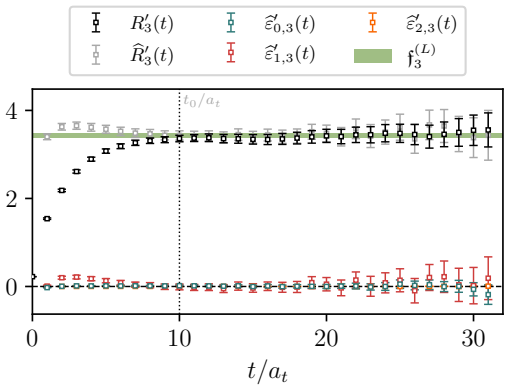

(d) Level 3.

Figure 6.5: Ratio of two-point correlators $R'_{\mathfrak{n}}(t)$ (unimproved current) for discrete states in the [100] A_1 irrep compared with the extracted constants $\mathfrak{f}_{\mathfrak{n}}^{(L)}$, the expected contributions from lower energy levels, $\widehat{\varepsilon}'_{\mathfrak{m},\mathfrak{n}}(t)$, and the sum of all contributions, $\widehat{R}'_{\mathfrak{n}}(t)$.

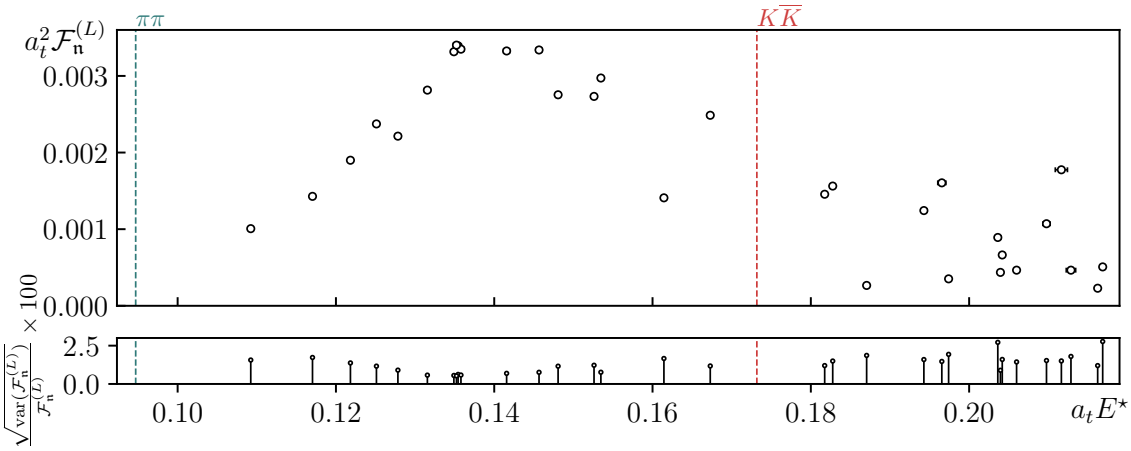

Figure 6.6: Finite volume form factor in the $\pi\pi$ elastic region and above the $K\overline{K}$ threshold. The fractional statistical uncertainties for the form factor values are shown in the bottom panel.

Chapter 7

Finite-volume correction of the production amplitudes

In this section we will implement the technology described in Sec. 2.1.1 regarding the finite-volume correction of matrix elements for states in the two-meson sector. The finite-volume correction factors are influenced by both the scattering dynamics in $\mathcal{M}$ and the kinematics of the geometric function F which encodes the finite-volume effects. We will present two alternative prescriptions to perform the finite volume correction. From one of these we find a quantitative description of the flavor content of each finite volume energy level, while the other prescription proves more practical for the extraction of infinite volume amplitudes. We used the latter prescription to extract the form factors to be presented in Chapter 8. We close this chapter by discussing the error propagation going into the finite-volume correction factors, which dominate the error budget of the infinite volume form factors.

7.1 Finite-volume correction of the timelike form factors

We consider here the timelike form factor amplitude of Eq. (1.38), with the decomposition given by Eq. (1.40). We use the decomposition of the finite-volume matrix element given by Eq. (6.13), to rewrite Eq. (2.3) in terms of the finite volume form factor and the smooth

functions $\mathcal{F}_a$,

$$\mathcal{F}_{\mathfrak{n}}^{(L)} = \sum\nolimits_a \sqrt{\tfrac{2E_{\mathfrak{n}}^{\star}}{-\mu_0'^{\star}}}\,(\mathbf{w}_0)_a \tfrac{1}{k_a^{\star}}\,\mathcal{F}_a\big(s = E_{\mathfrak{n}}^{\star 2}\big)\,, \tag{7.1}$$

$$= \sum\nolimits_a \tilde{r}_{\mathfrak{n},a}(L)\,\mathcal{F}_a\big(s = E_{\mathfrak{n}}^{\star 2}\big)\,, \tag{7.2}$$

where we have introduced the finite volume correction in terms of the factor $\tilde{r}_{\mathfrak{n},a}(L)$, which we also call the LL factor, although it is different, but closely related, to the quantity $\widetilde{\mathcal{R}}$, introduced in Eq. (2.5). The factor $\tilde{r}_{\mathfrak{n},a}(L)$ implements one power of relative momentum, stemming from the P-wave nature of the production.

Equation (7.2) allows us to relate the finite volume form factors to the infinite volume smooth functions for the energy values of the finite volume spectra. The LL factors $\tilde{r}_{\mathfrak{n},a}(L)$ can be calculated with Eq. (2.6) employing the scattering amplitude $\mathcal{M}(s)$, which was determined in Chapter 5. As we will see, all the terms in Eq. (7.2) are real, because the complex phases associated with the rescattering effects of the infinite volume amplitudes are canceled by the finite volume correction $\widetilde{\mathcal{R}}$. When writing Eq. (7.2) we have chosen to restate Eq. (2.3) in a form where these cancellations have been explicitly implemented.

In the case of *elastic* scattering, Eq.(7.2) features only one term in the summation, meaning that we can trivially invert it to obtain the value of the infinite volume amplitude at $s = E_{\mathfrak{n}}^{\star 2}$. In the context of a coupled-channel system, this will no longer be feasible. Instead, we can parameterize the energy dependence of the smooth functions $\mathcal{F}_a$ and, by considering multiple levels, perform a fit to constrain the infinite volume form factors.

To compute the LL factors, $\tilde{r}_{\mathfrak{n},a}(L)$, we employ the parameterizations of the scattering amplitude described in Chapter 5. At every solution of the quantization condition, Eq. (2.2), we eigendecompose the matrix $\mathbb{M} = \mathcal{M}^{-1} + F$ to find the vector $\mathbf{w}_0$ associated with the vanishing eigenvalue. Because the matrix $\mathbb{M}$ is symmetric, $\mathbb{M}^{\intercal} = \mathbb{M}$, the eigenvectors are normalized by demanding that $\mathbf{w}_0^{\intercal}\mathbf{w}_0 = 1$. Then we calculate the slope using

finite differences and projecting to the subspace of the vanishing eigenvector,

$$\mu_0'^{\star} = \frac{1}{2\,\Delta E}\,\mathbf{w}_0^{\intercal}\cdot\left(\left[\mathcal{M}^{-1}+F\right]_{E_{\mathfrak{n}}^{\star}+\Delta E} - \left[\mathcal{M}^{-1}+F\right]_{E_{\mathfrak{n}}^{\star}-\Delta E}\right)\cdot\mathbf{w}_0\,. \tag{7.3}$$

We then combine the slope and the eigenvectors to compute the LL factor

$$\tilde{r}_{\mathfrak{n},a}(L) = \sqrt{\frac{2E_{\mathfrak{n}}^{\star}}{-\mu_0'^{\star}}}\,\frac{(\mathbf{w}_0)_a}{k_a^{\star}}\,. \tag{7.4}$$

The uncertainties associated with the scattering amplitude are propagated into $\tilde{r}_{\mathfrak{n},a}(L)$ using jackknife via the ensemble of the scattering matrix parameter values. The covariance among different values of $\tilde{r}_{\mathfrak{n},a}$ need to have a special prescription, as described in Sec. 7.4.

As shown in Appendix B of Ref. [85], in the case that $\mathcal{M}(s)$ features a *narrow resonance*, for energies near to the resonance mass, the finite-volume correction factor becomes volume-independent and has elements proportional to the coupling of the resonance to each channel, a,

$$\tilde{r}_{\mathfrak{n},a}(L) \approx \sqrt{16\pi}\,\frac{c_a}{k_a^{\star}} + \mathcal{O}\left(\tfrac{\Gamma_R}{m_R}\right)\,. \tag{7.5}$$

This reflects the dominance in the scattering at these energies of a spatially localized state whose wavefunction does not sample the boundary of the finite-volume. At energies where $\mathcal{M}$ describes *weak* scattering and the solutions to Eq. (2.2) lie close to non-interacting meson-pair energies, the value of $\tilde{r}_{\mathfrak{n},a}(L)$ is set largely by properties of the geometric matrix $F(E,\mathbf{P},L)$ related to how the meson-pair relative momentum directions subduce into the irrep under consideration. We present the calculation of the finite-volume corrections in the case of a non-interacting system in App. D, with a few examples for a system of identical scalars in an S-wave and a P-wave. Between these two extremes the finite-volume correction factor is sensitive to both $\mathcal{M}$ and $F(E,\mathbf{P},L)$.

7.2 Elastic finite-volume correction

When we consider elastic scattering in a single partial-wave the matrix $\mathbb{M}$ has a single entry, and $\tilde{r}_{\mathfrak{n},a}(L)$ has one component. In that case Eq. (7.2) simplifies, and we can directly relate the finite volume form factors to the timelike form factor of the pion,

$$f_\pi(s) = \frac{\mathcal{M}_{\pi\pi,\pi\pi}(s)}{k^{\star 2}_{\pi\pi}} \frac{\mathcal{F}^{(L)}_{\mathfrak{n}}}{\tilde{r}_{\mathfrak{n}}(L)}\,, \tag{7.6}$$

where $s = E^{\star 2}_{\mathfrak{n}}$, and for convenience we drop the channel index from $\tilde{r}_{\mathfrak{n}}(L)$. We can also relate the smooth function of Eq. (1.41) to the finite volume form factor

$$\mathcal{F}(s) = \frac{\mathcal{F}^{(L)}_{\mathfrak{n}}}{\tilde{r}_{\mathfrak{n}}(L)}\,. \tag{7.7}$$

In Fig 7.1 we present values of $\tilde{r}_{\mathfrak{n}}(L)$ for the 17 energy levels below $K\overline{K}$ threshold, computed using the *reference elastic* amplitude of Eq. (5.6). For comparison we also show the value of $\sqrt{16\pi}\hat{c}_{\pi\pi}$ computed from the reference elastic amplitude, and given in Eq. (5.8). We observe that the value of $\tilde{r}_{\mathfrak{n}}$ for the energy levels close to $a_t E^\star \sim 0.135$ almost saturates to $\sqrt{16\pi}\hat{c}_{\pi\pi}$, as expected from the presence of a narrow resonance.

Different values of $\tilde{r}_{\mathfrak{n}}$ are observed for the two highest levels presented, each with $\mathbf{P} = [111]$, lying close to the $\pi_{110}\pi_{100}$ non-interacting energy at $a_t E^\star_{\text{n.i.}} \approx 0.16$. These values reflect the difference between a nearly non-interacting helicity 0 $\pi\pi$ state subduced into the A_1 irrep, and helicity ± 1 states subduced into E_2, and the same pattern of magnitudes can be observed in the lattice QCD computed matrix elements for the corresponding states in Fig 6.6.

7.3 Finite-volume correction for a coupled-channel system

Here we are interested in the coupled-channel system of $\pi\pi$ and $K\overline{K}$ in a P-wave, where $\mathbb{M}$ becomes a 2×2 matrix, and $\tilde{r}_{\mathfrak{n},a}(L)$ has two components. Above the $K\overline{K}$ threshold,

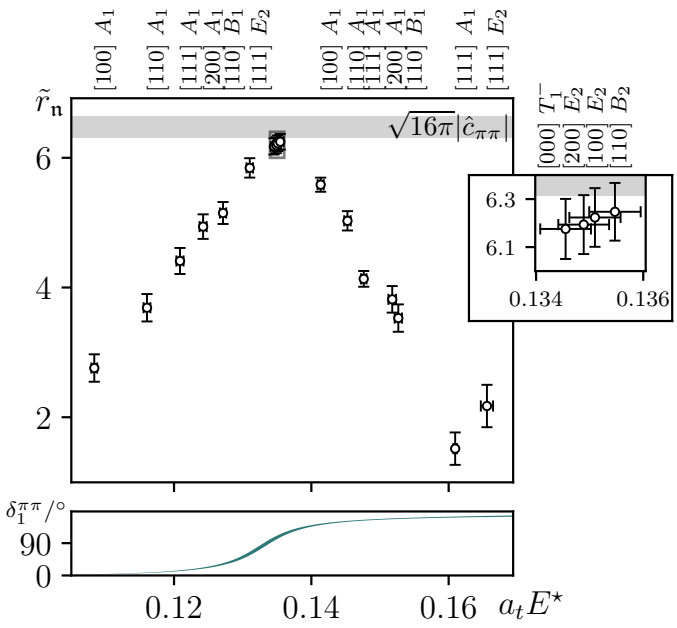

Figure 7.1: Elastic $\pi\pi$ finite-volume factors, $\tilde{r}_{\mathfrak{n}}$ computed using the *reference elastic* scattering amplitude parameterization.

the matrix $\mathbb{M}$ is real and symmetric, and the components of $\mathbf{w}_0$ are real. Above $\pi\pi$ threshold, but below $K\overline{K}$ threshold $\mathbb{M}$ is no longer real, and the presence of $\ell = 1$ angular momentum barrier factors in $\mathcal{M}$ and F causes $(\mathbf{w}_0)_a \propto k_a^\star$ such that kinematically closed channels become imaginary components of the vector. In the computation of $\tilde{r}_{\mathfrak{n}}$, this phase is cancelled by the explicit factor of $1/k_a^\star$ in Eq. (7.4), yielding a real valued correction vector (see also the discussion in Appendix A of Ref. [79]).

Explicit values of $\tilde{r}_{\mathfrak{n},a=\pi\pi,K\overline{K}}$ are shown in Fig. 7.2, computed using the *reference coupled-channel* amplitude parameterization, Eq. (5.10), which successfully described the finite-volume spectra presented in Section 5.2.2. Levels below $K\overline{K}$ threshold have values of $\tilde{r}_{\mathfrak{n},\pi\pi}$ in close agreement with the values computed using the *reference elastic* amplitude, as presented in Fig 7.1. The corresponding $K\overline{K}$ components are observed to be quite uncertain, as expected given the lack of constraint on $K\overline{K}$ well below its kinematic threshold[1]. Above $K\overline{K}$ threshold, the $\pi\pi, K\overline{K}$ components are of similar magnitude – that the $K\overline{K}$ components do not obviously dominate for levels lying close to $K\overline{K}$ non-interacting

[1]See Appendix A1 of Ref. [79] for a discussion of closed channels within this formalism.

energies is a result of having already extracted a factor of the scattering matrix, $\mathcal{M}$, from the quantity being finite-volume corrected, see Eq. (2.6).

We add the values of the couplings $\sqrt{16\pi}|\hat{c}_a|$ from Eq. (5.13) as an inset in Fig. 7.2, to compare to the value of the finite volume correction $\tilde{r}_{\mathfrak{n},a}(L)$. In the plots we draw an orange horizontal band around the mass of the ρ-meson resonance, $m_R \pm \Gamma_R/2$, to identify the energy levels for which we expect the relation of Eq. (7.5) to approximately hold. We indeed find that for the levels inside and close to the band, the histograms of $\tilde{r}_{\mathfrak{n},a}$ are approximately equal to those of $\sqrt{16\pi}|\hat{c}_a|$.

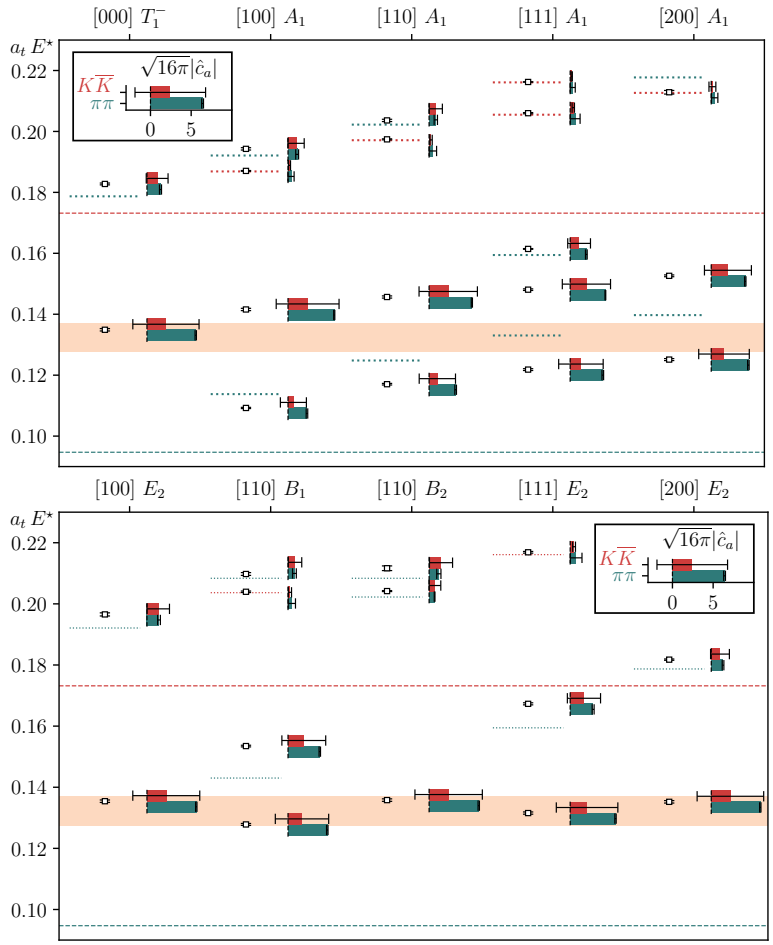

Figure 7.2: Histograms for each energy level show the magnitudes of finite-volume factors, $\left|\tilde{r}_{\mathfrak{n},a}\right|$, for $a = \pi\pi$ (blue bar) and $a = K\overline{K}$ (red bar) computed using the *reference coupled-channel* scattering amplitude. Non-interacting $\pi\pi$ (blue) and $K\overline{K}$(red) energies are indicated by the horizontal dotted lines.

7.3.1 Flavor content of the finite-volume levels

As mentioned before, the prescription chosen to express the finite volume correction given by Eq. (7.2) results from extracting a factor of the scattering matrix from the finite volume correction, to cancel the phases resulting from the rescattering after the production of the two-meson system. However, as seen from Fig. 7.2, this choice effectively causes the finite volume correction to have sizeable components for both channels, even far below the threshold of $K\overline{K}$.

This does not pose a contradiction to the expectation that closed channels have exponentially suppressed effects on finite volume energies and matrix elements. In fact, as shown in Appendix A1 of Ref. [79], the LL factors below $K\overline{K}$ threshold have a volume-independent ratio,

$$\frac{\tilde{r}_{\mathfrak{n},K\overline{K}}(L)}{\tilde{r}_{\mathfrak{n},\pi\pi}(L)} = \frac{k^{\star}_{\pi\pi}\,\mathcal{M}_{\pi\pi,K\overline{K}}}{k^{\star}_{K\overline{K}}\,\mathcal{M}_{\pi\pi,\pi\pi}} + \dots\,, \tag{7.8}$$

where we neglect corrections that get suppressed exponentially as the energy $E^{\star}_{\mathfrak{n}}$ decreases away from the $K\overline{K}$ threshold. We use this relation to rewrite Eq. (7.2) in the elastic energy region,

$$\mathcal{F}^{(L)}_{\mathfrak{n}} = \tilde{r}_{\mathfrak{n},\pi\pi}(L)\left(\mathcal{F}_{\pi\pi} + \frac{k^{\star}_{\pi\pi}\mathcal{M}_{\pi\pi,K\overline{K}}}{k^{\star}_{K\overline{K}}\mathcal{M}_{\pi\pi,\pi\pi}}\mathcal{F}_{K\overline{K}}\right) + \dots\,, \tag{7.9}$$

where the factor in parenthesis is the same factor appearing in Eq. (1.40),

$$f_{\pi} = \frac{\mathcal{M}_{\pi\pi,\pi\pi}}{k^{\star 2}_{\pi\pi}}\left(\mathcal{F}_{\pi\pi} + \frac{k^{\star}_{\pi\pi}\mathcal{M}_{\pi\pi,K\overline{K}}}{k^{\star}_{K\overline{K}}\mathcal{M}_{\pi\pi,\pi\pi}}\mathcal{F}_{K\overline{K}}\right), \tag{7.10}$$

and we recover the expression for the elastic finite volume correction of Eq. (7.6) which did not take into consideration the contributions from the $K\overline{K}$ channel.

To illustrate the independence of the finite volume matrix elements from the $K\overline{K}$ channel below its threshold, as well as the contribution of each channel to the finite volume matrix above the $K\overline{K}$ threshold, we compute the vectors $\mathbf{v}_0$ defined in Eq. (2.5). The finite

volume form factor in terms of the vectors $\mathbf{v}_0$ is given by

$$\mathcal{F}_{\mathfrak{n}}^{(L)} = \sqrt{\frac{2E_{\mathfrak{n}}^{\star}}{\lambda_0'^{\star}}} \sum\nolimits_a (\mathbf{v}_0)_a \, k_a^{\star} \, f_a(s) \,, \tag{7.11}$$

where $\lambda_0'^{\star}$ is defined in Eq. (2.5). In this case the components of $\mathbf{v}_0$ directly weigh the contribution of each of the timelike form factors f_a. In Fig. 7.3 we show the absolute value of each of the components $|(\mathbf{v}_0)_a|$ as a percentage of the sum $|(\mathbf{v}_0)_{\pi\pi}| + \left|(\mathbf{v}_0)_{K\overline{K}}\right|$, for all the energy levels considered in this work. The blue area represents the $\pi\pi$ component, while the red area is the $K\overline{K}$ component. This prescription makes explicit the fact that the finite volume form factors below $K\overline{K}$ threshold are mostly independent of the timelike form factor of the kaon, as can be noted from all the pie charts in the elastic energy region being almost entirely blue.

Above the $K\overline{K}$ threshold, we observe that the dominant component of the vector $\mathbf{v}_0$ always corresponds to the flavor of the closest non-interacting energy. This matches the expected behavior of a weakly interacting coupled channel, where each energy level can be approximately identified to a specific channel. In this case we can identify seven finite volume levels with dominant flavor contribution from the $K\overline{K}$ channel. The determination of the kaon timelike form factor in Chapter 8 will be largely constrained by these seven finite volume form factors.

To close this section we emphasize that we will use Eq. (7.2) to determine the infinite volume amplitudes in Chapter 8, and that we only employed Eq. (7.11) in this section to illustrate the contribution from each infinite-volume timelike form factor to the finite volume form factors.

7.4 Correlation among the LL factors

So far we have employed jackknife resampling to propagate statistical uncertainties. However, we find that some extra care is needed when applying this technique to calculate the

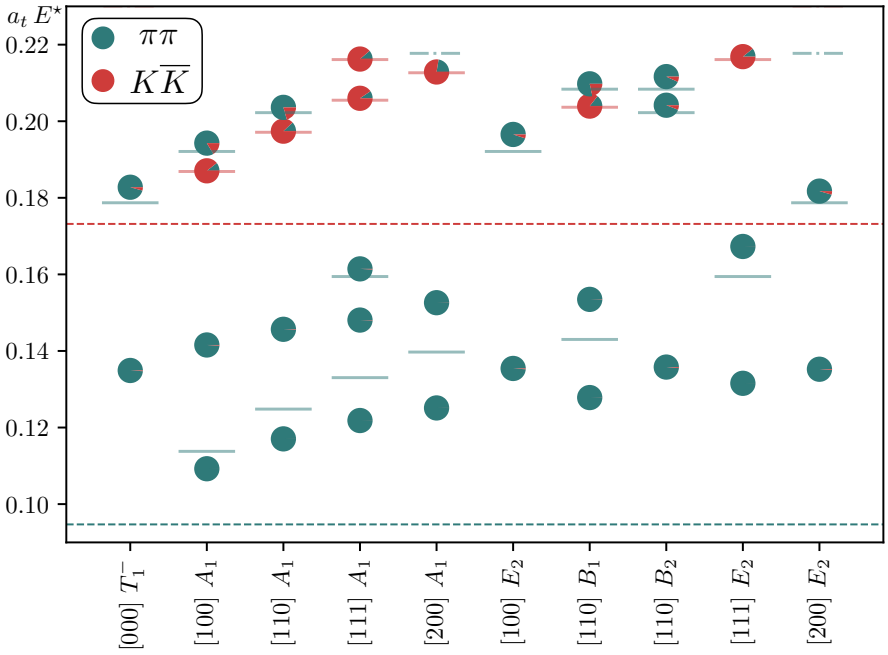

Figure 7.3: Absolute value of the components of the finite-volume correction vector $|(\mathbf{v}_0)_a|$, illustrated as percentages of $|(\mathbf{v}_0)_{\pi\pi}| + |(\mathbf{v}_0)_{K\overline{K}}|$, for $a = \pi\pi$ (blue section) and $a = K\overline{K}$ (red section) computed using the *reference coupled-channel* scattering amplitude. The horizontal lines identify the non-interacting energies of this volume, with the same color coding as before, dot-dashed lines indicate non-interacting energies where the associated operator was not included in the variational basis.

covariance of the LL factors. We will show why this is the case by describing the determination of the smooth function $\mathcal{F}(s)$ with Eq. (7.7) when applying the jackknife resampling as described in Sec. 2.2.6.1.

We calculate $\tilde{r}_{\mathfrak{n}}(L)$ with Eqs. (7.3) and (7.4) in the elastic approximation by employing the parameterization of the reference elastic scattering amplitude of Eq. (5.6). Jackknife ensembles for each of the parameters of the scattering amplitude parameterization were obtained when fitting the amplitude to the lattice spectra. To propagate the error further to the LL factors we compute $\tilde{r}_{\mathfrak{n}}(L)$ over jackknife.

Once we have calculated $\tilde{r}_{\mathfrak{n}}(L)$, the $\mathcal{F}(s)$ data is obtained with Eq. (7.7), combining the LL factor and the finite volume form factor again with jackknife. We expect to be able to describe this data with a smooth function of s over the elastic energy region, e.g. a low-order polynomial in s, given that it does not have a right hand cut, as described in

Sec. 1.5.2. Furthermore, a parameterization of $\mathcal{F}(s)$ is necessary if we want to extrapolate the function into the complex s-plane to determine properties of the ρ-meson resonance defined at the pole.

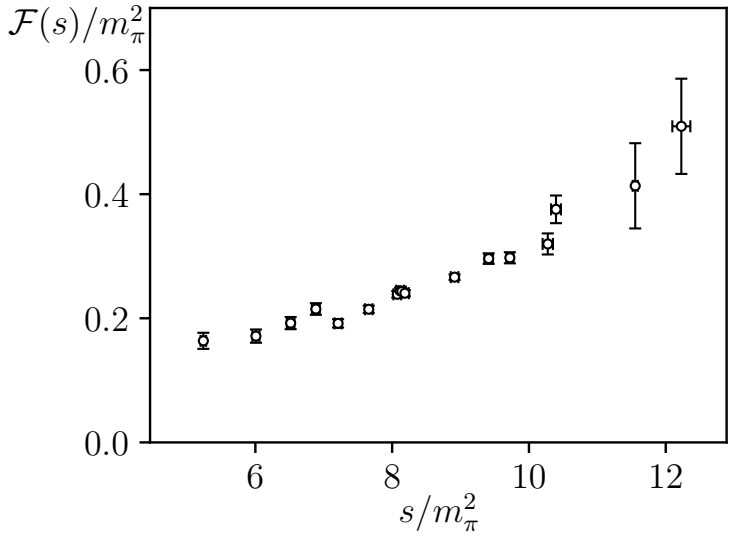

Figure 7.4: Values of $\mathcal{F}(s)$ determined from the finite volume correction of $\mathcal{F}_{\mathfrak{n}}^{(L)}$ according to Eq. (7.7).

We show the values of $\mathcal{F}(s)$ derived from Eq. (7.7) in the elastic energy region in Fig. 7.4. We observe that the data appears to increase smoothly with s, in contrast to the finite volume form factor $\mathcal{F}_{\mathfrak{n}}^{(L)}$, which showed an enhancement close to the resonance mass, and a significant variation between the two data points close to $a_t E^\star = 0.16$, see Fig. 6.6.

However, when performing a correlated fit to the $\mathcal{F}(s)$ data in Fig. 7.4 with a low-order polynomial in s, we generically get as a result a function that systematically underestimates most of the data points, and has values of $\chi^2/N_{\text{dof}} \gg 1$. This type of behavior is typical of data suffering the D'Agostini bias [95], which arises whenever there is a high degree of correlation among different data points. Upon close inspection we find that the culprit of this behavior are indeed the correlations among the different $\mathcal{F}(s)$ data, given by the off-diagonal elements of the matrix $\mathbb{C}[\mathcal{F}(s)]$, which has diagonal elements equal to one.[2]

[2]The matrix $\mathbb{C}[X]$ for the dataset $\{X_{\mathfrak{n}}\}$ has elements equal to the covariance among data points divided by their standard deviation, i.e. $\mathbb{C}[\mathcal{X}]_{\mathfrak{nm}} = \text{cov}(X_{\mathfrak{n}}, X_{\mathfrak{n}})/(\sigma_{X_{\mathfrak{n}}}\sigma_{X_{\mathfrak{m}}})$.

This matrix is inverted when we calculate the χ^2 function of the correlated fit.

The eigenvalues of the matrix $\mathbb{C}[\mathcal{F}(s)]$ have a different qualitative behavior than those of the correlation matrix $\mathbb{C}[\mathcal{F}_{\mathfrak{n}}^{(L)}]$, i.e. among the $\mathcal{F}_{\mathfrak{n}}^{(L)}$ data. In the latter case we find that when we order them by magnitude, the eigenvalues slowly decrease, and the correlation matrix has a condition number[3] of order $\sim 10^2$ for the 17 elastic energy levels. In the former case, the eigenvalues dramatically drop in value after the first two, and the condition number of the matrix is of order $\sim 10^4$. Finally, when we check the eigenvalues of the correlation matrix $\mathbb{C}[\tilde{r}_{\mathfrak{n}}(L)]$ among the LL factors, we find again that they dramatically decrease after the first two, and the condition number of the matrix is of order $\sim 10^{12}$, with at least half of the lowest eigenvalues being 10^{-11} times smaller than the largest eigenvalue.

That this is the case should not be a surprise, because jackknife ensembles of $\tilde{r}_{\mathfrak{n}}(L)$, to first order in the errors of the scattering parameters, can only fluctuate in the ensemble subspace spanned by the ensembles of the small set of scattering parameters, which explains that only a couple of eigenvalues of $\mathbb{C}[\tilde{r}_{\mathfrak{n}}(L)]$ are non-negligible.

This effect is quite significant when we perform fits to the $\mathcal{F}(s)$ data because the fractional uncertainty of the LL factors is greater than the fractional uncertainty of $\mathcal{F}_{\mathfrak{n}}^{(L)}$, see Figs. 6.6 and 7.1. This ends up generating jackknife ensembles for $\mathcal{F}(s)$ with an artificially high correlation among each other that do not reflect the magnitude of correlations among the original input data, i.e. the discrete finite-volume energy levels and the matrix elements. We illustrate this by showing in Fig. 7.5 the correlation matrix of the energy levels $\mathbb{C}(E_{\mathfrak{n}}^{\star})$, which has a condition number ≈ 25.

In place of the data correlation for $\tilde{r}_{\mathfrak{n}}(L)$ computed using the amplitude parameterization, we adopt one which inherits the energy-level correlation, with the following motivation. In a linearised approximation to error propagation, if the Jacobian were known, we

[3]The condition number of a symmetric matrix is given by ratio of its largest eigenvalue to the smallest eigenvalue.

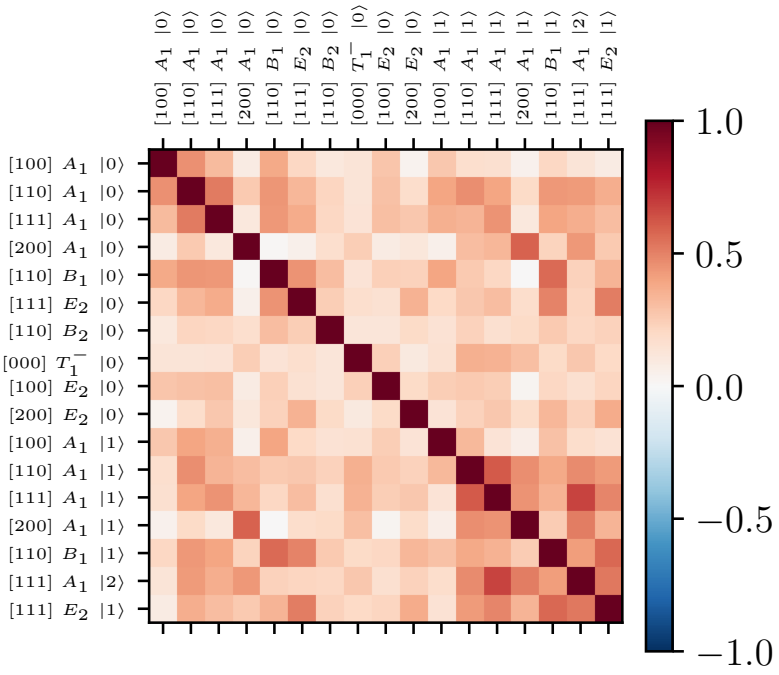

Figure 7.5: Data correlation matrix for the energy-level values, $\mathbb{C}[E_\mathfrak{n}^\star]$, with rows and columns ordered by increasing energy from left to right, and from top to bottom, respectively.

would calculate the covariance among $\tilde{r}_\mathfrak{n}(L)$ values using

$$\mathrm{cov}(\tilde{r}_\mathfrak{n}, \tilde{r}_\mathfrak{m}) = \sum\nolimits_{\mathfrak{n}'\mathfrak{m}'} \frac{\partial \tilde{r}_\mathfrak{n}}{\partial E^\star_{\mathfrak{n}'}} \,\mathrm{cov}(E^\star_{\mathfrak{n}'}, E^\star_{\mathfrak{m}'})\, \frac{\partial \tilde{r}_\mathfrak{m}}{\partial E^\star_{\mathfrak{m}'}} \,. \tag{7.12}$$

However, to a good approximation, we expect the finite-volume correlation factor computed with Eqs. (7.3) and (7.4) to be influenced predominantly by the *local* behavior of $\mathcal{M}$ and F around $E^\star_\mathfrak{n}$. This would imply that the Jacobian between $\{\tilde{r}_\mathfrak{n}(L)\}$ and the energies, $\{E^\star_{\mathfrak{n}'}\}$, is largely dominated by the diagonal elements, $\mathfrak{n} = \mathfrak{n}'$.

For instance, in an ideal scenario, where the lattice spectrum was determined for a large number of closely spaced volumes, L, and multiple lattice irreps, Λ, we would have access to a high density of states per energy unit. From this spectrum we could determine the scattering amplitude $\mathcal{M}(E^{\star 2}_\mathfrak{n})$ algebraically at a similarly high density, and in that case, the calculation of $\tilde{r}_\mathfrak{n}(L)$ would not require an explicit parameterization of $\mathcal{M}$, and

the uncertainty of each finite-volume correction factor would only be correlated to the uncertainty of the *nearby* energy levels.

Based on this observation, we approximate the Jacobian of Eq. (7.12) by a diagonal matrix $\frac{\partial \tilde{r}_{\mathfrak{n}}}{\partial E^{\star}_{\mathfrak{n}'}} \propto \delta_{\mathfrak{n},\mathfrak{n}'}$. In practice, we implement this procedure by shifting and reweighing the jackknife ensemble of each energy level to match the mean and error of the respective finite-volume correction factor according to the values computed using the parameterization of $\mathcal{M}$ and Eqs. (7.3), (7.4). With this prescription it is not necessary to compute the magnitude of the Jacobian elements, however we still require knowledge of their sign. These are extracted from the correlation between the 'model' energy, i.e. the solution of Eq. (2.2), and $\tilde{r}_{\mathfrak{n}}(L)$, both extracted from a parameterization of $\mathcal{M}$,[4] these are shown on the top row of Fig. 7.6.

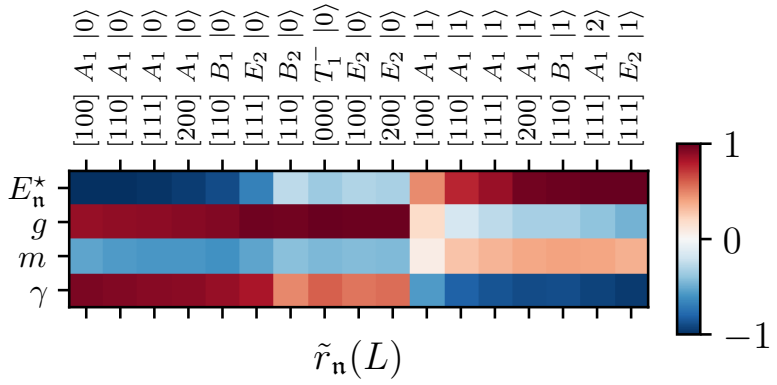

Figure 7.6: Data correlation between $\tilde{r}_{\mathfrak{n}}$ and the respective Lüscher energy solution $E^{\star}_{\mathfrak{n}}$, as well as the scattering parameters in the *reference elastic* parameterization. Here the ordering of states around the ρ-resonance is slightly different than in Fig. 7.1 because in that case the x-axis corresponds to the value of the Lüscher energy solution from the elastic reference amplitude, and in this case we employ the ordering of Fig. 7.5 which uses the spectra extracted from the lattice.

An exception to this behavior are those levels with energies very close to the resonance mass, i.e. the four levels in the inset of Fig. 7.1. As mentioned before, the value of $\tilde{r}_{\mathfrak{n}}(L)$ for these levels is equal to the resonance coupling, modulo rather small finite-width corrections, and we observe that for these levels $\tilde{r}_{\mathfrak{n}}(L)$ is mostly uncorrelated with the respective energy

[4]Support for this prescription is found empirically in the fact that the absolute value of this correlation value is consistent with 1 for most energy levels.

value. This is illustrated in Fig. 7.6, where we see that their strongest correlation (for the *reference elastic* parameterization) is with the g parameter. From the spectra of Fig. 5.3 we note that these levels are the farthest from any non-interacting energy level, and as such they are the least sensitive to finite-volume effects.

To account for this observation, for these levels we adopt a modified procedure, where instead of using only the energy level data, we add a linear combination of the fluctuations on the scattering parameters, with the parameter g having the highest contribution. For $\tilde{r}_{\mathfrak{n}}(L)$ for 'on-resonance' levels, we form a linear combination of the ensembles of the scattering parameters and the corresponding energy level,

$$\vec{\tilde{r}}_{\mathfrak{n}}(L) = x_E\, \vec{E}^{\star}_{\mathfrak{n}} + x_g\, \vec{g} + x_m\, \vec{m} + x_\gamma\, \vec{\gamma} = \sum\nolimits_i x_i\, \vec{p}_i. \tag{7.13}$$

where we use the vector notation $\vec{p}_i$ to emphasize that we are manipulating the quantity p_i in the jackknife ensemble space. The quantities $\vec{p}_i$ have been previously shifted and reweighted, so that they have zero mean and unit covariance, i.e. $\langle \vec{p}_i \rangle = 0$ and $\langle \vec{p}_i{}^2 \rangle = 1$.

To obtain the coefficients x_i we demand that the covariance between the generated $\vec{\tilde{r}}_{\mathfrak{n}}$ ensemble and each of the $\vec{p}_i$ quantities reproduces the covariance $\mathrm{cov}(\vec{p}_i, \vec{\tilde{r}}_{\mathfrak{n}}(L))$ shown in Fig. 7.6. Mathematically, this translates into the system of equations

$$\sum\nolimits_j \langle \vec{p}_i\, \vec{p}_j \rangle\, x_j = \mathrm{corr}(p_i, \tilde{r}_{\mathfrak{n}}(L))\,, \tag{7.14}$$

where the matrix $\langle \vec{p}_i\, \vec{p}_j \rangle$ is calculated using the corresponding lattice energy level and the scattering parameters. Equation (7.14) represents a linear system of equations from which the coefficients x_i can be easily obtained. We find that the value of $\left\langle \vec{\tilde{r}}_{\mathfrak{n}}(L)^2 \right\rangle$ extracted in this way is equal to unity, providing a self-consistency check of this procedure. Finally, we reweight and shift $\vec{\tilde{r}}_{\mathfrak{n}}(L)$ to obtain a jackknife ensemble with the mean and error of $\tilde{r}_{\mathfrak{n}}(L)$.

It is not immediately obvious how to extend the procedure we just described from the

elastic analysis to the coupled channel case, given that multiple components $\tilde{r}_{\mathfrak{n},a}(L)$ are associated with each level. Furthermore, we need the correlation between the components of $\tilde{r}_{\mathfrak{n}}$ to reproduce the correlation between different elements of the scattering amplitude, see Eq. (7.8).

We instead choose to estimate the impact of the uncertainty of the finite-volume correction by means of a "systematic" covariance, $C^{\text{syst.}}$, applied to the finite-volume matrix elements $\mathcal{F}_{\mathfrak{n}}^{(L)}$. We add this systematic covariance matrix to the statistical covariance matrix of $\mathcal{F}_{\mathfrak{n}}^{(L)}$ to obtain a total covariance, which in turn is used in the χ^2 function minimized for the determination of the smooth functions $\mathcal{F}_a(s)$.

To calculate the magnitude of the diagonal elements of this covariance we first note that for levels below the $K\overline{K}$ threshold the component $\tilde{r}_{\mathfrak{n},K\overline{K}}$ cannot be precisely determined (by the nature of the finite-volume formalism). Therefore, we assign the relative uncertainty of the "relevant" $\tilde{r}_{\mathfrak{n},\pi\pi}$ as the systematic relative uncertainty of the corresponding $\mathcal{F}_{\mathfrak{n}}^{(L)}$. We note that following this procedure for the elastic analysis we obtain results consistent with the alternative procedure of replacing the correlation of the finite-volume correction factors by that of the energies and propagating the error over jackknife.

Above the $K\overline{K}$ threshold we have a weakly interacting system, where each state in the spectrum is close to a non-interacting energy. This allows us to unambiguously assign a dominant component $\tilde{r}_{\mathfrak{n},a}(L)$ to each level. Furthermore, following the expectations outlined about the correlation between the finite-volume correction factor and the energy value, we find that out of the two, this component is always the most correlated with the energy solution of the quantization condition. Once we picked the dominant component a, we again assign the relative uncertainty of $\tilde{r}_{\mathfrak{n},a}$ as the "systematic" relative uncertainty of the corresponding $\mathcal{F}_{\mathfrak{n}}^{(L)}$.

Finally, to obtain off-diagonal elements of $C^{\text{syst.}}$, showing the correlation of the finite-volume correction across the spectrum, we mimic the prescription used in the elastic analysis. This means that we will once again use the correlation matrix of the energy levels, or the appropriately constructed linear combinations for the levels close to the resonance.

This correlation matrix is multiplied by the magnitude of the diagonal elements determined above to obtain $C^{\text{syst.}}$.

We also explored an alternative procedure to determine the diagonal elements of $C^{\text{syst.}}$ to corroborate the consistency of our prescription. This second option was inspired by the iterative fit method described in Ref. [126]. In this case we use the value of the "model", $\sum_a \tilde{r}_{a,\mathfrak{n}}(L)\mathcal{F}_a(E_{\mathfrak{n}}^{\star 2})$, to multiply the relative uncertainty of the finite-volume correction factor and obtain an absolute systematic error for each diagonal element of $C^{\text{syst.}}$. In the first iteration we pick the solution from our previous prescription to determine $C^{\text{syst.}}$ and minimize the χ^2 with this systematic covariance. This yields new values for $\mathcal{F}_a(s)$, which are then used to recompute $C^{\text{syst.}}$ and repeat the minimization. We find that this process converges after a few iterations.

This concludes the description of the calculation of the LL factors. In the next chapter we will present the determination of the infinite volume form factors.

Chapter 8

Infinite volume amplitudes: the π and K vector-isovector form factors

In this chapter we will combine together the results of the previous three chapters to calculate the isovector-vector form factors of the pion and the kaon. In the case of the pion we can directly obtain the form factor in the spacelike region and the elastic timelike energy region, from the the individual finite volume matrix elements (once the appropriate finite volume correction has been performed). In the case of the analysis of the $\pi\pi/K\overline{K}$ as a coupled-channel system, we can only obtain a parameterization of their energy dependence by fitting the finite volume matrix elements with Eq. (7.2). Finally, we will utilize these form factors to determine electromagnetic properties of the ρ and the π mesons.

8.1 Pion form factor

We begin by presenting the data for the spacelike and timelike form factor over the elastic energy region. The spacelike data was obtained in Sec. 6.2 from the $R_{3\text{pt}}$ ratio of correlation functions and shown in Fig. 8.1a. The timelike data $\mathcal{F}(s)$, after the finite-volume correction was performed, was presented in Fig. 7.4. We employ Eq. (1.41), and the error propagation for the finite volume correction described in Sec. 7.4, to obtain the timelike form factor

data shown in Fig. 8.1b.

Alongside the data we show the Omnès factor, $\Omega(s)$, introduced in Sec. 1.5.2.1. The calculation of $\Omega(s)$ will be presented in Sec. 8.1.2, where we also analytically continue $\Omega(s)$ for $s < 0$. We clearly see that the bulk of the energy dependence is captured, both for the spacelike and the timelike data, with only a mild energy dependence needed in $\mathcal{F}_\Omega(s)$, to form f_π according to Eq. (1.45).

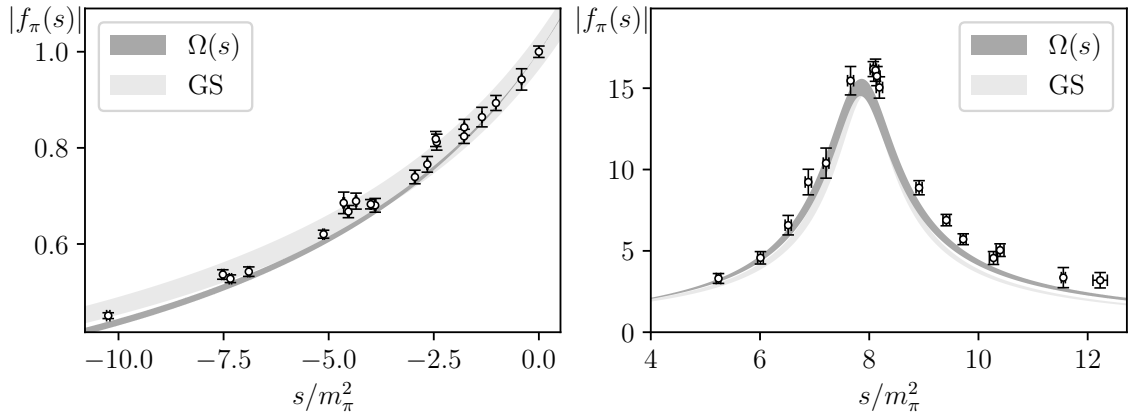

(a) Spacelike region.

(b) Timelike region.

Figure 8.1: Pion form factor in the (a) spacelike and (b) timelike elastic regions. Superimposed are the Omnès function calculated from the *reference elastic* amplitude, and the Gounaris-Sakurai (GS) form determined by describing the finite-volume spectra.

Also shown in these figures is a commonly-used parameterization known as the Gounaris-Sakurai (GS) form [122], which corresponds to a parameterization of the form of Eq. (1.41), where $\mathcal{F}$ is a constant determined by demanding $f_\pi(0) = 1$. The scattering amplitude $\mathcal{M}$ of the GS parameterization, given in Tab. 5.4, is an elastic K-matrix with a pole describing the ρ resonance, along with a pole-subtracted Chew-Mandelstam phase-space. The use of a dispersively improved phase-space removes the spurious singularity otherwise present at $s = 0$ and thus makes an extrapolation into the space-like region somewhat plausible.

8.1.1 Timelike elastic pion form factor

Over the energy region of elastic scattering between the $\pi\pi$ threshold and the $K\overline{K}$ threshold, $\mathcal{F}(s)$ can be parameterized using a low-order polynomial in s,

$$\mathcal{F}(s)/m_\pi^2 = \sum_{n=0} c_n \cdot \left(\frac{s - s_0}{s_0}\right)^n , \tag{8.1}$$

where we choose $\sqrt{s_0} = 0.135\, a_t^{-1} = 2.85\, m_\pi$, centering on the resonance peak, for convenience.

As seen in Fig. 8.2, fits linear or quadratic in s can capture the observed energy dependence, with the quadratic fit having parameters,

$$\begin{array}{lll} c_0 = & 0.2359\,(28) & \begin{bmatrix} 1 & -0.3 & -0.6 \\ & 1 & 0.7 \\ & & 1 \end{bmatrix} \\ c_1 = & 0.265\,(26) & \\ c_2 = & 0.20\,(7) & \end{array}$$

$$\chi^2/N_{\rm dof} = \tfrac{25.4}{17-3} = 1.82\,, \tag{8.2}$$

where parameter correlations are seen to not be excessive. The fit form does not impose any constraints regarding the value of f_π over the spacelike region, neither does it impose charge conservation $f_\pi(0) = 1$. This is because we do not expect the form factor parameterization of Eq. (1.41) to be reliable far below $\pi\pi$ threshold. We can improve on this fitting the data instead with a dispersive representation of f_π, to which we turn in the next Section.

8.1.2 Pion form factor across the spacelike and timelike regions

To describe *simultaneously* the timelike and spacelike pion form factor data related by crossing symmetry, see Figs. 1.2, we need to employ a functional form which is consistent with the analytic properties that f_π should satisfy on the complex s-plane over a wide s range. The Omnès function, introduced in Sec. 1.5.2.1, satisfies the properties of analyticity, crossing symmetry, and unitarity over over all the complex s-plane that f_π should satisfy if we assume that only elastic scattering is allowed.

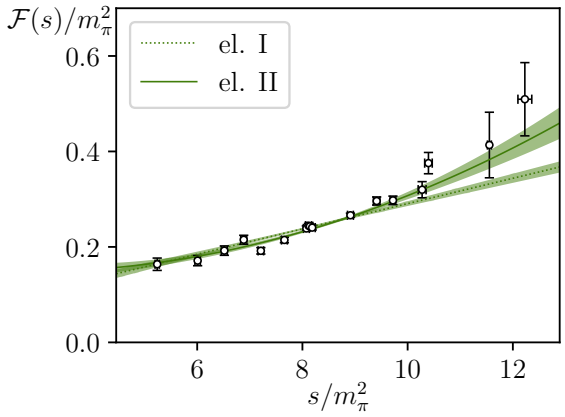

Figure 8.2: Polynomial descriptions of $\mathcal{F}(s)$ – linear in s (el. I) and quadratic in s (el. II).

To calculate Eq. (1.48), our *reference elastic* scattering amplitude provides an elastic phase-shift from $\pi\pi$ threshold up to $K\overline{K}$ threshold, and comparison with the *reference coupled-channel* amplitude shows that the $\pi\pi$ phase-shift continues as given by the parameterization to somewhat higher energies. In practice we will use this form in the integral defining $\Omega(s)$ in Eq. (1.48) up to $\sqrt{s_a} = 1.2 \cdot (2m_K)$, and at energies higher than this a simple parameterization,

$$\delta(s > s_a) = \pi - \big(\pi - \delta_{\rm ref}(s)\big)\frac{2}{1 + (s/s_a)^{3/4}}\,,$$

similar to the one proposed in Ref. [29].[1] In practice the Omnès factor at low energies, where we require it, is not particularly sensitive to the details of this continuation, owing to the subtraction suppressing the contribution of high energies in the integral.

The function $\mathcal{F}_\Omega(s)$ obtained by dividing the Omnès factor out from the timelike and spacelike form factor data can be parameterized and a description of the lattice data obtained. Describing all data simultaneously requires spanning a large energy region, and

[1]This form enforces an asymptotic return of the phase-shift to π, correcting for the threshold behavior built into the parameterization which ceases to be appropriate at high energies. In fact Ref. [29] used $\delta_{\rm ref}(s_a)$ in place of $\delta_{\rm ref}(s)$ in this expression but since the phase-shift of the *elastic reference* parameterization has almost reached its asymptotic value at $\sqrt{s_a} = 2.2 \cdot (2m_\pi)$, there is no practical difference between the two choices, and any small difference generated in $\Omega(s)$ can be absorbed into the smooth function $\mathcal{F}_\Omega(s)$.

it proves helpful to make use of a *conformal mapping* of s into a variable $z(s)$, defined as,

$$z(s) = \frac{\sqrt{s_c - s_0} - \sqrt{s_c - s}}{\sqrt{s_c - s_0} + \sqrt{s_c - s}}\,, \tag{8.3}$$

where this variable maps the entire complex plane of s, excluding the real s axis above s_c, into a unit disk in z centered so that $z(s_0) = 0$. Suitable choice of s_c can reflect the fact that we expect there to be cuts due to inelastic channels at higher energies, and s_0 can be selected to conveniently distribute the data to be fitted around $z = 0$. A polynomial in $z(s)$ will not have singularities, as desired, in the timelike elastic scattering region, or the spacelike region.

Writing a parameterization of $\mathcal{F}_\Omega(s)$ as a low-order polynomial in $z(s)$,

$$\mathcal{F}_\Omega(s) = Q + \sum_{n=1} d_n \cdot \left(z(s)^n - z(0)^n\right), \tag{8.4}$$

where the constraint from the fixed electric charge of the pion, $f_\pi(s{=}0) = \mathcal{F}_\Omega(s{=}0) = Q = 1$, is simply imposed, we can describe the lattice data across both spacelike and timelike regions, as shown in Fig. 8.3. With $\sqrt{s_0} = 0.135\, a_t^{-1}$ and $\sqrt{s_c} = 0.22\, a_t^{-1} = 1.27 \cdot (2m_K)$, the parameter values for a quadratic description are,

$$\begin{aligned} d_1 &= \quad 1.85\,(12) \qquad \begin{bmatrix} 1 & 0.8 \\ & 1 \end{bmatrix} \\ d_2 &= \quad 7.0\,(5) \end{aligned}$$

$$\chi^2/N_{\text{dof}} = \tfrac{85.4}{37-2} = 2.44\,. \tag{8.5}$$

The corresponding pion form factor for this description of $\mathcal{F}_\Omega(s)$ in presented in Fig. 8.4. The somewhat large χ^2/N_{dof} is dominated by points in the spacelike region which have high statistical precision. Discretization effects which are small in absolute terms, but of comparable size to the small statistical errors could explain this observation.

Finally, note that for all the results found for the timelike form factor, the phase of $f_\pi(s > (2m_\pi)^2)$ is always equal to the phase-shift $\delta_1^{\pi\pi}$ by construction, as demanded by

Watson's theorem. This is the case because all our parameterizations satisfy the unitarity constraint over the timelike elastic region, as they inherit the branch cut structure from the scattering amplitude $\mathcal{M}$ or directly from the dispersive integral of the phase-shift.

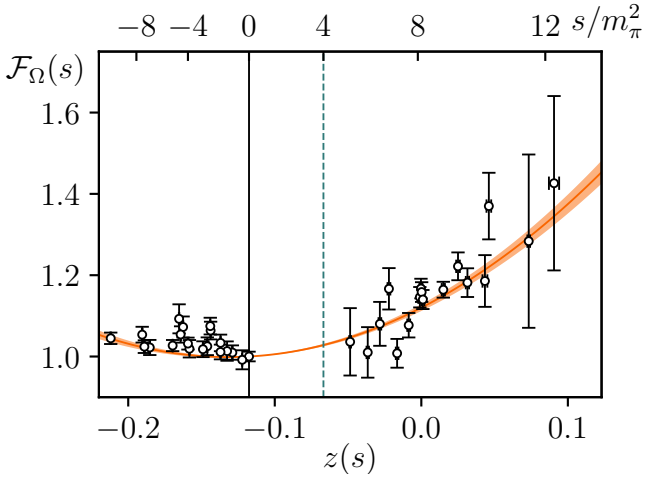

Figure 8.3: Ratio of the form factor data, $|f_\pi(s)|$ (as presented in Fig. 8.1b), to the Omnès function, $\Omega(s)$, as a function of the conformal map variable of Eq. (8.3). The curve shows the polynomial fit of Eq. (8.5).

8.2 Coupled-channel timelike form factors

The finite volume formalism presented in Sec. 2.1.1 dictates that the matrix elements of the discrete finite-volume states are given by a linear combination of all the production amplitudes with a consistent set of quantum numbers and whose final states can go on shell. In a sense, the determination of the pion form factor above the $K\overline{K}$ threshold from a finite-volume calculation provides as well the kaon timelike form factor. However, the amplitudes cannot be extracted following the procedure used in the elastic regime because there is no longer a one-to-one mapping between finite volume matrix elements, and infinite volume form factors. Instead, we have to employ Eq. (7.2), to be able to constrain the infinite volume form factors, via a χ^2 minimization against the values of $\{\mathcal{F}_{\mathfrak{n}}^{(L)}\}$.

We implement the effect of the correlated uncertainty on the finite volume correction

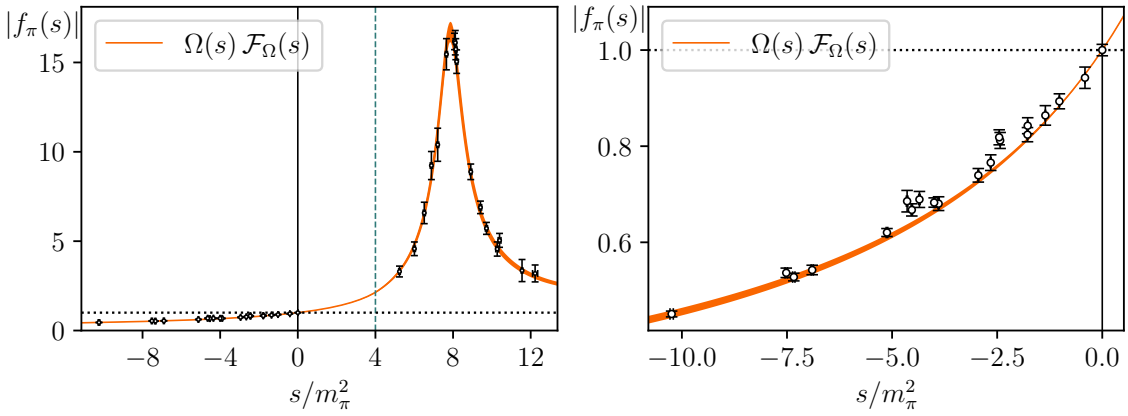

(a) Energy dependence across spacelike and timelike regions.

(b) Zoom over the spacelike region.

Figure 8.4: Pion form factor across spacelike and timelike regions, and energy-dependent description by Omnès modulated by the quadratic $F_\Omega(s)$ of Eq. (8.5).

factors, $\tilde{r}_{\mathfrak{n},a}$, in terms of a "systematic" contribution to the data covariance in the fit χ^2,

$$\begin{aligned}\chi^2 = \sum_{\mathfrak{n},\mathfrak{m}} \Big[\mathcal{F}_\mathfrak{n}^{(L)} - \big(\tilde{r}_{\mathfrak{n},\pi\pi}\mathcal{F}_{\pi\pi}(s) + \tilde{r}_{\mathfrak{n},K\overline{K}}\mathcal{F}_{K\overline{K}}(s)\big)\Big] \\ \cdot \big(C^{\text{stat.}} + C^{\text{syst.}}\big)^{-1}_{\mathfrak{n},\mathfrak{m}} \\ \cdot \Big[\mathcal{F}_\mathfrak{m}^{(L)} - \big(\tilde{r}_{\mathfrak{m},\pi\pi}\mathcal{F}_{\pi\pi}(s) + \tilde{r}_{\mathfrak{m},K\overline{K}}\mathcal{F}_{K\overline{K}}(s)\big)\Big],\end{aligned}$$

which augments the "statistical" covariance of the $\mathcal{F}_\mathfrak{n}^{(L)}$. The total error is shown in Fig. 8.5, which shows the the finite volume correction dominates the uncertainty when compared with Fig. 6.6, where the error bars are *also* plotted for each data point, but are too small to be visible behind the circles, and in that case we opted to show them as well in the bottom panel. This "systematic" covariance is computed using the resampled $\tilde{r}_{\mathfrak{n},a}$ introduced in Section 7.4 whose data covariance inherits that of the energy levels. For each energy level, only the dominant component, $a = \pi\pi$ or $K\overline{K}$ is used to compute the covariance.

To describe the infinite volume form factors we use the parameterization of Eq. (1.40), with the *reference coupled-channel* scattering amplitude determined in Sec. 1.5.1.2. The smooth functions $\mathcal{F}_a$ are parameterized with low order polynomials in s, analogous to

Eq. (5.2.2),

$$\mathcal{F}_a(s)/m_\pi^2 = \sum_{n=0}^{N_a} h_{a,n} \cdot \left(\tfrac{s-s_0}{s_0}\right)^n . \tag{8.6}$$

We emphasize here that the function $\mathcal{F}_{\pi\pi}(s)$ obtained in the coupled-channel case does not have to resemble the similarly named function in the *elastic* case, presented in Sec. 8.1.1. This can be seen by considering $f_\pi(s)$, which should be similar between the two cases, and which has a representation,

$$f_\pi = \frac{1}{k^{\star\,2}_{\pi\pi}} \mathcal{M}_{\pi\pi,\pi\pi} \left[\mathcal{F}_{\pi\pi} + \frac{k^\star_{\pi\pi}}{k^\star_{K\overline{K}}} \frac{\mathcal{M}_{\pi\pi,K\overline{K}}}{\mathcal{M}_{\pi\pi,\pi\pi}} \mathcal{F}_{K\overline{K}} \right], \tag{8.7}$$

in the coupled-channel case, where we have factored out the elastic $\pi\pi$ scattering in analogy to Eq. (1.41). Below the $K\overline{K}$ threshold, the expression within square brackets is real and smooth (because the ratio of scattering amplitude components does not posses the $\pi\pi$ branch cut), and serves as the effective $\mathcal{F}$ in the prior elastic case.

Model	$N_{\pi\pi}$	$N_{K\overline{K}}$	N_{dof}	χ^2/N_{dof} reference	$\gamma^{(1)}$	ref. iter.
a	1	0	$32-3$	5.51	2.62	5.26
b	0	1	$32-3$	4.39	2.41	4.90
c	1	1	$32-4$	4.53	2.48	4.92
d	2	0	$32-4$	4.87	2.55	5.28

Table 8.1: Global description of full set of timelike finite-volume matrix elements. Variations in polynomial order in Eq. (8.6) used with *reference coupled-channel* scattering amplitude (fifth column), an alternative coupled channel amplitude with more parameter freedom, Eq. (5.15) (sixth column), and *reference coupled-channel* amplitude with a modified iterative fitting strategy described at the end of Sec 7.4 (seventh column).

We describe all the $\mathcal{F}^{(L)}_{\mathfrak{n}}$ data shown in Fig. 6.6 using the finite volume correction factors $\tilde{r}_{\mathfrak{n},a}(L)$ computed from the *reference coupled-channel* amplitude and smooth functions $\mathcal{F}_{\pi\pi}, \mathcal{F}_{K\overline{K}}$ each described by polynomials of order 1, leading to the result summarized in Fig. 8.5. The description given by the green points is observed to be in good qualitative agreement with the constraining lattice data, with a few points having significant deviations which produce a somewhat large χ^2/N_{dof}.

Examining Figs. 8.2 and 8.4a we see that the points which are most discrepant in the

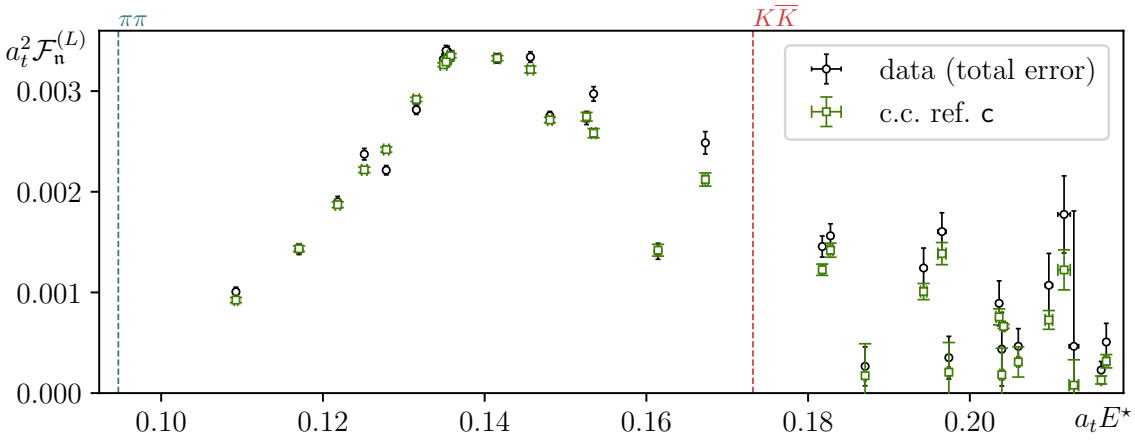

Figure 8.5: Finite volume form factor (open black circles) with errorbars modified to account for the fractional uncertainty on the finite-volume correction factors, coming from the diagonal elements of the "systematic" covariance, as described in the text. Global description using the *reference coupled-channel* scattering amplitude, and order-1 polynomial forms for $\mathcal{F}_{\pi\pi}(s), \mathcal{F}_{K\overline{K}}(s)$ (green squares).

coupled-channel description were also somewhat discrepant in the elastic description, and that the larger effect in the current case may largely reflect the different approach for propagating the finite-volume factor uncertainty.

Tab. 8.1 presents variations of both the polynomial orders used in $\mathcal{F}_{\pi\pi}(s)$, $\mathcal{F}_{K\overline{K}}(s)$, and the form used for the coupled-channel scattering amplitude, where we consider a second functional form of the K-matrix, given in Eq. (5.15), which includes an additional linear term in s with a set of $\gamma^{(1)}$ coefficients. The reduction in the χ^2 values for the varied scattering amplitude can be entirely associated with the decreased precision of the finite-volume correction factors, which is implemented as a larger systematic error on the data.

The final column of Tab. 8.1 shows an alternative choice for the determination of the "systematic" covariance, where the magnitude of the diagonal elements are determined iteratively from the mean value of the model $\sum_a \tilde{r}_{\mathrm{n},a}\mathcal{F}_a$. This prescription was inspired by the fitting procedure described in Ref. [126], more details can be found in that reference and at the end of Sec 7.4. We found consistent results from both methods to determine the "systematic" covariance, including the determination of the decay constant of the ρ-meson described in the following section, and shown in Fig. 8.8.

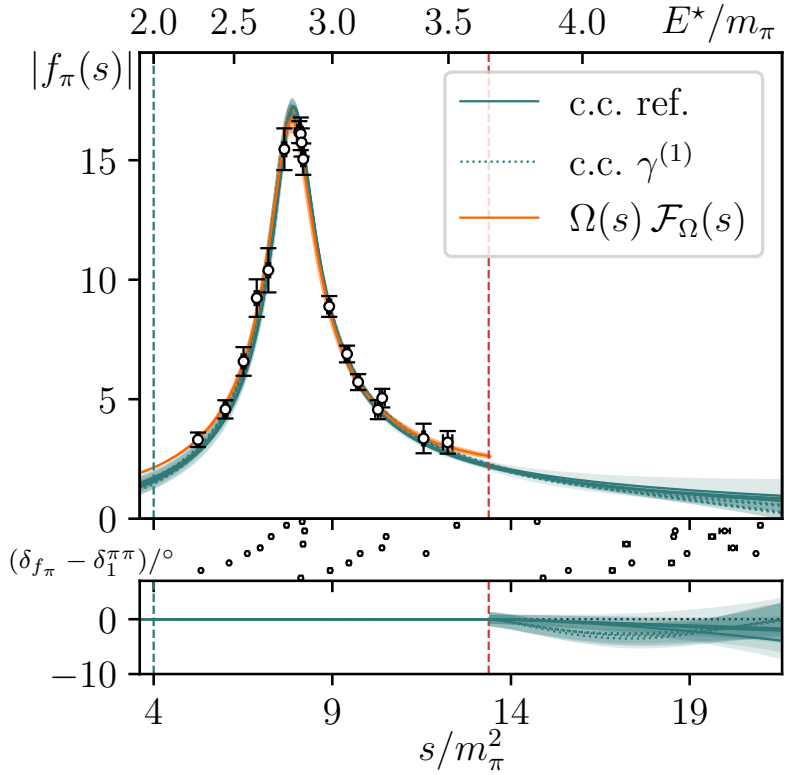

Figure 8.6: Timelike pion form factor using coupled-channel amplitude parameterizations showing variations detailed in Table 8.1(blue curves). Also shown the discrete elastic determinations of Section 8.1.1 and the corresponding elastic Omnès description. The bottom panel shows the form factor phase difference with respect to the $\pi\pi$ phase-shift. The points in between panels show the energy of the levels used to constrain the form factor energy dependence. The red dotted vertical line indicates the $K\overline{K}$ threshold.

The timelike pion form factor for these descriptions is shown in Fig. 8.6, where we see only modest spread over the different parameterizations, and rather close agreement with the result of Sec. 8.1.2 described in terms of the Omnès function over the elastic region. The bottom panel of Fig. 8.6 shows the difference between the form factor phase and the $\pi\pi$ P-wave phase-shift, which above the $K\overline{K}$ threshold need not coincide.[2] However, due to the inelasticity in the scattering amplitude being close to 1, indicating little $\pi\pi, K\overline{K}$ channel coupling we expect a small phase difference, and indeed we observe that the differences agree with zero.

[2]Watson's theorem equating the production phase to the scattering phase-shift applies rigorously only in the elastic region.

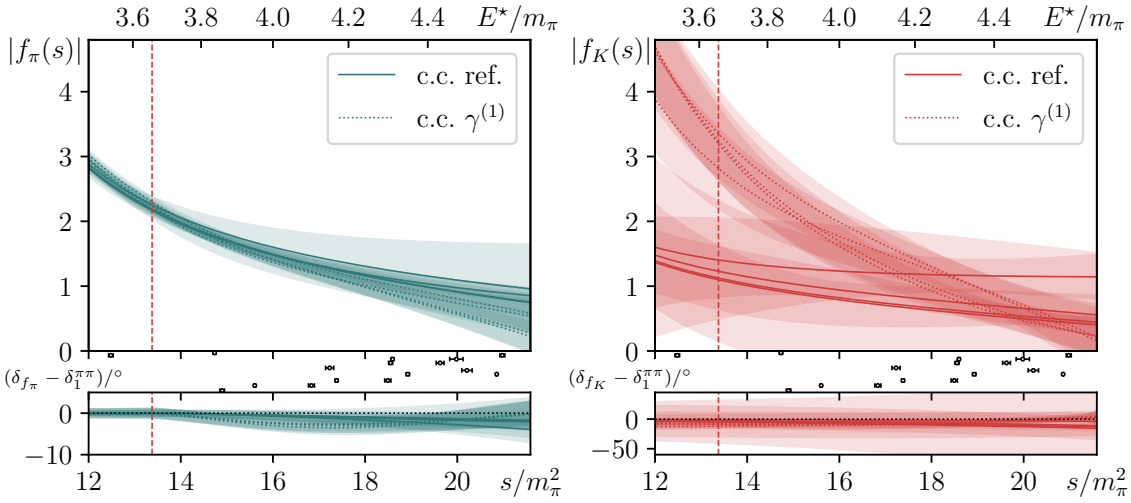

(a) Pion timelike form factor.

(b) Kaon isovector timelike form factor.

Figure 8.7: Coupled-channel parameterization variations of Table 8.1 plotted over the inelastic energy region. The red dotted vertical line indicates the $K\overline{K}$ threshold.

In Fig. 8.7 we show the timelike pion and kaon (isovector) form factors for energies above the $K\overline{K}$ threshold, where we observe a much greater sensitivity to the choice of scattering amplitude parameterization in the kaon case. In particular the kaon form factor using the "$\gamma^{(1)}$" parameterization inherits a larger coupling to the ρ from the scattering amplitude, and more of a resemblance to the tail of the resonance. Nevertheless, the kaon amplitudes broadly agree within the fairly large uncertainties. They differ most at and below $K\overline{K}$ threshold, but this is precisely where the finite-volume approach becomes weak, as the contribution of the production amplitude to the finite volume matrix elements is exponentially suppressed below its threshold (see Appendix A of Ref. [79]). In the current case, this can be understood in terms of the poorly constrained value of the coupling of the $K\overline{K}$ channel with the ρ-resonance. For a narrow resonance the value of f_a at the resonance mass m_R is approximated by,

$$f_a = -i\sqrt{16\pi}\frac{\hat{c}_a}{m_R\Gamma_R}\mathcal{F}_{\mathfrak{n}}^{(L)} + \mathcal{O}\left(\frac{\Gamma_R}{m_R}\right), \tag{8.8}$$

and the value of $\hat{c}_{K\overline{K}}$ varies significantly between the *reference coupled-channel* and the

"$\gamma^{(1)}$" scattering parameterizations, with a greater value in the latter case.

To conclude this chapter we can employ the computed form factors to extract electromagnetic properties of the π and ρ hadrons.

8.3 π and ρ parameters from form factors

The spacelike form factor is typically characterized by its slope at zero momentum transfer, what is commonly referred to as the 'charge radius' $\langle r_\pi^2 \rangle^{1/2}$, where[3]

$$\langle r_\pi^2 \rangle \equiv 6 \, \frac{d}{ds} f_\pi(s) \Big|_{s=0} . \tag{8.9}$$

We determine this quantity from the parameterization in Eq. (8.5), obtaining $\langle r_\pi^2 \rangle^{1/2} = 0.614(7)$ fm. This value sits in between the experimental pion charge radius, $\langle r_\pi^2 \rangle^{1/2} = 0.659(4)$ fm, and kaon charge radius, $\langle r_K^2 \rangle^{1/2} = 0.560(31)$ fm, reported by the PDG [10]. From the effective field theory result of Ref. [127], this is the radius that we would expect, given our lattice pion mass lies between the physical pion and kaon masses. In particular Ref. [127] shows that the radius of the pseudoscalar meson, using the effective field theory defined by the chiral symmetry breaking pattern of QCD, is an analytic function of its mass except for a logarithmic singularity at $m_\pi = 0$. This result is also consistent with previous analyses of timelike form factors determined at similar pion masses in the lattice [38, 39].

The timelike pion form factor is dominated by the contribution of the ρ resonance, and at the resonance pole, the $\pi\pi$ production amplitude factorizes into the coupling of the ρ-meson to the $\pi\pi$ system and to the electromagnetic current,

$$\mathcal{H}^\mu_{\pi\pi,m} = \frac{\sqrt{16\pi}\, c_{\pi\pi}}{s_R - s} \, \langle \rho(\mathbf{P}, m) \big| \mathcal{J}^\mu \big| 0 \rangle \, .$$

[3] See Ref. [45], and references therein, for a discussion about the proper interpretation of this quantity when it is comparable to the Compton wavelength of the system.

The current-vector matrix element can be expressed in terms of a Lorentz-invariant ρ-photon coupling, which we choose to parameterize in a dimensionless form,

$$\left\langle \rho(\mathbf{P}, m) \middle| \mathcal{J}^{\mu} \middle| 0 \right\rangle \; = \epsilon^{\mu *}(P, m)\, f_V\, m_R^2 \,, \tag{8.10}$$

where $m_R^2 = \mathrm{Re}(s_R)$.

One definition of the ρ meson decay partial width into an electron-positron pair,

$$\Gamma_{\rho \to e^+ e^-} = \frac{4\pi\alpha^2}{3} m_R |f_V|^2 \,,$$

uses this coupling, and use of the PDG average of $\Gamma_{\rho \to e^+ e^-}$ can thus provide an estimate for $|f_V|$. A more consistent approach, which was taken in Ref. [128], would be to describe the $e^+e^- \to \pi\pi$ cross-section energy dependence using the infinite-volume amplitude parameterizations presented earlier, and analytically continue them to the pole, yielding a complex valued f_V.

Practical extraction of f_V coupling from our lattice-constrained amplitudes varies slightly depending upon the form of the amplitude construction. In the elastic case using K-matrix parameterizations, we may simply use the $\pi\pi$ coupling from the scattering amplitude and the singularity-free function, $\mathcal{F}(s)$, evaluated at the pole location [128],

$$f_V = -\sqrt{\frac{4}{3}} \frac{1}{m_R^2} \sqrt{16\pi}\, \hat{c}_{\pi\pi}\, \mathcal{F}(s_R) \,.$$

In the case of the Omnès parameterization of Eq. (1.45) one needs to analytically continue the Omnès function Ω into the unphysical Riemann sheet. This can be achieved by multiplying Ω by the S-matrix evaluated in the unphysical Riemann sheet where the scattering amplitude houses the resonance pole.

In the coupled-channel case, the extracted coupling value is independent of whether it

is pulled from the pion or kaon form factor, in both cases being,

$$f_V = -\sqrt{\frac{4}{3}}\frac{1}{m_R^2}\sqrt{16\pi}\left(\hat{c}_{\pi\pi}\mathcal{F}_{\pi\pi}(s_R) - \hat{c}_{KK}\mathcal{F}_{KK}(s_R)\right). \tag{8.11}$$

In Fig. 8.8 we summarize our determinations of f_V using extractions from elastic and coupled-channel parameterizations of various forms. The values are seen to be in good agreement, and as expected for a calculation at an unphysical quark mass, they differ somewhat from the experimental value following from the PDG's $\rho \to e^+e^-$ partial width. The errorbars include the uncertainties on the resonance parameters, c_a and s_R, extracted from the scattering amplitude, as well as those of the smooth functions $\mathcal{F}_a$, which are estimated from the variance of the $\mathcal{F}_{\mathfrak{n}}^{(L)}$ data and the finite-volume correction factors. The orange and purple points show two different strategies for handling the error propagation from the finite-volume correction factors, as discussed in Sec. 7.4. Green points differ from the orange ones by the functional form of the scattering amplitude used to describe the spectra and to calculate the finite-volume factors, see Eq. (5.15) in Sec. 5.2.2.

The value coming from the Omnès parameterization serves as a conservative estimate at $m_\pi = 284$ MeV,

$$\begin{aligned} f_V &= 0.224(6)\, e^{-i\pi\cdot 0.0418(27)} \quad [-0.09]\,, \\ \Gamma_{\rho\to e^+e^-} &= 8.9(5)\ \text{keV}\,, \end{aligned}$$

where the coupling is observed to be close to being real valued, with small correlation between magnitude and phase (the number in square brackets).

A mild pion mass dependence was observed in Ref. [129] where the ρ was studied using only two light quark flavors and without explicit finite-volume correction (as it was either stable or very narrow at the pion masses considered), and in Refs. [35, 36] similarly for three flavors.

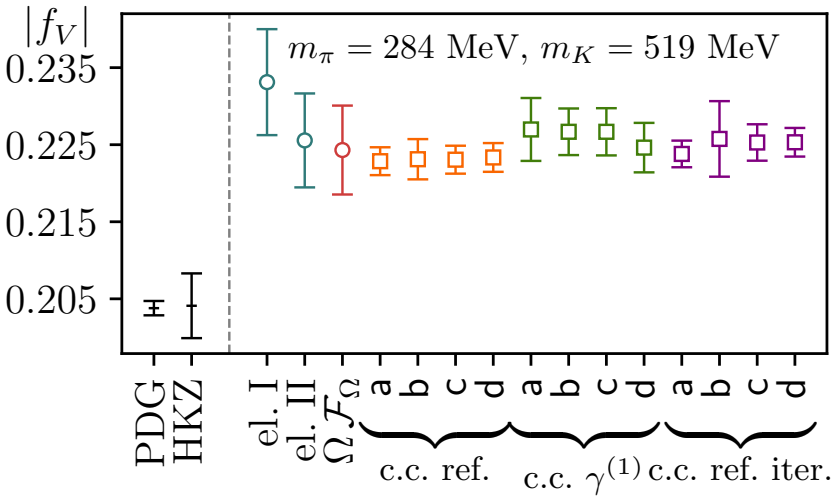

Figure 8.8: Vector decay constant, f_V, for the ρ meson. The first two values correspond to the experimental extraction reported by the PDG[10] and the dispersive description of experimental data by Hoferichter et. al. [HKZ] [128]. Subsequent values are the result of this analysis, for only the elastic region (circles) and also including the coupled channel region (squares).

This concludes our presentation of the results from this lattice calculation. We found that the pion form factor, determined using the coupled-channel formalism, aligns with the elastic result, serving as a consistency check. Moreover, we determine the kaon isovector timelike form factor for the first time from QCD, albeit with considerable uncertainty. We anticipate that applying this technology to a system with a more evenly distributed flavor split associated with the finite volume states, as described in Fig. 7.3 with 25 $\pi\pi$ dominated levels versus 7 $K\overline{K}$ dominated levels, will yield comparable errors for the form factors in each of the considered channels.

Additionally, we successfully described the finite volume matrix elements over two disjoint kinematic regions, allowing us to interpolate the unphysical region depicted between the vertical lines in Fig. 8.4a. While the unphysical kinematic region cannot be experimentally realized for a current interacting with an isolated pion, the value of f_π in this region can be probed with physical kinematics when employing the on-shell decomposition of $\mathcal{W}_{\text{df}}$ given in Chapter 3. This involves processes with two hadrons, one of them would need to be a charged pion, interacting together with the electromagnetic current. In that case the

initial and final states can have different invariant masses, allowing for small and positive values of current virtualities, with the formalism of Chapter 3 restricted to virtualities less than $4m_\pi^2$. The dispersive determination using the Omnès function, which is an analytic improvement over the GS parameterization, might in general be helpful to fully describe the on-shell decomposition of amplitudes that feature the pion form factor as a subprocess.

For example, future calculations of amplitudes of the form $2 \xrightarrow{\mathcal{J}} 2$ from lattice QCD, e.g. to extract the ρ-meson resonance charge radius by employing external two-pion states, will likely benefit from an analytically improved function describing the single pion form factor, f_π, that was constrained with *both* timelike and spacelike data. This is because the two-hadron matrix elements that can be extracted from the lattice are allowed to access kinematics with spacelike virtuality $Q^2 \leq 0$, as well as timelike virtuality $0 > Q^2 > -4m_\pi^2$.

Chapter 9

Summary and Outlook

Examination of poles and their residues in scattering and transition amplitudes computed using Lattice QCD provides a promising avenue for understanding the spectrum and exploring the internal arrangement of quarks and gluons within hadrons. The field's achievements have been driven by various efforts, including the deployment of high-performance computing hardware and the development of algorithmic techniques. Notably, one key advancement has been the derivation and implementation of the appropriate "finite-volume" formalism for extracting amplitudes from LQCD spectra and matrix elements.

These techniques have proven effective for studying interactions between pairs of hadrons, and more recently, three-hadron systems have also begun to be explored [117, 130, 131, 132]. Similarly, the feasibility of extracting transitions to two hadrons in the elastic energy region has been established, even in cases where partial-wave mixing is induced by finite volume effects [85].

For the first time, we successfully implemented the extraction of a coupled-channel transition amplitude from a Lattice QCD dataset. Specifically, we calculated the electromagnetic timelike form factor of the pion within the elastic region and also above the kaon-antikaon threshold, where we extracted the timelike kaon isovector form factor. By comparing our results to an analysis restricted to the elastic energy region, we demonstrated the consistency of the coupled-channel formalism with the established elastic formalism.

Notably, in our specific case where a vector meson resonance appears within the elastic energy region, we found that the extraction of resonance parameters is consistent between the elastic and coupled-channel analyses, with the latter providing a more precise result due to increased data constraining the amplitudes.

In this calculation we also described the analytic behavior of the pion form factor in a wide energy region that included spacelike virtualities and the elastic timelike energy region. The procedures for extracting the spacelike and timelike form factors from LQCD differ significantly. In the spacelike region, LQCD matrix elements directly correspond to their infinite volume counterparts, up to exponentially suppressed corrections. However, in the timelike region, we applied a non-trivial finite volume correction to each matrix element. Subsequently, we demonstrated that the data in these two regions can be described simultaneously by a single parameterization that incorporates the analytical properties of the form factor related to causality, conservation of probability, and crossing symmetry. This is in part possible thanks to the absence of a left hand cut on the timelike form factor. Specifically, we used a dispersive integral featuring only a right-hand cut. This consistency check validates the finite volume formalism implemented for the timelike region.

An important requirement for the calculation in the timelike region was the extraction of energies and matrix elements beyond the ground state of the lattice for several momenta and irreps. In total we determined 32 energy levels across ten different irreps, resolving reliably up to five different energy levels in one irrep. This was achieved thanks to the possibility of generating a large and diverse variational basis to overlap with the states. This basis included operators that mimic the wave functions of single-meson and non-interacting meson-meson states. For the two-meson operators in our basis, we employed all combinations for which their non-interacting energy fell within the kinematic region where we wanted to obtain the infinite volume amplitudes.

The solution of the GEVP of a correlation matrix made with the operator basis we just described gave us access to the energies of these states and the linear combinations of operators with optimal overlap for each level. The correlation functions constructed with

these optimized operators latch primarily to a single state, and have minimal contamination from other states. In particular, minimizing the contribution from lower energy states is essential to extract matrix elements that are dynamically suppressed with respect to those of the lower energy states. In practice, we found that ratios of correlation functions constructed with optimized operators, along with an operator corresponding to the insertion of the isovector component of the electromagnetic current, were most convenient for extracting the matrix elements.

The finite volume correction, the LL factor, for a coupled-channel transition is mathematically formed by a vector in channel space. Each component of this vector indicates the dynamic mixing of the asymptotic two-hadron states into each of the stationary states of the finite volume. In the elastic case, where the LL factor is a single number, there exists a one-to-one correspondence between finite volume matrix elements and the infinite volume pion form factor. This correspondence allows for a direct determination at each of the energies within the elastic spectra. However, this is not the case for a coupled-channel analysis. In this scenario, each matrix element provides a constraint for a linear combination of the form factors, weighted by the components of the LL factor.

A similar obstacle arises in the determination of scattering amplitudes in coupled-channel systems, and we employ a similar technique to circumvent it: proposing a functional form for the energy dependence of the form factors with variable parameters. By varying these parameters, we minimize the difference between the calculated finite volume matrix element and that obtained from the parameterization. It has proven useful to split the energy dependence of the form factors into two components: one describing the strong scattering behavior, which varies significantly with energy due to the nearby ρ resonance, and another representing a slowly varying function of energy that describes the production of the system. This splitting results from finding a parameterization that satisfies unitarity in the coupled-channel region.

This result improves on the technique to extract only the elastic timelike form factor [37, 38, 39]. It also moves a step forward with respect to previous extractions of the decay

constant of the ρ, which neglected the finite volume corrections associated with the LL factor and the analytic continuation to the resonance pole [35, 36].

Continuum methods, employing the Schwinger-Dyson equation, can also be used to calculate the timelike form factor of pseudoscalars [133, 48]. These methods could, in principle, be compared to the results of this work by tuning the input parameters to reproduce the masses of the pseudoscalars on this lattice. Decay constants extracted from the lattice can also be compared with these continuum methods, for example the calculations of Refs. [48, 134].

The continuum methods can provide a complimentary picture to LQCD of the non-perturbative dynamics of QCD at the hadronic scales. In general, the accuracy of the truncation necessary in these methods, e.g. the "rainbow-ladder" description of the quark-gluon vertex and the gluon propagator [135], cannot be known *a priori*, and predictions can have uncontrolled systematic errors. However, continuum methods do not suffer from the finite-volume effects present in the multi-hadron sector of LQCD, which requires a different formalism for each type of process. Nonetheless, within the two- and three-hadron sectors, including amplitudes with one or two external currents, the LQCD community has been quite successful in formulating corrections that remove all power-like finite-volume effects, with the remaining exponentially suppressed being negligible for modern computations. Going beyond the three-hadron sector from the lattice, a promising avenue is to consider spectral functions to calculate inclusive rates [136].

The second main result presented in this thesis is the formulation of a prescription to extract elastic form factors of resonances from finite volume matrix elements and energies. This result builds on the formulations used in modern LQCD calculations to extract resonance parameters: the mass, the width, the couplings, and transition form factors. This extraction would consist of a two-step process.

The first step involves calculating $\mathcal{W}$ amplitudes ($2 \xrightarrow{\mathcal{J}} 2$), where initial and final

two-hadron states couple to a resonance. This calculation is performed by applying the appropriate finite volume correction to the corresponding finite volume matrix elements obtained via LQCD. In the second step, we describe the energy and virtuality dependence of $\mathcal{W}$ using a parameterization consistent with unitarity and analyticity. This allows for a controlled analytic continuation to the resonance pole. Finally, the form factor is proportional to the residue of $\mathcal{W}$ at this pole. It is important to note that this structure involves a double pole: one in the initial state energy and another in the final state energy.

For the second step of calculating resonance form factors, we obtained a decomposition of $\mathcal{W}$ in terms of amplitudes of sub-processes, known kinematic functions, and unknown dynamic functions that are constrained to be real within the physical region. This decomposition of $\mathcal{W}$ is conceptually similar to the description of the two-body scattering amplitude $\mathcal{M}$ in terms of a real valued K-matrix. To derive the decomposition, we solve for $\mathcal{W}$ in the integral equation describing the amplitude to all-orders in the strong interaction, this ensures that the result is consistent with unitarity and analyticity. The integrals describing rescattering can be separated into two contributions: unknown dynamic functions, like the K-matrix, and known kinematic functions, like the phase space. Thanks to this splitting, the integral equations can be reformulated in terms of algebraic relations in the partial-wave and channel space, which can be solved to obtain the decomposition of $\mathcal{W}$.

The analytic representation of $\mathcal{W}$, in particular its unknown dynamical functions, can be constrained from computed finite-volume spectra and the corresponding finite-volume matrix elements. The representation of $\mathcal{W}$ contains a term involving the scattering amplitude, $\mathcal{M}$, of the initial state *and* the final state. The presence of the factors of $\mathcal{M}$, leads to poles in the initial and final energies, with a residue that is proportional to the resonance form factor. An appropriate analytic representation of $\mathcal{W}$ is essential to perform this analytic continuation.

9.1 Future work

The results presented here are only applicable within energy regions where at most two hadrons can go on shell, although they can be applied above the threshold of multiple two-hadron channels. Progress towards studying transitions involving three hadrons is underway, see for example Ref. [116]. Another avenue of research is to consider spectral functions to calculate inclusive rates [136]. Transitions with two current insertions have also been considered, and future calculations of processes like $\gamma\gamma \to \pi\pi$ from LQCD are possible, the finite volume corrections are known [137], as well as the analytic representation of the infinite volume amplitude [110]. The formalism presented for the $\mathcal{W}$ amplitude is also restricted to spinless hadrons, and a generalization for particles with spin will be necessary if we foresee to implement this technique to systems with nucleons. Finally, these techniques only take into account the leading order electroweak contribution, which is sufficient for the study of resonance properties, but higher order contributions could be needed if applied to a precision calculation that needs to be compared to an experimental result, e.g. calculations of CP-violating decays.

The technology implemented for the calculation of a coupled-channel transition from LQCD can be employed to study other hadronic systems when coupled to an external currents. Let us first illustrate this with an example, and later we will list various systems where these results serve as a proof-of-principle of the finite-volume technology.

On the light-flavor sector, there is evidence for hybrid states with exotic quantum numbers $J^{PC} = 1^{-+}$. There is consensus on an isovector π_1 state [138, 139], as well as an indication of an isoscalar η_1 partner [140, 141]. The partial width of the π_1 to different two-hadron channels has been calculated in a lattice where the quark mass is such that only two-hadron channels are open [70]. Another LQCD study calculated the radiative width $\Gamma(J/\psi \to \gamma\eta_1)$, the only channel where the η_1 has been observed experimentally, but neglected the finite-volume effects associated with the unstable nature of the η_1 [142].

Closer comparison to experimental results could be achieved by calculating *simultane-*

ously the radiative production as well as the hadron decay. This type of calculations has been carried out for the ρ [143, 144] and the $K^\star$ [85], which decay into the elastic $\pi\pi$ and $K\pi$ channels, respectively. When calculating a similar amplitude for the $J^{PC} = 1^{-+}$ octet in LQCD, multiple decaying channels would have to be taken into account, even at higher than physical pion masses, due to the small mass splitting between the vector mesons and the pseudoscalar singlet.

This work provides a demonstration on how to perform this type of coupled-channel radiative transition analysis, which in this case involved $\gamma \to \pi\pi/K\overline{K}$ in the context of the ρ channel. This results in the simultaneous extraction of the radiative coupling of the resonance (in this case $\gamma \to \rho$), as well as the strong decay width of the ρ. Other systems of interest that require the implementation of the coupled-channel technology presented here are the CP-violation observed in the $D^0 \to \pi\pi/K\overline{K}$ decays [145], and the isospin breaking corrections of kaon decays, i.e. $K \to \pi^0\pi^0/\pi^+\pi^-$.

The completion of a prescription to map LQCD matrix elements to $2 \xrightarrow{\mathcal{J}} 2$ transitions, opens the door to study a new type of amplitudes that had not been previously accessible by first-principles QCD. This allows the calculation of properties of resonances, such as their electromagnetic form factors or gravitational form factors. For example, in the case of the ρ meson, the extraction of its elastic form factors from $\mathcal{W}$ could be compared with results whenever it is stable under the strong interaction [94, 146], allowing us to study the effect of quark mass variation on the form factors.

The extension of the $2 \xrightarrow{\mathcal{J}} 2$ technology to take into account hadrons with spin could also have a significant impact on the SM and Beyond the Standard Model phenomenology. For instance it would allow us to constrain low energy constants of nuclear models, which in turn could be used to predict neutrinoless double beta decay rates, and interaction cross-sections between a neutrino and a nucleus. The former is sensitive to the nature of the neutrino, which is possibly the only Majorana fermion in the SM, while the latter is relevant for neutrino oscillation experiments, see Ref. [147] for a discussion about the potential applications of LQCD for nuclear physics.

The results presented in this work bring us a step closer to the direct calculation of structural properties of resonant states from first-principles. Furthermore, the determination of coupled-channel transition amplitudes from QCD can be employed as a resource complementary to experimental efforts studying the hadron spectrum as well as SM phenomenology.

Appendix A

Infinite series identities

We will use the following shorthand notation for infinite *geometric* series

$$[A]^g \equiv \sum_{n=0}^{\infty} A^n = 1 + A + A \cdot A + A \cdot A \cdot A + \dots . \tag{A.1}$$

With this notation, some useful identities are

$$[A \cdot B]^g \cdot A = A \cdot [B \cdot A]^g , \tag{A.2}$$

$$[A]^g = 1 + A \cdot [A]^g = 1 + [A]^g \cdot A = (1 - A)^{-1} , \tag{A.3}$$

where the last equality might imply an analytic continuation to define the inverse over all possible values of A other than $A = 1$. This means that if $|A| > 1$, the series should not discarded as divergent, but as placeholder for the function $(1 - A)^{-1}$, which is finite for $A \neq 1$. We also employ the identity

$$[A \cdot (B + C)]^g = (1 - A \cdot C)^{-1} \cdot (1 - A \cdot C) \cdot (1 - A \cdot B - A \cdot C)^{-1} , \tag{A.4}$$

$$= (1 - A \cdot C)^{-1} \cdot (1 - A \cdot B \cdot (1 - A \cdot C)^{-1})^{-1} , \tag{A.5}$$

$$= [A \cdot C]^g \cdot [A \cdot B \cdot [A \cdot C]^g]^g , \tag{A.6}$$

where we have taken into account that different elements may not commute, and therefore the inverse is defined to be $(A \cdot B)^{-1} = B^{-1} \cdot A^{-1}$.

Appendix B

Analytic continuations to unphysical sheets

This appendix heavily draws from App. B of Ref. [98]. In this appendix, we review the analytic continuation of $\mathcal{M}$ to the unphysical sheet, and illustrate how the procedure extends to the transition amplitude $\mathcal{W}$. Physical scattering amplitudes on the real s axis are boundary values of an analytic function, which has a discontinuity across the branch cut given by the unitarity relation Eq. (1.18). Therefore, we can formally define the second sheet amplitude by continuing through the branch cut, using the boundary condition

$$\mathcal{M}^{\mathrm{II}}(s_{\pm}) = \mathcal{M}(s_{\mp})\,, \tag{B.1}$$

where we have defined the short-hand notation $s_{\pm} = s \pm i\epsilon$ and assume that $\epsilon \to 0^{+}$. Using this short-hand, the unitarity relation in Eq. (1.20) can be expressed as

$$\mathcal{M}(s_{+}) - \mathcal{M}(s_{-}) = 2i\,\rho(s_{+})\mathcal{M}(s_{-})\mathcal{M}(s_{+})\,, \tag{B.2}$$

where we have used the Schwarz reflection principle $\mathcal{M}^{*}(s) = \mathcal{M}(s^{*})$. For technical convenience, we choose to continue the amplitude to the second sheet in the upper-half s plane, i.e. $\mathcal{M}^{\mathrm{II}}(s_{+}) = \mathcal{M}(s_{-})$. We then use the Schwarz reflection principle to extend

the result to the lower-half s plane, which is nearest to the physical region assuming the usual $+i\epsilon$ prescription. The result is identical if one chooses to continue to the lower-half plane directly, however we find this approach convenient to simplify the later derivation for the $2 \xrightarrow{\mathcal{J}} 2$ amplitude. Assuming a continuation to the upper-half plane, we now insert Eq. (B.1) into (B.2), and solve for $\mathcal{M}^{\text{II}}$ to find

$$\mathcal{M}^{\text{II}}(s) = \frac{1}{1 + 2i\,\rho(s)\mathcal{M}(s)}\mathcal{M}(s)\,. \tag{B.3}$$

One can make similar arguments for the lower-half plane, with an additional boundary condition for the phase space factor $\rho(s_+) = -\rho(s_-)$, finding the same form as Eq. (B.3).

In the case of the $2 \xrightarrow{\mathcal{J}} 2$ amplitude $\mathcal{W}$, we have to analytically continue both the initial and final state invariant mass squares s_i and s_f, respectively. It is sufficient to consider $\mathcal{W}_{\text{df}}$ since this is the only contribution which can have both initial and final state resonance poles. Since both variables are continued, we impose the boundary condition

$$\mathcal{W}_{\text{df}}^{\text{II,II}}(s_{f,\pm}, Q^2, s_{i,\pm}) = \mathcal{W}_{\text{df}}(s_{f,\mp}, Q^2, s_{i,\mp})\,, \tag{B.4}$$

where the double superscript indicates both variables are continued to their respective second sheets. The on-shell representation Eq. (3.6) ensures that the imaginary part of $\mathcal{W}_{\text{df}}$ takes the form

$$\begin{aligned}\text{Im}\,\mathcal{W}_{\text{df}}(s_f, Q^2, s_i) = {}& \mathcal{M}^*(s_f)\rho(s_f)\mathcal{W}_{\text{df}}(s_f, Q^2, s_i) + \mathcal{W}_{\text{df}}^*(s_f, Q^2, s_i)\rho(s_i)\mathcal{M}(s_i) \\ & + \mathcal{M}^*(s_f)f(Q^2)\text{Im}\,\mathcal{G}(s_f, Q^2, s_i)\,\mathcal{M}(s_i)\,,\end{aligned} \tag{B.5}$$

which shows there is an additional singular term arising from the triangle function. This additional term implies that we cannot just continue both the external $\mathcal{M}$ functions in Eq. (3.6), but that we also need to continue $\mathcal{G}$.

We first write the imaginary part as the difference

$$\begin{aligned} 2i\,\mathrm{Im}\,\mathcal{W}_{\mathrm{df}}(s_f,Q^2,s_i) &= \mathcal{W}_{\mathrm{df}}(s_{f,+},Q^2,s_{i,+}) - \mathcal{W}^*_{\mathrm{df}}(s_{f,+},Q^2,s_{i,+})\,, \\ &= \mathcal{W}_{\mathrm{df}}(s_{f,+},Q^2,s_{i,+}) - \mathcal{W}_{\mathrm{df}}(s_{f,-},Q^2,s_{i,-})\,, \end{aligned} \tag{B.6}$$

where in the second line we used the extension of the Schwarz reflection principle for multivariate functions, the edge-of-the-wedge theorem, to write the conjugated amplitude as a function of variables evaluated on the lower-half plane, i.e. $\mathcal{W}^*_{\mathrm{df}}(s_{f,+},Q^2,s_{i,+}) = \mathcal{W}_{\mathrm{df}}(s_{f,-},Q^2,s_{i,-})$. Using the Schwarz reflection principle for the scattering amplitudes, Eqs. (B.5) and (B.6) give us the relation

$$\begin{aligned} \mathcal{W}_{\mathrm{df}}(s_{f,+},Q^2,s_{i,+}) - \mathcal{W}_{\mathrm{df}}(s_{f,-},Q^2,s_{i,-}) &= 2i\,\mathcal{M}(s_{f,-})\rho(s_{f,+})\mathcal{W}_{\mathrm{df}}(s_{f,+},Q^2,s_{i,+}) \\ &\quad + 2i\,\mathcal{W}_{\mathrm{df}}(s_{f,-},Q^2,s_{i,-})\rho(s_{i,+})\mathcal{M}(s_{i,+}) \\ &\quad + 2i\,\mathcal{M}(s_{f,-})f(Q^2)\mathrm{Im}\,\mathcal{G}(s_{f,+},Q^2,s_{i,+})\,\mathcal{M}(s_{i,+})\,. \end{aligned} \tag{B.7}$$

We now impose the boundary conditions Eqs. (B.1) and (B.4), again continuing to the upper-half planes, the $\mathcal{W}$ amplitude on the second sheets is given by

$$\begin{aligned} \mathcal{W}^{\mathrm{II,II}}_{\mathrm{df}}(s_f,Q^2,s_i) &= \frac{1}{1+2i\,\mathcal{M}(s_f)\rho(s_f)}\mathcal{W}_{\mathrm{df}}(s_f,Q^2,s_i)\left[\,1-2i\,\rho(s_i)\mathcal{M}^{\mathrm{II}}(s_i)\,\right] \\ &\quad + \mathcal{M}^{\mathrm{II}}(s_f)f(Q^2)\,\left[\,\mathcal{G}(s_f,Q^2,s_i) - 2i\,\mathrm{Im}\mathcal{G}(s_f,Q^2,s_i)\,\right]\,\mathcal{M}^{\mathrm{II}}(s_i)\,, \end{aligned} \tag{B.8}$$

where we have extended the domain from near the real axis to the entire upper-half complex planes. We now use the on-shell form Eq. (3.6), as well as (B.3) to construct an on-shell form

$$\begin{aligned} \mathcal{W}^{\mathrm{II,II}}_{\mathrm{df}}(s_f,Q^2,s_i) &= \mathcal{M}^{\mathrm{II}}(s_f)\Big\{\,\mathcal{A}_{22}(s_f,Q^2,s_i) \\ &\quad + f(Q^2)\left[\,\mathcal{G}(s_f,Q^2,s_i) - 2i\,\mathrm{Im}\,\mathcal{G}(s_f,Q^2,s_i)\,\right]\,\Big\}\,\mathcal{M}^{\mathrm{II}}(s_i)\,, \end{aligned} \tag{B.9}$$

where the term in square brackets is precisely the triangle function on the unphysical sheets as presented in Eq. (3.13), using similar arguments as above. As claimed in Sec. 3.3, this gives the analytic continuation of $\mathcal{W}_{\rm df}$ on to the second Riemann sheets in both variables, Eq. (3.12). A similar procedure holds for arbitrary currents with the two hadrons in an arbitrary partial wave, noting that the Lorentz structure does not introduce any physical singularities in the s_i/s_f planes.

Appendix C

Bayesian model average and resampling methods

This appendix addresses the implementation of the Bayesian Model Averaging (BMA) described in Ref. [124], with the jackknife resampling described in Sec. 2.2.6.1. We find that a prescription to implement the BMA mean and error is to form a linear combination of the jackknife ensembles of each model, weighted by the model probability, e.g. with the Akaike Information Criterion (AIC), and then to inflate the error of the ensemble to match the BMA prescription.

Let the parameter a be the estimator of the mean of the observable $\mathcal{A}$,

$$a = \frac{1}{N}\sum_{i}^{N} \mathcal{A}^i \,, \tag{C.1}$$

where the index i indicates each element of an ensemble $\{\mathcal{A}\}$ of independent and identically distributed random variables. The expectation value and variance of a are equal to

$$\langle a \rangle = \langle \mathcal{A} \rangle \,, \tag{C.2}$$

$$\left\langle (a - \langle a \rangle)^2 \right\rangle = \frac{\sigma^2_{\mathcal{A}}}{N} \,, \tag{C.3}$$

where $\sigma^2_{\mathcal{A}} \equiv \left\langle (\mathcal{A} - \langle \mathcal{A} \rangle)^2 \right\rangle$. This last quantity can be calculated from the unbiased estimator

$$\sigma_a^2 = \frac{1}{N(N-1)} \sum_i^N (\mathcal{A}^i - a)^2 \,, \tag{C.4}$$

$$\left\langle \sigma_a^2 \right\rangle = \frac{\sigma^2_{\mathcal{A}}}{N} \,. \tag{C.5}$$

From the central limit theorem we expect a to follow a normal distribution, as long as $\sigma^2_{\mathcal{A}}$ is finite.

Suppose we have different models, M_α, to describe a data set, and from each we can obtain the observable $\mathcal{A}$. In this case we will have access to different ensembles $\{\mathcal{A}_\alpha\}$ of the observable, we will use the notation $\mathcal{A}^i_\alpha$ for elements of each these ensembles. Latin indices will be used for the ensemble index, whereas greek indices will label models. The expectation values of the mean estimator of each ensemble will be denoted as

$$\langle a \rangle_\alpha \equiv \langle a_\alpha \rangle = \left\langle \frac{1}{N} \sum_i^N \mathcal{A}^i_\alpha \right\rangle \,, \tag{C.6}$$

which might be a bit of an abuse in notation, but will come in handy when relating to the Bayesian Model Average (BMA) of Ref. [124]. The mean square error of the mean estimator of each model is

$$\sigma^2_{a,\alpha} = \frac{1}{N(N-1)} \sum_i^N (\mathcal{A}^i_\alpha - a_\alpha)^2 \,, \tag{C.7}$$

$$\left\langle \sigma^2_{a,\alpha} \right\rangle = \frac{\sigma^2_{\mathcal{A}_\alpha}}{N} \,. \tag{C.8}$$

where we introduced $\sigma^2_{\mathcal{A}_\alpha}$ as the variance of the observable when estimated with model M_α. Let us form a new ensemble and call it the *averaged ensemble* $\{\mathcal{A}_{\rm avg}\}$, as a weighted sum of the model ensembles with probabilities p_α associated with each model, e.g. the AIC

weights,

$$\mathcal{A}^i_{\rm avg} \equiv \sum_{\alpha\in M} \mathcal{A}^i_\alpha \, p_\alpha \, . \tag{C.9}$$

The mean estimator of this new ensemble is,

$$a_{\rm avg} = \frac{1}{N}\sum_{i=1}^{N} \mathcal{A}^i_{\rm avg} = \frac{1}{N}\sum_{i=1}^{N}\sum_{\alpha\in M} \mathcal{A}^i_\alpha p_\alpha \, , \tag{C.10}$$

$$= \sum_{\alpha\in M} a_\alpha p_\alpha \, . \tag{C.11}$$

where a_α is the estimator of the mean of the observable given the data is described by model M_α. The expectation value of this quantity, being a linear operation, is equal to

$$\langle a_{\rm avg}\rangle = \sum_{\alpha\in M} \langle a\rangle_\alpha \, p_\alpha \tag{C.12}$$

This equation is identical in structure to Eq. (6.17), so we can claim that

$$\langle a\rangle_{\rm BMA} = \langle a_{\rm avg}\rangle \, . \tag{C.13}$$

Next we calculate the error on the estimator of the mean square error of $a_{\rm avg}$,

$$\sigma^2_{a_{\rm avg}} = \frac{1}{N(N-1)}\sum_{i=1}^{N} (\mathcal{A}^i_{\rm avg} - a_{\rm avg})^2 \, , \tag{C.14}$$

$$= \frac{1}{N(N-1)}\sum_{i=1}^{N} \left(\sum_{\alpha\in M} p_\alpha(\mathcal{A}^i_\alpha - a_\alpha)\right)^2 , \tag{C.15}$$

$$= \sum_{\alpha,\beta\in M} p_\alpha p_\beta \frac{1}{N(N-1)}\sum_{i=1}^{N} (\mathcal{A}^i_\alpha - a_\alpha)(\mathcal{A}^i_\beta - a_\beta) \, , \tag{C.16}$$

$$= \sum_{\alpha,\beta\in M} p_\alpha p_\beta \sigma^2_{a,\alpha\beta} \, , \tag{C.17}$$

$$\left\langle \sigma^2_{a_{\rm avg}} \right\rangle = \sum_{\alpha,\beta\in M} p_\alpha p_\beta \frac{\sigma^2_{\mathcal{A}_\alpha \mathcal{A}_\beta}}{N} \, , \tag{C.18}$$

where we adopted the definition $\sigma^2_{a,\alpha\alpha} \equiv \sigma^2_{a,\alpha}$. The expectation value of this quantity, is

the weighted sum, with the probabilities $p_\alpha p_\beta$, of all the elements of the covariance matrix,

$$\frac{\sigma^2_{\mathcal{A}_\alpha \mathcal{A}_\beta}}{N} = \Big\langle (a_\alpha - \langle a \rangle_\alpha)(a_\beta - \langle a \rangle_\beta) \Big\rangle \,. \tag{C.19}$$

Note that trying to implement the same abuse of notation for the expectation value as we did for $\langle a \rangle_\alpha$ is ambiguous. This expectation is evaluated over configurations and contains estimators from two different models, which was not needed or considered for the results presented in Ref. [124].

The important point is that the expectation value of Eq. (C.18) is not analogous to Eq. (6.18), which in this notation would be given by

$$\sigma^2_{a,\mathrm{BMA}} = \sum_{\alpha \in M} p_\alpha \sigma^2_{a,\alpha} + \frac{1}{2} \sum_{\alpha,\beta} p_\alpha p_\beta (a_\alpha - a_\beta)^2 \,. \tag{C.20}$$

Their difference is given by,

$$\sigma^2_{a,\mathrm{BMA}} - \sigma^2_{a_{\mathrm{avg}}} = \frac{1}{2} \sum_{\alpha,\beta \in M} p_\alpha p_\beta \big((a_\alpha - a_\beta)^2 + \sigma^2_{a,\alpha} - 2\sigma^2_{a,\alpha\beta} + \sigma^2_{a,\beta} \big) \,, \tag{C.21}$$

$$\Big\langle \sigma^2_{a,\mathrm{BMA}} \Big\rangle - \Big\langle \sigma^2_{a_{\mathrm{avg}}} \Big\rangle = \frac{1}{2} \sum_{\alpha,\beta \in M} p_\alpha p_\beta \bigg((\langle a \rangle_\alpha - \langle a \rangle_\beta)^2 + \frac{2}{N} \Big(\sigma^2_{\mathcal{A}_\alpha} - 2\sigma^2_{\mathcal{A}_\alpha \mathcal{A}_\beta} + \sigma^2_{\mathcal{A}_\beta} \Big) \bigg) \,, \tag{C.22}$$

where we the quantities on the right hand side are greater or equal to zero, meaning that the variance of the BMA prescription is always greater or equal than the variance of the averaged ensemble. Notice that the difference between the BMA errors and $\sigma^2_{a_{\mathrm{avg}}}$ has a term of order zero in addition to the $1/N$ term. This means that this difference is not a statistical bias, but a systematic effect. In practice we notice that this effect is typically on the order of 10% for the datasets presented in this work.

Appendix D

Finite volume correction in weakly interacting systems

In this appendix we present a few simple examples of the calculation of the finite volume corrections in the limit of a two-meson non-interacting system. In this case we can associate each level to a meson pair with momentum type $\mathbf{k}$ and $\mathbf{P}-\mathbf{k}$, and total momentum $\mathbf{P}$. Note that the wave function of the system will be given by the linear combination of the contributions with momentum $R\,\mathbf{k}$, for all rotations R in the little group of $\mathbf{P}$, as given in Eq. (2.20).

In the non-interacting case it is most convenient to utilize the correction given by Eq. (2.5), which in the non-interacting limit of a single channel reduces to

$$\widetilde{\mathcal{R}}_{\ell,\ell'}^{\Lambda\mu,\mathbf{P},\mathbf{k}} = 2E_{\text{n.i.}} \lim_{E\to E_{\text{n.i.}}} (E-E_{\text{n.i.}}) F_{\ell,\ell'}^{\Sigma}(E,\mathbf{P},L)\,, \tag{D.1}$$

where we have set K-matrix to zero, $\mathcal{K}(s)=0$, and $F_{\ell,\ell'}^{\Sigma} = F_{\ell,\ell'} - i\rho\,\delta_{\ell,\ell'}$. We use the state labeling $|\mathfrak{n}\rangle = |\Lambda\mu,\mathbf{P},\mathbf{k}\rangle$ with $\Lambda\mu$ the lattice irrep and the row within. Since we only deal with simple cases, we assume that each partial-wave ℓ is only subduced to the irrep Λ once, which is in general not the case. The non-interacting energy is given by $E_{\text{n.i.}} = \omega_k + \omega_{Pk}$, where $\omega_k = \sqrt{\mathbf{k}^2+m^2}$ and $\omega_{Pk} = \sqrt{(\mathbf{P}-\mathbf{k})^2+m^2}$.

Let us look first at the case of an S-wave, which only subduces to one-dimensional irreps, so we can drop the row label μ, and we use the expression for $F_{0,0}$ in the S-wave given in App. B.2 of Ref. [111],

$$\widetilde{\mathcal{R}}_{0,0}^{\Lambda,\mathbf{P},\mathbf{k}} = 2E_{\text{n.i.}} \lim_{E\to E_{\text{n.i.}}} (E - E_{\text{n.i.}}) \frac{1}{L^3} \sum_{\mathbf{q}} \frac{1}{2\omega_q} \frac{1}{E - (\omega_q - \omega_{Pq})} \frac{1}{E - (\omega_q + \omega_{Pq})}\,, \tag{D.2}$$

where L^3 is the lattice volume, and the summation goes over all allowed lattice momenta $\mathbf{q} = \frac{2\pi}{L}\mathbf{d}$, with $\mathbf{d}$ a triplet of integers. This equation simplifies to

$$\widetilde{\mathcal{R}}_{0,0}^{\Lambda,\mathbf{P},\mathbf{k}} = \frac{\omega_k + \omega_{Pk}}{2L^3\omega_k\omega_{Pk}} \lim_{E\to E_{\text{n.i.}}} \sum_{\mathbf{q}} \frac{E - (\omega_k + \omega_{Pk})}{E - (\omega_q + \omega_{Pq})}\,. \tag{D.3}$$

In the case where particles are identical, the finite-volume correction for $\mathbf{P} = 0$ is equal to

$$\widetilde{\mathcal{R}}_{0,0}^{A_1^+,\mathbf{0},\mathbf{k}} = \frac{1}{L^3\omega_k} N_k\,, \tag{D.4}$$

where N_k is the number of different allowed lattice rotations of momentum $\mathbf{k}$. In the case of non zero momentum for identical particles we get contributions from $\mathbf{q} = \mathbf{k}$ as well as $\mathbf{q} = \mathbf{P} - \mathbf{k}$, which will not be related by a rotation in the little group of $\mathbf{P}$, and the finite volume correction is equal to

$$\widetilde{\mathcal{R}}_{0,0}^{\Lambda,\mathbf{P},\mathbf{k}} = \frac{\omega_k + \omega_{Pk}}{L^3\omega_k\omega_{Pk}} N_{Pk}\,, \tag{D.5}$$

where N_{Pk} is the number of different momenta $R\,\mathbf{k}$ that can be generated from the rotation R, which belongs to the little group of $\mathbf{P}$.

In this prescription the finite volume correction is given by

$$\mathcal{F}_{\Lambda\mu,\mathbf{P},\mathbf{k}}^{(L)} = r_{\mathbf{P},\mathbf{k}}^{\Lambda\mu,\ell}(L)\, f(E_{\text{n.i.}}^2)\,, \tag{D.6}$$

where $f(s)$ is an infinite volume production form factor from a current with $J = \ell$, from

which the threshold behavior of $k^{\star\ell}$ has been removed, and the finite-volume correction is given by

$$r^{\Lambda\mu,\ell}_{\mathbf{P},\mathbf{k}}(L) = k^{\star\ell}\sqrt{\widetilde{\mathcal{R}}^{\Lambda\mu,\mathbf{P},\mathbf{k}}_{\ell,\ell}}\,, \tag{D.7}$$

which we can define in this case because we are only looking at examples where $\widetilde{\mathcal{R}}$ is diagonal in partial-wave space, which is in general not the case.

We can now specialize back to the case of $\ell = 0$, to find the finite volume correction for several states

$$\frac{r^{A_1^+,0}_{[000],[000]}}{m} = (mL)^{-3/2}\,, \tag{D.8}$$

$$\frac{r^{A_1^+,0}_{[000],[100]}}{m} = \frac{1}{mL}\sqrt{\frac{6}{\omega_1 L}}\,, \tag{D.9}$$

$$\frac{r^{A_{1/2},0}_{[100],[100]}}{m} = \frac{1}{(mL)^{3/2}}\sqrt{\frac{\omega_1+m}{\omega_1}}\,, \tag{D.10}$$

$$\frac{r^{A_{1/2},0}_{[100],[010]}}{m} = \frac{2}{mL}\sqrt{\frac{\omega_1+\omega_2}{\omega_1\omega_2 L}}\,. \tag{D.11}$$

where we used the notation $k = |\mathbf{k}|^2$ for the subindex of ω_k.

In the case of an arbitrary partial wave ℓ, ignoring the possible multiple embeddings of the wave into the irrep Λ, using F from App. B.2 of Ref. [111], Eq. (D.3) becomes

$$\begin{aligned}\widetilde{\mathcal{R}}^{\Lambda\mu,\mathbf{P},\mathbf{k}}_{\ell,\ell'} = \frac{\omega_k+\omega_{Pk}}{2L^3\omega_k\omega_{Pk}} \\ \times \lim_{E\to E_{\text{n.i.}}} \sum_{\mathbf{q}} \mathcal{S}^{\Lambda\mu}_{\lambda}\mathcal{D}^{(\ell)}_{m\lambda}(\mathbf{P})\mathcal{Y}_{\ell m}(\mathbf{q}^\star)\mathcal{Y}^*_{\ell m'}(\mathbf{q}^\star)\mathcal{D}^{(\ell')*}_{\lambda' m'}(\mathbf{P})\mathcal{S}^{\Lambda\mu}_{\lambda'} \\ \times \frac{E-(\omega_k+\omega_{Pk})}{E-(\omega_q+\omega_{Pq})}\,.\end{aligned} \tag{D.12}$$

where $\mathcal{S}^{\Lambda\mu}_{\lambda}$ is the subduction coefficient, which can be found in Refs. [60, 61], $\mathcal{Y}_{\ell m}$ was introduced in Eq. (3.73), and $\mathcal{D}^{(\ell)}$ is the Wigner-D matrix, evaluated for the rotation defined by $R\,\hat{z} = \hat{\mathbf{P}}$.

We can calculate the finite volume correction for a couple of simple cases in the P-wave

$$\frac{r^{T_1^{\pm},1}_{[000],[100]}}{m} = \frac{1}{mL}\sqrt{\frac{6}{\omega_1 L}}\,, \tag{D.13}$$

$$\frac{r^{A_{1/2},1}_{[100],[100]}}{m} = \frac{1}{(mL)^{3/2}}\sqrt{\frac{3(\omega_1+m)}{\omega_1}}\,. \tag{D.14}$$

and we can note that the finite volume correction for the S-wave and P-wave subduced to the state $\left|A_{1/2},[100],[100]\right\rangle$, where the '1/2' index depends on the parity of the system, differs by a factor of $\sqrt{3}$.

Bibliography

[1] W. E. Lamb. Nobel Lecture. www.nobelprize.org, Nobel Foundation, 1955.

[2] Patrick Koppenburg. List of hadrons observed at the LHC. LHCb-FIGURE-2021-001, Mar 2021. See 2022 update online.

[3] R. Hofstadter and R. W. McAllister. Electron Scattering From the Proton. *Phys. Rev.*, 98:217–218, 1955.

[4] W. Xiong et al. A small proton charge radius from an electron–proton scattering experiment. *Nature*, 575(7781):147–150, 2019.

[5] Haiyan Gao and Marc Vanderhaeghen. The proton charge radius. *Rev. Mod. Phys.*, 94(1):015002, 2022.

[6] Kenneth G. Wilson. Confinement of Quarks. *Phys. Rev. D*, 10:2445–2459, 1974.

[7] Gerard 't Hooft and M. J. G. Veltman. Regularization and Renormalization of Gauge Fields. *Nucl. Phys. B*, 44:189–213, 1972.

[8] Georges Aad et al. (ATLAS). Observation of a new particle in the search for the Standard Model Higgs boson with the ATLAS detector at the LHC. *Phys. Lett. B*, 716:1–29, 2012.

[9] Serguei Chatrchyan et al. (CMS). Observation of a New Boson at a Mass of 125 GeV with the CMS Experiment at the LHC. *Phys. Lett. B*, 716:30–61, 2012.

[10] R. L. Workman et al. (Particle Data Group). Review of Particle Physics. *PTEP*, 2022:083C01, 2022.

[11] Arthur M. Jaffe and Edward Witten. Quantum Yang-Mills theory. 2000.

[12] M. Albaladejo and J. A. Oller. On the size of the sigma meson and its nature. *Phys. Rev. D*, 86:034003, 2012.

[13] Shuang-shi Fang, Bastian Kubis, and Andrzej Kupsc. What can we learn about light-meson interactions at electron–positron colliders? *Prog. Part. Nucl. Phys.*, 120:103884, 2021.

[14] R. R. Akhmetshin et al. (CMD-2). Measurement of e+ e- —> pi+ pi- cross-section with CMD-2 around rho meson. *Phys. Lett. B*, 527:161–172, 2002.

[15] R. R. Akhmetshin et al. (CMD-2). Reanalysis of hadronic cross-section measurements at CMD-2. *Phys. Lett. B*, 578:285–289, 2004.

[16] V. M. Aul'chenko et al. Measurement of the e+ e- —> pi+ pi- cross section with the CMD-2 detector in the 370 - 520-MeV c.m. energy range. *JETP Lett.*, 84:413–417, 2006.

[17] R. R. Akhmetshin et al. (CMD-2). High-statistics measurement of the pion form factor in the rho-meson energy range with the CMD-2 detector. *Phys. Lett. B*, 648:28–38, 2007.

[18] M. N. Achasov et al. Study of the process e+ e- —> pi+ pi- in the energy region 400 < s**(1/2) < 1000-MeV. *J. Exp. Theor. Phys.*, 101(6):1053–1070, 2005.

[19] M. N. Achasov et al. Update of the e+ e- —> pi+ pi- cross-section measured by SND detector in the energy region 400-MeV < s**(1/2) < file1000-MeV. *J. Exp. Theor. Phys.*, 103:380–384, 2006.

[20] S. Binner, Johann H. Kuhn, and K. Melnikov. Measuring sigma(e+ e- —> hadrons) using tagged photon. *Phys. Lett. B*, 459:279–287, 1999.

[21] F. Ambrosino et al. (KLOE). Measurement of $\sigma(e^+e^- \to \pi^+\pi^-\gamma(\gamma)$ and the dipion contribution to the muon anomaly with the KLOE detector. *Phys. Lett. B*, 670:285–291, 2009.

[22] F. Ambrosino et al. (KLOE). Measurement of $\sigma(e^+e^- \to \pi^+\pi^-)$ from threshold to 0.85 GeV^2 using Initial State Radiation with the KLOE detector. *Phys. Lett. B*, 700:102–110, 2011.

[23] D. Babusci et al. (KLOE). Precision measurement of $\sigma(e^+e^- \to \pi^+\pi^-\gamma)/\sigma(e^+e^- \to \mu^+\mu^-\gamma)$ and determination of the $\pi^+\pi^-$ contribution to the muon anomaly with the KLOE detector. *Phys. Lett. B*, 720:336–343, 2013.

[24] A. Anastasi et al. (KLOE-2). Combination of KLOE $\sigma\big(e^+e^- \to \pi^+\pi^-\gamma(\gamma)\big)$ measurements and determination of $a_\mu^{\pi^+\pi^-}$ in the energy range $0.10 < s < 0.95$ GeV^2. *JHEP*, 03:173, 2018.

[25] Bernard Aubert et al. (BaBar). Precise measurement of the e+ e- —> pi+ pi- (gamma) cross section with the Initial State Radiation method at BABAR. *Phys. Rev. Lett.*, 103:231801, 2009.

[26] J. P. Lees et al. (BaBar). Precise Measurement of the $e^+e^- \to \pi^+\pi^-(\gamma)$ Cross Section with the Initial-State Radiation Method at BABAR. *Phys. Rev. D*, 86:032013, 2012.

[27] M. Ablikim et al. (BESIII). Measurement of the $e^+e^- \to \pi^+\pi^-$ cross section between 600 and 900 MeV using initial state radiation. *Phys. Lett. B*, 753:629–638, 2016. [Erratum: Phys.Lett.B 812, 135982 (2021)].

[28] M. Fujikawa et al. (Belle). High-Statistics Study of the tau- —> pi- pi0 nu(tau) Decay. *Phys. Rev. D*, 78:072006, 2008.

[29] Gilberto Colangelo, Martin Hoferichter, and Peter Stoffer. Two-pion contribution to hadronic vacuum polarization. *JHEP*, 02:006, 2019.

[30] J. P. Lees et al. (BaBar). Initial-State Radiation Measurement of the e^+e^-– > $\pi^+\pi^-\pi^+\pi^-$ Cross Section. *Phys. Rev. D*, 85:112009, 2012.

[31] J. P. Lees et al. (BaBar). Study of the process $e^+e^- \to \pi^+\pi^-\eta$ using initial state radiation. *Phys. Rev. D*, 97:052007, 2018.

[32] J. R. Pelaez, A. Rodas, and J. Ruiz De Elvira. Global parameterization of $\pi\pi$ scattering up to 2 GeV. *Eur. Phys. J. C*, 79(12):1008, 2019.

[33] G. Breit and E. Wigner. Capture of Slow Neutrons. *Phys. Rev.*, 49:519–531, 1936.

[34] Maxim Mai, Ulf-G. Meissner, and Carsten Urbach. Towards a theory of hadron resonances. *Phys. Rept.*, 1001:1–66, 2023.

[35] Wei Sun, Andrei Alexandru, Ying Chen, Terrence Draper, Zhaofeng Liu, and Yi-Bo Yang (χQCD). Anatomy of the ρ resonance from lattice QCD at the physical point. *Chin. Phys. C*, 42(6):063102, 2018.

[36] Thomas DeGrand and Ethan T. Neil. Repurposing lattice QCD results for composite phenomenology. *Phys. Rev. D*, 101(3):034504, 2020.

[37] Xu Feng, Sinya Aoki, Shoji Hashimoto, and Takashi Kaneko. Timelike pion form factor in lattice QCD. *Phys. Rev. D*, 91(5):054504, 2015.

[38] Christian Andersen, John Bulava, Ben Hörz, and Colin Morningstar. The $I = 1$ pion-pion scattering amplitude and timelike pion form factor from $N_\mathrm{f} = 2 + 1$ lattice QCD. *Nucl. Phys. B*, 939:145–173, 2019.

[39] Felix Erben, Jeremy R. Green, Daniel Mohler, and Hartmut Wittig. Rho resonance, timelike pion form factor, and implications for lattice studies of the hadronic vacuum polarization. *Phys. Rev. D*, 101(5):054504, 2020.

[40] S. R. Amendolia et al. (NA7). A Measurement of the Space - Like Pion Electromagnetic Form-Factor. *Nucl. Phys. B*, 277:168, 1986.

[41] T. Horn et al. (Jefferson Lab F(pi)-2). Determination of the Charged Pion Form Factor at Q**2 = 1.60 and 2.45-(GeV/c)**2. *Phys. Rev. Lett.*, 97:192001, 2006.

[42] V. Tadevosyan et al. (Jefferson Lab F(pi)). Determination of the pion charge form-factor for Q**2 = 0.60-GeV**2 - 1.60-GeV**2. *Phys. Rev. C*, 75:055205, 2007.

[43] H. P. Blok et al. (Jefferson Lab). Charged pion form factor between Q^2=0.60 and 2.45 GeV^2. I. Measurements of the cross section for the $^1\mathrm{H}(e, e'\pi^+)n$ reaction. *Phys. Rev. C*, 78:045202, 2008.

[44] G. M. Huber et al. (Jefferson Lab). Charged pion form-factor between Q**2 = 0.60-GeV**2 and 2.45-GeV**2. II. Determination of, and results for, the pion form-factor. *Phys. Rev. C*, 78:045203, 2008.

[45] Robert L. Jaffe. Ambiguities in the definition of local spatial densities in light hadrons. *Phys. Rev. D*, 103(1):016017, 2021.

[46] J. P. Lees et al. (BaBar). Measurement of the spectral function for the $\tau^- \to K^- K_S \nu_\tau$ decay. *Phys. Rev. D*, 98(3):032010, 2018.

[47] Dominik Stamen, Deepti Hariharan, Martin Hoferichter, Bastian Kubis, and Peter Stoffer. Kaon electromagnetic form factors in dispersion theory. *Eur. Phys. J. C*, 82(5):432, 2022.

[48] A. S. Miramontes and Adnan Bashir. Timelike electromagnetic kaon form factor. *Phys. Rev. D*, 107(1):014016, 2023.

[49] Kenneth M. Watson. The Effect of final state interactions on reaction cross-sections. *Phys. Rev.*, 88:1163–1171, 1952.

[50] R. Omnes. On the Solution of certain singular integral equations of quantum field theory. *Nuovo Cim.*, 8:316–326, 1958.

[51] K. Symanzik. Continuum Limit and Improved Action in Lattice Theories. 1. Principles and φ^4 Theory. *Nucl. Phys. B*, 226:187–204, 1983.

[52] Christof Gattringer and Christian B. Lang. *Quantum chromodynamics on the lattice*, volume 788. Springer, Berlin, 2010.

[53] R. Sommer. A New way to set the energy scale in lattice gauge theories and its applications to the static force and α_s in SU(2) Yang-Mills theory. *Nucl. Phys. B*, 411:839–854, 1994.

[54] L. Maiani and M. Testa. Final state interactions from Euclidean correlation functions. *Phys. Lett. B*, 245:585–590, 1990.

[55] M. Luscher. Volume Dependence of the Energy Spectrum in Massive Quantum Field Theories. 1. Stable Particle States. *Commun. Math. Phys.*, 104:177, 1986.

[56] M. Luscher. Volume Dependence of the Energy Spectrum in Massive Quantum Field Theories. 2. Scattering States. *Commun. Math. Phys.*, 105:153–188, 1986.

[57] Raúl A. Briceño, Juan V. Guerrero, Maxwell T. Hansen, and Alexandru M. Sturzu. Role of boundary conditions in quantum computations of scattering observables. *Phys. Rev. D*, 103(1):014506, 2021.

[58] Raul A. Briceno. Two-particle multichannel systems in a finite volume with arbitrary spin. *Phys. Rev. D*, 89(7):074507, 2014.

[59] Luka Leskovec and Sasa Prelovsek. Scattering phase shifts for two particles of different mass and non-zero total momentum in lattice QCD. *Phys. Rev. D*, 85:114507, 2012.

[60] Jozef J. Dudek, Robert G. Edwards, Michael J. Peardon, David G. Richards, and Christopher E. Thomas. Toward the excited meson spectrum of dynamical QCD. *Phys. Rev. D*, 82:034508, 2010.

[61] Christopher E. Thomas, Robert G. Edwards, and Jozef J. Dudek. Helicity operators for mesons in flight on the lattice. *Phys. Rev. D*, 85:014507, 2012.

[62] David C. Moore and George Tamminga Fleming. Angular momentum on the lattice: The Case of non-zero linear momentum. *Phys. Rev. D*, 73:014504, 2006. [Erratum: Phys.Rev.D 74, 079905 (2006)].

[63] Jozef J. Dudek, Robert G. Edwards, Christopher E. Thomas, and David J. Wilson (Hadron Spectrum). Resonances in coupled $\pi K - \eta K$ scattering from quantum chromodynamics. *Phys. Rev. Lett.*, 113(18):182001, 2014.

[64] David J. Wilson, Jozef J. Dudek, Robert G. Edwards, and Christopher E. Thomas. Resonances in coupled $\pi K, \eta K$ scattering from lattice QCD. *Phys. Rev. D*, 91(5):054008, 2015.

[65] David J. Wilson, Raul A. Briceno, Jozef J. Dudek, Robert G. Edwards, and Christopher E. Thomas. Coupled $\pi\pi, K\bar{K}$ scattering in P-wave and the ρ resonance from lattice QCD. *Phys. Rev. D*, 92(9):094502, 2015.

[66] Jozef J. Dudek, Robert G. Edwards, and David J. Wilson (Hadron Spectrum). An a_0 resonance in strongly coupled $\pi\eta$, $K\overline{K}$ scattering from lattice QCD. *Phys. Rev. D*, 93(9):094506, 2016.

[67] Graham Moir, Michael Peardon, Sinéad M. Ryan, Christopher E. Thomas, and David J. Wilson. Coupled-Channel $D\pi$, $D\eta$ and $D_s\bar{K}$ Scattering from Lattice QCD. *JHEP*, 10:011, 2016.

[68] Raul A. Briceno, Jozef J. Dudek, Robert G. Edwards, and David J. Wilson. Isoscalar $\pi\pi, K\overline{K}, \eta\eta$ scattering and the σ, f_0, f_2 mesons from QCD. *Phys. Rev. D*, 97(5):054513, 2018.

[69] Antoni J. Woss, Christopher E. Thomas, Jozef J. Dudek, Robert G. Edwards, and David J. Wilson. b_1 resonance in coupled $\pi\omega$, $\pi\phi$ scattering from lattice QCD. *Phys. Rev. D*, 100(5):054506, 2019.

[70] Antoni J. Woss, Jozef J. Dudek, Robert G. Edwards, Christopher E. Thomas, and David J. Wilson (Hadron Spectrum). Decays of an exotic 1^{-+} hybrid meson resonance in QCD. *Phys. Rev. D*, 103(5):054502, 2021.

[71] John Bulava et al. (Baryon Scattering (BaSc)). Lattice QCD study of $\pi\Sigma$-$\mathrm{K}^{-}\mathrm{N}$ scattering and the $\Lambda(1405)$ resonance. *Phys. Rev. D*, 109(1):014511, 2024.

[72] Sasa Prelovsek, Sara Collins, Daniel Mohler, M. Padmanath, and Stefano Piemonte. Charmonium-like resonances with $J^{PC} = 0^{++}$, 2^{++} in coupled $D\overline{D}$, $D_s\overline{D}_s$ scattering on the lattice. *JHEP*, 06:035, 2021.

[73] Antoni J. Woss, David J. Wilson, and Jozef J. Dudek (Hadron Spectrum). Efficient solution of the multichannel Lüscher determinant condition through eigenvalue decomposition. *Phys. Rev. D*, 101(11):114505, 2020.

[74] Raul A. Briceno, Jozef J. Dudek, and Ross D. Young. Scattering processes and resonances from lattice QCD. *Rev. Mod. Phys.*, 90(2):025001, 2018.

[75] Laurent Lellouch and Martin Luscher. Weak transition matrix elements from finite volume correlation functions. *Commun. Math. Phys.*, 219:31–44, 2001.

[76] Harvey B. Meyer. Lattice QCD and the Timelike Pion Form Factor. *Phys. Rev. Lett.*, 107:072002, 2011.

[77] Raúl A. Briceño, Maxwell T. Hansen, and André Walker-Loud. Multichannel $1 \to 2$ transition amplitudes in a finite volume. *Phys. Rev. D*, 91(3):034501, 2015.

[78] Raúl A. Briceño and Maxwell T. Hansen. Multichannel $0 \to 2$ and $1 \to 2$ transition amplitudes for arbitrary spin particles in a finite volume. *Phys. Rev. D*, 92(7):074509, 2015.

[79] Raúl A. Briceño, Jozef J. Dudek, and Luka Leskovec. Constraining $1+\mathcal{J} \to 2$ coupled-channel amplitudes in finite-volume. *Phys. Rev. D*, 104(5):054509, 2021.

[80] Huey-Wen Lin et al. (Hadron Spectrum). First results from 2+1 dynamical quark flavors on an anisotropic lattice: Light-hadron spectroscopy and setting the strange-quark mass. *Phys. Rev. D*, 79:034502, 2009.

[81] Robert G. Edwards, Balint Joo, and Huey-Wen Lin. Tuning for Three-flavors of Anisotropic Clover Fermions with Stout-link Smearing. *Phys. Rev. D*, 78:054501, 2008.

[82] David J. Wilson, Raul A. Briceno, Jozef J. Dudek, Robert G. Edwards, and Christopher E. Thomas. The quark-mass dependence of elastic πK scattering from QCD. *Phys. Rev. Lett.*, 123(4):042002, 2019.

[83] Arkaitz Rodas, Jozef J. Dudek, and Robert G. Edwards. Constraining the quark mass dependence of the lightest resonance in QCD. 4 2023.

[84] Arkaitz Rodas, Jozef J. Dudek, and Robert G. Edwards (Hadron Spectrum). Quark mass dependence of $\pi\pi$ scattering in isospin 0, 1, and 2 from lattice QCD. *Phys. Rev. D*, 108(3):034513, 2023.

[85] Archana Radhakrishnan, Jozef J. Dudek, and Robert G. Edwards (Hadron Spectrum). Radiative decay of the resonant K* and the $\gamma K \to K\pi$ amplitude from lattice QCD. *Phys. Rev. D*, 106(11):114513, 2022.

[86] Jozef J. Dudek, Robert G. Edwards, Nilmani Mathur, and David G. Richards. Charmonium excited state spectrum in lattice QCD. *Phys. Rev. D*, 77:034501, 2008.

[87] Benoit Blossier, Michele Della Morte, Georg von Hippel, Tereza Mendes, and Rainer Sommer. On the generalized eigenvalue method for energies and matrix elements in lattice field theory. *JHEP*, 04:094, 2009.

[88] Martin Luscher and Ulli Wolff. How to Calculate the Elastic Scattering Matrix in Two-dimensional Quantum Field Theories by Numerical Simulation. *Nucl. Phys. B*, 339:222–252, 1990.

[89] G. Parisi. The Strategy for Computing the Hadronic Mass Spectrum. *Phys. Rept.*, 103:203–211, 1984.

[90] G. Peter Lepage. The Analysis of Algorithms for Lattice Field Theory. In *Theoretical Advanced Study Institute in Elementary Particle Physics*, 6 1989.

[91] Jozef J. Dudek, Robert G. Edwards, and Christopher E. Thomas (Hadron Spectrum). Energy dependence of the ρ resonance in $\pi\pi$ elastic scattering from lattice QCD. *Phys. Rev. D*, 87(3):034505, 2013. [Erratum: Phys.Rev.D 90, 099902 (2014)].

[92] Jozef J. Dudek, Robert G. Edwards, Balint Joo, Michael J. Peardon, David G. Richards, and Christopher E. Thomas. Isoscalar meson spectroscopy from lattice QCD. *Phys. Rev. D*, 83:111502, 2011.

[93] Jozef J. Dudek, Robert G. Edwards, and Christopher E. Thomas. S and D-wave phase shifts in isospin-2 pi pi scattering from lattice QCD. *Phys. Rev. D*, 86:034031, 2012.

[94] Christian J. Shultz, Jozef J. Dudek, and Robert G. Edwards. Excited meson radiative transitions from lattice QCD using variationally optimized operators. *Phys. Rev. D*, 91(11):114501, 2015.

[95] G. D'Agostini. On the use of the covariance matrix to fit correlated data. *Nucl. Instrum. Meth. A*, 346:306–311, 1994.

[96] Michael Peardon, John Bulava, Justin Foley, Colin Morningstar, Jozef Dudek, Robert G. Edwards, Balint Joo, Huey-Wen Lin, David G. Richards, and Keisuke Jimmy Juge (Hadron Spectrum). A Novel quark-field creation operator construction for hadronic physics in lattice QCD. *Phys. Rev. D*, 80:054506, 2009.

[97] B. Efron. Bootstrap Methods: Another Look at the Jackknife. *Annals Statist.*, 7(1):1–26, 1979.

[98] Raúl A. Briceño, Andrew W. Jackura, Felipe G. Ortega-Gama, and Keegan H. Sherman. On-shell representations of two-body transition amplitudes: Single external current. *Phys. Rev. D*, 103(11):114512, 2021.

[99] L. D. Landau. On analytic properties of vertex parts in quantum field theory. *Nucl. Phys.*, 13(1):181–192, 1959.

[100] Vladimir Gribov. *Strong Interactions of Hadrons at High Energies : Gribov Lectures on Theoretical Physics*. Oxford University Press, 2009.

[101] Raúl A. Briceño, Maxwell T. Hansen, and Andrew W. Jackura. Consistency checks for two-body finite-volume matrix elements: I. Conserved currents and bound states. *Phys. Rev. D*, 100(11):114505, 2019.

[102] Jiunn-Wei Chen, Gautam Rupak, and Martin J. Savage. Suppressed amplitudes in n p —> d gamma. *Phys. Lett. B*, 464:1–11, 1999.

[103] David B. Kaplan, Martin J. Savage, and Mark B. Wise. A Perturbative calculation of the electromagnetic form-factors of the deuteron. *Phys. Rev. C*, 59:617–629, 1999.

[104] V. N. Gribov. Analytic properties of the partial wave amplitudes and the asymptotic behavior of the scattering amplitude. *Sov. Phys. JETP*, 15:873, 1962.

[105] T. Bauer, J. Gegelia, and S. Scherer. Magnetic moment of the Roper resonance. *Phys. Lett. B*, 715:234–240, 2012.

[106] A. I. Machavariani and Amand Faessler. Ward-Takahashi identity, soft photon theorem and the magnetic moment of the Delta resonance. 3 2007.

[107] Raúl A. Briceño and Maxwell T. Hansen. Relativistic, model-independent, multichannel $2 \to 2$ transition amplitudes in a finite volume. *Phys. Rev. D*, 94(1):013008, 2016.

[108] R. E. Cutkosky. Singularities and discontinuities of Feynman amplitudes. *J. Math. Phys.*, 1:429–433, 1960.

[109] Feng-Kun Guo, Xiao-Hai Liu, and Shuntaro Sakai. Threshold cusps and triangle singularities in hadronic reactions. *Prog. Part. Nucl. Phys.*, 112:103757, 2020.

[110] Keegan H. Sherman, Felipe G. Ortega-Gama, Raúl A. Briceño, and Andrew W. Jackura. Two-current transition amplitudes with two-body final states. *Phys. Rev. D*, 105(11):114510, 2022.

[111] Alessandro Baroni, Raúl A. Briceño, Maxwell T. Hansen, and Felipe G. Ortega-Gama. Form factors of two-hadron states from a covariant finite-volume formalism. *Phys. Rev. D*, 100(3):034511, 2019.

[112] Raul A. Briceno and Zohreh Davoudi. Moving multichannel systems in a finite volume with application to proton-proton fusion. *Phys. Rev. D*, 88(9):094507, 2013.

[113] V. Bernard, D. Hoja, U. G. Meissner, and A. Rusetsky. Matrix elements of unstable states. *JHEP*, 09:023, 2012.

[114] William Detmold and Michael Flynn. Finite-volume matrix elements in multi-boson states. *Phys. Rev. D*, 91(7):074509, 2015.

[115] S. R. Beane, P. F. Bedaque, A. Parreno, and M. J. Savage. Two nucleons on a lattice. *Phys. Lett. B*, 585:106–114, 2004.

[116] Maxwell T. Hansen, Fernando Romero-López, and Stephen R. Sharpe. Decay amplitudes to three hadrons from finite-volume matrix elements. *JHEP*, 04:113, 2021.

[117] Maxwell T. Hansen, Raul A. Briceño, Robert G. Edwards, Christopher E. Thomas, and David J. Wilson (Hadron Spectrum). Energy-Dependent $\pi^+\pi^+\pi^+$ Scattering Amplitude from QCD. *Phys. Rev. Lett.*, 126:012001, 2021.

[118] Bernard Aubert et al. (BaBar). The $e^+e^- \to \pi^+\pi^-\pi^+\pi^-$, $K^+K^-\pi^+\pi^-$, and $K^+K^-K^+K^-$ cross sections at center-of-mass energies 0.5-GeV - 4.5-GeV measured with initial-state radiation. *Phys. Rev. D*, 71:052001, 2005.

[119] Bernard Aubert et al. (BaBar). The e+ e- —> 2(pi+ pi-) pi0, 2(pi+ pi-) eta, K+ K- pi+ pi- pi0 and K+ K- pi+ pi- eta Cross Sections Measured with Initial-State Radiation. *Phys. Rev. D*, 76:092005, 2007. [Erratum: Phys.Rev.D 77, 119902 (2008)].

[120] M. Nozar et al. (E852). A Study of the reaction pi- p —> omega pi- p at 18-GeV/c: The D and S decay amplitudes for b(1)(1235) —> omega pi. *Phys. Lett. B*, 541:35–44, 2002.

[121] Jozef J. Dudek, Robert G. Edwards, Peng Guo, and Christopher E. Thomas (Hadron Spectrum). Toward the excited isoscalar meson spectrum from lattice QCD. *Phys. Rev. D*, 88(9):094505, 2013.

[122] G. J. Gounaris and J. J. Sakurai. Finite width corrections to the vector meson dominance prediction for $\rho \to e^+e^-$. *Phys. Rev. Lett.*, 21:244–247, 1968.

[123] J. Gasser and H. Leutwyler. Quark Masses. *Phys. Rept.*, 87:77–169, 1982.

[124] William I. Jay and Ethan T. Neil. Bayesian model averaging for analysis of lattice field theory results. *Phys. Rev. D*, 103:114502, 2021.

[125] Alexander Segner, Andrew Hanlon, Andreas Risch, and Hartmut Wittig. Setting the Scale Using Baryon Masses with Isospin-Breaking Corrections. In *Proceedings of The 39th International Symposium on Lattice Field Theory — PoS(LATTICE2022)*, volume 430, page 084, 2023.

[126] Craig McRae and P. G. Blunden. Novel approach to the global analysis of proton form factors in elastic electron-proton scattering. *Phys. Rev. C*, 109(1):015503, 2024.

[127] M. A. B. Beg and A. Zepeda. Pion radius and isovector nucleon radii in the limit of small pion mass. *Phys. Rev. D*, 6:2912–2918, 1972.

[128] Martin Hoferichter, Bastian Kubis, and Marvin Zanke. Radiative resonance couplings in $\gamma\pi\to\pi\pi$. *Phys. Rev. D*, 96(11):114016, 2017.

[129] K. Jansen, C. McNeile, C. Michael, and C. Urbach (ETM). Meson masses and decay constants from unquenched lattice QCD. *Phys. Rev. D*, 80:054510, 2009.

[130] Tyler D. Blanton, Fernando Romero-López, and Stephen R. Sharpe. $I = 3$ Three-Pion Scattering Amplitude from Lattice QCD. *Phys. Rev. Lett.*, 124(3):032001, 2020.

[131] Matthias Fischer, Bartosz Kostrzewa, Liuming Liu, Fernando Romero-López, Martin Ueding, and Carsten Urbach. Scattering of two and three physical pions at maximal isospin from lattice QCD. *Eur. Phys. J. C*, 81(5):436, 2021.

[132] Tyler D. Blanton, Andrew D. Hanlon, Ben Hörz, Colin Morningstar, Fernando Romero-López, and Stephen R. Sharpe. Interactions of two and three mesons including higher partial waves from lattice QCD. *JHEP*, 10:023, 2021.

[133] Ángel S. Miramontes, Hèlios Sanchis Alepuz, and Reinhard Alkofer. Elucidating the effect of intermediate resonances in the quark interaction kernel on the timelike electromagnetic pion form factor. *Phys. Rev. D*, 103(11):116006, 2021.

[134] Fredy F. Mojica, Carlos E. Vera, Eduardo Rojas, and Bruno El-Bennich. Mass spectrum and decay constants of radially excited vector mesons. *Phys. Rev. D*, 96(1):014012, 2017.

[135] Craig D. Roberts and Anthony G. Williams. Dyson-Schwinger equations and their application to hadronic physics. *Prog. Part. Nucl. Phys.*, 33:477–575, 1994.

[136] Maxwell T. Hansen, Harvey B. Meyer, and Daniel Robaina. From deep inelastic scattering to heavy-flavor semileptonic decays: Total rates into multihadron final states from lattice QCD. *Phys. Rev. D*, 96(9):094513, 2017.

[137] Raúl A. Briceño, Andrew W. Jackura, Arkaitz Rodas, and Juan V. Guerrero. Prospects for $\gamma\star\gamma\star\to\pi\pi$ via lattice QCD. *Phys. Rev. D*, 107(3):034504, 2023.

[138] C. Adolph et al. (COMPASS). Odd and even partial waves of $\eta\pi^-$ and $\eta'\pi^-$ in $\pi^- p \to \eta^{(\prime)}\pi^- p$ at 191 GeV/c. *Phys. Lett. B*, 740:303–311, 2015. [Erratum: Phys.Lett.B 811, 135913 (2020)].

[139] A. Rodas et al. (JPAC). Determination of the pole position of the lightest hybrid meson candidate. *Phys. Rev. Lett.*, 122(4):042002, 2019.

[140] M. Ablikim et al. (BESIII). Observation of an Isoscalar Resonance with Exotic JPC=1-+ Quantum Numbers in J/$\psi\to\gamma\eta\eta$'. *Phys. Rev. Lett.*, 129(19):192002, 2022. [Erratum: Phys.Rev.Lett. 130, 159901 (2023)].

[141] M. Ablikim et al. (BESIII). Partial wave analysis of $J/\psi \to \gamma\eta\eta'$. *Phys. Rev. D*, 106(7):072012, 2022. [Erratum: Phys.Rev.D 107, 079901 (2023)].

[142] Feiyu Chen, Xiangyu Jiang, Ying Chen, Ming Gong, Zhaofeng Liu, Chunjiang Shi, and Wei Sun. 1-+ hybrid meson in J/ψ radiative decays from lattice QCD. *Phys. Rev. D*, 107(5):054511, 2023.

[143] Raul A. Briceno, Jozef J. Dudek, Robert G. Edwards, Christian J. Shultz, Christopher E. Thomas, and David J. Wilson. The resonant $\pi^+\gamma \to \pi^+\pi^0$ amplitude from Quantum Chromodynamics. *Phys. Rev. Lett.*, 115:242001, 2015.

[144] Constantia Alexandrou, Luka Leskovec, Stefan Meinel, John Negele, Srijit Paul, Marcus Petschlies, Andrew Pochinsky, Gumaro Rendon, and Sergey Syritsyn. $\pi\gamma \to \pi\pi$ transition and the ρ radiative decay width from lattice QCD. *Phys. Rev. D*, 98(7):074502, 2018. [Erratum: Phys.Rev.D 105, 019902 (2022)].

[145] Roel Aaij et al. (LHCb). Observation of CP Violation in Charm Decays. *Phys. Rev. Lett.*, 122(21):211803, 2019.

[146] Dimitra A. Pefkou, Daniel C. Hackett, and Phiala E. Shanahan. Gluon gravitational structure of hadrons of different spin. *Phys. Rev. D*, 105(5):054509, 2022.

[147] Christian Drischler, Wick Haxton, Kenneth McElvain, Emanuele Mereghetti, Amy Nicholson, Pavlos Vranas, and André Walker-Loud. Towards grounding nuclear physics in QCD. *Prog. Part. Nucl. Phys.*, 121:103888, 2021.

VITA

Felipe Gilberto Ortega Gama

Felipe Gilberto Ortega Gama was born in Toluca, State of Mexico, Mexico. He attended Tecnológico de Monterrey in Mexico, pursuing a B.Sc. in Engineering Physics. Later, he completed an M.Sc. degree in the PSI program at the Perimeter Institute and the University of Waterloo in Canada. In 2018, he joined William & Mary to work on hadronic physics and study the non-perturbative aspects of quantum chromodynamics. After graduation, he will become a postdoctoral fellow at the University of California, Berkeley.